Mechanics Regulate Stem Cell Differentiation and Tissue Development

by

Jonathon M Muncie

DISSERTATION

Submitted in partial satisfaction of the requirements for degree of

DOCTOR OF PHILOSOPHY

in

Bioengineering

in the

GRADUATE DIVISION

of the

UNIVERSITY OF CALIFORNIA, SAN FRANCISCO
AND
UNIVERSITY OF CALIFORNIA, BERKELEY

Approved:

DocuSigned by:
Valerie Weaver
48C0A2F0F26A4A7...

Valerie Weaver

Chair

DocuSigned by:
Todd McDevitt
[illegible]

Todd McDevitt

DocuSigned by:
[illegible]
1C64F66851A942B...

Sanjay Kumar

Committee Members

To my parents, Kimberly and Michael Muncie,

and my brother, Christopher Muncie

ACKNOWLEDGEMENTS

I am proud to present the body of work in this dissertation and to have earned my Ph.D., but it is not an accomplishment I could have completed on my own. There are a number of individuals, both in and outside of the scientific community, whose support made this possible and to whom I am sincerely grateful. While it is challenging to properly express this gratitude in relatively few words, I will do my best.

First and foremost, I want to thank Professor Allen Liu at the University of Michigan. I applied to work in Professor Liu's laboratory the summer following my sophomore year of undergraduate. At the time, Professor Liu was starting his laboratory, and although he interviewed more qualified candidates with previous research experience, he took a chance and hired me because I expressed an interest in a career of research. I spent a year and a half in Professor Liu's lab and it is almost certain that I would not have been admitted to this Ph.D. program without that experience. Moreover, Professor Liu has continued to serve as a scientific mentor, and it has been truly a pleasure to keep in touch and meet up at scientific meetings over the course of my graduate studies.

Of course, I must thank my graduate advisor and mentor, Professor Valerie Weaver, who also took a chance on me when I came to her as a "bright-eyed, bushy-tailed first-year graduate student" (her words) and asked to work on stem cell biology, rather than in her field of expertise, cancer biology. Professor Weaver has been an excellent graduate advisor – she gave me the opportunity to explore many areas of interest, she challenged me to persevere through periods when progress felt slow, and she advocated for me in many professional arenas, ultimately helping me to publish my work and to obtain a Postdoctoral position. When I reflect on my professional growth over the course of my graduate studies, it is astounding how far I have come, and it is clear that Professor Weaver facilitated much of that growth.

I also owe a great deal of thanks to all the members of the Weaver Lab I was fortunate enough to work with over the past few years. In particular, a huge thank you to Dr. Johnathon Lakins, who not only developed and optimized many of the key tools and methodologies that made my work possible, but also served as a day-to-day mentor and helped me think through and crystalize many of the key ideas and hypotheses that drove this work. Thanks also to Dr. Laralynne Przybyla, who was a Postdoc in the Weaver Lab when I started and was tasked with teaching me stem cell culture, how to make polyacrylamide hydrogels, and was my go-to person for the endless stream of questions I had about designing experiments, finding reagents in the lab, etc. If not for her patience and generosity with her time, I might have really struggled through my first couple of years in the lab. Finally, thank you to Nadia Ayad, another graduate student in the Weaver Lab interested in stem cell biology whom I had the pleasure to mentor when she rotated through the Weaver Lab. Nadia's level of proficiency from the start challenged me to be a better scientist, and I think it is no coincidence that the most productive time period of my graduate studies was the same time period during which I served as her mentor.

I would like to thank the Graduate Program in Bioengineering at UC Berkeley and UCSF for giving me the opportunity to pursue a Ph.D. in such an exceptional environment. In particular, I would like to thank my other dissertation committee members, Professors Todd McDevitt and Sanjay Kumar. Their critical and constructive feedback was instrumental in guiding this work along the way, and each of them served as a mentor to me in a capacity well beyond their responsibility as a committee member. I am also grateful to the UCSF Discovery Fellowship, not only for financially supporting my travel to a number of scientific meetings, but also because receiving the award was a major source of affirmation and motivation after numerous rejection letters from other fellowships.

I am also extremely grateful and fortunate to have had the support of an incredible group of friends: Dave Monteiro, Roberto Falcon-Banchs, Karen Samy, Courtney Mazur, Allison Drain, Rami

Botros, and Nick Smith. When I moved to the Bay Area six years ago, I had no friends or family anywhere nearby. This close-knit group of friends truly became like a second family to me. I treasure my individual friendships with each of them, and all the amazing experiences we shared together will certainly become cherished memories I will hold on to for the rest of my life.

A special thank you to Ivana Vasic, the best partner I could ask for. It's hard to believe I didn't meet Ivana until about halfway through my Ph.D., as now it is impossible to imagine how I would have accomplished this without her limitless care and support. She was there to lift me up when I faced personal and professional challenges, and she has likewise been there with me to celebrate the culmination of all this work. I also want to thank Ivana's parents Bane and Dragana, and her sister Jelena, who all generously took me in and let me stay with them for more than 8 weeks during the height of the COVID-19 pandemic. It was during that time at their home in Tucson, Arizona when I actually wrote the majority of this dissertation, and I will always remember those days when I look back on this work.

Finally, thank you to my entire family, and especially my parents and brother, for whom I've dedicated this dissertation. I have been so fortunate to belong to such a loving, caring, and supportive family. They have been behind me for every pursuit and challenge I have taken on, and there is no way I could have accomplished this without them. I know it was difficult for them, as it was for me, when I moved away from home to pursue this degree. I hope I can make them happy and proud by always continuing to strive for success in their honor.

CONTRIBUTIONS

Przybyla, L., **Muncie, J. M.**, & Weaver, V. M. (2016a). Mechanical control of epithelial-to mesenchymal transitions in development and cancer. Annual Review of Cell and Developmental Biology, 32, 527-554.

Muncie, J. M., & Weaver, V. M. (2018). The physical and biochemical properties of the extracellular matrix regulate cell fate. In: Current Topics in Developmental Biology (Vol. 130, pp. 1-37). Academic Press.

Libby, A. R., Joy, D. A., So, P. L., Mandegar, M. A., **Muncie, J. M.**, Mendoza-Camacho, F. N., ... & McDevitt, T. C. (2018). Spatiotemporal mosaic self-patterning of pluripotent stem cells using CRISPR interference. Elife, 7, e36045.

Muncie, J. M., Falcón-Banchs, R., Lakins, J. N., Sohn, L. L., & Weaver, V. M. (2019). Patterning the geometry of human embryonic stem cell colonies on compliant substrates to control tissue-level mechanics. JoVE (Journal of Visualized Experiments), (151), e60334.

Eliazer, S., **Muncie, J. M.**, Christensen, J., Sun, X., D'Urso, R. S., Weaver, V. M., & Brack, A. S. (2019). Wnt4 from the niche controls the mechano-properties and quiescent state of muscle stem cells. Cell Stem Cell, 25(5), 654-665.

Muncie, J. M., Ayad, N. M., Lakins, J. N., Xue, X., Fu, J., & Weaver, V. M. (2020). Mechanical tension promotes formation of gastrulation-like nodes and patterns mesoderm specification in human embryonic stem cells. Developmental Cell. https://doi.org/10.1016/j.devcel.2020.10.015

"It is not birth, marriage, or death, but gastrulation, which is truly the most important time in your life."

Lewis Wolpert (1986)

ABSTRACT

Mechanics Regulate Stem Cell Differentiation and Tissue Development

by

Jonathon M Muncie

Engineering functional tissues and organs from stem cells requires simultaneous control over both cell fate and organization of tissue architecture. Cell-generated forces, such as cytoskeletal contractility, traction stresses, and cell-cell tension have long been recognized as critical drivers of tissue morphogenesis; nevertheless, it has remained unclear whether these physical forces also directly regulate cell fate decisions by modulating biochemical signaling pathways. In this work, we demonstrated that human embryonic stem cells (hESCs) cultured on compliant engineered substrates self-organize to form discrete gastrulation nodes that foster mesoderm specification. We identified a mechanism whereby localized high cell-adhesion tension induces mesoderm specification by enhancing Wnt/β-catenin signaling, and furthermore, we showed that application of mechanical tension via stretching is sufficient to induce mesoderm specification. Additionally, we demonstrated that cell adhesion proteins and regulators of cytoskeletal contractility control pattern formation in human induced pluripotent stem cells (hiPSCs), independent of cell fate specification. Further, we discovered that a specific Wnt ligand from the niche regulates muscle stem cell (SC) quiescence via Rho signaling that promotes SC contractility. Finally, we developed a novel protocol for performing atomic force microscopy (AFM) on mouse bone marrow to enable characterization of the biophysical properties of the hematopoietic stem cell (HSC) niche. Together, these findings underscore the interplay between tissue organization, cell-generated forces, and morphogen-dependent differentiation. This body of work demonstrates that mechanical forces play a direct role in cell fate specification during development and regulate stem cell function in the adult organism.

TABLE OF CONTENTS

LIST OF FIGURES

LIST OF TABLES

LIST OF ABBREVIATIONS

AFM	atomic force microscopy
AJC	apical junctional complex
bFGF	basic fibroblast growth factor
BMP	bone morphogenetic protein
BrdU	bromodeoxyuridine
CDH1	cadherin-1 (or: E-cadherin)
cDNA	complementary DNA
CI	confidence interval
CRISPR	clustered regularly interspaced short palindromic repeats
CRISPRi	CRISPR interference
DDR	discoidin domain receptor
DMEM	Dulbecco's modified eagle medium
DNA	deoxyribonucleic acid
DOX	doxycycline
ECM	extracellular matrix
EDL	extensor digitorum longus
eMHC	embryonic myosin heavy chain
EMT	epithelial to mesenchymal transition
EpCAM	epithelial cell adhesion marker
FACS	fluorescence-activated cell sorting
FGF	fibroblast growth factor
FN1	fibronectin 1

GAG	glycosaminoglycan
GFP	green fluorescent protein
gRNA	guide RNA
GSC	goosecoid
HA	hyaluronic acid
HDR	homology-directed repair
HEK	human embryonic kidney (cells)
hESC	human embryonic stem cell
Hh	hedgehog
hiPSC	human induced pluripotent stem cell
hPSC	human pluripotent stem cell
HSC	hematopoietic stem cell
IF	immunofluorescent
IGF	insulin-like growth factor
IGFBP	insulin growth factor binding protein
IPA	isopropyl alcohol
iPSC	induced pluripotent stem cell
ISH-HCR	*in situ* hybridization via hybridization chain reaction
KD	knockdown
KSR	knockout serum replacement
MEC	mammary epithelial cell
mESC	mouse embryonic stem cell
MLC	myosin light chain
MMP	matrix metalloproteinase

MSC	mesenchymal stem cell
MSGN1	mesogenin 1
MSM	monolayer stress microscopy
MyoD	myoblast determination protein 1
OSR1	odd-skipped related transcription factor 1
PA	polyacrylamide
PBS	phosphate buffered saline
PCR	polymerase chain reaction
PDGFA	platelet-derived growth factor subunit A
PDMS	polydimethylsiloxane
PFA	paraformaldehyde
pFAK	phosphorylated focal adhesion kinase
PMEF	primary mouse embryonic fibroblast
pMLC	phosphorylated myosin light chain
PMZ	posterior marginal zone
PPS	potassium persulfate
pSFK	phosphorylated src-family kinase
qPCR	quantitative polymerase chain reaction
QSC	quiescent satellite cell
rBM	reconstituted basement membrane
RNA	ribonucleic acid
ROCK1	rho-associated coiled-coil containing protein kinase
ROI	region of interest
RSPO3	R-spondin 3

RT-PCR	reverse transcription polymerase chain reaction
SC	satellite cell (or: muscle stem cell)
SD	standard deviation
SEM	standard error of the mean
SFK	src-family kinase
Shh	sonic hedgehog
TA	tibialis anterior
TBXT	T-box transcription factor T (or: T[brachyury])
TBX6	T-box transcription factor 6
TFM	traction force microscopy
TGF-β	transforming growth factor β
TMX	tamoxifen
WT	wildtype
Y654	tyrosine 654 of β-catenin

CHAPTER 1

Introduction

Portions of this chapter have been adapted from text published in the peer-reviewed book chapter titled "The Physical and Biochemical Properties of the Extracellular Matrix Regulate Cell Fate" by **Jonathon M. Muncie** and Valerie M. Weaver in Current Topics in Developmental Biology, Extracellular Matrix and Egg Coats (2018), edited by Eveline S. Litscher and Paul M. Wassarman.

TISSUE ENGINEERING

Tissue engineering involves using a combination of materials and scaffolds, cells, and supplemental molecules to generate biologically functional tissues and organs (Figure 1.1). The goal of tissue engineering is to use engineered tissues in applications related to improving health. These potential applications typically fall into one of two categories: i) using engineered tissues as model systems for screening the safety and efficacy of novel therapeutics, or ii) transplanting engineered tissues into patients to treat diseased or damaged tissues and organs. While the material scaffolds and supplemental molecules used in tissue engineering are undoubtably important, arguably the most significant feature of an engineered tissue is the cellular component. In certain applications, primary adult cells can be biopsied or cultured in the lab and then assembled along with any required scaffolding or biochemical molecules to form the engineered tissue (Makris et al., 2015; L. Wang et al., 2017). However, many cell types cannot be biopsied or maintained in culture for multiple passages, and thus, these cell types must be generated *in vitro*. This is accomplished by using stem or progenitor cells and differentiating them to specialized cell types (Trounson & DeWitt, 2016). While much progress has been made in developing protocols for differentiating stem cells to desired cell types, there remain a large number

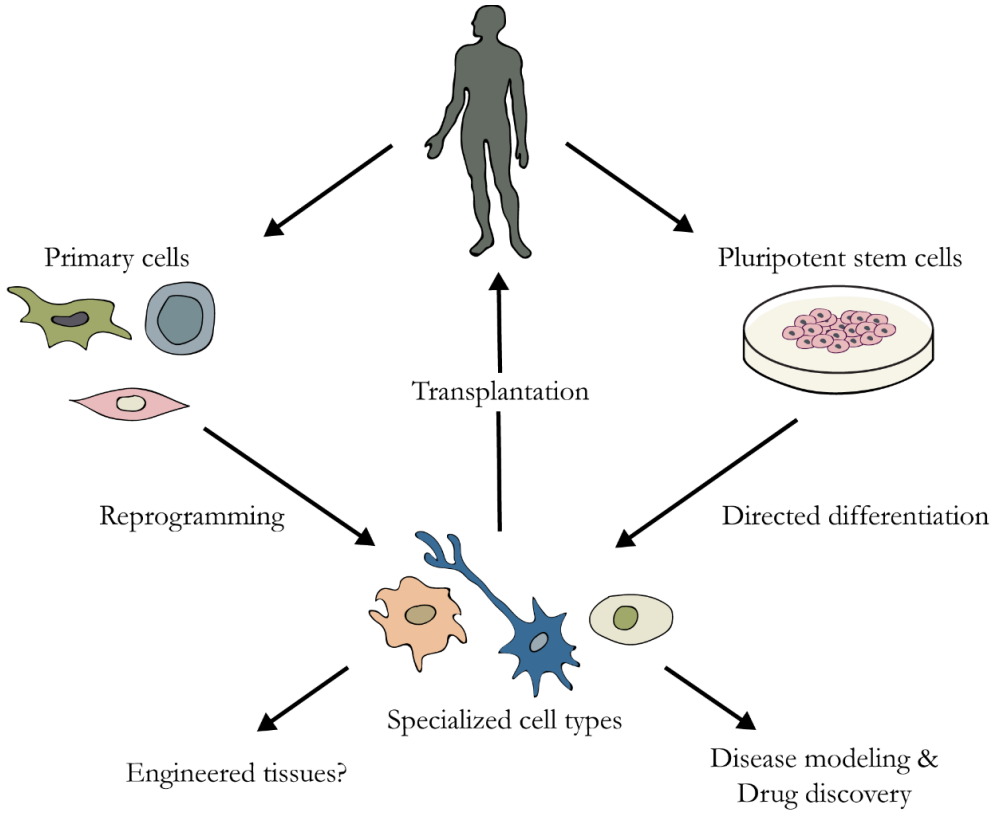

Figure 1.1: An overview of tissue engineering and regenerative medicine.
Schematic illustrating the overarching goals of tissue engineering and regenerative medicine. Primary cells isolated from human subjects or pluripotent and multipotent stem cells are used to derive specialized cell types *in vitro*. A variety of engineering and biological techniques can then be used to attempt to assemble these cell types into model systems, and ultimately, functional tissues and organs, that can be used for disease modeling and drug discovery. The ultimate goal of regenerative medicine is to transplant these engineered tissues into diseased patients to restore healthy physiology.

of challenges in using the generated cells to form functional tissues.

Many of the challenges associated with using differentiated stem cells in tissue engineering applications are due to the inherent complexity of human tissues and organs – most tissues consist of a large variety of different cell types, organized in very specific 3D architectures that are necessary for tissue function, and require vascularization and integration with other organ systems in the body. In order to overcome these challenges, we turn to developmental biology for inspiration. During development, a relatively small number of pluripotent stem cells grow, divide, and undergo tightly

coordinated programs differentiation and morphogenesis that lead to the co-emergence of all the tissues and organs that make up a living organism. By better understanding the mechanisms that regulate development, we hope to learn how to drive the co-emergence and 3D organization of multiple cell types from stem cells *in vitro*, and ultimately improve our ability to engineer functional tissues in the laboratory.

EARLY DEVELOPMENT AND GASTRULATION

The process of embryonic development begins when a sperm successfully fuses with an egg, forming a fertilized zygote. This zygote then undergoes a number of rounds of cell division, termed cleavage, and these cells organize to form the blastocyst, consisting of the inner cell mass and blastocyst cavity, surrounded by the trophoblast. The inner cell mass then segregates to form the epiblast and hypoblast, and subsequently gastrulation begins. Among these processes of early development, gastrulation is of particular note because it marks the first cell fate decision of the embryo proper, as the epiblast differentiates into the three primary germ layers: ectoderm, mesoderm, and endoderm.

Interestingly, the chicken serves as an excellent model organism for studying gastrulation because the physical organization of the embryo at this stage is similar to that of human (Figure 1.2; Mikawa et al., 2004; Shahbazi & Zernicka-Goetz, 2018). In both cases, the epiblast lays flat atop the hypoblast (called the bilaminar disc, in humans) at the beginning of gastrulation. As gastrulation progresses, tissue movements (termed "Polonaise" movements, in chicken) drive cells of the epiblast towards the midline at the posterior of the embryo, forming a transient structure called the primitive streak, which elongates anteriorly throughout gastrulation (Gräper, 1929; Mikawa et al., 2004; Voiculescu et al., 2014). As epiblast cells reach the primitive streak, they undergo an epithelial to mesenchymal transition (EMT) and ingress ventrally to form additional cell layers as they

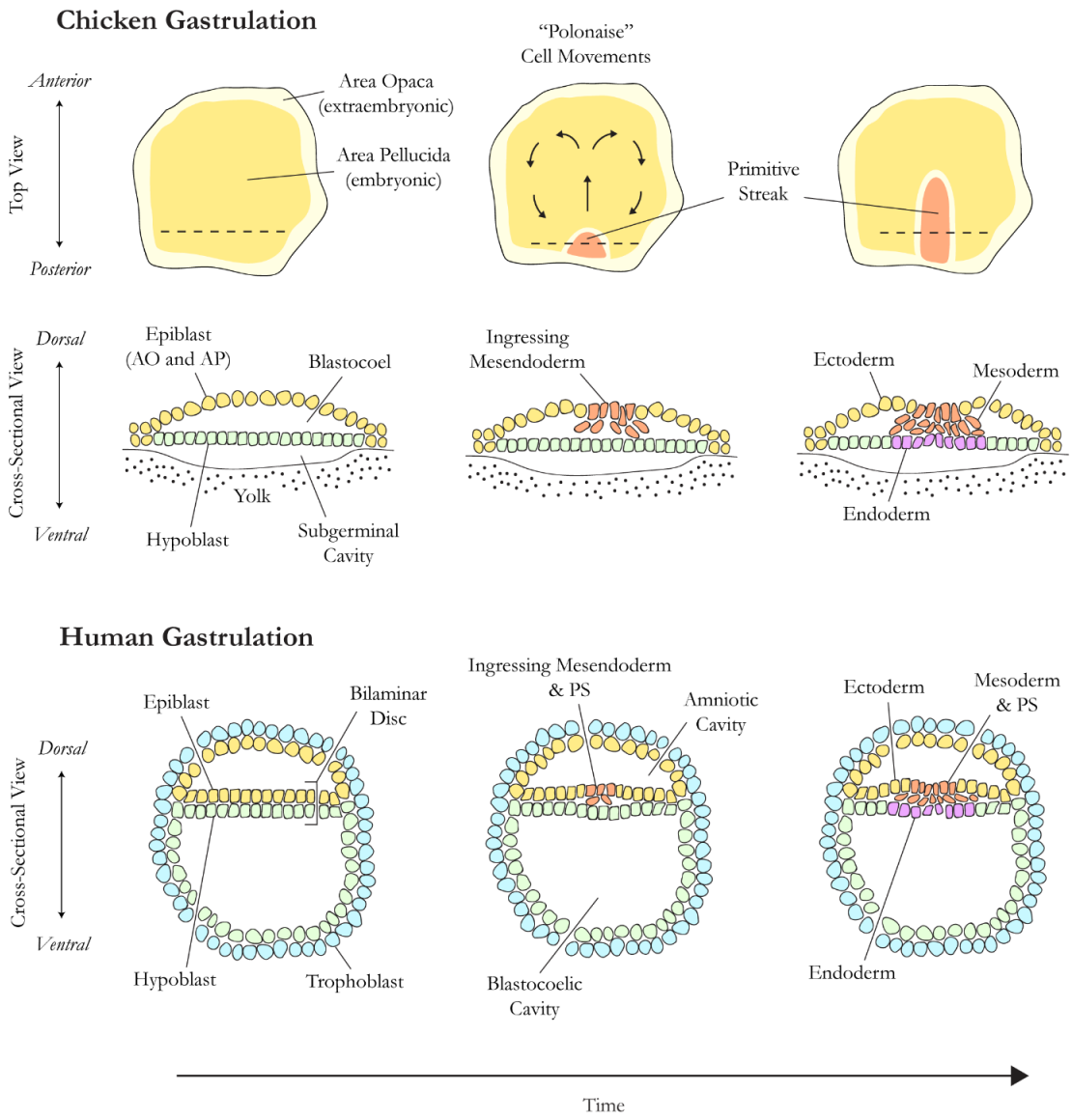

Figure 1.2: Schematic of gastrulation in chicken and human embryos.
Schematic illustrating the similarities and differences of gastrulation in chicken and human embryos. In the chicken, fluid-like "Polonaise" movements drive pluripotent epiblast cells towards the posterior midline of the embryo, causing formation and elongation of the primitive streak. It is unknown whether similar movements occur in the human embryo. In both organisms, cells at the primitive streak undergo an epithelial to mesenchymal transition (EMT) and ingress to form additional cell layers as they simultaneously differentiate to mesendoderm progenitors, which later undergo further cell fate specification to become the mesoderm and definitive endoderm germ layers. Cells that remain in the epiblast during gastrulation become specified to the ectoderm germ layer.
AO = Area Opaca. AP = Area Pellucida. PS = Primitive Streak.

simultaneously ddfifferentiate to form the mesoderm and endoderm germ layers. The cells that remain in the dorsal layer (previously the epiblast), form the ectoderm germ layer.

As is clear from our current understanding, gastrulation involves cell fate decisions that are intimately tied to a critical morphogenesis that lays the foundational body plan of the future organism. Thus, further insight into the biological mechanisms that co-regulate these processes could yield critical discoveries that advance our ability to engineer tissues *in vitro*. Throughout the remainder of this Chapter, I will review what is currently known about the roles of the extracellular matrix (ECM), morphogen signaling, and cell- and tissue-level forces in early development and gastrulation, and identify the key open questions that were addressed through the studies presented in the subsequent Chapters of this dissertation.

THE EXTRACELLULAR MATRIX AND DEVELOPMENT

Overview

The ECM is a complex network of proteins, polysaccharides, and water that comprise the acellular stromal microenvironment in all tissues and organs. Historically, the ECM was thought to serve primarily to provide structural information required to maintain the physical integrity of the tissue. However, it is now understood that the ECM is a biologically active component of all tissues that directs cell fate and influences tissue development and homeostasis.

As organisms develop, they continuously generate and reorganize their ECM to provide the necessary structural framework to support the growth and development of emerging tissues. The ECM in turn provides critical biochemical and biophysical cues that guide cell fate, drive morphogenetic movements to sculpt the tissue, and induce tissue-specific differentiation. The concept of "dynamic reciprocity," which maintains that the evolving ECM dictates cell and tissue fate which then feedback to modulate ECM composition and organization, represents a critical concept in

developmental biology (Bissell et al., 1982; Paszek & Weaver, 2004). "Tensional homeostasis" incorporates the viscoelasticity of the ECM and cell tension into the dynamic reciprocity paradigm, thereby providing a unified working hypothesis with which to understand how the evolving biochemical and biophysical properties of the ECM direct development and maintain tissue homeostasis.

In fact, the ECM is quite dynamic (Lu et al., 2011; Page-McCaw et al., 2007; Streuli, 1999). The protein components of the ECM are turned over regularly, and the cells within the tissue are actively engaged in remodeling their local ECM (Bonnans et al., 2014). Virtually all cells produce and secrete ECM proteins into their microenvironment, together with matrix metalloproteinases (MMPs), which degrade ECM proteins (Bonnans et al., 2014; Mecham, 2012; Page-McCaw et al., 2007). Cells also assemble and disassemble their local ECM by binding specific residues on matrix proteins and exerting physical forces generated by actomyosin contractility to modify the three-dimensional (3D) conformation and organization of these proteins (Ohashi et al., 2002; Pankov et al., 2000; C. Zhong et al., 1998). Cellular remodeling can promote interactions between different ECM molecules or reveal cryptic binding sites within the ECM molecule that promote cell adhesion and proliferation (G Baneyx et al., 2001; Gretchen Baneyx et al., 2002; C. Zhong et al., 1998). The ability of the ECM to be constantly remodeled and reorganized is critical for development, tissue-specific differentiation, and stem cell fate specification.

The ECM is also a key component of the adult stem cell niche – the local microenvironment that sustains stem cell quiescence and facilitates the maintenance of stem cells through regulated self-renewal and retention of multipotency. The ECM physically buffers stem cells that reside within the niche from differentiation cues, sequesters critical growth factors and morphogens, and facilitates efficient nutrient exchange to sustain the long-term growth, survival, and multipotency of the stem cells.

ECM Composition

The main functional units of the ECM are cell-secreted macromolecular proteins. There are four general classes of ECM proteins: collagens, proteoglycans, glycoproteins, and elastins (Figure 1.3; Tsang et al., 2010).

Collagens provide the tissue with tensile strength and structural integrity (Gordon & Hahn, 2010; Lodish et al., 2000). Collagens are composed of three alpha chains that assemble into heterotrimeric and homotrimeric molecules, various combinations which comprise the 28 recognized types of collagen. Fibrillar collagens are the most common type and are assembled in woven triple-helical structures that arise from long repeating stretches of Gly-X-Y residues in the alpha chains. In these repeated stretches, X is typically proline and Y is typically hydroxyproline. These triple helices then self-assemble into thin and thick fibrils. Nonfibrillar collagens arise from disruptions in the Gly-X-Y repeats of the alpha chains. Instead of forming fibrils, these nonfibrillar collagens form mesh-like networks in the ECM, such as collagen IV found in basement membranes.

The biochemical and mechanical properties of fibrillar collagens are largely dependent on post-translational modifications that drive the cross-linking of the collagen fibrils, and thus dictate the tensile strength of the tissue. Proline and lysine residues on procollagens are hydroxylated intracellularly by specific enzymes (Yamauchi & Sricholpech, 2012). These hydroxylated residues can be further modified within the cell by enzyme-mediated glycosylation, resulting in the addition of galactose or glucose. Collagen glycosylation alters cell–collagen interactions, and thus broadly influences the biological functions of collagen, such as the ability of collagens to direct angiogenesis or bone mineralization (Jürgensen et al., 2011; Palmieri et al., 2010; Tenni et al., 1993). Once procollagens are secreted to the extracellular space and are self-assembled into fibrils, specific lysine and hydroxylysine residues are deaminated by an enzyme called lysyl oxidase (LOX) that produces reactive aldehyde groups that initiate covalent cross-links via condensation reactions. Lysyl oxidase

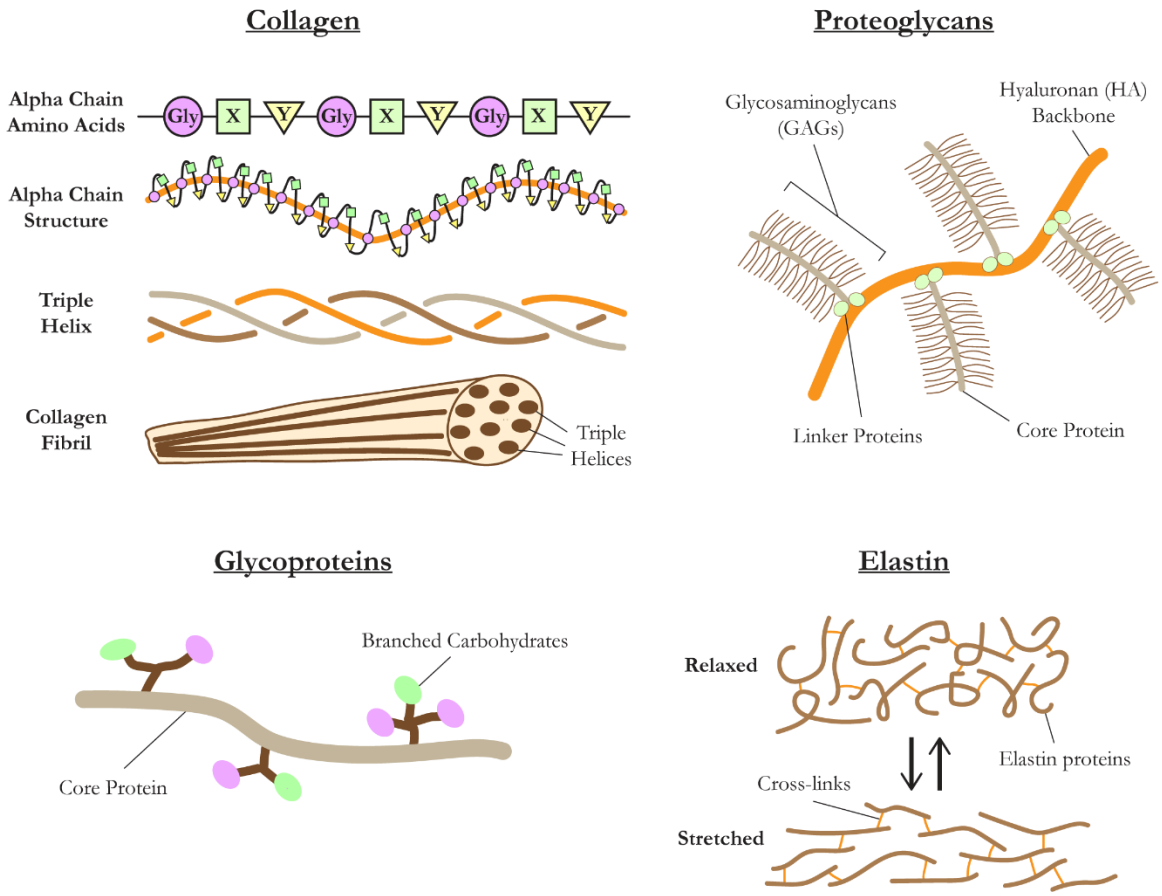

Figure 1.3: The key components of the extracellular matrix.
Schematic illustrating the biochemical composition and organization of each of the four key components of the extracellular matrix: collagens, proteoglycans, glycoproteins, and elastins.

and hydroxylase cross-linking are critical for the tensile strength and structural stability of tissues, and loss of their activity has deleterious consequences to the organism, including bone fragility, cardiovascular disease, and in some instances, lethality (Kagan & Li, 2003; Mäki et al., 2002). Thus, extracellular post-translational modifications to fibrillar collagen expand its structure-function and modify its biological role in tissues.

Proteoglycans consist of a core protein domain covalently linked to glycosaminoglycans (GAGs; Mouw et al., 2014). These GAGs form long, negatively charged, linear repeats of disaccharide units, and provide proteoglycans with their unique ability to bind water, which is critical for imparting

compressive resistance to tissues. Aggrecan and versican are common examples of proteoglycans that are ubiquitously expressed in many tissues. Hyaluronan, or hyaluronic acid (HA), is a common GAG that is also abundantly expressed in all tissues but has unique properties because it does not covalently attach to peptides (Laurent & Fraser, 1992). Thus, while not a true proteoglycan, HA possesses similar biological functions exhibited by proteoglycans. HA is abundantly expressed in the brain, where it forms a relatively "loose" and unorganized network. However, HA can also bind and form cross-links with other proteoglycans and glycoproteins, such as versican and tenascin, to support more condensed perineural networks (PNNs) that stiffen the neuronal microenvironment (Kwok et al., 2011). The formation of PNNs coincides with brain stiffening, reduced neuron growth and extension, and loss of plasticity in the developing brain, illustrating how tissue-specific biochemical properties of the ECM guide cell fate and tissue development (Kwok et al., 2011; Yamaguchi, 2000).

Glycoproteins are similar to proteoglycans in that they consist of peptide units and covalently bound carbohydrate groups. However, whereas proteoglycans are characterized by long, linear chains of repeating disaccharides, glycoproteins contain bulky, branched carbohydrates with no, or few, repeating structures. Glycoproteins serve as connector molecules within the ECM because they contain functional groups that recognize and bind to other ECM molecules, as well as to cell adhesion proteins, secreted growth factors, and morphogens. Fibronectin and laminin are two predominant and important glycoproteins found in the ECM.

Fibronectin is secreted into the extracellular microenvironment and then forms polymerized fibrils with other fibronectin molecules or with collagen by a cell-dependent process termed fibrillogenesis (Kadler et al., 2008; Singh et al., 2010). In fact, cross-linking of collagen by LOX depends upon fibronectin, emphasizing the importance of intimate interactions between ECM proteins in regulating the structure-function of individual components (Kubow et al., 2009). The RGD sequence (Arg-Gly-Asp), which can bind to specific cellular transmembrane proteins called integrins,

is a particularly important cell-binding motif within the fibronectin molecule. However, the strength of cell–integrin interactions with fibronectin is greatly enhanced through binding to the separate fibronectin synergy sequence (Schwarzbauer & DeSimone, 2011; Sechler et al., 1997). Fibroblasts, in particular, are capable of unfolding fibronectin to reveal cryptic cell-binding sites, including the synergy sequence (Friedland et al., 2009; Seong et al., 2013; M. L. Smith et al., 2007). Once revealed, the synergy sequence can then be ligated by cellular α5β1 integrin to potentiate intracellular tension and alter epithelial or endothelial morphogenesis or fibroblast function (Benito-Jardón et al., 2017; Friedland et al., 2009; Miroshnikova et al., 2017). In this way, fibronectin structure-function can be distinctly modulated by cell-generated force to alter cell and tissue function.

Laminins are composed of α, β, and γ heterotrimer chains that connect via central domains to form cross-shaped, Y-shaped, or single-arm structures (Mouw et al., 2014; Timpl & Brown, 1994). Laminins are localized to the basal lamina of tissues and function primarily to connect various components of the ECM. Laminins are classified according to their subunit composition, such that laminin 111 refers to laminin trimers comprised of α1, β1, and γ1 chains (Aumailley et al., 2005). Laminin heterogeneity generates significant functional diversity. For instance, while laminin 111 polymerizes to form a meshwork that contributes to the tissue basement membrane, laminin 332, secreted during wound healing and hair follicle development, is subject to extensive proteolytic cleavage, which is critical for its ability to facilitate coordinated keratinocyte migration (Sugawara et al., 2008).

Elastin is a unique structural protein that imparts, as its name suggests, elastic properties to tissues such as the skin and vasculature. Whereas fibrillar collagen provides tensile strength to resist deformation, elastin provides tissues with resilience, so that when they are stretched, they can return to their original conformation. Elastins are typically more hydrated and flexible in their relaxed, as compared to their stretched, state. The precise structure-function relationship that attributes this

unique property of elastins is still a matter of debate, but is frequently described as the relaxed state being entropically favorable toward stretched configurations (Debelle & Tamburro, 1999).

In the preceding text, we have reviewed the different types of ECM proteins as discrete units according to their individual structure and functional properties. Nevertheless, it is important to appreciate that the tissue-specific biochemical and physical properties of the ECM arise from its complex organization, post-translational modifications, and its ability to be dynamically remodeled; and these are absolutely critical for the ECM's ability to influence cell and tissue fate.

The ECM is Critical for Proper Development

Beginning in the 1980s and early 1990s, the ECM was recognized as a critical regulator of embryogenesis and tissue-specific development. Gene analysis and manipulation studies in model organisms revealed that several developmental defects could be mapped back to ECM proteins (Adams & Watt, 1993). In *Caenorhabditis elegans*, *dpy-13* (dumpy) was identified as a member of the collagen gene family, and mutations to *dpy-13* were shown to cause a short and chunky body shape (von Mende et al., 1988). Mutations to *Sqt-1* and *clb-2* were also identified as sequences for collagen proteins that caused significant developmental defects in body shape, with the *clb-2* mutation causing embryonic lethality (Guo et al., 1991; Kramer et al., 1988). Mutations to *unc-6*, a sequence for a laminin-related protein, caused defects in neural development that resulted from misguiding of axon extensions (Ishii et al., 1992). Similar studies in *Drosophila* identified mutations to the gene-coding sequences of laminin A and the *Drosophila* analog for fibrinogen, which both led to significant developmental defects (Baker et al., 1990; Hortsch & Goodman, 1991). Furthermore, mutations to *Drosophila* integrins, the cellular receptors for ECM proteins, generated a host of defects ranging from wing, to eye, to muscle development (Brower & Jaffe, 1989; Leptin et al., 1989; T. Volk et al., 1990; Wilcox et al., 1989; Zusman et al., 1990).

In addition to mapping genetic mutations to ECM proteins and receptors, function-blocking manipulations of cell–ECM interactions have served to illustrate the importance of cell–matrix adhesions in tissue development. Decoupling interactions between mesodermal progenitors and fibronectin using function-blocking antibodies in the blastocoel roof of amphibian embryos prevented development from proceeding beyond gastrulation (Boucaut et al., 1984, 1985). Later in development, injection of the integrin-binding motif of fibronectin, the RGD peptide, prevented the proper establishment of left/right asymmetry in *Xenopus* embryos (Yost, 1992). Similarly, injection of RGD-containing peptides in *Gallus gallus domesticus* (chicken) embryos prevented neural crest cell migration (Boucaut et al., 1984).

ECM-Receptor Interactions Regulate Cell Fate

The ECM influences cell fate by binding to cell surface receptors that recognize specific ECM moieties. Once bound to the ECM, these cellular receptors alter cell growth, survival, motility, and differentiation by initiating intracellular signaling and cytoskeletal reorganization. The cellular receptors that bind to the ECM include integrins as well as discoidin domain receptors (DDRs), CD44, and Robo receptors.

Integrins, which are the best-studied ECM receptors, are transmembrane heterodimer molecules that bind to specific ECM residues and interact with adhesion plaque proteins and cytoskeletal linker proteins via their cytoplasmic tail. There are 18 alpha subunits and 8 beta subunits, which combine to form 24 distinct integrin heterodimers (Hynes, 2002). The combination of the alpha and beta subunits that recognize and bind different ECM molecules imparts functional specificity to integrins. Not only do integrins facilitate the physical interaction of cells with the ECM, but they also induce intracellular signaling, alter cytoskeletal organization, and stimulate cellular tension to regulate cell growth and survival, promote invasion and migration, and direct cell differentiation and stem cell fate.

Integrin adhesion and signaling are highly context dependent. For instance, α5β1, αvβ5, α6β1, and α9β1 integrins are highly expressed in mouse embryonic stem cells (mESCs), and their combined ligation to peptide-conjugated polyethylene glycol (PEG) hydrogels with fibronectin-derived peptide sequence RGDSP, CCN1-derived sequence TTSWSQ, and the tenascin-C-derived sequence AEIDGIE, can maintain their pluripotency in culture (S. T. Lee et al., 2010). By contrast, preventing the initial, but not the late, ligation of the collagen-binding integrins α1β1 and α2β1, using function-blocking antibodies, inhibited osteoblast differentiation of both multipotent 2T3 cells and freshly harvested bone marrow cells (Jikko et al., 1999; Mizuno et al., 2000). Indeed, blocking integrin binding to collagen I reduced osteoblast differentiation even in the presence of a constitutively active bone morphogenetic protein 2 (BMP-2) receptor, presumably by blocking BMP-2 receptor activation. Similarly, knocking down the fibronectin receptor α5β1 integrin prevented osteoblast differentiation of human mesenchymal stem cells (MSCs), whereas its activation and ligation by collagen promoted osteoblast differentiation (Hamidouche et al., 2009).

Integrins are critical regulators of cell fate during tissue-specific development and differentiation. For instance, Fässler and colleagues used β1-integrin-deficient embryonic stem cells to demonstrate the importance of β1 integrin in early cardiogenesis (Fässler et al., 1996). Similarly, although conditional β1 integrin knockdown in mammary epithelial cells (MECs) had no effect on branching morphogenesis of the adolescent mammary gland, lack of β1 integrin prevented pregnancy-associated MEC alveolar differentiation (Klinowska et al., 1999; Naylor et al., 2005). Thus, in the absence of β1 integrin, MECs failed to lactate, presumably because the cells could not respond to prolactin to activate transcription 5 (STAT5) signaling that is critically required for beta casein expression (Xu et al., 2009). Indeed, early studies identified β1 integrin signaling as necessary for MEC growth and survival (Boudreau et al., 1995; Klinowska et al., 1999; Naylor et al., 2005). These findings

underscore the critical context-dependent role of integrins in ECM-dependent regulation of stem cell fate.

Analogous to integrin receptors, the DDR subfamily of receptor tyrosine kinases that bind to extracellular collagens also modulate cell growth, survival, migration, and tissue morphogenesis by activating intracellular signaling and regulating gene transcription. For instance, DDR1 binding to collagen promotes the pluripotency of mESCs via Ras-mediated activation of phosphoinositide 3-kinase (PI3K)/Akt, and extracellular signal-regulated kinase (ERK), which both regulate BMI-1 (Suh & Han, 2011). Similarly, DDR2 ligation by collagen and ERK activation is critical for runt-related transcription factor 2 (Runx2) induction of osteogenic differentiation that likely explains the dwarfism and aberrant bone formation observed in the DDR2-null mouse (Labrador et al., 2001; Y. Zhang et al., 2011).

CD44 receptors, which bind to hyaluronan (HA), elicit profound effects on cell behavior by activating intracellular signaling and altering cytoskeletal organization. Thus, inhibiting CD44 binding to HA significantly reduced hematopoietic stem/progenitor cell (HSC/HPC) homing and engraftment into the bone marrow, presumably by impeding association with their endothelium and endosteum niche (Avigdor et al., 2004). Similarly, a role for CD44 in cell differentiation was underscored in CD44-null mice, which exhibited severely compromised keratinocyte differentiation and epidermal barrier formation, due to the fact that HA ligation is critical for lamellar body formation and secretion, and epidermal barrier development (Bourguignon et al., 2006). Interestingly, the CD44-null mice also had significantly reduced levels of extracellular HA, implicating cellular ligation in HA homeostasis.

Roundabout (Robo) proteins are another group of transmembrane receptors that bind to ECM glycoproteins termed Slits. Robo protein adhesion is critical for branching morphogenesis in the mammary gland (Macias et al., 2011), and Slit binding to Robo4 mediates HSC homing to the

bone marrow niche and efficient bone marrow engraftment (Smith-Berdan et al., 2011). In *Drosophila*, Robo–Slit interactions play an integral role in mediating intestinal tissue homeostasis. *Drosophila* intestinal epithelial cells secrete Slit, which suppresses endocrine lineage differentiation by binding and activating Robo2 receptors on adjacent stem cell progenitors (Biteau & Jasper, 2014).

Together, these studies clearly demonstrate that ECM proteins, and the cellular receptors they interact with, are critical regulators of cell differentiation and tissue development (Figure 1.4 A).

The ECM Directs Cell Migration During Development

ECM-directed cell migration is a critical determinant of cell fate specification during development (Figure 1.4 B). This concept was demonstrated by studies exploring the impact of cell–ECM interactions in heart development. The heart originates as a bi-layered tube formed by the ECM-dependent migration of myocardial precursors from the left and right lateral sides toward the midline of the organism. Zebrafish hearts exhibit serious developmental defects when mutations are induced in the fibronectin-encoding *natter* gene that impede myocardial precursor migration (Trinh & Stainier, 2004). Similarly, morpholino-mediated knockdown of zebrafish fibronectin in early embryogenesis compromised cardiac development in a manner that could be rescued by injection of exogenous fibronectin (Matsui et al., 2007).

Coordinated and directed ECM deposition is also a critical aspect of neural crest cell migration during embryogenesis. Neural crest cells migrate from the dorsal region of the developing neural tube and contribute to multiple cell types and tissues, including neurons and osteoblasts (Knecht & Bronner-Fraser, 2002). Conditional knockout of β1 integrin in mouse neural crest precursors compromised fibronectin, laminin, tenascin, and collagen IV deposition, prevented neural crest cell migration, and led to lethal neuronal defects, emphasizing the link between ECM deposition and tissue development (Pietri et al., 2004). It has also been demonstrated that the ECM components versican and aggrecan exhibit attractive and repellent effects, respectively, on neural crest cell migration

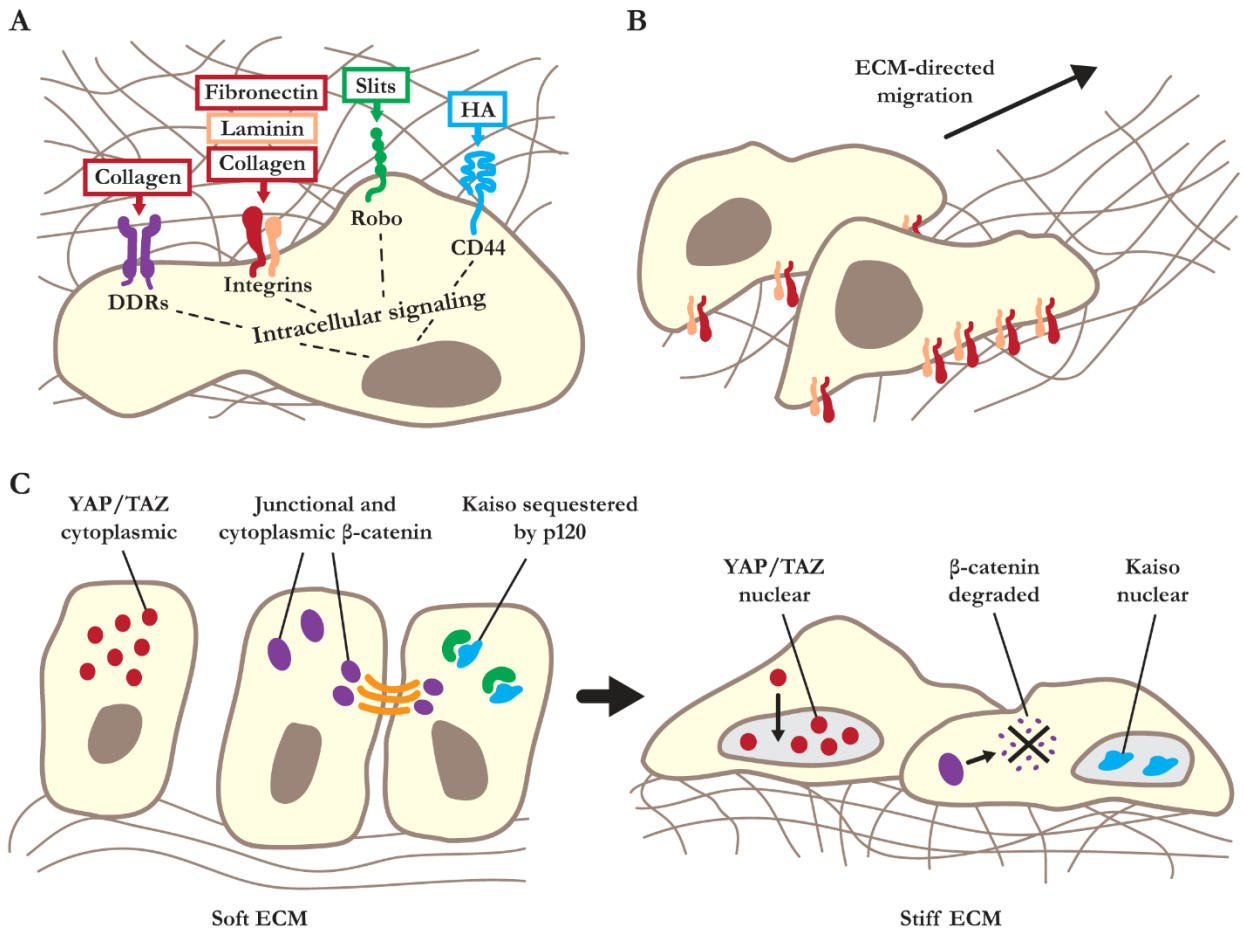

Figure 1.4: The ECM regulates development through multiple mechanisms.
(A) ECM proteins interact directly with cellular receptors to stimulate intracellular signaling that can regulate cell function and direct cell fate.
(B) The ECM facilitates cell migration that is critical for proper morphogenesis and tissue development.
(C) The stiffness of the ECM can influence multiple signaling pathways that are responsible for driving cell fate decisions during development.

(Perissinotto et al., 2000). Moreover, laminin α5 appears to restrict neural crest cell migration along confined pathways, as was illustrated by the unfettered broad migration of neural crest cells and compromised development of the organism when this laminin chain was knocked out (Coles et al., 2006). Not surprisingly, distinct ECM components direct cell migration in different tissues during development. For example, fibronectin facilitates migration of cranial neural crest cells, whereas vitronectin, collagen I, and laminin do not (Alfandari et al., 2003).

While these and other experiments emphasize the importance of the ECM in development, the main inference from these pioneering studies is that the ECM provides structural integrity to maintain cell adhesion-dependent tissue organization and that it facilitates directed cell migration. Over the past several decades this perspective has expanded to encompass a role for the ECM and its receptors as instructive developmental regulators that can direct cell fate.

ECM Stiffness Regulates Cell Fate

All tissues within the body exhibit distinct mechanical properties that reflect their structure-function and that are imparted predominantly by the composition and organization of their ECM. For example, the brain is quite soft, and this compliance primarily reflects the abundance of hydrated HA found in the ECM. By contrast, bone is very rigid, and this stiffness is mainly due to high amounts of densely packed, mineralized, cross-linked collagens. The stiffness of the ECM in specific differentiated tissues is not only critical for the structure and function of the tissue but also regulates the growth, survival, and motility of the cellular constituents and may even direct their lineage-specific differentiation (Figure 1.4 C).

Human MSCs may be directed to differentiate down multiple independent lineages, apparently simply by varying substrate elasticity (Engler et al., 2006). Thus, MSCs could be induced to display neurogenic markers when cultured on soft substrates (100–1000 Pa), analogous to the measured compliance of brain tissue, myogenic markers on substrates of intermediate stiffness (8000–17,000 Pa), reflecting the stiffness of skeletal muscle, and osteogenic markers on the most rigid substrates (25,000–40,000 Pa), representing the values measured in cortical bone tissue. Inhibition of non-muscle myosin abolished elasticity-dependent differentiation of these MSCs, implying actomyosin contractility is likely necessary to transduce information about the elasticity of the ECM via signaling pathways that regulate cell fate.

Neural stem cell differentiation was similarly found to be modulated by substrate stiffness (Saha et al., 2008), such that adult neural stem cells cultured in neurogenic media differentiated into neurons with the highest efficiency on substrates with an elasticity that is most similar to the brain (500 Pa). Even in mixed media that enables differentiation to multiple lineages, adult neural stem cells apparently only committed to a neuronal fate on softer substrates (100–500 Pa), and to a glial fate on stiffer substrates (1000–10,000 Pa). Importantly, only on the softest substrates (10 Pa) did the adult neural stem cells stop proliferating and develop prominent neural processes, recapitulating the distinctive behavior documented previously by neural versus glial cells on soft and stiff matrices (Flanagan et al., 2002).

Matrix elasticity can directly regulate cell proliferation by modulating cyclin D1-dependent G1 cell cycle progression (Klein et al., 2009). The ability of ECM stiffness to modulate cell cycle progression could explain why MSC quiescence is induced by plating the cells on soft polyacrylamide gels with a compliance that is similar to that measured in the central bone marrow, whereas the same cells proliferate and differentiate into adipocytes and osteoblasts when plated on stiffer substrates (Winer et al., 2009). Regardless, recognizing the impact of ECM compliance on cell cycle transit has permitted the development of culture conditions that maintain the pluripotency of both embryonic and induced pluripotent stem cells, and may help to design new strategies to potentiate induced pluripotent stem cell generation (Dixon et al., 2014; Y. Li et al., 2017).

Although it is entirely plausible that ECM compliance can directly specify stem cell fate, it is more likely these effects are mediated through modulation of cellular responses to growth factors and morphogens. This concept was recently illustrated by studies showing enhanced mesoderm differentiation of human embryonic stem cells (hESCs) mediated by culturing the cells on highly compliant substrates (Laralynne Przybyla et al., 2016c). In this study, hESCs plated on soft (400 Pa) and stiff (60,000 Pa) substrates failed to undergo spontaneous differentiation. However, upon

morphogen-induced differentiation, the hESCs plated on the softest substrates, recapitulating the elasticity of the early embryo, underwent highly efficient mesoderm progenitor differentiation, as compared to those plated on the stiffer substrates. These findings suggest matrix elasticity may serve to "prime" cells for tissue-specific differentiation. Indeed, hESCs interacting with the softest matrix showed reduced cell–ECM integrin adhesions and developed strong cell–cell adhesions that promoted apical–basal polarity, sequestered β-catenin, P120 catenin, and Kaiso at the adherens junctions, and reduced levels of secreted Wnt inhibitors.

In recent years, signaling events that converge on the coactivators Yes-associated protein and transcriptional coactivator with PDZ-binding motif (YAP/TAZ) have become a major area of interest, as evidence has emerged that their activity can be directly regulated by ECM stiffness (Hao et al., 2014). Further, YAP/TAZ are key components of the Hippo signaling pathway, which regulates organ size during development (Zhao et al., 2011). The relationship between the Hippo pathway and YAP/TAZ was first uncovered in *Drosophila*, where overexpression of the YAP homologue resulted in dramatic tissue overgrowth, phenocopying loss of Hippo signaling (Huang et al., 2005). Conversely, mutation of the YAP homologue prevented normal growth and expansion of developing tissues. Later, mechanistic studies revealed that activation of the Hippo signaling cascade ultimately results in phosphorylation of YAP and TAZ, preventing their nuclear localization and sequestering them to the cytoplasm where they undergo proteasomal degradation (Hong & Guan, 2012). In their unphosphorylated form, YAP/TAZ are shuttled to the nucleus, where they associate with other transcription factors and activate gene expression.

Direct evidence for the role of mechanotransduction in regulating YAP/TAZ signaling emerged when it was found that YAP nuclear translocation was induced by culturing cells on stiff substrates or by fostering cell spreading using large patterned ECM ligands (Dupont et al., 2011). By contrast, nuclear YAP translocation was prevented when cells were plated on soft substrates or when

cell spreading was prevented. Consistently, YAP/TAZ nuclear translocation was found to be necessary for the induction of MSC differentiation in a RhoA GTPase-dependent manner that required actomyosin-mediated cytoskeletal tension. Nevertheless, it is likely that ECM-mediated regulation of Hippo signaling during development is mediated by both biochemical and biomechanical cues.

MORPHOGEN SIGNALING AND DEVELOPMENT

Signaling Pathways

Secreted molecules called morphogens, or growth factors, and their inhibitors, mediate signaling between cells and regulate development in the early embryo. These morphogens act through defined intracellular signaling pathways to modulate gene expression and determine cell fate. Among the most important and best understood signaling pathways in development are the transforming growth factor β (TGF-β), bone morphogenic protein (BMP), Wnt, and hedgehog (Hh) pathways. In this section, I briefly review the current understanding of each of these pathways, and subsequently, I describe how gradients of these molecules regulate cell fate decisions at specific stages of development.

The TGF-β and BMP signaling pathways are often grouped together and referred to as "TGF-β/BMP signaling" because the mechanism of signal propagation is largely similar in both pathways (Figure 1.5 A). Signaling occurs when a TGF-β or BMP ligand binds a type II transmembrane receptor (Weiss & Attisano, 2013). This binding induces heteromeric complex formation with type I receptors, and subsequent phosphorylation and activation of Smads (Smad 2/3 for TGF-β signaling and Smad 1/5/9 for BMP signaling). Phosphorylation of these Smads facilitates their association with Smad 4 (for both pathways) and the resulting Smad complexes are then capable of translocating to the nucleus to regulate gene expression (C. S. Hill, 2009). Nuclear Smads resulting from TGF-β/BMP signaling

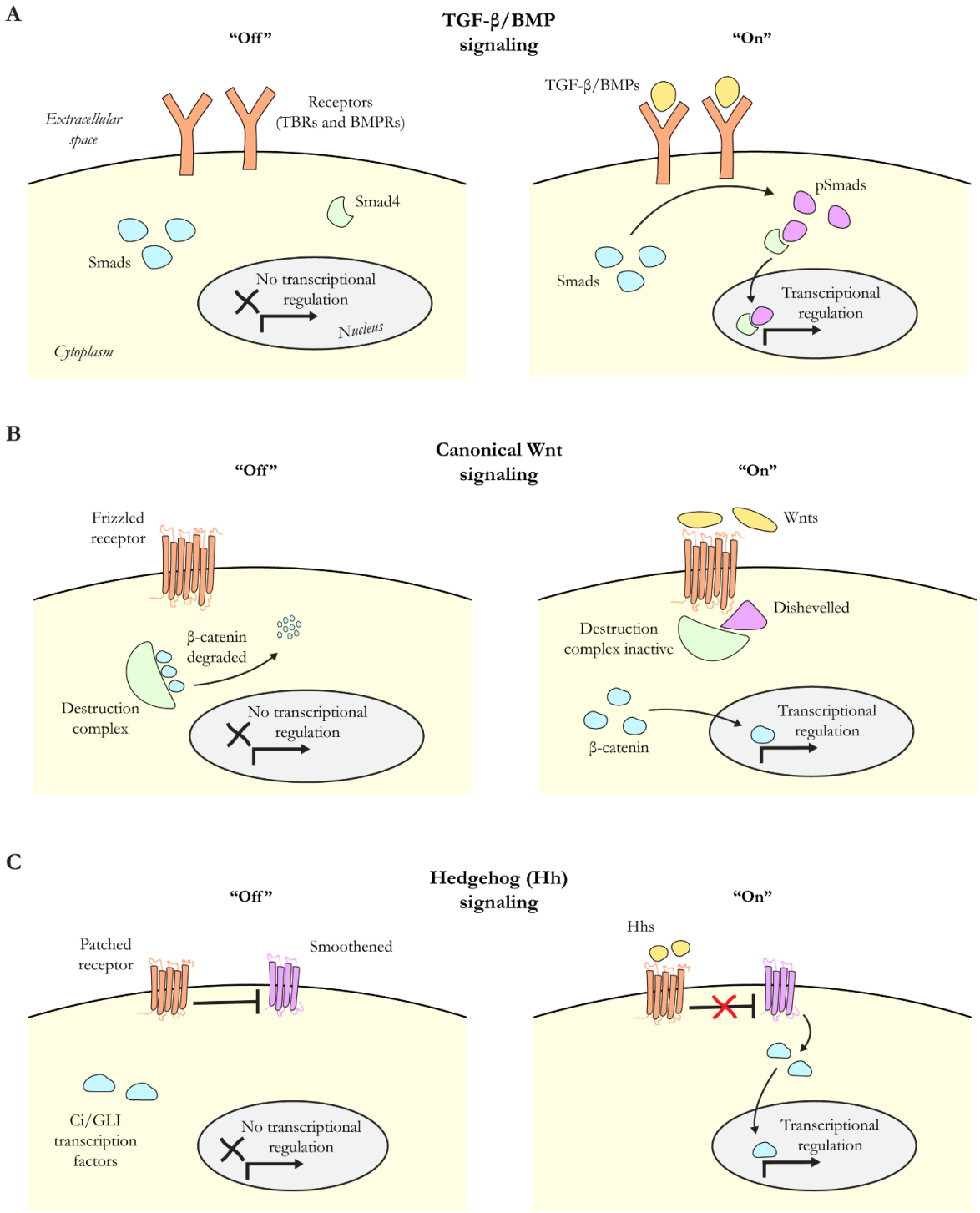

Figure 1.5: Key signaling pathways that regulate cell fate decisions.
(A) TGF-β/BMP signaling is activated by the binding of extracellular ligands (freely diffusing or ECM-bound) to receptors at the plasma membrane. Ligand-receptor binding ultimately leads to phosphorylation and nuclear translocation of Smads that regulate gene transcription.
(B) Canonical Wnt signaling is activated by the binding of secreted Wnts to transmembrane Frizzled receptors. This binding results in the association of Dishevelled and a (*caption continued on next page*)

(*caption continued from previous page*) number of additional proteins that make up what is termed the "β-catenin destruction complex." This promotes nuclear translocation of non-degraded β-catenin, which can regulate gene transcription.
(C) Hedgehog signaling is activated when secreted hedgehog ligands bind Patched receptors at the plasma membrane. This binding releases the inhibition of the Smoothened protein, which mediates nuclear translocation of Ci/GLI transcription factors to regulate gene expression.
TBRs = TGF-β receptors. BMPRs = BMP receptors.

exert a large range of biological effects on gene regulation by partnering with a number of other transcription factors and regulatory units. In this way, the effects of TGF-β/BMP signaling are wide-ranging and context-dependent, and thus, these signaling pathways are used in a number of processes throughout development and in the adult organism (Abdel-Latif et al., 2008; Akhurst et al., 1990; Chen et al., 2012; Dabovic et al., 2002; Dickson et al., 1993; Erlebacher & Derynck, 1996; Goumans et al., 2008; van der Kraan et al., 2009).

Canonical Wnt signaling, also referred to as Wnt/β-catenin signaling, begins with a Wnt ligand binding to transmembrane Frizzled receptors (Figure 1.5 B). In vertebrates, there are as many as 19 distinct Wnt ligands, enabling the canonical Wnt pathway to regulate a vast and diverse set of processes during development (Clevers & Nusse, 2012; Voloshanenko et al., 2017). The binding of Wnt ligands to Frizzled receptors causes recruitment of Disheveled proteins to the plasma membrane, where they polymerize and activate. Disheveled activation then leads to sequestration and inactivation of a number of proteins, collectively referred to as "the destruction complex" for their function in degrading cytoplasmic β-catenin. Thus, by inactivating the destruction complex, Wnt signaling leads to stabilization and build-up of cytoplasmic β-catenin, which promotes translocation of β-catenin to the nucleus. Upon reaching the nucleus, β-catenin binds with TCF/LEF complexes and other co-activators to regulate gene transcription (Behrens et al., 1996; Molenaar et al., 1996). Interestingly, β-catenin also serves as a structural protein, mediating binding between adherens junctions and the actin cytoskeleton (Brunet et al., 2013; W. J. Nelson & Nusse, 2004; Röper et al., 2018). This presents an

additional route for Wnt/β-catenin signaling, potentially independent of Wnt ligands. β-catenin released from adherens junction can result in excess cytoplasmic β-catenin and promote nuclear translocation and transcriptional regulation.

Hedgehog (Hh) signaling involves the interaction of two different transmembrane proteins: Patched and Smoothened (Figure 1.5 C). In the absence of Hh ligands, the Patched receptor inhibits the Smoothened protein and prevents signal transduction (Cohen, 2003). Binding of Hh ligands to Patched releases the inhibition on Smoothened and allows the signal to propagate. The details of precisely how Smoothened mediates signaling are poorly understood, but it ultimately promotes nuclear translocation of Ci/GLI transcription factors that regulate Hh target genes. There are three known hedgehog ligands in mammals: Sonic Hedgehog (Shh), Desert Hedgehog (Dhh), and Indian Hedgehog (Ihh), with Shh being the most studied and best understood with respect to its regulatory functions in development.

Morphogen Gradients in Development

During development, growth factors are produced and secreted by cells in a particular region of the embryo and then diffuse through the extracellular space and can exert their effect on any of the cells they come in contact with. In light of this, morphogen signaling in development is often conceptualized as gradients of individual ligands, with a high concentration of ligand present in the region with cells serving as the source and decreasing concentrations moving away from the source cells. Morphogen gradients provide a framework for understanding how secretion of a single ligand can lead to a variety of cell fates. Assuming that the concentration of ligand corresponds to the strength of signaling induced by that ligand, and further assuming that different thresholds of signal strength result in distinct cell fates, then the location of a cell relative to a particular morphogen gradient may determine the fate of that cell. Indeed, there are a number of examples in development where cell fate decisions and morphogenic processes are known to be regulated by this principle.

One particularly stereotyped example of how morphogen gradients regulate cell fate in development is the patterning of neuronal subtypes in the developing spinal cord of mouse embryos (Figure 1.6 A; Jessell, 2000). Following closure of the neural tube, Shh is secreted from the ventral floor plate and a ventral-to-dorsal gradient of Shh is formed (high concentration ventrally, low concentration dorsally). Remarkably, in the ventral half of the neural tube, this graded concentration of Shh leads directly to five distinct progenitor domains, and subsequently, five distinct post-mitotic neuron types (V0-V3 interneurons as well as motor neurons). There are two classes of homeodomain proteins expressed by progenitor cells in the ventral neural tube that allow each cell to interpret its position within the Shh gradient. These homeodomain proteins are regulated downstream of Shh signaling and complex interactions between the two classes of proteins mediate the formation of the five progenitor domains. Proteins in the first class are repressed by Shh signaling, with repression occurring at a different threshold for each protein within the class; conversely, proteins in the second class are activated by particular levels of Shh signaling (Jessell, 2000; Martí & Bovolenta, 2002). Adding an extra layer of complexity to the system, complementary class one and class two proteins expressed in neighboring domains are capable of co-repression, serving as a mechanism to clarify boundaries between the domains (Briscoe & Ericson, 2001; Jessell, 2000; Martí & Bovolenta, 2002). Ultimately, this system produces five domains with five unique combinations of expression of class one and class two homeodomain proteins, thus determining the patterning of five unique neuronal fates.

Shh can also serve as a guidance molecule, acting along with BMP and Wnt to direct the morphogenesis of commissural neurons that arise in the dorsal neural tube of mice (Figure 1.6 B; Yam & Charron, 2013). As these commissural neurons begin developing, BMP7 is secreted from the dorsal roof plate of the neural tube, resulting in a dorsal-to-ventral gradient opposite the Shh gradient. Shh acts as a chemoattractant for the extending axons of the commissural neurons, while BMP7 prevents midline crossing. Together, these two signaling gradients cause the axons to elongate in the ventral

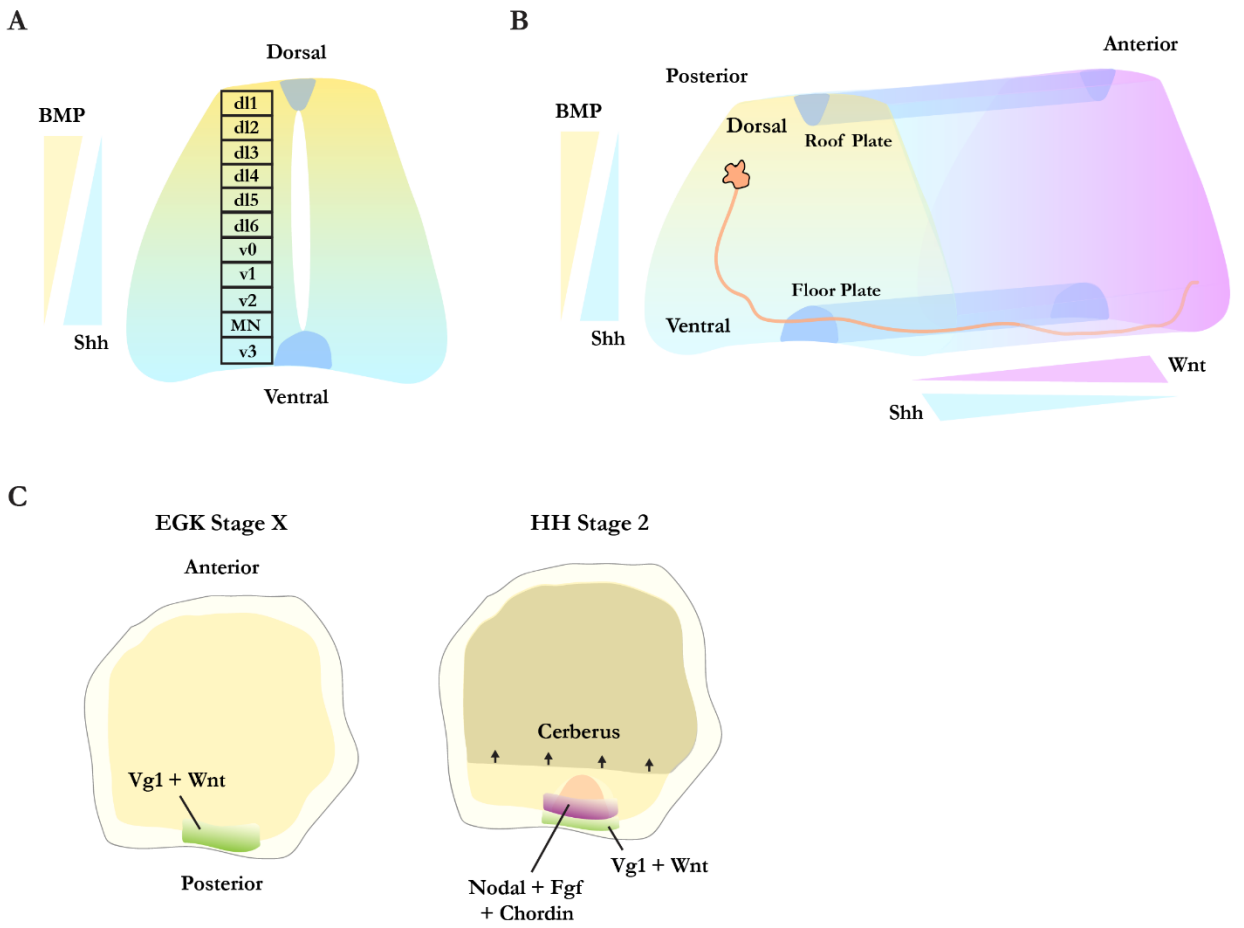

Figure 1.6: Examples of morphogen gradients that regulate early development.
(A) BMP and Sonic hedgehog (Shh) gradients determine the cell fates of developing dorsal and ventral interneurons in the mouse neural tube.
(B) A dorsal-ventral gradient of BMP and Shh, along with a posterior-anterior gradient of Shh-Wnt guides commissural axon development in the mouse neural tube. High concentrations of BMPs in the dorsal region prevent developing axons from crossing the midline, directing their growth ventrally. Once reaching the ventral region of the neural tube, axons cross the midline, whereupon Shh acts a chemorepellent and Wnt a chemoattractant, guiding axon elongation in the anterior direction, towards the brain.
(C) A combination of morphogens regulates gastrulation in the chicken. Just prior to gastrulation, Vg1 and Wnt are secreted in the posterior marginal zone and contribute to patterning the location of primitive streak formation. Vg1 and Wnt stimulate Nodal expression in the posterior of the epiblast, which acts to specify mesendoderm. Nodal can only act on cells released from inhibition by Cerberus being secreted by the hypoblast (underneath the epiblast), which moves anteriorly underneath the hypoblast as gastrulation progresses. Secreted Fgf and Chordin also act to pattern the primitive streak and specify mesendoderm at the posterior midline.
dl1-dl6 = dorsal interneurons. v1-v3 = ventral interneurons. MN = motor neurons.

direction. Once they reach the ventral neural tube, the axons are free of the BMP7's inhibitory effects and they cross the midline. Remarkably, once the axons have crossed the midline, Shh acts as a chemorepellent and drives axons anteriorly, towards the developing brain (Bourikas et al., 2005). This anterior extension is assisted by an anterior-to-posterior gradient of Wnt, which acts as a chemoattractant (Lyuksyutova et al., 2003). Despite some of the specific mechanisms remaining a mystery, such as how Shh switches from a chemoattractant to a chemorepellent after axons cross the midline, this example of commissural neuron development illustrates how a combination of morphogen gradients can lead to a complex and precisely patterned morphogenesis that is critical for the proper development of a healthy organism.

Morphogen gradients also play important roles in regulating gastrulation during early development (Figure 1.6 C). Prior to formation of the primitive streak in chicken embryos (EGK Stage X), Vg1 and Wnt are secreted by cells in the posterior of the embryo, near the border of the area pellucida and area opaca, a region referred to as the posterior marginal zone (PMZ). The overlapping activities of Vg1 and Wnt secreted from the PMZ seem to induce Nodal in neighboring cells of the area pellucida epiblast (I. Skromne & Stern, 2001; Isaac Skromne & Stern, 2002). However, Nodal is initially inhibited by Cerberus, which is secreted by hypoblast cells underlying the epiblast (Bertocchini & Stern, 2002). Around this time (just prior to HH Stage 2), the BMP inhibitor Chordin is secreted by cells of Koller's Sickle, which neighbors the PMZ, and this repression of BMP activity mediates primitive streak formation (Bertocchini et al., 2004). Initiation of the streak also seems to be stimulated by FGFs, secreted by both the hypoblast and Koller's Sickle (Chapman et al., 2002; Karabagli et al., 2002). Once the streak is formed and as gastrulation progresses, the underlying hypoblast moves anteriorly relative to the epiblast, releasing the inhibition of Nodal by Cerberus. The anteriorly moving activity of Nodal, along with FGF signaling, is responsible for the elongation of the streak in the anterior direction. These findings illustrate that gradients of various morphogens, as well

as their respective inhibitors, are critical for gastrulation and serve to control the spatiotemporal development of the primitive streak.

Morphogens and the ECM

The ECM controls the availability and presentation of growth factors and morphogens. This ECM-soluble-factor binding function is mediated primarily by the extracellular proteoglycans and heparin sulfates that contain binding sites for a multitude of growth factors and secreted morphogens and enzymes. The binding of soluble secreted factors to the ECM creates a signaling "reservoir" that can be rapidly accessed by the cells within the tissue. ECM binding of growth factors also modulates and sometimes potentiates the cellular signaling elicited by these molecules and can in some instances also bind inhibitors to temper signaling.

Members of the transforming growth factor beta (TGF-β) superfamily, including BMPs and TGF-β, play a major role in regulating embryogenesis, tissue development, and stem cell fate. The BMPs and TGF-β bind to specific cellular receptors and activate intracellular signaling to alter cell and tissue behavior by regulating gene expression (ten Dijke & Hill, 2004). Through their receptor activation, BMPs and TGF-β regulate a multitude of developmental programs including gastrulation during early development and tissue-specific differentiation such as cardiogenesis, chondrogenesis, and osteoblast differentiation (Abdel-Latif et al., 2008; Akhurst et al., 1990; Chen et al., 2012; Dabovic et al., 2002; Dickson et al., 1993; Erlebacher & Derynck, 1996; Goumans et al., 2008; van der Kraan et al., 2009). Given their critical role during embryogenesis and tissue homeostasis, it is not surprising that the storage, release, and activation of TGF-β and BMPs are both tightly regulated by ECM binding (Robertson et al., 2015; Wipff et al., 2007).

To begin with, cells secrete TGF-β in its inactive form, whereupon it associates with a large macromolecular protein aggregate termed the latent TGF-β complex. Proteins within the latent complex contain the RGD peptide, which can then be recognized by cellular transmembrane

receptors, including integrin αvβ6. Integrin-mediated binding of the latent protein complex can then release the active TGF-β ligand from the latent complex in an actomyosin tension-dependent manner (Hinz, 2015).

BMPs also bind to the ECM, and this influences tissue development by generating BMP gradients that critically direct cell migration and differentiation. For example, BMPs directly bind to specific collagen 11α and collagen IV domains (X. Wang et al., 2008), and bound BMP has been shown to direct body axis formation, regulate heart development, and control sensory neuron development in the inner ear (Chang et al., 2008; Khetarpal et al., 1994; Larraín et al., 2000; H. Li et al., 2005). Furthermore, BMPs also associate with fibrillins, which are ECM glycoproteins (Sengle et al., 2008), and this interaction is critical for the patterning that drives proper limb digit formation (Arteaga-Solis et al., 2001). Similarly, the simultaneous dynamic ECM remodeling and collagen fibrillogenesis that are absolutely critical for chondrogenesis and the cartilage-to-bone transition are tightly choreographed by ECM-bound BMPs (Yoon et al., 2005; Zhu et al., 1999). The ECM-bound BMP not only stimulates cell migration and differentiation, but its ECM-bound inhibitors may also repress signaling and differentiation, as has been proposed by studies in a simplified embryogenesis model (Warmflash et al., 2014).

ECM-bound growth factors can elicit profound effects on tissue development and differentiation. This concept was elegantly illustrated by studies conducted in *Xenopus* embryos, in which platelet-derived growth factor subunit A (PDGFA) bound to ectodermal-generated fibronectin was shown to be absolutely critical for the directional migration of mesoderm germ layer cells during gastrulation (Keller, 2005). The importance of ECM binding of PDGFA was illustrated by showing that expression of either a dominant-negative PDGFA receptor or reducing the level of matrix-bound PDGFA both severely compromised mesoderm migration toward the animal pole (Nagel et al., 2004).

Similarly, IGF-I and IGF-II are often highly abundant in tissues where they associate with the ECM, even when no insulin-like growth factor (IGF) mRNA can be easily detected (Han et al., 1987; D. J. Hill et al., 1989). This ECM-associated IGF has been shown to play an instructive role in directed neural development and was found to be critical for inducing oligodendrocyte differentiation from neural progenitors (Hsieh et al., 2004), and for the cooperative BMP-mediated induction of chondrogenesis from adipose-derived MSCs (An et al., 2010). The ECM also modulates IGF signaling through competitive binding of their carrier proteins the insulin growth factor binding proteins (IGFBPs). The association of IGFBPs to the ECM not only retards their MMP-mediated degradation but additionally alters the cellular-binding affinity for IGF-1, as was illustrated by a seven-fold decrease in IGF-1 binding affinity induced by ECM-bound IGFBP-5 (J. I. Jones et al., 1993; Martin et al., 1999).

Yet another example of how matrix-bound growth factors can influence tissue development is demonstrated by FGF, which associates strongly with ECM-localized or membrane-tethered proteoglycans that contain heparin sulfate side chains (Jia et al., 2009). In fact, there are several different FGFs, each with different affinities for particular heparin sulfate side chains, such that variations in ECM composition can demonstrate unique specificity for sequestering particular FGFs (Harada et al., 2009). The proteoglycan association of FGFs can also stabilize interactions between FGFs and FGF receptors to influence cellular FGF signaling and cell fate (Ornitz, 2000). More frequently, however, proteolytic release of FGFs from the heparin sulfate-containing proteoglycans permits binding of the FGF ligand to cellular FGF receptors to stimulate cellular signaling and regulate cell growth, survival, and migration. Released FGF is key for tissue-specific differentiation, including lung and mammary gland branching morphogenesis (Cardoso, 2006; Patel et al., 2007; Pond et al., 2013; Tholozan et al., 2007).

CELL- AND TISSUE-LEVEL FORCES IN DEVELOPMENT

It is clear from simply observing developing embryos that physical forces must be required to drive morphogenesis and facilitate the organization of cells into complex 3D tissue architectures that are indispensable for healthy tissue and organ function. The fundamental basis of these physical forces lies in cellular contractility, generated by the combined function of cytoskeletal and motor proteins. These contractile forces are then transmitted between cells via junctional proteins and across tissues via both cellular and ECM adhesions. Thus, physical forces act at both the cell- and tissue-level to power morphogenesis during development.

In fact, cell- and tissue-level forces are known to be important for stages of development we have already discussed. During gastrulation, ingression of cells at the primitive streak requires complete apical constriction, mediated by actomyosin contractility (Voiculescu et al., 2014). Upon completing an EMT and fully ingressing, these cells then utilize molecular motors and adhesion proteins to actively migrate basally and away from the streak to form the mesoderm and endoderm germ layers (Figure 1.7 A). During neurulation, cell- and tissue-level forces are critical for facilitating folding and closure of the neural tube (Figure 1.7 B; Nikolopoulou et al., 2017). Rapid expansion of incisions made in the non-neural ectoderm (Lewis, 1947), and more recently with laser ablation in the deep ectoderm (Morita et al., 2012), reveal that a large magnitude of isotropic stress is transmitted throughout the closing neural folds (Jacobson & Gordon, 1976). At the cellular level, the bending and folding of the neural plate as it closes is mediated by actomyosin-controlled apical constriction and apicobasal elongation of epithelial cells (L. A. Davidson & Keller, 1999; Inoue et al., 2016). Actomyosin contractility is also required for coordinated cell movements and cell intercalation that occurs as the neural tube closes (Heisenberg & Bellaïche, 2013; Nishimura et al., 2012; Sokol, 2016). Similarly, large-scale coordination of cellular movements, cell intercalation, and actomyosin

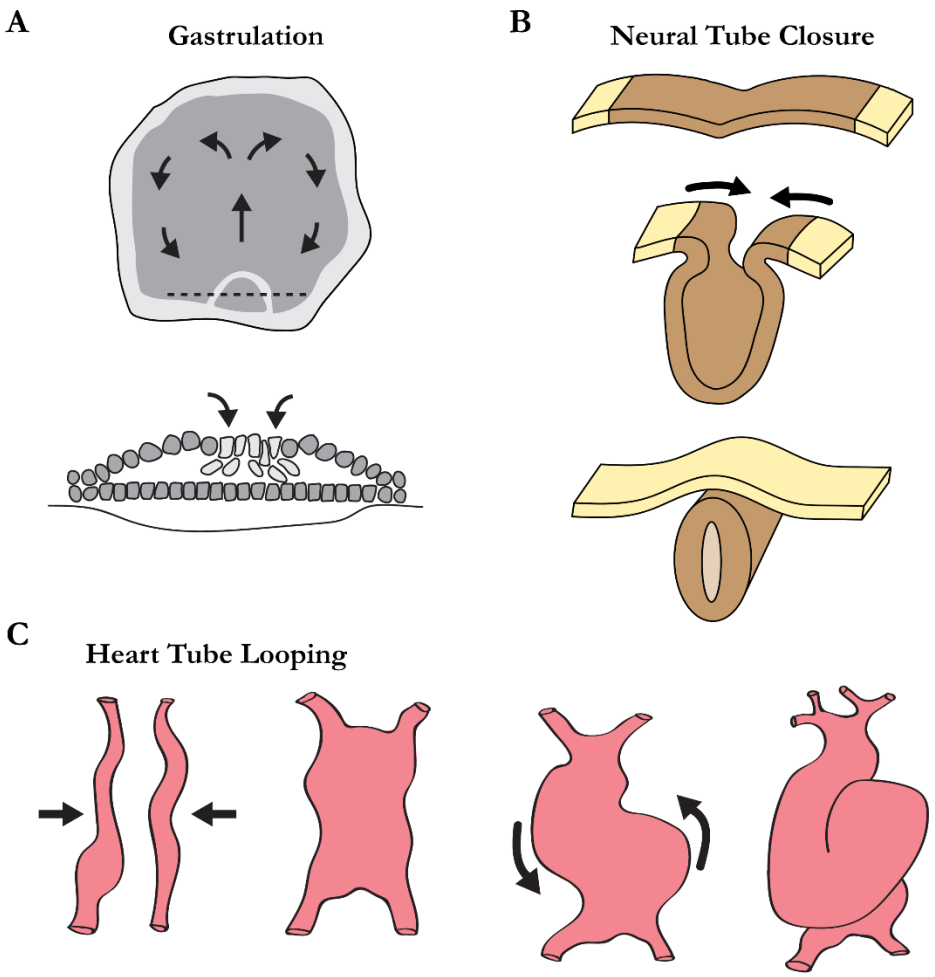

Figure 1.7: Cell- and tissue-level forces are critical for morphogenesis and tissue development.
(A) Tissue-level forces underlie the "Polonaise" movements that drive formation and elongation of the primitive streak during gastrulation, while cell-generated forces are required to mediate ingression of cells that pass through the primitive streak and form the mesoderm and endoderm germ layers.
(B) Cell- and tissue-level forces are required for the morphogenesis that occurs within the neural plate and leads to formation and closure of the neural tube.
(C) Cell-generated forces enable the migration of mesoderm cells that form the primary and secondary heart fields, and subsequently, tissue-level forces drive heart tube looping.

contractility are required for heart tube looping and for cell compaction during somitogenesis (Figure 1.7 C; McMillen & Holley, 2015; Ramasubramanian et al., 2013).

While the significance of cell- and tissue-level forces in morphogenesis of the embryo is readily apparent, the molecular mechanisms that regulate such complex behaviors are somewhat less clear.

Moreover, in many contexts it remains unknown whether these physical forces also affect cell fate decisions, in addition to guiding cell and tissue movements. One of the main questions examined in this dissertation is whether and how mechanical forces may alter molecular signaling events to influence cell fate specification in a human embryonic stem cell model of gastrulation.

MODELING EARLY DEVELOPMENT WITH HUMAN EMBRYONIC STEM CELLS

Human embryonic stem cells (hESCs) are a powerful model with which to study the mechanisms that regulate early human development because they can be maintained in pluripotent conditions *in vitro*, are derived from human sources and faithfully represent the human genome, and can be stimulated to undergo differentiation towards more specialized cell types. Recently, hESCs were shown to differentiate into multiple distinct germ layer progenitors upon stimulation with a single morphogen: BMP4 (Warmflash et al., 2014). Remarkably, these hESC colonies not only generated the various germ lineages that form during gastrulation, they also exhibited the capacity to self-organize. Following BMP4 stimulation, the germ lineages consistently arose in reproducible spatial patterns of concentric rings, reminiscent of a bullseye pattern. This radial patterning was attributed to differences in BMP receptor accessibility throughout the colonies, along with a reaction-diffusion model of the exogenously added BMP and endogenously secreted inhibitors (Etoc et al., 2016; Tewary et al., 2017). These two phenomena combined lead to a proposed mechanism whereby effective BMP signaling is highest at the colony border and lowest at the colony center, with the graded decrease from periphery to center leading to the radial patterning of distinct cell fates.

While these prior studies effectively illustrated the capacity of hESCs to self-organize patterns of the early germ layers, there remained a number of open questions. All of the prior studies were performed on rigid tissue culture plastic, which fails to recapitulate the compliance of the early embryo. Moreover, the bullseye patterns exhibited in these studies do not match the spatial patterning of germ

layers that occurs during gastrulation. This presents the possibility that the mechanical properties of the microenvironment influence the patterning of cell fate specification, and that a compliant matrix is required for a more faithful recapitulation of gastrulation. Additionally, the previous studies lacked an examination of the spatiotemporal dynamics of hESC self-organization, making it impossible to compare the presented findings to the morphogenesis that occurs during gastrulation in the embryo.

The primary goal of this dissertation work was to recapitulate the mechanical properties of the embryo in an hESC model of early development and examine the dynamics of hESC self-organization, with a focus on mesoderm specification. Furthermore, we used our developed system to answer questions about how mechanical forces, and cellular tension in particular, modulate the signaling pathways that drive cell fate specification. Through this work we demonstrate that mechanics not only drive morphogenesis during development, but also co-regulate cell fate.

CHAPTER 2

Human Embryonic Stem Cells Self-Organize Gastrulation Nodes on Compliant Substrates

This chapter is adapted from work published in the peer-reviewed article titled "Mechanical tension promotes formation of gastrulation-like nodes and patterns mesoderm specification in human embryonic stem cells" by **Jonathon M. Muncie**, Nadia M.E. Ayad, Johnathon N. Lakins, Xufeng Xue, Jianping Fu, and Valerie M. Weaver in Developmental Cell (2020).

INTRODUCTION

Gastrulation – wherein cells of the embryonic epiblast simultaneously segregate and differentiate into the three primary germ layers: ectoderm, mesoderm, and endoderm – requires precise coordination of morphogenesis and cell fate specification. The morphogenesis that occurs during gastrulation relies on cell tension and tissue-level forces to facilitate the physical re-organization of epiblast cells into the primary germ layers (Hamada, 2015; Ko & Martin, 2020; Paré & Zallen, 2020; Voiculescu et al., 2014; Williams & Solnica-Krezel, 2017). As embryogenesis progresses, tissue-level forces sculpt the embryo by driving neural tube closure, mediating somitogenesis, and guiding heart tube looping (McMillen & Holley, 2015; Ramasubramanian et al., 2013; Taber, 2014; Turlier & Maître, 2015; Vijayraghavan & Davidson, 2017). Thus, cell- and tissue-level forces play an intimate role in directing the structure and function of the emerging organism. Yet, whether these forces may directly influence cell fate specification during early embryogenesis by modifying cell signaling, transcription, and tissue-specific differentiation, and how, remains less well understood.

Remarkably, hESCs will self-organize to recapitulate patterns of the primary germ layers, even in the absence of extraembryonic tissues (Shao et al., 2017; Simunovic et al., 2019; Warmflash et al., 2014; Zheng et al., 2019). Prior studies using hESCs underscored the importance of tissue organization in early human development, and implicated morphogen gradients and receptor accessibility as two key mechanisms that regulate primary germ layer patterning (Blin et al., 2018; Chhabra et al., 2019; Etoc et al., 2016; Manfrin et al., 2019; Martyn et al., 2019; Q. Smith et al., 2018; Tewary et al., 2019; Warmflash et al., 2014). The coordination of cellular contractility throughout many cells in multicellular tissues can give rise to tissue-level forces that are dependent on tissue organization. Cell-adhesion tension, in particular, is spatially enhanced by specific tissue geometries (Gomez et al., 2010; Kilian et al., 2010; J. Lee et al., 2016; C. M. Nelson et al., 2005). This raises the intriguing possibility that tissue geometry modulates local cell-adhesion tension to spatially direct hESC self-organization and fate specification.

Here we explored the role of cell-adhesion tension in the generation of spatially-patterned, gastrulation nodes in hESCs. We used hESCs cultured on geometrically-defined ECMs of tuned elasticity to recapitulate the biophysical properties of the early embryo and promote gastrulation-like morphogenesis. Using this system, we implicated tension as an additional key regulator of cell fate patterning, and emphasize the versatility of hESCs as a tractable model with which to study early human development.

RESULTS

Compliant Substrates Promote Self-Organization of hESC Gastrulation Nodes

To study the interplay between tissue mechanics and early development, we designed reproducible culture strategies that foster hESC self-organization and consistently permit a gastrulation-like phenotype following BMP4 stimulation. hESCs plated as confined circular colonies on ECM-

patterned rigid glass substrates (Elastic modulus, E = 10^9 to 10^{10} Pa) exhibit a radial pattern of primary germ layer specification following BMP4 stimulation (Warmflash et al., 2014). This has been attributed to restriction of BMP/SMAD signaling to the margins of these colonies, combined with the presumptive role of endogenously secreted BMP inhibitors concentrated at the colony interior and consistent with a reaction-diffusion model (Etoc et al., 2016; Tewary et al., 2017). By contrast, hESCs plated at high densities (3,000-4,000 cells/mm^2) using "funnels" on polyacrylamide hydrogels (PA; E = 10^2 to 10^5 Pa) modified with laminin-rich reconstituted basement membrane (rBM; Matrigel equivalent) self-assemble disc-shaped colonies and undergo enhanced mesoderm specification upon BMP4 stimulation when cultured on the soft (E = 10^2 to 10^3 Pa) versus the stiff (E = 10^4 to 10^5 Pa) substrates (L. Przybyla et al., 2016b; Laralynne Przybyla et al., 2016c). Atomic force microscopy (AFM) measurements of the gastrulation-stage chicken epiblast, which resembles these hESC disc cultures in size and shape (Mikawa et al., 2004; Shahbazi et al., 2016), yielded values within the soft (10^2 to 10^3 Pa) elasticity range (Figure 2.1 A-B). Thus, we developed a system for BMP4-induced differentiation on embryo-like compliant PA gels (Figure 2.2 A). For technical reasons, we chose the softest PA gel condition that was experimentally compatible with both confined and unconfined culture methods (E = 2,700 Pa). Importantly, hESCs cultured on 2,700 Pa substrates and stimulated with BMP4 exhibited similar levels of mesoderm specification as on 400 Pa substrates (Figure 2.1 C), which most closely recapitulate the elasticity of the chicken embryo (Figure 2.1 A-B).

Live-imaging of H2B-mCherry-labelled nuclei following BMP4-mediated differentiation (50 ng/ml; 24 to 48 hours) revealed that multiple discrete regions of highly dense hESCs formed near the periphery of these unconfined colonies on soft hydrogels (Figure 2.2 B-D). High-magnification spinning disc confocal imaging of a subset of these colonies showed that the hESCs ingressed basally within the observed nodes to ultimately assemble into a second cellular layer that expressed the mesoderm marker T(brachyury) (Figure 2.3 A). This cellular behavior is highly reminiscent of

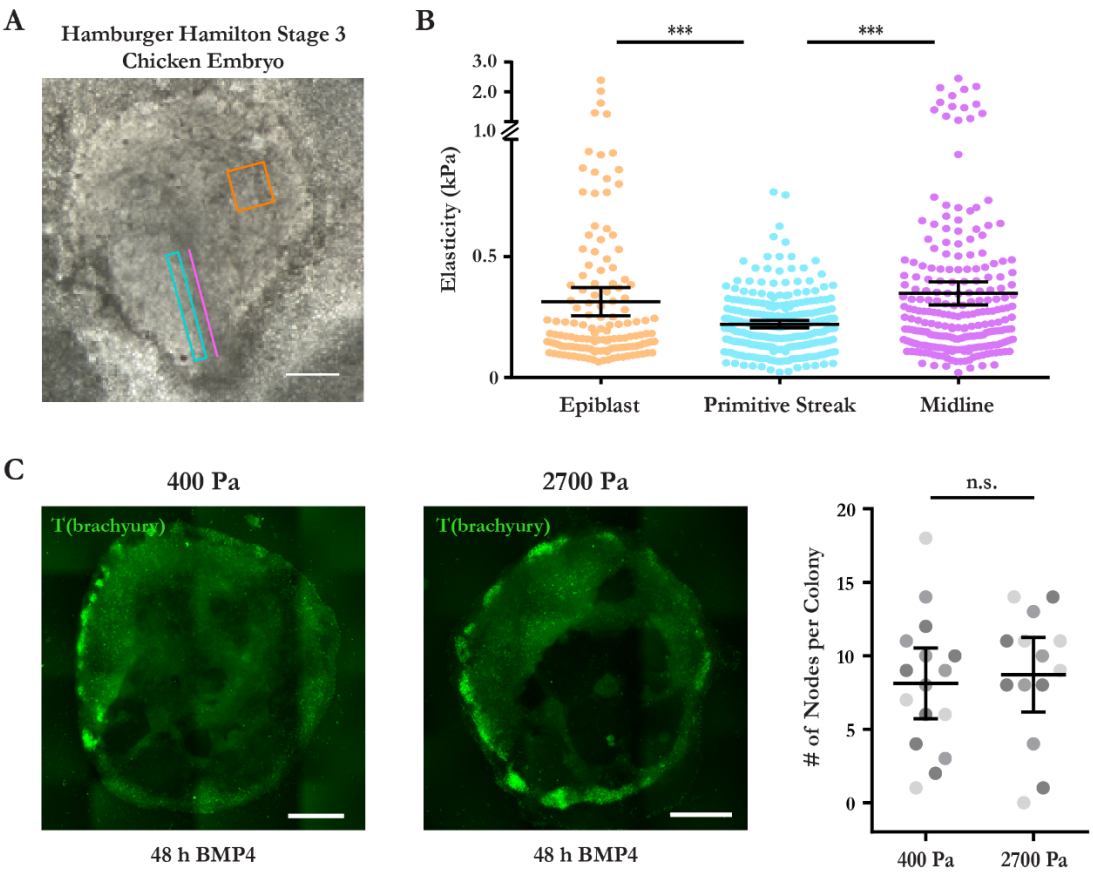

Figure 2.1: Compliance of the extracellular microenvironment of gastrulation-stage chicken embryos.

(A) Representative brightfield image of an HH stage 3 chicken embryo extracted and prepared for atomic force microscopy measurements. Colored rectangles and line on the image indicate regions within the embryo where measurements were taken, corresponding to the data presented in (B). Scale bar = 500 μm.

(B) Atomic force microscopy measurements of HH stage 3 chicken embryos, grouped by regions of the embryo within which the measurements were taken. Data was collected from embryos prepared on four separate days (N = 4, 2, 1, and 3 embryos measured each day). Epiblast n = 140, primitive streak n = 260, and midline n = 236 elasticity measurements.

(C) Representative immunofluorescent images showing T(brachyury) expression within gastrulation nodes 48 h following BMP4 stimulation of hESC colonies cultured on 400 Pa and 2700 Pa polyacrylamide hydrogels. Scatter plot (right) displaying quantification of the number of gastrulation nodes observed per hESC colony at 48 h BMP4 on 400 Pa and 2700 Pa hydrogels. n = 16 (4, 6, 6) colonies from 400 Pa gels and n = 14 (5, 4, 5) colonies from 2700 Pa gels. Scale bars = 500 μm.

Line and bars represent mean ± 95% CI. ***$p < 0.001$. Pa = pascals. kPa = kilopascals. n.s. = not significant.

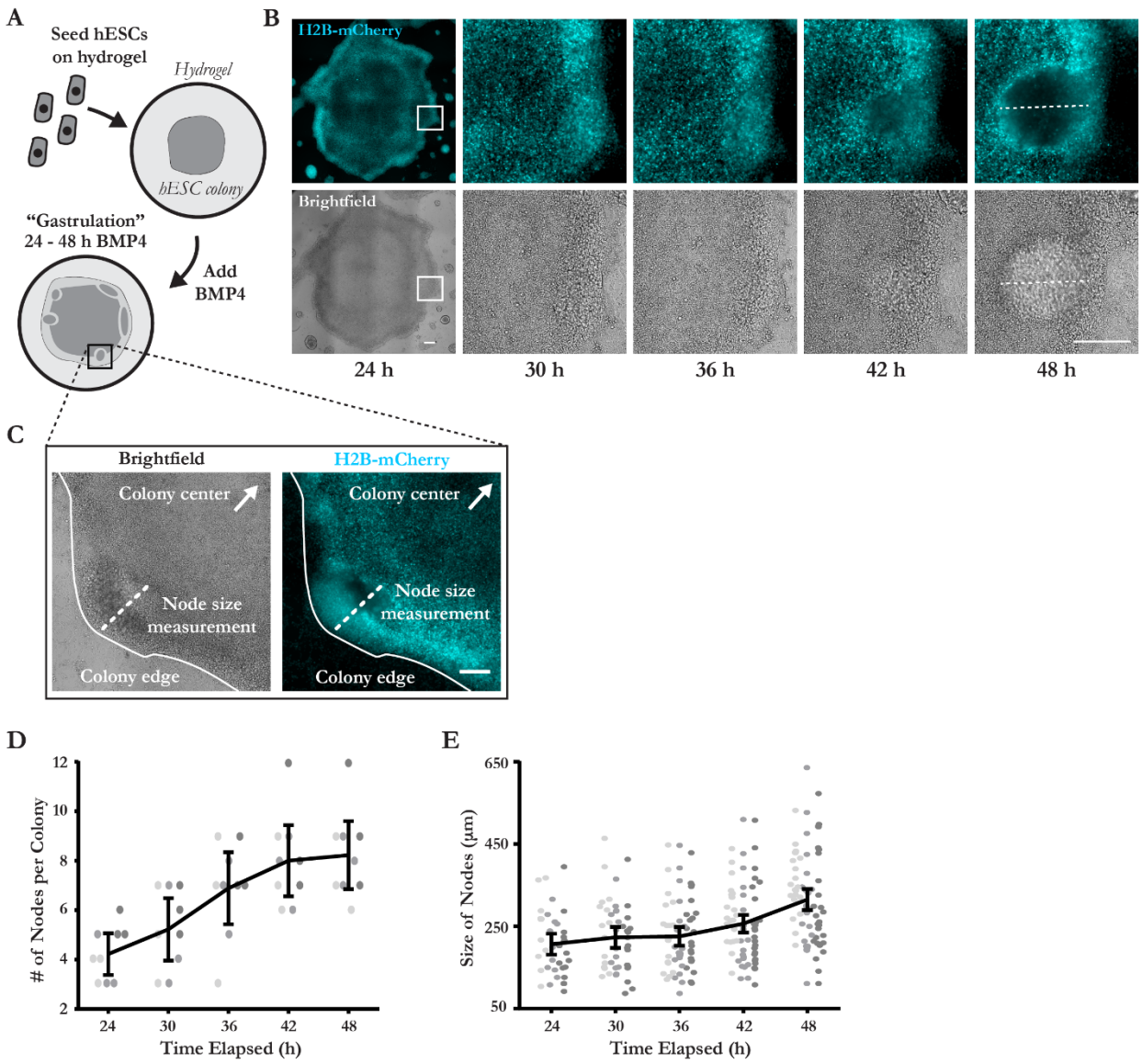

Figure 2.2: hESCs on compliant substrates self-organize gastrulation nodes.
(A) Cartoon of hESCs seeded on compliant (2,700 Pa) hydrogels and stimulated with BMP4.
(B) Representative time-lapse images of hESC colonies stimulated with BMP4. White rectangles indicate the region shown magnified in subsequent panels. Dashed lines indicate gastrulation node. Scale bars = 250 μm.
(C) Representative images of an H2B-mCherry hESC colony after 48 h BMP4 stimulation. The dashed white line indicates the size measurement of the identified gastrulation node taken along the radial axis of the colony, as plotted in (E). Scale bar = 200 μm.
(D) Plot of the number of nodes formed between 24 and 48 h BMP4. n = 9 (3, 3, 3) colonies.
(E) Plot of node size between 24 and 48 h BMP4. The dashed line in (C) indicates node size measurement. Data points represent the size of each node identified from n = 9 colonies (3, 3, 3).
For (D), (E): Data from independent experiments represented by different shades of gray and line and bars represent mean ± 95% CI.

gastrulation, wherein cells of the developing epiblast ingress at the embryo midline to form a secondary transient structure called the primitive streak, which gives rise to the mesoderm and endoderm germ layers (Shahbazi et al., 2019; Shahbazi & Zernicka-Goetz, 2018; Simunovic & Brivanlou, 2017; Voiculescu et al., 2014; Williams & Solnica-Krezel, 2017). Analogous to the embryonic primitive streak

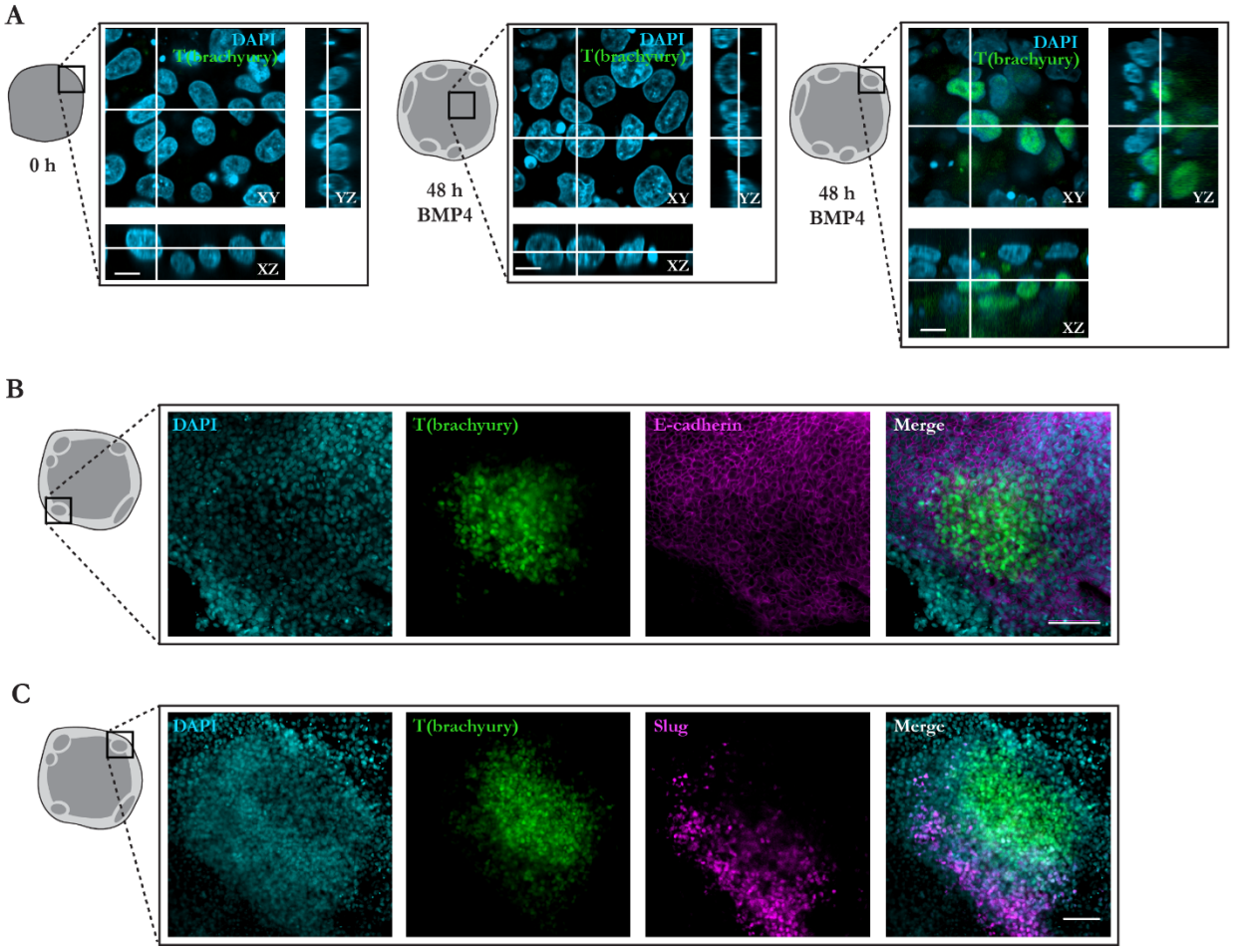

Figure 2.3: Cells undergo EMT and ingress within gastrulation nodes.
(A) Representative spinning-disk confocal z-stack reconstructions before and 48 h after BMP4 stimulation showing T(brachyury) expression and nuclei (DAPI) within pluripotent colonies (left), the central regions of BMP4 treated colonies (middle), and within the gastrulation nodes (right). Scale bars = 10 μm.
(B) Representative images of nuclei (DAPI), T(brachyury) expression, E-cadherin, and composite in the gastrulation nodes at 48 h BMP4. Scale bar = 100 μm.
(C) Representative images of nuclei (DAPI), T(brachyury) expression, Slug, and composite in the gastrulation nodes at 48 h BMP4. Scale bar = 100 μm.
Rectangles on colony cartoons indicate imaged regions.

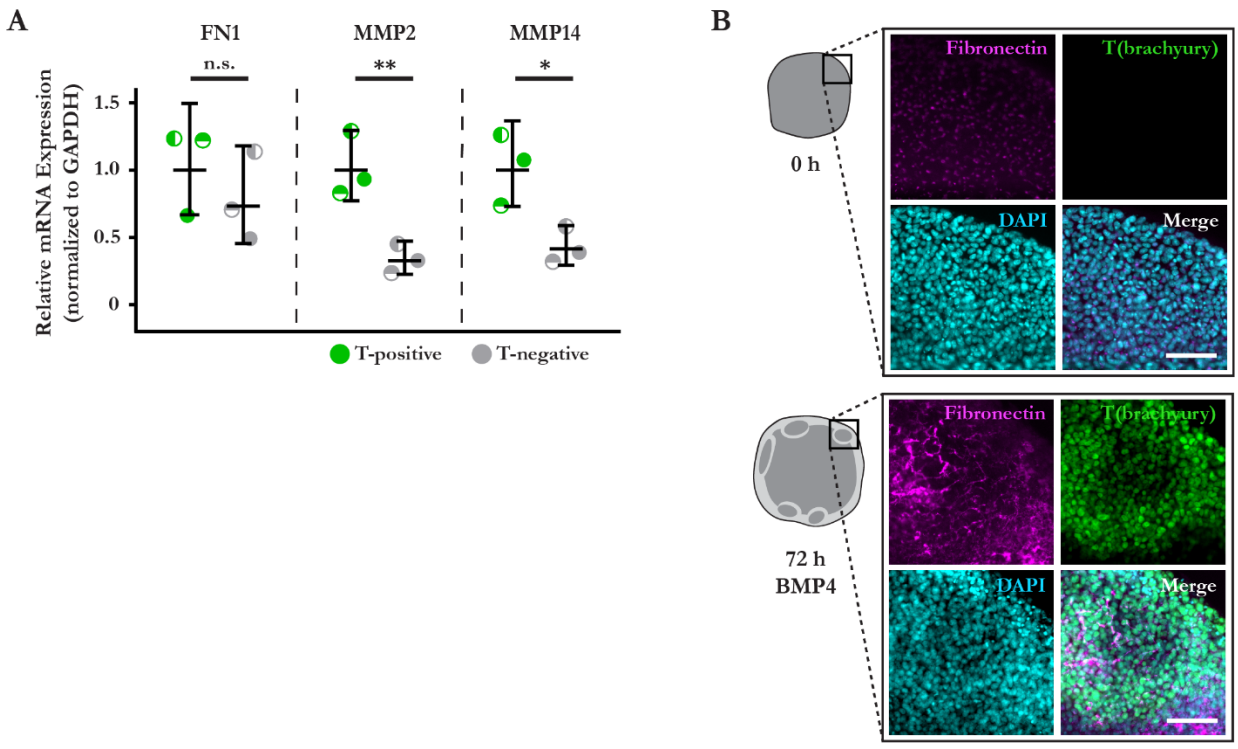

Figure 2.4: Cells in gastrulation nodes remodel the ECM.
(A) Relative mRNA expression levels of fibronectin and matrix metalloproteinases (MMPs) in T-positive and T-negative cells isolated from geometrically-confined hESC colonies on compliant hydrogels following 36 h of BMP4 stimulation. Line and bars represent mean ± 95% CI. *$p < 0.05$, **$p < 0.01$. n.s. = not significant.
(B) Representative immunofluorescent images of fibronectin, T(brachyury), nuclei (DAPI), and composite in the gastrulation nodes prior to and after 72 h BMP4. Rectangles on colony cartoons indicate imaged regions. Scale bars = 100 μm.

that elongates as gastrulation progresses, these gastrulation nodes in the hESC colonies similarly continued to expand between 24 and 48 hours post-BMP4-stimulation (Figure 2.2 E). Consistent with gastrulation, the hESCs that expressed T(brachyury) in the gastrulation nodes also lost E-cadherin, indicating they had undergone an epithelial to mesenchymal transition (EMT; Figure 2.3 B). Indeed, the cells adjacent to the gastrulation nodes expressed another EMT marker, Slug, implying they were in the process of ingression and undergoing mesoderm specification (Figure 2.3 C).

Cells within these gastrulation nodes also demonstrated a trend towards increased expression of fibronectin and significant upregulation of key matrix metalloproteinases (MMPs) involved in

remodeling the ECM during gastrulation, namely, MMP2 and MMP14 (Figure 2.4 A; Kyprianou et al., 2020; J. Zhang et al., 2003). By 72 hours post-BMP4-stimulation, we observed deposition and fibrillogenesis of fibronectin within the gastrulation nodes (Figure 2.4 B). These data provide evidence that the ingressing mesoderm-specified cells actively remodeled their ECM, likely to facilitate further ingression and migration of mesoderm progenitors, as in the embryo (Lance A. Davidson et al., 2008; Keller, 2005; Kyprianou et al., 2020).

These findings illustrate our ability to reproducibly induce a gastrulation phenotype, indicative of early embryogenesis, in self-organized nodes of hESCs resembling the primitive streak that forms during gastrulation in the embryo (Figure 2.5). The mesoderm specification that we observed arising near the colony periphery in our hESC model bears some similarity to the radial organization documented in earlier studies of hESCs plated on patterned glass substrates (Etoc et al., 2016; Tewary et al., 2017; Warmflash et al., 2014). However, the formation of discrete gastrulation nodes in unconfined hESC colonies on compliant PA gels is distinct from the apparent continuous concentric ring patterns of the primary germ layers observed in these prior models, and instead, is morphologically more reminiscent of the discrete primitive streak. This distinction underscores the

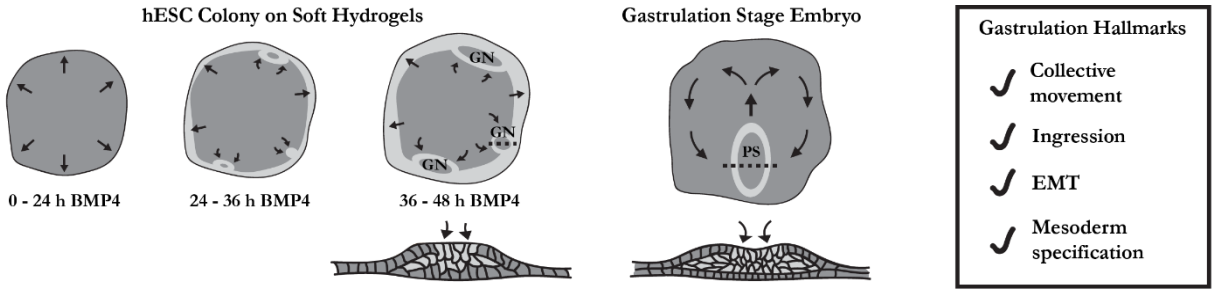

Figure 2.5: Self-organized gastrulation nodes resemble embryonic primitive streak.
Schematic of the gastrulation phenotype observed in hESC colonies on compliant hydrogels, compared to gastrulation in the embryo. Cross-sections along dashed lines are depicted below the schematics. GN = gastrulation node. PS = primitive streak. EMT = epithelial to mesenchymal transition.

importance of recapitulating the biophysical properties of the local microenvironment in faithfully modeling self-organization of the early embryo.

Real-Time Monitoring of hESC Gastrulation Nodes

To explore the mechanisms regulating the self-organization that fosters the gastrulation phenotype in hESCs cultured on compliant substrates, we built a T(brachyury)-mNeonGreen-reporter hESC line (T-reporter) using CRISPR homology-directed repair (HDR; Chu et al., 2015; San Filippo et al., 2008) to facilitate monitoring the temporal development of the nodes in real-time (Figure 2.6 A). After using a commercial antibody for T(brachyury) to validate that the T-reporter system effectively conveyed expression levels following BMP4 differentiation (Figure 2.6 B-C), we conducted gene expression analysis on fluorescence-activated cell sorted (FACS) populations of the T-reporter hESCs post-BMP4-stimulation (36 hours) to assess additional fate specification markers of the cells in these gastrulation nodes (Figure 2.7 A). Quantitative polymerase chain reaction (qPCR) revealed that the isolated T-positive hESCs expressed high levels of the mesoderm markers T(brachyury) and goosecoid

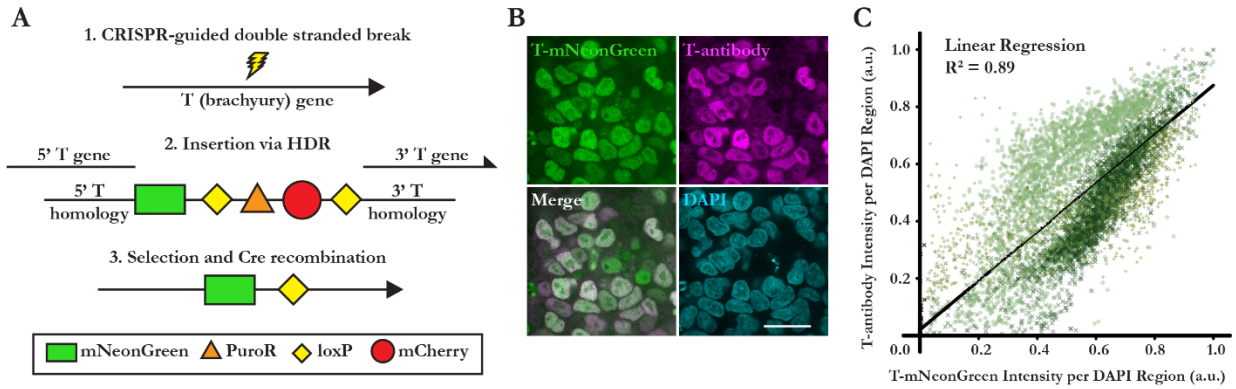

Figure 2.6: T-mNeonGreen hESC reporter system for real-time monitoring of gastrulation nodes.
(A) Schematic representation of the T-mNeonGreen reporter system. HDR = homology-directed repair.
(B) Representative images of T(brachyury) labeled by the T-reporter, an antibody to T, composite, and nuclei (DAPI). Scale bar = 20 μm.
(C) Plot of fluorescence intensity of T-mNeonGreen versus T-antibody per segmented nuclei. n = 33 (10, 13, 10). a.u. = arbitrary units.

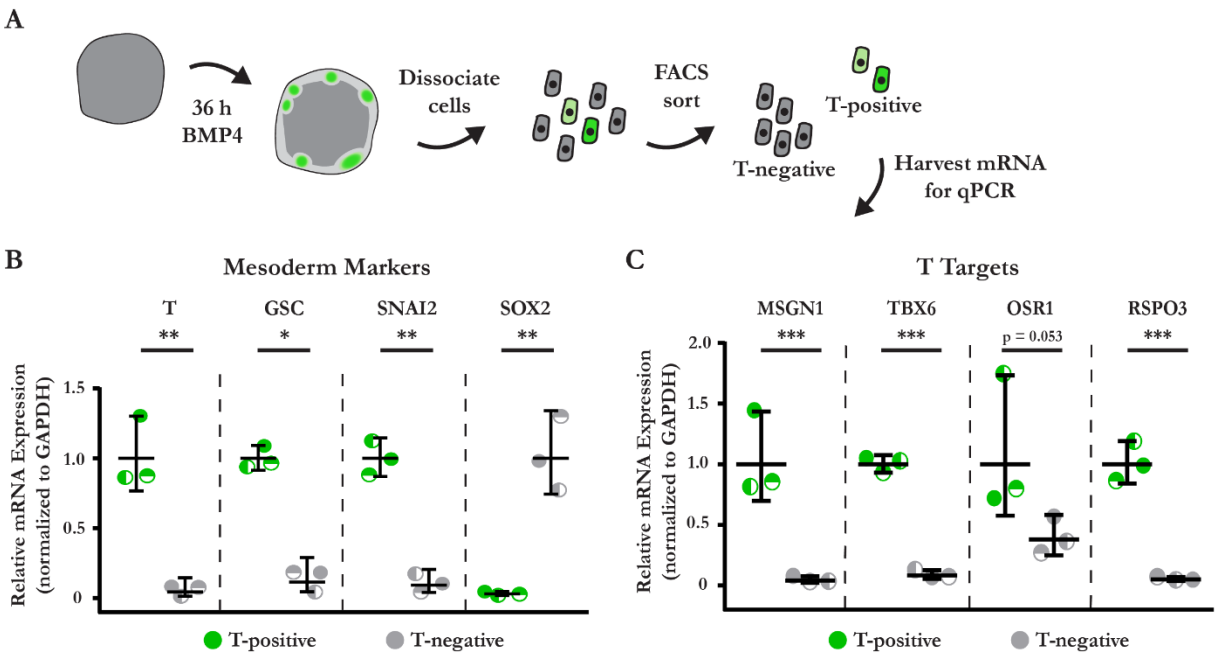

Figure 2.7: Gene expression analysis of mesoderm markers and T targets for T-positive and T-negative hESCs.
(A) Cartoon of isolation protocol to compare gene expression between T-positive and T-negative cells.
(B) Relative mesoderm gene expression levels in T-positive and T-negative cells at 36 h BMP4.
(C) Relative expression levels of T targets in T-positive and T-negative cells at 36 h BMP4.
Line and bars represent mean ± 95% CI. *$p < 0.05$, **$p < 0.01$, and ***$p < 0.001$. GSC = Goosecoid. MSGN1 = Mesogenin 1, TBX6 = T-Box Transcription Factor 6, OSR1 = Odd-Skipped Related Transcription Factor 1, RSPO3 = R-Spondin 3.

(GSC), and the EMT marker Snai2, as compared to T-negative hESCs (Figure 2.7 B). By contrast, T-negative hESCs expressed high levels of the pluripotent marker Sox2, excluding them from mesodermal identity (Figure 2.7 B; Koch et al., 2017; Warmflash et al., 2014). Additionally, we found that direct transcriptional targets of T(brachyury) (Koch et al., 2017) were upregulated in the T-positive hESCs, verifying that the T-mNeonGreen fusion protein did not compromise downstream transcriptional activity of T (Figure 2.7 C). The data confirm that mesoderm specification occurs primarily in the observed gastrulation nodes, and indicate that the cells ingressing within these nodes undergo transcriptional changes akin to the cells that pass through the primitive streak during early gastrulation.

Time-course imaging of T-reporter hESCs following BMP4 stimulation revealed that the dynamic behavior of the entire tissue-like structure fosters the induction and expansion of the gastrulation nodes (Figure 2.8 A). Coincident with T-expression and emergence of the gastrulation phenotype, the hESCs approximately 50 microns or 10 cell diameters inward from the colony periphery begin to assemble into multiple densely packed aggregates (Figure 2.8 B-E). These densely packed cellular aggregates progressively increased in size (Figure 2.8 D), presumably due to observed fluid-like collective movements that initially drive cells radially-outwards and then drive subpopulations back inward to contribute to the developing gastrulation nodes. These collective movements bear a striking resemblance to the "Polonaise" movements that drive epiblast cells toward the midline and establish the primitive streak in the gastrulating chicken embryo (Voiculescu et al., 2014). These data thus provide additional compelling evidence that recapitulating the compliance of the embryo enables self-organization of hESCs to facilitate coordinated programs of early embryogenesis (Figure 2.5).

Cell-Adhesion Tension Directs Gastrulation Node Organization to Specify Mesoderm

Previously, we showed that hESC colonies cultured on compliant hydrogels demonstrated a unique ability to generate regions of high tension near the periphery of colonies maintained in pluripotent conditions (L. Przybyla et al., 2016b). Traction force microscopy (TFM) measurements of hESC colonies were combined with monolayer stress microscopy to reveal that regions of high traction stresses corresponded to regions of high cell-adhesion tension. This can be explained by the epithelial structure of hESC colonies, which results in cell-cell tension being distributed through cellular adhesions and balanced by measurable cell-substrate stresses. Thus, we proceeded to use direct measurements of traction stresses as a readout for cell-adhesion tension.

We found that hESC colonies were uniquely capable of generating localized nodes of high cell-adhesion tension near the periphery of the colony, in approximately the same locations we observe

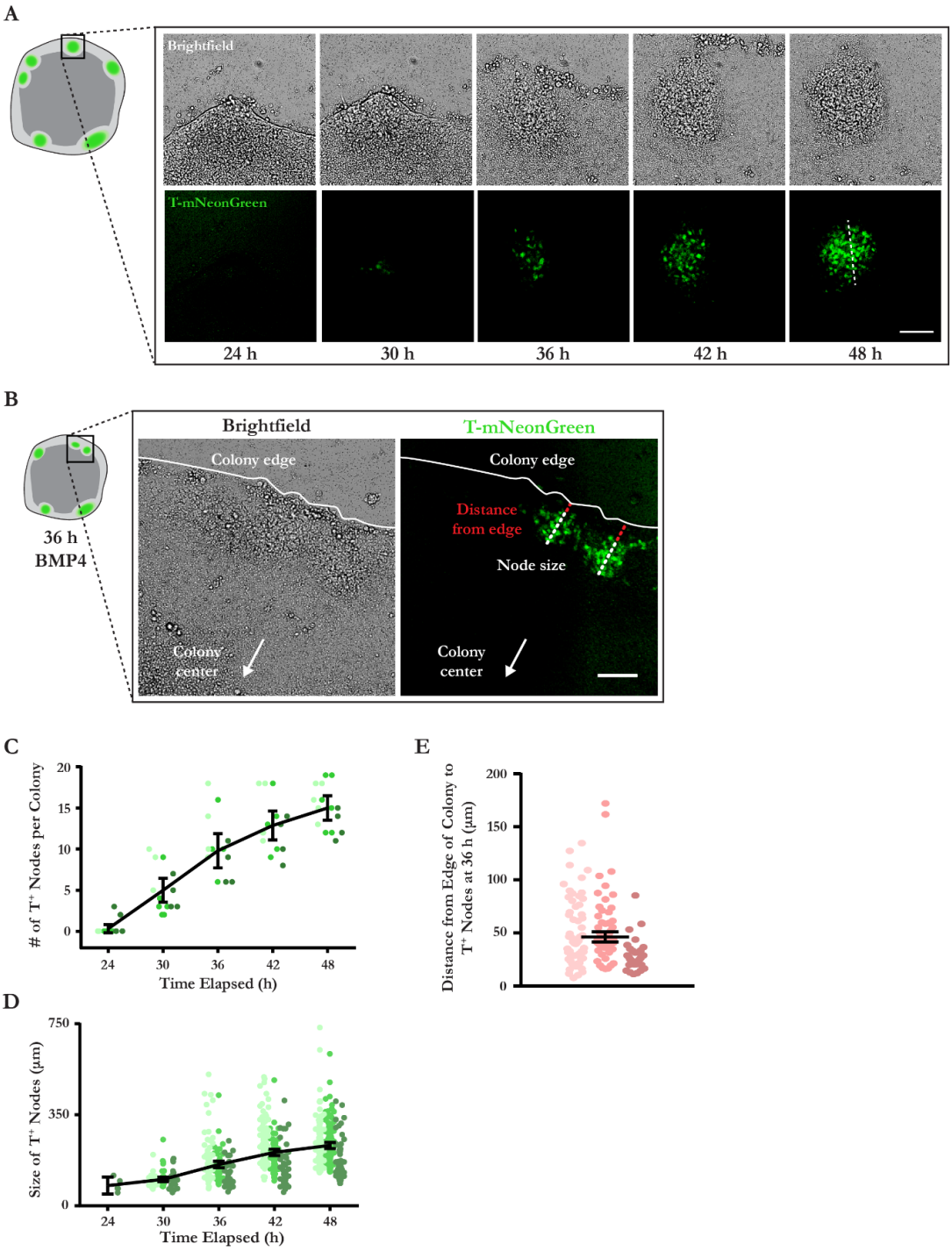

Figure 2.8: Real-time monitoring of gastrulation node formation using T-mNeonGreen reporter system.

(A) Representative time-lapse images of gastrulation nodes in the T-mNeonGreen reporter system. Rectangle on colony cartoon indicates imaged region. Dashed line indicates gastrulation node. Scale bar = 100 µm. (Caption continued on next page).

(B) Representative images of gastrulation nodes in the T-mNeonGreen reporter system after 36 h BMP4 stimulation. The dashed white lines indicate the size measurement (*caption continued on next page*)

(*caption continued from previous page*) of the identified gastrulation nodes taken along the radial axis of the colony. The dashed red lines indicate the "distance from edge" measurements, also taken along the radial axis of the colony. Scale bar = 100 μm.
(C) Plot of the number of nodes formed between 24 and 48 h BMP4. n = 15 (5, 6, 4) colonies.
(D) Plot of node size between 24 and 48 h BMP4. The dashed line in (B) indicates node size measurement. Data points represent the size of each node identified from n = 15 (5, 6, 4) colonies.
(E) Scatter plot of the "distance from edge" measurements taken for gastrulation nodes identified after 36 h of BMP4 stimulation. n = 15 (5, 6, 4) colonies.
For (C-E): Data from independent experiments represented by different shades of green or red. Line and bars represent mean ± 95% CI.

self-organized gastrulation nodes upon BMP4 stimulation. We proceeded to measure cell-adhesion tension in colonies of T-reporter hESCs and registered the resulting maps with the emerging gastrulation nodes using live-cell fluorescence imaging of the same colonies. Remarkably, the BMP4-stimulated gastrulation nodes developed precisely within the same hESC colony regions that exhibited the highest cell-adhesion tension (Figure 2.9 A-B). Importantly, we measured the regionally localized elevated cell-adhesion tension prior to BMP4 stimulation, indicating that these regions of high tension preceded, and were not the result of, mesoderm specification. The data thus imply that cell-adhesion tension regulates hESC self-organization to spatially direct the development of gastrulation nodes.

DISCUSSION

We used atomic force microscopy to directly measure the physical properties of gastrulation-stage chicken embryos. We determined that the compliance of the epiblast ranges from 100-2,000 Pa, with a mean of 318 Pa, and in line with what would be expected for a soft tissue. These measurements also revealed that the primitive streak is somewhat softer (mean = 224 Pa) than the surrounding epiblast, although the midline itself is significantly stiffer (mean = 353 Pa) than the streak as a whole. This suggests a potential role for compliance, or tissue stiffness, in the spatial patterning of the primitive streak and perhaps even in the regulation of cell ingression and fate commitment that accompanies gastrulating cells at the primitive streak. In fact, it was recently shown that ECM deposition at the

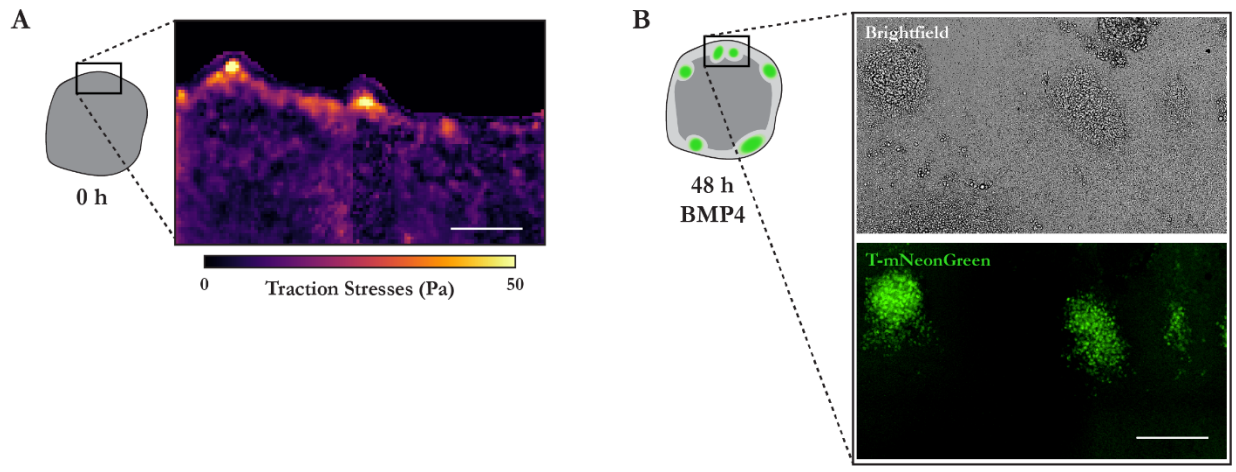

Figure 2.9: Regionally localized high cell-adhesion tension precedes gastrulation node formation.
(A) Representative traction stress map of the periphery of unconfined hESC colonies prior to BMP4 stimulation.
(B) Brightfield and T-mNeonGreen images 48 h after BMP4 in the same field of view where traction stresses were measured in (A).
Rectangles on colony cartoons indicate measured and imaged region.

midline, along with programmed cell death, controls ipsilateral ingression during gastrulation in chicken embryos (Maya-Ramos & Mikawa, 2020). We expect that future studies will reveal additional mechanisms by which tissue stiffness and ECM regulate the patterning of cell fate specification during early development.

In order to model early embryogenesis with hESCs, we developed a method to culture hESCs in large colonies representative of the geometry of the chicken epiblast on engineered compliant matrices of polyacrylamide conjugated with basement membrane extract to facilitate cell attachment. We tuned the stiffness of these matrices to approximately the order of magnitude (10^3 Pa) measured for the gastrulation-stage chicken epiblasts. Technical limitations, namely hydrogel tearing and reduced cell attachment, prevented us from generating even softer matrices (10^2 Pa). By inducing differentiation of these hESC colonies with BMP4, we observed the self-organization of distinct gastrulation nodes near the periphery of hESC colonies. The colonies exhibited collective cell movements that led to the

formation of these nodes, akin to the "Polonaise" movements of the chicken embryo, and cells within the nodes demonstrated several key characteristics of gastrulation, including expression of mesoderm specification markers, downregulation of E-cadherin, expression EMT genes, and cell ingression that was concomitant with T(brachyury) expression and established additional cell layers in the basal direction. Moreover, our system for culturing hESCs on compliant hydrogels facilitated measurements of regionally localized cell-adhesion tension using TFM and revealed that these gastrulation nodes arose specifically in regions that exhibited high cell-adhesion tension, consistently near the periphery of colonies. Thus, our findings indicate a link between cell-generated forces, tissue geometry, and mesoderm specification in an hESC model of gastrulation.

Prior studies illustrated that variations in BMP receptor accessibility and secreted morphogen concentrations lead to patterning of mesoderm specification within a concentric ring inwards from the hESC colony edge (Chhabra et al., 2019; Etoc et al., 2016; Manfrin et al., 2019; Martyn et al., 2019; Tewary et al., 2017, 2019; Warmflash et al., 2014). Our studies expand upon these findings to suggest that colonies of hESCs cultured on compliant substrates are particularly useful for studying the physical and molecular regulators of early embryogenesis, because they self-organize discrete gastrulation nodes that expand radially, distinctly resembling the formation and elongation of the primitive streak in the developing embryo (Mikawa et al., 2004; Voiculescu et al., 2014). Moreover, similar to epiblast cells that reach the primitive streak, our studies showed that the hESCs that contribute to these gastrulation nodes undergo EMT and ingress to form additional cell layers as they concomitantly begin expressing key mesoderm genes. The observed similarities between the gastrulation nodes in hESC colonies and the embryonic primitive streak suggest that this system could prove to be a powerful model with which to dissect the interplay between tissue-level forces, cytoskeletal tension, and the signaling and transcriptional programs that regulate early development. Indeed, the cultured hESC system, combined with tissue patterning and tuned biophysical ECMs,

lends itself to super-resolution imaging, single-cell sequencing techniques, quantitative force measurements, and physical manipulations that are challenging to perform using intact embryos, and which should yield critical fundamental insight into the process of human embryogenesis.

CHAPTER 3

A Method for Patterning hESC Colonies to Study the Interplay Between Tissue Organization, Cell-Adhesion Tension, and Gastrulation

This chapter adapted from work published in the peer-reviewed article titled "Patterning the geometry of human embryonic stem cell colonies on compliant substrates to control tissue-level mechanics" by **Jonathon M. Muncie**, Roberto Falcón-Banchs, Johnathon N. Lakins, Lydia L. Sohn, and Valerie M. Weaver in Journal of Visualized Experiments (2019).

INTRODUCTION

Through the work presented in Chapter 2 we discovered that gastrulation nodes emerge in hESC colonies cultured on compliant substrates and stimulated with BMP4. These self-organized gastrulation nodes specifically arose in regions of high cell-cell tension that seemed to consistently localize near the periphery of the colonies. We hypothesized that by manipulating hESC colony geometry we could predictably dictate the regional localization of high cell-cell tension, as previously demonstrated with patterned colonies of epithelial cells (Gomez et al., 2010; Kilian et al., 2010; J. Lee et al., 2016; C. M. Nelson et al., 2005), and thus control the spatial patterning of the emerging gastrulation nodes.

To address this hypothesis, we sought to develop a method for reproducibly culturing hESC colonies in defined geometries on compliant substrates that recapitulate the elasticity of the early embryo microenvironment. We modified our previous methods (Lakins et al., 2012; L. Przybyla et al., 2016b) for culturing hESCs on polyacrylamide hydrogels to provide robust control over the geometry

of the colonies. We achieved this by first patterning ECM ligands, namely matrigel, onto glass coverslips through microfabricated stencils, as previously reported (Q. Li et al., 2016). We then designed a novel technique to transfer the patterned ligand to the surface of polyacrylamide hydrogels during polymerization. The method we describe here involves using photolithography to fabricate a silicon wafer with the desired geometric patterns, creating stamps of theses geometric features with polydimethylsiloxane (PDMS), and using these stamps to generate the stencils that ultimately allow patterning of ligand onto the surface of glass coverslips and transfer to polyacrylamide.

In addition to recapitulating the mechanical environment of the early embryo, confining hESC colonies on polyacrylamide enabled the measurement of tissue tension within these confined colonies using traction force microscopy (TFM), as reported in our previous method (L. Przybyla et al., 2016b). In brief, fluorescent beads were embedded in the polyacrylamide and used as fiducial markers. Cell-generated forces were calculated by imaging the displacement of these beads after seeding hESCs onto the patterned substrates. Furthermore, the resulting traction stress maps were combined with traditional assays, such as immunostaining, to demonstrate that measurements of tissue tension can be combined with readouts of protein expression and localization within confined hESC colonies in order to examine how cell-generated forces may regulate or modulate signaling pathways that determine cell fate. We developed this method with the expectation that it will be utilized by our group, as well as others, to reveal that mechanical forces play a critical role in the patterning of cell fate specification during early embryonic development that is currently overlooked.

PROTOCOL

1. Preparation of Silicon Wafer with Geometric Features

1.1 Create a photomask with desired geometric features. Use computer-aided drafting software to design the features. For use with negative photoresist, make features opaque and the remainder of the mask transparent.

> NOTE: For patterning onto 18 mm diameter coverslips, group features for each experimental condition into 10 x 10 mm areas to ensure the stencils generated in Step 3 fit onto coverslips.

1.2 Spin coat negative photoresist onto a 100 mm silicon wafer. Use the photoresist data sheet to determine the speed and length of spin to generate a film thickness of 100-250 μm.

> NOTE: The film thickness should be adjusted such that the aspect ratio of the width of the patterns to the height of the stencil is as close to 1:1 as possible. However, we recommend a minimum thickness of 100 μm, as anything less produces delicate stencils that easily tear.

1.3 Process the photoresist according to the product data sheet. This typically involves a soft bake, UV exposure with photomask in a mask aligner, post exposure bake, development, and hard bake. As an example, the procedure used to process the wafers used in this protocol is outlined in Table 3.1.

> NOTE: Be cautious when handling silicon wafers as they are fragile. Once generated, wafers can be used repeatedly, so long as they are not damaged.

2. Preparation of Coverslips

2.1 Prepare acid-washed "top" coverslips.

2.1.1 Place 18 mm diameter #1 thickness coverslips into a glass petri dish. The appropriate number of coverslips depends on the size of the dish. For a 100 mm dish, prepare 50-100 coverslips at a time. Volume amounts given through the remainder of this section correspond to a 100 mm dish.

Table 3.1: Example wafer modification protocol using SU8 negative photoresist

1.	Spin coat wafer with SU8-3050	Spin at 1,000 RPM for 30 s
2.	Soft bake wafer on hot plate	i. 3 min at 65 °C
		ii. 45 min at 95 °C
		iii. 3 min at 65 °C
		iv. Cool to room temperature
3.	Expose in mask aligner	i. Align wafer and photomask in mask aligner
		ii. Expose with energy of 250 mJ/cm^2
		▪ e.g. for lamp with intensity of 11 mW/cm^2, expose for 23 s
4.	Post-exposure bake on hot plate	i. 1 min at 65 °C
		ii. 15 min at 95 °C
		iii. 1 min at 65 °C
		iv. Cool to room temperature
5.	Develop	i. Agitate in SU8 Developer, approx. 5-10 min
		ii. Check development with isopropyl alcohol (IPA)
		▪ If under-developed, IPA rinse will produce a white residue

2.1.2 Add 20 ml of 1 M HCl to the petri dish and gently shake the dish to disperse the coverslips. Ensure all the coverslips are submerged and release air bubbles from between the coverslips. Incubate overnight at room temperature with gentle shaking.

CAUTION: HCl is acidic and corrosive: Use caution and wear appropriate PPE while working with HCl.

2.1.3 Decant HCl from the dish. Add 20 ml ultrapure water and wash with gentle shaking for 10 min. Discard water and repeat for a total of five washes.

2.1.4 After discarding the final wash, add 20 ml 100% ethanol to the dish. Using forceps, remove coverslips individually and arrange between two pieces of filter paper to dry.

2.1.5 Store dried coverslips in a sealed container. Acid-washed coverslips can be prepared in advance and stored for a month or longer in dust-free conditions.

2.2 Prepare glutaraldehyde-activated "bottom" coverslips (refer to previous methods for additional details; Lakins et al., 2012; L. Przybyla et al., 2016b).

2.2.1 Place 18 mm diameter #1 thickness coverslips into a petri dish.

2.2.2 Add 20 ml of 0.2 M HCl to the petri dish and gently shake the dish to disperse the coverslips. Ensure all the coverslips are submerged and release air bubbles from between the coverslips. Incubate overnight at room temperature with gentle shaking.

2.2.3 Decant HCl from the dish. Add 20 ml ultrapure water and wash with gentle shaking for 10 min. Discard water and repeat for a total of five washes.

2.2.4 After discarding the final wash, add 20 ml of 0.1 M NaOH and shake gently to disperse and submerge coverslips. Incubate at room temperature with gentle shaking for 1 h.

2.2.5 Decant NaOH from the dish. Add 20 ml ultrapure water and wash with gentle shaking for 10 min. Discard water and repeat for a total of five washes.

2.2.6 After discarding the final wash, add 20 ml of a 1:200 dilution of 3-aminopropyltrimethoxysilane in ultrapure water and shake gently to disperse and submerge coverslips. Incubate at room temperature with gentle shaking for 1 h or overnight.

CAUTION: 3-aminopropyltrimethoxysilane is flammable and can cause skin irritation. Handle with care, wear appropriate PPE, and discard waste according to local disposal regulations.

2.2.7 Decant the diluted 3-aminopropyltrimethoxysilane solution from the dish. Add 20 ml ultrapure water and wash with gentle shaking for 10 min. Discard water and repeat for a total of at least five washes. It is critical to remove all 3-aminopropyltrimethoxysilane before proceeding.

2.2.8 After discarding the final wash, add 20 ml of a 1:140 dilution of 70% glutaraldehyde in phosphate buffered saline (PBS) and shake gently to disperse and submerge coverslips. Incubate at room temperature with gentle shaking for 1 h or overnight.

CAUTION: 70% glutaraldehyde is toxic and can cause skin irritation. Handle with care, wear appropriate PPE, and discard waste according to local disposal regulations.

2.2.9 Decant the diluted glutaraldehyde solution from the dish. Add 20 ml ultrapure water and wash with gentle shaking for 10 min. Discard water and repeat for a total of five washes.

2.2.10 After discarding the final wash, add 20 ml of 100% ethanol. Using forceps, remove coverslips individually and arrange between two pieces of filter paper to dry.

2.2.11 Store dried coverslips in a sealed container. Glutaraldehyde-activated coverslips can be prepared in advance and stored for up to six months.

3. Generation of Stencils for Patterning ECM Ligand

3.1 Generate polydimethylsiloxane (PDMS) intermediate stamps.

3.1.1 Mix PDMS base with PDMS curing agent at a 10:1 ratio, by weight. Mix thoroughly.

NOTE: For the initial application of PDMS, prepare approximately 100 g of PDMS to fill a 100 mm dish. For subsequent applications, remove PDMS from only the center of the dish where the silicon wafer features are located and prepare 20-30 g of new PDMS.

3.1.2 Degas the PDMS mixture in a desiccator for 30-60 min or until all air bubbles are removed.

3.1.3 Place the modified silicon wafer from Step 1 into a plastic 100 mm dish. Slowly and evenly pour the PDMS mixture over the surface of the wafer. Tap the dish on the work surface to release any air bubbles from the surface of the wafer.

3.1.4 Degas the PDMS mixture poured over the wafer for 10 min or until all air bubbles are removed or have come to the surface of the PDMS.

3.1.5 Bake the PDMS at 70 °C for 2 h. Allow to cool to room temperature.

3.1.6 Using a scalpel or box cutter, cut out the section of PDMS from the center of the dish that contains the geometric features.

3.1.7 Cut the PDMS into roughly 10 x 10 mm squares, each containing the features for a single experimental condition. These are referred to as "stamps" in subsequent steps of the protocol.

3.2 Generate flat slabs of PDMS.

3.2.1 Mix PDMS base with PDMS curing agent at an 8:1 ratio, by weight. Prepare approximately 20 g for each 100 mm dish to be used. Mix thoroughly.

3.2.2 Degas the PDMS mixture in a desiccator for 30-60 min or until all air bubbles are removed.

3.2.3 Slowly and evenly pour the PDMS into a clean 100 mm dish. Tap the dish on the work surface to release any air bubbles.

3.2.4 Bake the PDMS at 70 °C for 2 h. Allow to cool to room temperature.

3.2.5 Remove the PDMS from the dish. Invert such that the surface of the PDMS that was in contact with the bottom of the dish is facing up.

3.2.6 For each stamp generated in Step 3.1, cut a 15 x 15 mm square of PDMS. These are referred to as "flat slabs" in subsequent steps of the protocol.

3.3 Generate stencils.

3.3.1 Arrange flat slabs of PDMS on the lid of a 150 mm dish, or other flat surface for easier handling. Ensure sufficient spacing between slabs, e.g. for a 150 mm dish, arrange nine flat slabs with even spacing.

3.3.2 Invert each stamp generated in Step 3.1 onto a flat slab of PDMS, such that the features on the stamp are in contact with the flat slab of PDMS. Gently press on the top of the stamp with forceps to ensure even contact.

3.3.3 Carefully prop the lid holding PDMS stamp/slab pairs up on the base of the dish, such that the lid rests at an angle. This assists the wicking of the UV-curable polymer in the next step.

3.3.4 Place a small drop of UV-curable polymer at the top interface of each stamp/slab pair. The polymer will be wicked between the two by surface tension, assisted by gravity.

NOTE: Many different UV-curable polymers may work in this protocol. We selected Norland Optical Adhesive 74 for the following properties: i) Fast curing upon exposure to UV light, ii)

Easy removal from PDMS stamps upon curing, iii) Robust adhesion to glass coverslips with manual pressure.

3.3.5 Once the polymer has been completely wicked through, place the lid with stamp/slab pairs flat on the work surface. Place a small drop of UV-curable polymer at each of the remaining three sides of each stamp/slab interface.

3.3.6 Using a 200 µl pipette tip, connect the drops of polymer around the edges of the stamp/slab interface. This creates a border that will hold ligand solution in Step 4.

NOTE: Be careful when working the polymer around the edges of the stamp. If the stamp/slab interface is disrupted, the polymer will wick underneath the features and the stencil will not form properly.

3.3.7 Carefully place the stamp/slab pairs into a UV-sterilization box. Use the sterile "Str" power setting and expose for 10 min.

3.3.8 Remove the stamp/slab pairs from the UV-sterilization box. Using two pairs of forceps, gently remove the PDMS stamp while holding down the flat slab and stencil that formed from the UV-curable polymer.

3.3.9 Using forceps, carefully remove the stencil and invert it such that the surface that was in contact with the flat slab of PDMS is facing up.

NOTE: The stencils are delicate. Be careful while handing them, especially while initially removing them from the PDMS, so that they do not tear.

3.3.10 Place the inverted stencils back into a UV-sterilization box. Use the sterile "Str" power setting and expose for 3 min.

4. Patterning ECM Ligand on Coverslips

4.1 Press stencils onto acid-washed coverslips.

4.1.1 Place one acid-washed coverslip for each stencil onto a clean piece of laboratory film.

4.1.2 Using forceps, carefully place each stencil, flat-side-down, onto an acid-washed coverslip. Place such that features are centered on the coverslip.

4.1.3 Place a small piece of laboratory film on top of each stencil. Firmly and evenly press down on the stencil to create strong contact between the stencil and the coverslip.

NOTE: **This is a critical step!** Press firmly and across the entire surface of the stencil. If sufficient contact is not created, the ligand solution will leak between the stencil and the coverslips and the patterning will fail.

OPTIONAL: To confirm sufficient contact between the stencil and the coverslip, pipette 100 μl of ultrapure sterile water onto the surface of each stencil and incubate at room temperature. After 1 h, check for leaking. Aspirate water from successfully bonded stencils and proceed.

4.2 Plasma clean the surface of the stenciled coverslips to increase hydrophilicity.

4.2.1 Place coverslips with stencils into a plasma cleaner. Apply high power plasma for 30 s.

4.3 Prepare ECM ligand solution.

NOTE: All subsequent steps should be completed in sterile conditions, if possible.

4.3.1 Place sterile 100 mM HEPES, 100 mM NaCl, pH 8.0 solution on ice. Once ice cold, add matrigel and collagen to achieve concentrations of 225 μg/ml and 25 μg/ml, respectively.

NOTE: Different ECM ligands can be used with this method. For different ligands, additional optimization may be required to determine ideal concentration, incubation time, and incubation temperature. See discussion section for more information.

OPTIONAL: For troubleshooting or for ligand visualization, include a fluorescently tagged ligand in the ligand solution.

4.3.2 Pipette ligand solution onto the surface of each stencil. For stencils made from 10 x 10 mm square stamps, apply 100 µl per stencil.

4.3.3 Check for air bubbles in stencil features. If necessary, use fine-tipped forceps or a 2 µl pipette tip to remove air bubbles from features.

NOTE: **This is a critical step!** If air bubbles remain trapped at the surface of the coverslip, the ligand will not adsorb to the surface and the resulting pattern will be incomplete.

4.3.4 Place stenciled coverslips with ligand into a dish, wrap with laboratory film, and incubate at 4 °C overnight.

5. Transfer of Ligand to Polyacrylamide Gel

5.1 Remove ligand solution and stencil from each coverslip.

5.1.1 Aspirate ligand solution from the surface of a stencil. Ligand solution can be collected and stored at 4 °C and reused for up to a month.

5.1.2 Using forceps, briefly submerge the coverslip with stencil into a dish containing sterile PBS to wash.

5.1.3 Briefly submerge the coverslip with stencil into a second dish of sterile PBS to wash.

5.1.4 Remove the stencil from the surface of the coverslip. Be careful to not break the coverslip.

5.1.5 Briefly submerge the coverslip into a dish containing ultrapure sterile water to remove salts from the PBS washes. Tap the edge of the coverslip to a delicate task wipe to wick away excess water.

5.1.6 Dry the coverslip under an inert gas, such as nitrogen. Mark the underside of the coverslip to keep track of orientation from this point forward. Be careful to keep the patterned side facing up.

5.1.7 Repeat steps 5.1.1 through 5.1.6 for each stenciled coverslip.

5.2 Make polyacrylamide hydrogels with patterned coverslips (refer to previous methods for additional details; Lakins et al., 2012; L. Przybyla et al., 2016b).

NOTE: Sterilize all cap holders, tubes, and spacers used to make polyacrylamide gels by washing with 10% bleach overnight, rinsing with water at least five times to remove bleach, and washing briefly in 70% ethanol. Place all pieces on delicate task wipes in a sterile biosafety cabinet to dry before use.

5.2.1 Prepare polyacrylamide solution to obtain desired hydrogel elasticity. See Table 3.2. Mix together all components except the fluorescent microspheres and the potassium persulfate (PPS).

NOTE: Prepare 1% potassium persulfate solution fresh each time.

5.2.2 Degas the polyacrylamide solution, microspheres, and PPS in separate tubes under vacuum for 30 min.

5.2.3 For each patterned coverslip, prepare a glutaraldehyde-activated "bottom" coverslip with a spacer (18 mm outer diameter, 14 mm inner diameter) placed on top.

Table 3.2: Polyacrylamide hydrogel formulations

			Volumes for 1 ml complete solution						
Elastic Modulus (Pa)	**Final % acrylamide**	**Final % Bis-acrylamide**	**ddH_2O (µl)**	**40% acrylamide (µl)**	**2% Bis-acrylamide (µl)**	**10x PBS (µl)**	**1% TEMED in ddH_2O (µl)**	**Microspheres 0.5% solids in ddH_2O (µl)**	**1% PPS in ddH_2O (µl)**
1050	3	0.1	565	75	50	100	75	60	75
2700	7.5	0.035	485	187.5	17.5	100	75	60	75
4000	7.5	0.05	477.5	187.5	25	100	75	60	75
6000	7.5	0.07	467.5	187.5	35	100	75	60	75

5.2.4 After degassing, briefly sonicate microspheres and add appropriate volume to polyacrylamide solution. Mix by pipetting up and down, being careful not to introduce air bubbles. Briefly sonicate.

5.2.5 Add appropriate volume of PPS to the polyacrylamide solution. Pipette up and down to mix the solution, being careful not to introduce air bubbles.

NOTE: After adding PPS, work rapidly to complete steps 5.2.6 through 5.2.11 before polyacrylamide polymerizes.

5.2.6 Pipette 75-150 μl (depending on thickness of spacer) to the center of each glutaraldehyde-activated coverslip.

5.2.7 Using forceps, place a patterned coverslip onto each glutaraldehyde-activated coverslip with polyacrylamide and spacer, such that the patterned ligand faces the polyacrylamide solution. If sufficient polyacrylamide solution was added, surface tension will wick the polyacrylamide between the two coverslips and no air bubbles will be present.

5.2.8 Pick up each polyacrylamide "sandwich" and carefully touch the side to a delicate task wipe to wick away excess polyacrylamide solution.

5.2.9 Carefully place each polyacrylamide "sandwich" into a cap holder with threads that are compatible with 15 ml conical-bottom tubes. The orientation should be such that the bottom of the glutaraldehyde coverslip is in contact with the bottom of the cap holder, and the patterned coverslip is on top.

5.2.10 Screw a 15 ml conical-bottom tube into each cap holder to hold the polyacrylamide "sandwiches" in place. The tubes should be tight to prevent leaking, but be careful to not overtighten and crack the coverslips.

5.2.11 Centrifuge the polyacrylamide "sandwiches" in the tubes in swing-buckets at 200 x g for 10 min at room temperature. Remove the tubes from the centrifuge and place in tube racks to maintain orientation for an additional 50 min to ensure full polymerization. Keep covered with foil to prevent bleaching of fluorescent microspheres.

NOTE: Centrifugation is critical when using this method to perform TFM. The centrifugal force moves all the microspheres to a single plane, which will ultimately be just below the surface of the hydrogel. This is ideal for imaging microsphere displacements that are used to calculate cell-generated traction stresses. If not performing TFM, microspheres can be left out of the polyacrylamide solution and polymerization can occur at the benchtop without centrifugation.

5.2.12 Remove polymerized polyacrylamide "sandwiches" from the tubes and submerge in PBS in a 100 mm dish. Wrap in laboratory film and incubate for 3 h at room temperature or overnight at 4 °C.

5.3 Prepare patterned gels for seeding cells.

5.3.1 Use scalpel and forceps to carefully remove the patterned coverslip and the spacer from the polyacrylamide "sandwich" while it remains submerged in PBS. The patterned ligand will have transferred to the polyacrylamide during polymerization and will remain after removing the coverslip. The polyacrylamide gel will remain attached to the glutaraldehyde-activated coverslip.

NOTE: **This is a critical step!** The polyacrylamide **must** be submerged in PBS while removing the coverslip or the ligand patterns will be destroyed.

5.3.2 Place each coverslip with patterned polyacrylamide into a cap holder. Place a gasket (18 mm outer diameter, 14 mm inner diameter) on top of the coverslip and around the polyacrylamide,

where the spacer was located. Screw a sawed-off 15 mm conical-bottom tube into the cap holder, forming a well with the patterned polyacrylamide at the bottom. These assemblies fit into the wells of a standard 12-well plate for easy handling.

5.3.3 Wash each gel by adding 500 µl of PBS to the well assembly. Incubate for 10 min at room temperature with gentle shaking. Remove PBS and repeat twice for a total of three washes.

5.3.4 After the final PBS wash, add 500 µl of knockout-DMEM media to gels and incubate at 37 °C overnight. Gels can be kept at 37 °C with media for up to 5 days before seeding cells.

5.3.5 The day before seeding cells, replace knockout-DMEM for complete KSR media and incubate at 37 °C overnight.

6. Culturing hESCs on Patterned Gels

NOTE: All methods described here pertaining to the use of hESCs have been approved by the Human Gamete, Embryo and Stem Cell Research (GESCR) Committee at the University of California San Francisco.

OPTIONAL: If planning to fix samples for immunostaining after TFM, take images of unstressed microsphere positions prior to seeding cells. In this case, fluorescently tagged ligand should be used in step 4.3.1 so that the eventual locations of cells will be known before seeding and microspheres can be imaged in those regions.

6.1 Maintain stock hESC cultures and secondary feeder-free cultures prepared on matrigel-coated plates in conditioned KSR media prior to seeding on patterned polyacrylamide gels (as previously described; L. Przybyla et al., 2016b).

NOTE: Generate conditioned KSR media by culturing irradiated mouse embryonic fibroblasts in KSR media supplemented with 4 ng/ml basic fibroblast growth factor (bFGF). Collecting and replace media every 24 h.

6.2 Aspirate media from hESCs. Briefly wash with knockout-DMEM media. Add 0.05% trypsin-EDTA supplemented with 10 μM Y27632 (Rho kinase inhibitor) and incubate at 37 °C for 5-10 min.

6.3 Add media with serum to inhibit trypsin. Gently aspirate media and pipette over the dish to remove cells. Continue pipetting gently to remove all cells and dissociate cell clusters to single cells.

6.4 Collect the cell suspension and centrifuge at 200 x g for 3 min.

6.5 Aspirate the supernatant and resuspend the pellet in an equivalent volume of KSR media to wash. Centrifuge at 200 x g for 3 min.

6.6 Aspirate the supernatant and resuspend the pellet in conditioned KSR media supplemented with 10 ng/ml bFGF and 10 μM Y27632.

6.7 Count the cells with a hemocytometer and adjust the cell suspension to a concentration of 300,000 cells per ml. Pipette 500 μl of the cell suspension onto each patterned gel (150,000 cells per gel).

6.8 Three hours after seeding, use a pipette to carefully aspirate the media from each gel and replace with fresh conditioned KSR media supplemented with 10 ng/ml bFGF and 10 μM Y27632. This removes excess cells that did not adhere to patterned regions of the polyacrylamide.

NOTE: **This is a critical step!** At this stage cells will be loosely adhered to the patterned ligand. Be very careful when swapping media to not detach the cells. Equal care should be taken with each of the media swaps in the subsequent steps.

6.9 Twenty-four hours after seeding, use a pipette to carefully aspirate the media and exchange for conditioned KSR media supplemented with 10 ng/ml bFGF and 5 μM Y27632.

6.10 Forty-eight hours after seeding, use a pipette to carefully aspirate the media and exchange for conditioned KSR media supplemented with 10 ng/ml bFGF. This removes the Rho kinase inhibitor from the media and experiments can begin the next day, 72 h after seeding.

7. Performing TFM

7.1 When desired, perform TFM as previously described (L. Przybyla et al., 2016b) under desired experimental conditions.

7.2 If unstressed microsphere positions were imaged before seeding cells, fix cells after taking stressed microsphere positions and perform immunostaining to determine localization of proteins of interest relative to regions of high and low traction forces.

RESULTS

The main challenge to overcome in attempting to culture hESCs in colonies of controlled geometry on compliant substrates is to generate a homogenous pattern of ECM-ligand on the surface of the substrate. The strategy presented in this method involves first generating the desired pattern on the surface of a glass coverslip and then subsequently transferring that pattern to the surface of a polyacrylamide hydrogel during polymerization of the gel (Figure 3.1 A). Thus, it is important to ensure the desired pattern is created successfully on the surface of the glass coverslip prior to proceeding to polymerization of the hydrogel and transfer of the pattern (Figure 3.1 B). Based on imaging of fluorescent ligand patterns transferred to polyacrylamide, the ligand appears to be present only in a single plane at the surface of the polyacrylamide, though we did not precisely characterize the thickness of this layer.

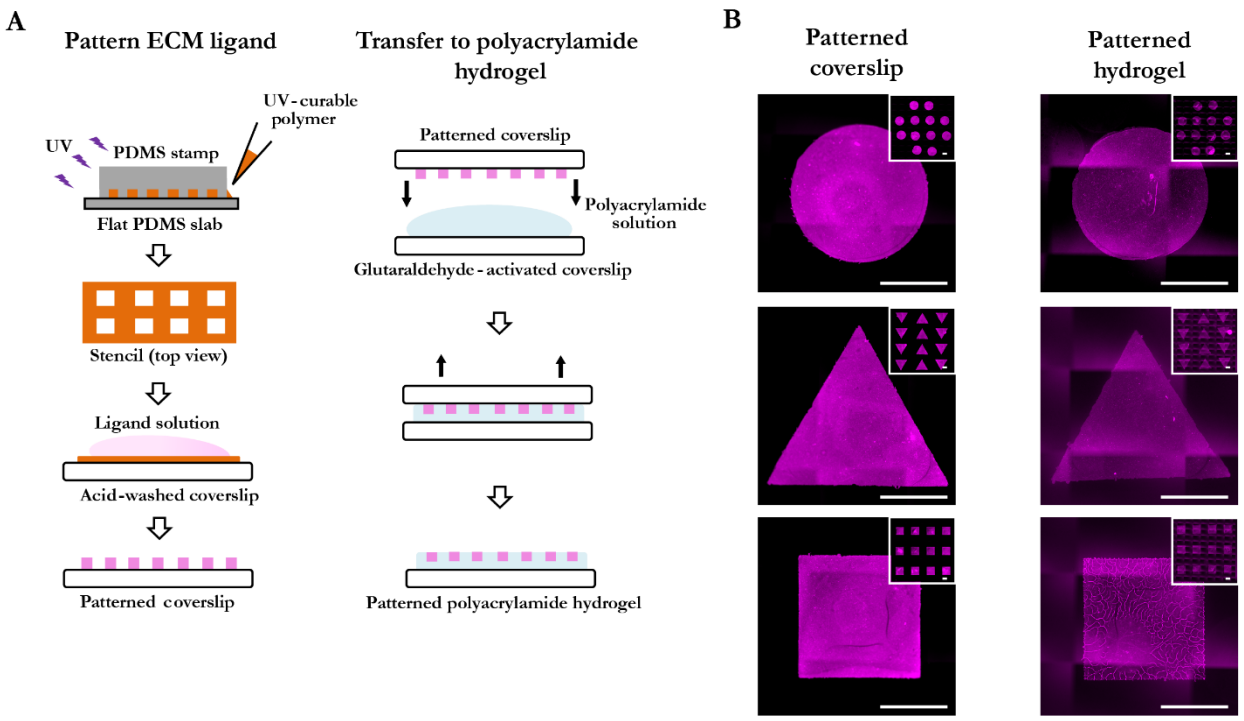

Figure 3.1: Patterning of ECM ligand onto acid-washed coverslips and transfer to polyacrylamide hydrogels.
(A) Cartoon summary of the developed protocol for patterning ECM ligand on acid-washed coverslips and transferring the patterned ligand to polyacrylamide hydrogels.
(B) Representative immunofluorescent images of patterned ECM ligand on acid-washed coverslips (left) and following transfer to polyacrylamide hydrogel (right). Biotin-tagged matrigel was patterned onto the coverslip and labeled with AlexaFluor555-streptavidin prior to transfer to polyacrylamide. Inserts show zoomed-out view of the full patterns generated. All scale bars = 500 μm.

There are two common types of defects observed following pattern generation on the glass coverslip, each with its own source of error. The first is the appearance of fluorescent ligand extending beyond the margins of the desired pattern (Figure 3.2 A; top), which results from leaking of the fluorescent ligand solution due to a small tear in the stencil or insufficient sealing of the stencil to the glass coverslip. The second is the appearance of an incomplete pattern (Figure 3.2 A; bottom), which is typically due to an air bubble trapped at the coverslip interface that prevents adsorption of the fluorescent ligand. The presented method for using stencils to generate patterns of ligand is demonstrably superior to the common technique of microcontact printing for the relatively large

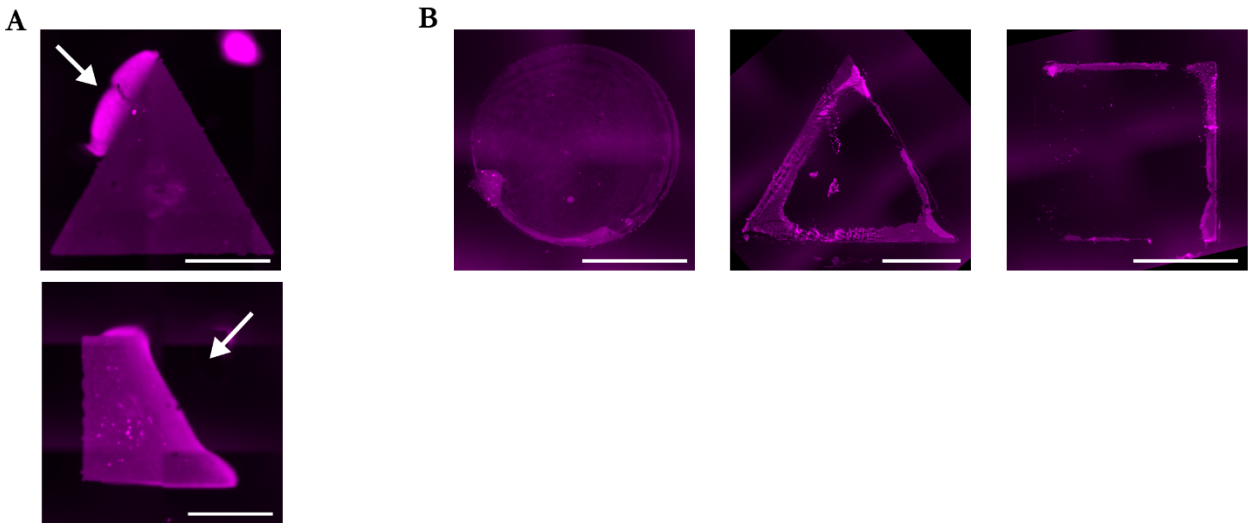

Figure 3.2: Non-ideal patterning results yielded by protocol errors and alternative methods.
(A) Representative immunofluorescent images demonstrating patterning defects of ligand on the glass coverslip. These result from common errors in the protocol, such as leaking of the ligand solution outside the patterned geometry (top; arrow indicates site of leak), and trapping of air bubbles inside the patterned geometries of the stencil upon adding the ligand solution (bottom; arrow indicates site of air bubble).
(B) Representative immunofluorescent images of ECM ligand patterned onto acid-washed coverslips via microcontact printing.
All scale bars = 500 μm.

geometries used in this method, i.e. for circular colonies 1 mm in diameter as well as triangles and squares of equivalent area. Microcontact printing patterns of ligand at this length scale results in heterogeneous transfer at the edges of patterns, with very little ligand deposited in the central regions of the patterns (Figure 3.2 B). This is clearly insufficient for consistently producing hESC colonies of specific geometries.

The ultimate measure of success for this method is the ability to culture hESCs in desired geometries on the patterned hydrogels (Figure 3.3). In order to achieve this, hESCs are seeded at a relatively high density (300,000 cells/mL) in the presence of a Rho kinase inhibitor (Y27632) and incubated for 3 h to facilitate adhesion to the patterns of ligand. Media is then replaced to remove non-adhered cells. Over the course of 72 h, the Y27632 is gradually diluted out of the media by a

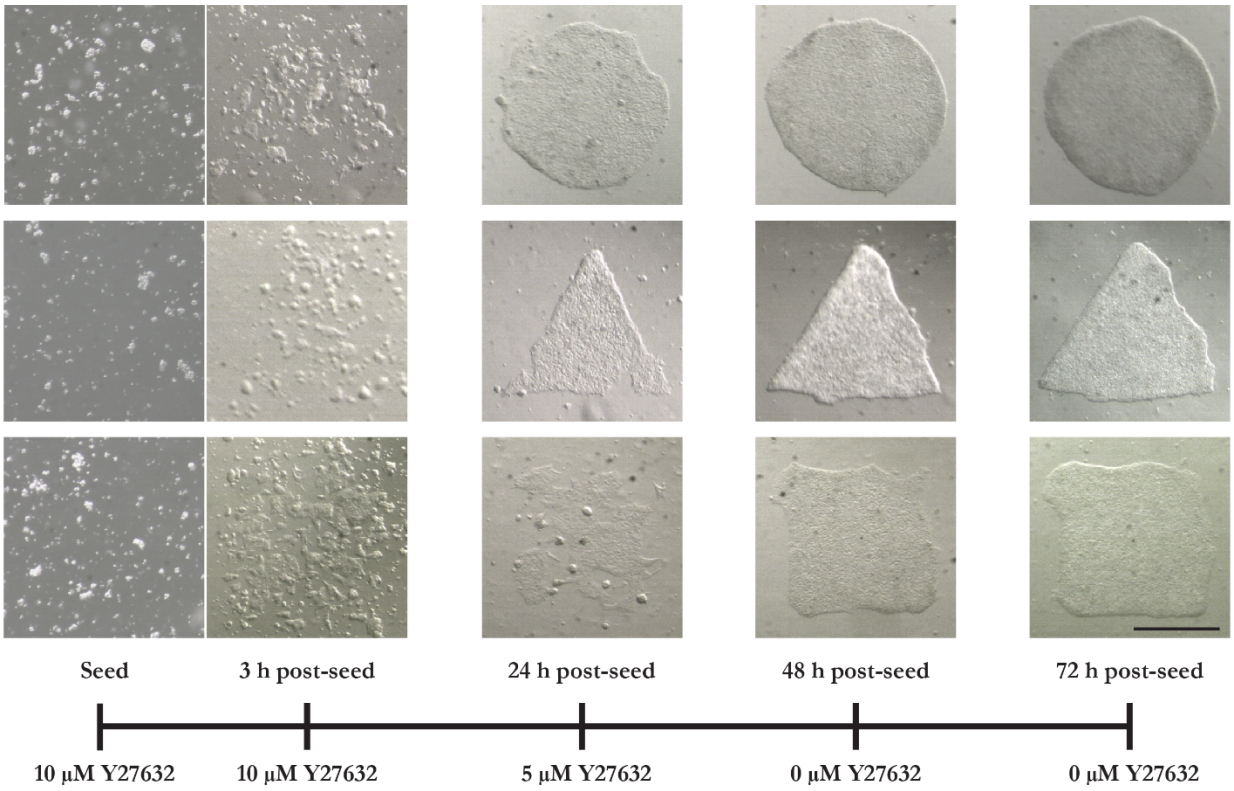

Figure 3.3: Seeding of hESCs onto ECM-patterned polyacrylamide hydrogels.
Representative brightfield images demonstrating successful seeding of hESCs onto polyacrylamide hydrogels with patterned ligand. The timeline at the bottom indicates the series of media changes used to remove unattached cells and dilute out the Y27632. Note that after initial seeding, cells adhere stochastically to various regions within the patterned ligand and then proliferate to fill the patterned regions over the course of 72 h. Scale bar = 500 μm.

series of media exchanges at 24 and 48 h post-seeding. Typically, the hESCs proliferate to complete the patterned geometries by 48-72 h, such that experiments can begin at 72 h post-seeding, once the Y27632 is completely removed from the media.

We attempted to increase the efficiency and throughput of generating geometrically confined hESC colonies on compliant substrates by reducing the cell seeding density, however, this led to inconsistency in achieving completed colonies. Cells seeded at 200,000 cells/ml, rather than 300,000 cells/ml, were not able to generate sufficient cell-cell contacts to survive the reduced concentration of Y27632 at 24 h post-seeding (Figure 3.4 A). It may be possible to generate complete patterns with

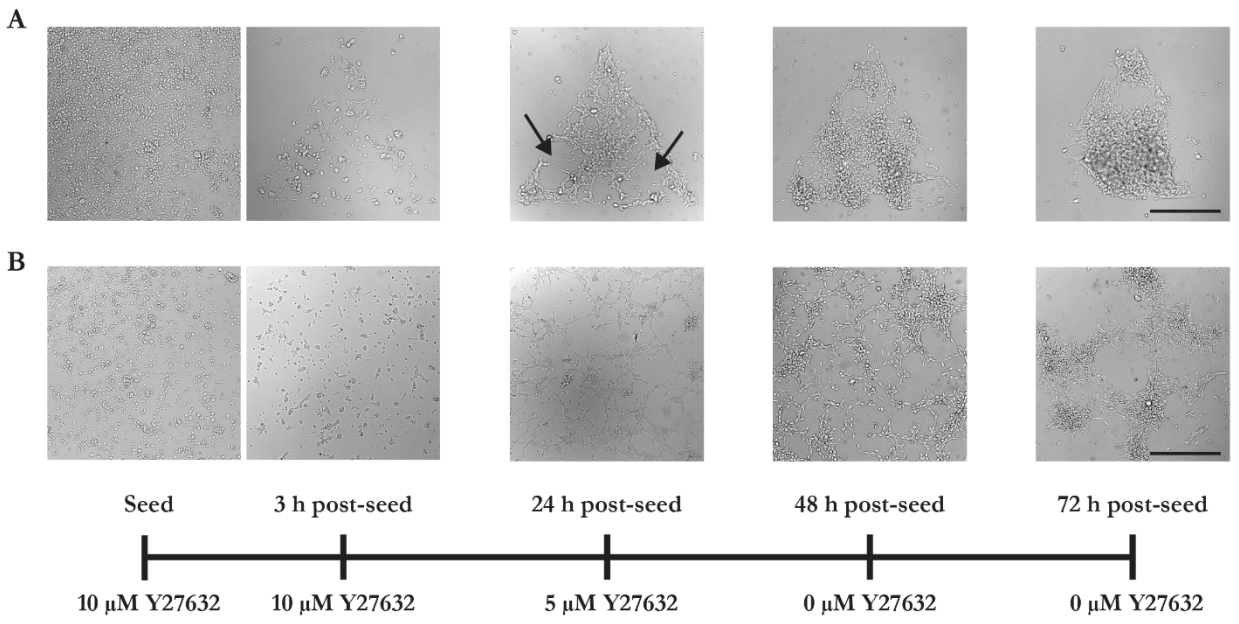

Figure 3.4: Low cell density seeding and unsuccessful ECM-patterning lead to failed geometric confinement of hESC colonies.
(A) Representative brightfield images of hESCs that fail to form completed colonies due to insufficient adherence of cells. Large gaps remaining in the colonies at 24 h post-seeding (arrows) are an early indicator of this issue.
(B) Representative brightfield images of hESCs that fail to form confined colonies due to errors in patterning that led to presence of ligand outside the desired geometries.
Scale bars = 500 μm.

lower cell densities by extending the period of Y27632 dilution; however, overall, it seems more efficient to seed at the higher 300,000 cells/ml density. Occasionally, errors in pattern generation that are not detected earlier in the protocol become apparent upon seeding of hESCs. One such error is the leaking of ligand solution underneath the stencil due to poor contact with the coverslip. This ultimately results in ligand being transferred to regions of the polyacrylamide outside the desired geometries, and unconfined growth of hESCs upon seeding (Figure 3.4 B).

Culturing hESC colonies in confined geometries on polyacrylamide hydrogels permits the measurement of traction stresses using traction force microscopy (TFM). These measurements are made by embedding fluorescent microspheres in the hydrogel and imaging the positions of these beads before and after seeding hESCs (Figure 3.5 A). The displacement of the beads following cell seeding

is a function of cell-generated forces and the elasticity of the hydrogel, thus the images of the bead positions can be used to generate maps of bead displacements and subsequently analyzed to calculate the underlying traction stresses. In circular colonies of hESCs, the largest traction stresses are found near the peripheral edge of the colonies, while the center of the colonies display uniformly low traction stresses (Figure 3.5 B). Interestingly, the highest traction stresses are found in clusters near the edge of the colonies, rather than forming a continuous ring of maximal stress. This implies that although colony geometry plays a key role in determining the distribution of traction stresses, more localized regulation and feedback determine the precise locations of maximal stress. Additionally, so long as the

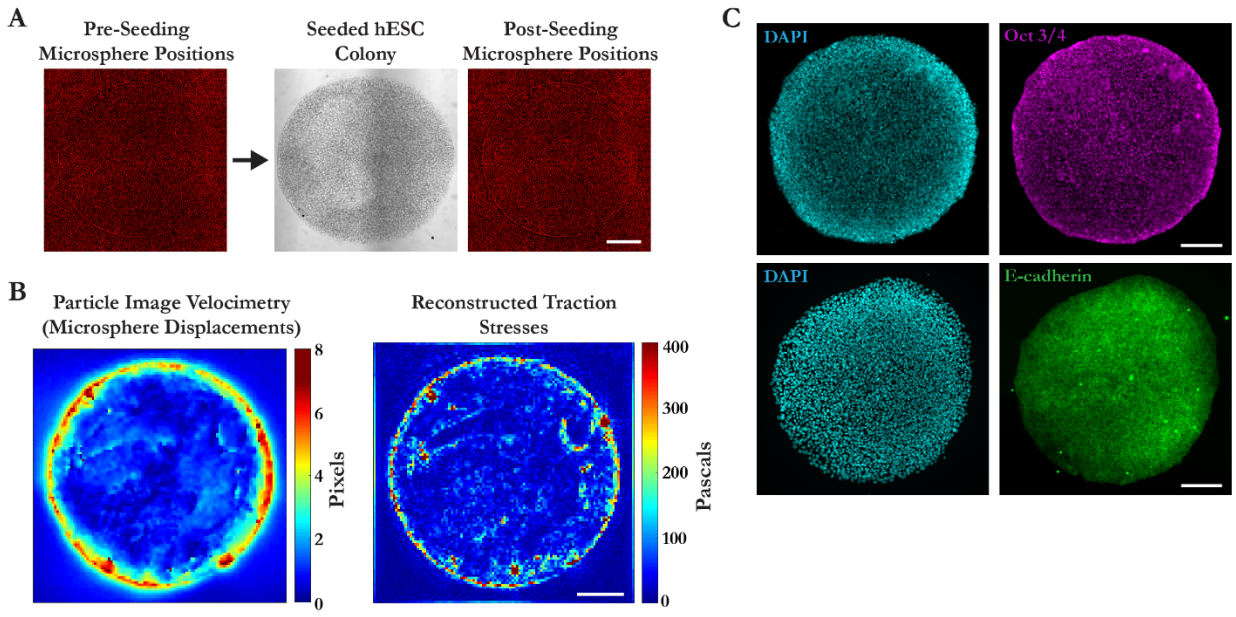

Figure 3.5: Regional localization of traction stresses and immunostaining of geometrically confined hESC colonies on compliant substrates.
(A) Representative immunofluorescent images of microspheres (red; left and right) within the polyacrylamide hydrogel before and after seeding a confined hESC colony (brightfield; middle).
(B) Representative particle image velocimetry (PIV) map depicting the displacement of microspheres due to traction stresses (left) and corresponding reconstructed traction stresses map (right).
(C) Representative immunostaining of confined hESC colonies on patterned polyacrylamide hydrogels, demonstrating the ability to compare localization of proteins of interest to distribution of traction stresses. Nuclei (DAPI) are shown, along with Oct-3/4 (top-right) and E-cadherin (bottom-right) expression.
All scale bars = 200 μm.

image of microsphere positions without adhered cells is taken prior to cell seeding, hESC colonies can be fixed for immunostaining of proteins of interest following traction stress measurements. Despite the observed non-uniform distributions of traction stresses, hESCs cultured as patterned circles in maintenance conditions display uniform expression of the pluripotency marker Oct-3/4 and cell adhesion molecule E-cadherin (Figure 3.5 C).

To further confirm that hESC colonies cultured on ECM-patterned compliant substrates remain pluripotent, we examined Oct-3/4 and E-cadherin expression within colonies patterned in a variety of geometries, including circles, squares, and triangles. As expected, immunofluorescent staining revealed that so long as hESCs were cultured in maintenance media, the colonies displayed homogeneous expression of both Oct-3/4 and E-cadherin (Figures 3.6 A-B). Furthermore, there were no apparent differences in Oct-3/4 and E-cadherin protein expression between colonies of different geometries (Figures 3.6 A-B). Levels of mRNA expression, determined by qPCR, confirmed there were no significant differences in expression of pluripotency markers Oct-3/4, Nanog, and Sox2 between colonies of different geometries, as well as when compared to expression levels prior to seeding hESCs on patterned substrates (Figure 3.6 C). Together, these data demonstrate that hESCs remain pluripotent when cultured on ECM-patterned compliant substrates using our method, and indicate that seeding hESCs on these substrates does not directly induce differentiation.

DISCUSSION

To simplify a long and detailed protocol, this method consists of three critical stages: 1) generating patterns of ECM ligand on glass coverslips, 2) transferring the patterns to polyacrylamide hydrogels during polymerization of the gel, and 3) seeding hESCs on the patterned hydrogel. There are critical steps that must be considered at each of these three stages. In order to generate high-fidelity patterns on the glass coverslips, the stencil must be firmly pressed onto the coverslip to prevent leaking of the

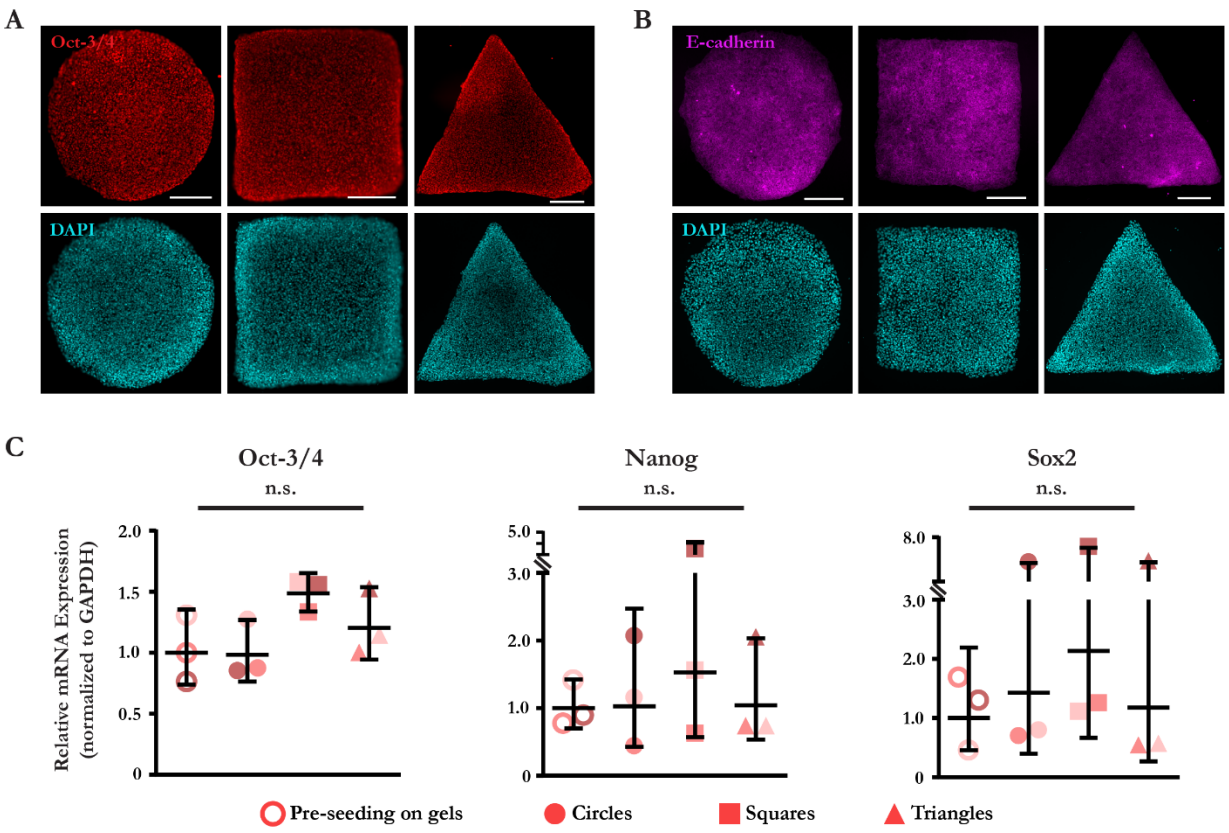

Figure 3.6: Geometrically confined hESC colonies on compliant substrates remain pluripotent in maintenance conditions.
(A) Representative immunofluorescent images of Oct-3/4 (top) and nuclei (DAPI; bottom) in geometrically confined colonies of hESCs on compliant hydrogels in maintenance conditions.
(B) Representative immunofluorescent images of E-cadherin (top) and nuclei (DAPI; bottom) in geometrically confined colonies of hESCs on compliant hydrogels in maintenance conditions.
(C) Bar graphs showing mRNA levels of pluripotency genes in geometrically confined colonies of hESCs on compliant hydrogels in maintenance conditions, relative to levels prior to seeding on hydrogels. Line and bars represent mean ± 95% CI. n.s. = not significant.
All scale bars = 250 μm.

ligand solution and all air bubbles must be removed after adding ligand solution to the surface of the stencil (Figure 3.2 A). If ligand solution does leak through the stencil due to poor contact with the coverslip, ligand will be transferred to the entire surface of the polyacrylamide hydrogel and hESCs will not be confined to the desired colony geometry (Figure 3.4 B). The most important step in transferring the patterned ligand to polyacrylamide is gently separating the top coverslip from the hydrogel while all components remain submerged in PBS. If the hydrogel does not remain submerged

during separation, the patterns may be completely destroyed. Furthermore, if the separation occurs too rapidly, the surface of the hydrogel may tear or be otherwise damaged. The softer the hydrogel, the more it is at risk for damage during separation. Finally, the user must pipette very carefully when exchanging media during the seeding and culture of hESCs on the patterned hydrogels. The hESCs remain loosely adhered throughout the protocol and the patterned colonies can be easily disrupted by careless or rushed pipetting.

In addition to the critical steps discussed above, there are a number of other steps that may require modification and troubleshooting when adapting this protocol for different applications. While the patterns demonstrated here are on the length scale of hundreds of microns to a millimeter, generating patterned features on silicon wafers with transparency photomasks and negative photoresist allows for feature sizes all the way down to 7-10 μm. Thus, this protocol could be adapted for confining the geometry of single cells or smaller colonies of a few cells on compliant substrates.

Two parameters that will likely require optimization when adapting this protocol for different cell types are the type of ECM ligand used and the concentration of the ligand in solution during adsorption to the glass coverslip through the stencils. A total ligand concentration of 250 μg/ml was sufficient for producing homogenous patterns of matrigel and facilitating attachment of hESCs (Figures 3.1 B and 3.3), though it may be possible to achieve similar results with lower concentrations. On the other hand, it may be necessary to further increase the concentration of ligand for cell types that are less adherent or for applications that require shorter incubation times. Increased concentration of ligand may also be required for different ECM ligands, such as fibronectin or collagen, which are less hydrophobic than matrigel and therefore may not adsorb to the hydrogel as strongly. Because the transfer of ligand from coverslip to hydrogel occurs during polymerization of the hydrogel, commonly used techniques for robustly cross-linking the ECM ligand to the hydrogel surface (such as sulfo-SANPAH treatment) are impossible. Using fluorescently labelled ECM ligands to enable visualization

of the patterns at each step of the protocol is extremely helpful when optimizing and troubleshooting these parameters.

Additionally, the protocol for seeding cells may require optimization depending on the cell type and media conditions used. For cells that adhere more rapidly or efficiently, a lower seeding density may be required to prevent cell-cell adhesions that span between patterns and result in aggregates rather than patterned monolayer colonies. For cells that display very poor attachment, a larger seeding density or longer length of time before the initial media swap may be required to facilitate complete formation of confined colonies (Figure 3.4 A).

A key limitation of this method is its technical complexity, which results in relatively low-throughput results compared to similar methods that involve culturing cells on patterned glass substrates (Warmflash et al., 2014). However, this drawback is far outweighed by the physiological relevance achieved by culturing confined hESC colonies on compliant substrates. By effectively recapitulating the mechanical properties of the early embryo, we will be able to better model and understand the processes that lead to self-organization of the primary germ layers.

An additional benefit of this method for confining hESC colonies on compliant polyacrylamide hydrogels versus hard glass substrates is that it is compatible with use of TFM to examine the link between the organization of an hESC colony, as a model of the early embryo, and the distribution of cell-generated forces that may underlie morphogenesis and cell fate specification. Confining hESC colonies results in distributions of traction stresses that are dependent on colony geometry (Figure 3.5 B). Despite the non-uniformity of these traction stresses, cells throughout the colonies remain pluripotent in maintenance conditions (Figures 3.5 C and 3.6). However, we hypothesize that the traction stress distributions may be involved in regulating patterns of cell fate specification by tuning the response to induction cues, such as soluble morphogens. We anticipate

that this method will allow us and other groups to better model the early human embryo with hESCs, leading to a more complete understanding of the fundamental processes that underlie human embryogenesis.

CHAPTER 4

Cell-Adhesion Tension Directs hESC Mesoderm Specification via Wnt/β-catenin Signaling

This chapter is adapted from work published in the peer-reviewed article titled "Mechanical tension promotes formation of gastrulation-like nodes and patterns mesoderm specification in human embryonic stem cells" by **Jonathon M. Muncie**, Nadia M.E. Ayad, Johnathon N. Lakins, Xufeng Xue, Jianping Fu, and Valerie M. Weaver in Developmental Cell (2020).

INTRODUCTION

In the studies presented in Chapter 2, we found that hESCs cultured on compliant matrices were capable of self-organizing to form gastrulation nodes upon stimulation with BMP4. Moreover, we demonstrated that these gastrulation nodes arose in regions that exhibited high cell-adhesion tension prior to BMP4 treatment. We consistently observed that these regions of high cell-adhesion tension developed in nodes near the periphery of hESC colonies, thus we hypothesized that the spatial localization of these nodes was determined, at least in part, by tissue organization and the geometry of the colonies. To address this hypothesis, we developed the method detailed in Chapter 3 to generate patterns of ECM ligand on engineered substrates in order to confine hESC colonies to specific, defined geometries on compliant polyacrylamide hydrogels.

Here, we used the method from Chapter 3 to control and manipulate the geometry of hESC colonies and demonstrated that high cell-adhesion tension not only coincides with the development of gastrulation nodes in hESC colonies, rather, it plays a direct role in fostering mesoderm

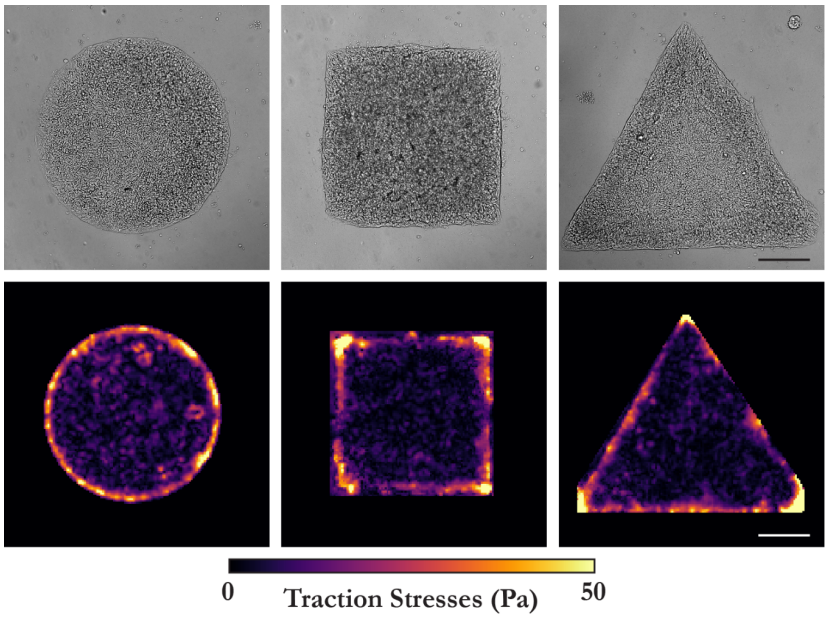

Figure 4.1: Colony geometry dictates regional localization of high cell-adhesion tension for geometrically confined hESCs on compliant hydrogels.
Representative brightfield images and corresponding traction stress maps measured for geometrically confined hESC colonies on compliant (2,700 Pa) polyacrylamide hydrogels before BMP4 stimulation. Scale bars = 250 μm. Pa = pascals.

specification. We demonstrated that ablating cell-adhesion tension reduces mesoderm specification, whereas mechanical stretching of colonies is sufficient to induce mesoderm specification. We identified a mechanism by which cell-adhesion tension transmitted across adherens junctions exposes a specific tyrosine residue on cell-junction-associated β-catenin, making it accessible for phosphorylation. Upon BMP4 stimulation, Src-family kinases (SFKs) enhance the phosphorylation, junctional release, and nuclear translocation of β-catenin to promote canonical Wnt signaling and induce mesoderm specification in the regions of high cell-adhesion tension. These findings underscore the interplay between tissue organization, cell-cell tension, and morphogen-dependent differentiation, and demonstrate that cell- and tissue-level forces directly influence the signaling pathways that regulate cell fate specification in early development.

RESULTS

Tissue Geometry Spatially Patterns Regions of High Cell-Adhesion Tension that Promote Mesoderm Specification

To test the relationship between cell-adhesion tension and gastrulation node induction, we confined hESC colonies to defined geometries using our method to precisely pattern ECM ligand on compliant substrates (described in detail in Chapter 3; Muncie et al., 2019). We determined that specific tissue geometries previously shown to promote localized tension within an epithelial cell colony (Gomez et al., 2010; Kilian et al., 2010; J. Lee et al., 2016; C. M. Nelson et al., 2005; Q. Smith et al., 2018) similarly induced high cell-adhesion tension in the hESC colonies maintained in pluripotent conditions. For instance, shapes such as squares and triangles fostered the highest cell-adhesion tension in the colony corners, whereas circles developed comparatively moderate levels of tension around their colony periphery (Figure 4.1).

As predicted, live-cell imaging of the T-reporter showed that following BMP4 stimulation, gastrulation nodes were initiated in the colony regions that displayed the highest cell- adhesion tension prior to differentiation, before mesoderm specification then spread throughout the colony periphery (Figures 4.2 A and 4.3). The averaged intensity of multiple cell-adhesion tension and T-expression plots confirmed that the initiation of mesoderm specification detectable by 30 hours of BMP4 stimulation on compliant substrates did indeed consistently arise within colony regions that displayed high cell-adhesion tension prior to BMP4 addition (Figure 4.2 B-C). By contrast, on highly rigid substrates we observed uniform initiation of mesoderm specification around the colony periphery, as previously reported (Figure 4.4 A-B; Smith et al., 2018; Warmflash et al., 2014). Geometric confinement of mouse ESC colonies on highly rigid substrates also leads to regional differences in local cell density that appear to pattern mesoderm specification (Blin et al., 2018). We noted that hESC colonies on compliant substrates exhibit nearly uniform cell density prior to BMP4 stimulation, with

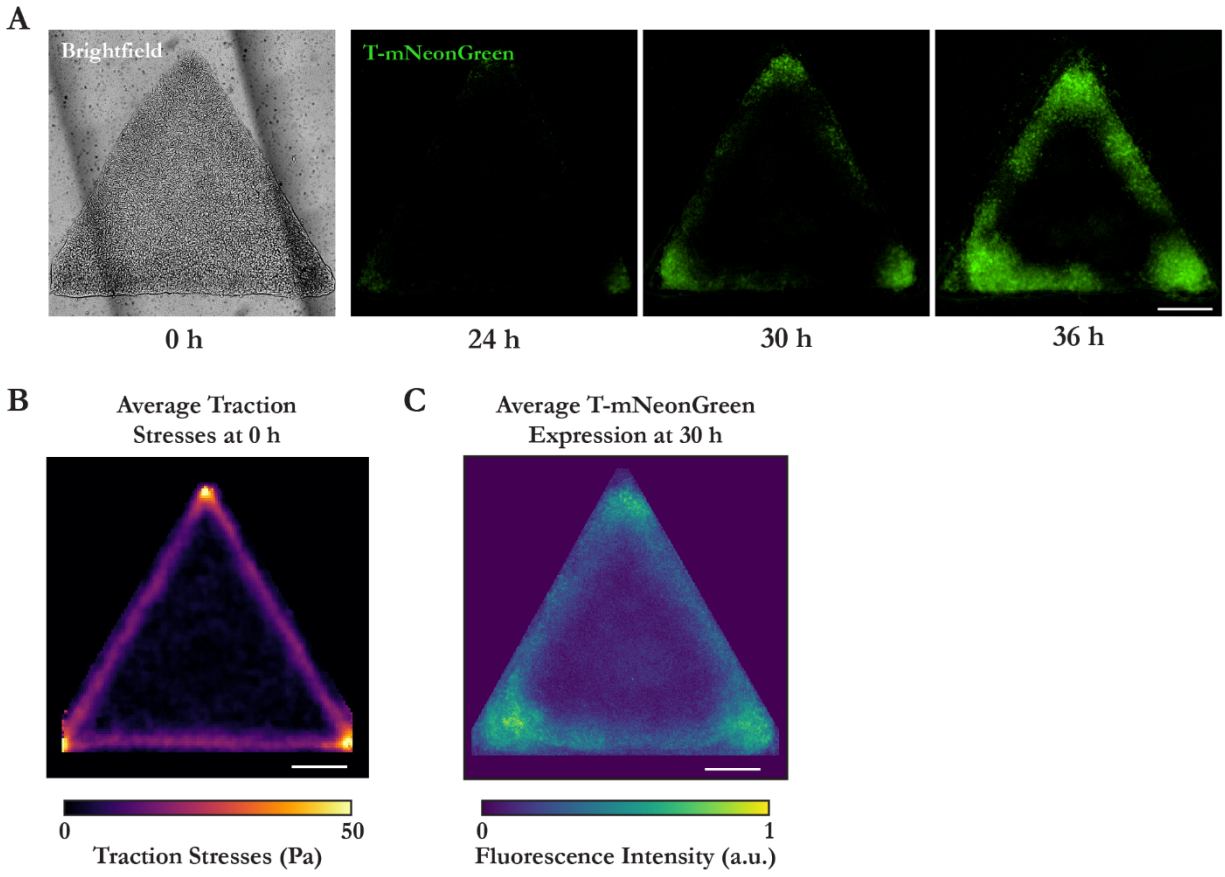

Figure 4.2: Regions of high cell-adhesion tension induce mesoderm specification in geometrically confined colonies of hESCs on compliant hydrogels.
(A) Representative brightfield and time-lapse images of T-mNeonGreen expression for geometrically confined triangle hESC colonies on compliant (2,700 Pa) polyacrylamide hydrogels following BMP4 stimulation.
(B) Map of average traction stresses measured for geometrically confined triangle hESC colonies on compliant (2,700 Pa) polyacrylamide hydrogels before BMP4 stimulation. n = 19 (3, 10, 6) colonies.
(C) Normalized average intensity map of T-mNeonGreen expression within geometrically confined triangle hESC colonies on compliant (2,700 Pa) polyacrylamide hydrogels at 30 h BMP4 stimulation. n = 12 (3, 1, 7, 1) colonies.
All scale bars = 250 μm. Pa = pascals. a.u. = arbitrary units.

a slight drop in density within 50 μm from the colony edge, and that there is no apparent correlation between the distribution of cell density and the initiation of mesoderm specification (Figure 4.5).

We next sought to differentiate between cell-adhesion tension and gradients of apically-secreted diffusible factors in hESC mesoderm specification. To facilitate a direct comparison of results with prior studies, we generated patterned substrates on tissue culture plastic (Etoc et al., 2016; Tewary

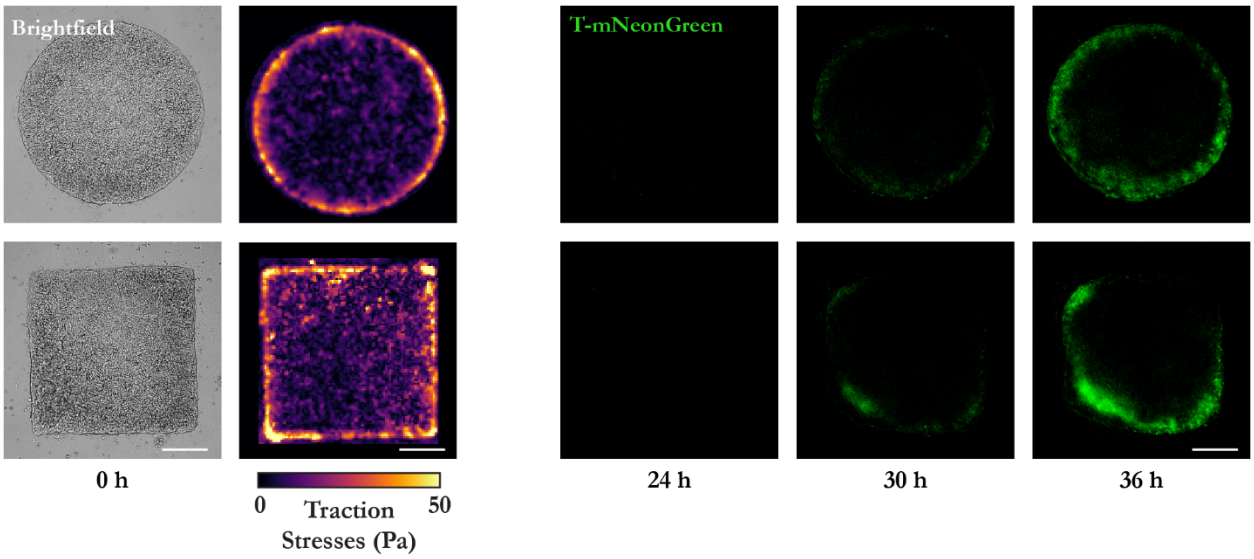

Figure 4.3: Representative patterns of cell-adhesion tension and subsequent mesoderm specification in geometrically confined circle and square hESC colonies on compliant hydrogels.
Representative brightfield images and corresponding traction stress maps of geometrically confined circle and square hESC colonies cultured on compliant (2,700 Pa) polyacrylamide hydrogels prior to BMP4 stimulation, and time-lapse images of T-mNeonGreen expression in the same colonies after BMP4 stimulation.

et al., 2017). Our design consisted of a triangle colony positioned with one corner inside the mouth of a Pac-Man colony, separated by the smallest feasible gap between the two colonies that was large enough to prevent colony fusion and cell-adhesion tension transmission (75 μm; Figure 4.6 A). We rationalized that if BMP inhibitors were secreted apically and were concentrated in a radially expanding gradient that permits high BMP signaling at the periphery of the colony and represses signaling at the center, then the cells in the triangle corner within the mouth of the Pac-Man colony would be exposed to high concentrations of inhibitory signals and would be unable to undergo mesoderm specification. However, contrary to this prediction, we observed mesoderm specification in the triangle corner within the mouth of the Pac-Man colony at equivalent levels to the distal corners (Figure 4.6 A-B). The findings indicate that if present, apically-secreted inhibitory signals are not the sole factor directing the patterning of mesoderm specification in these hESC colonies. Furthermore, these data provide

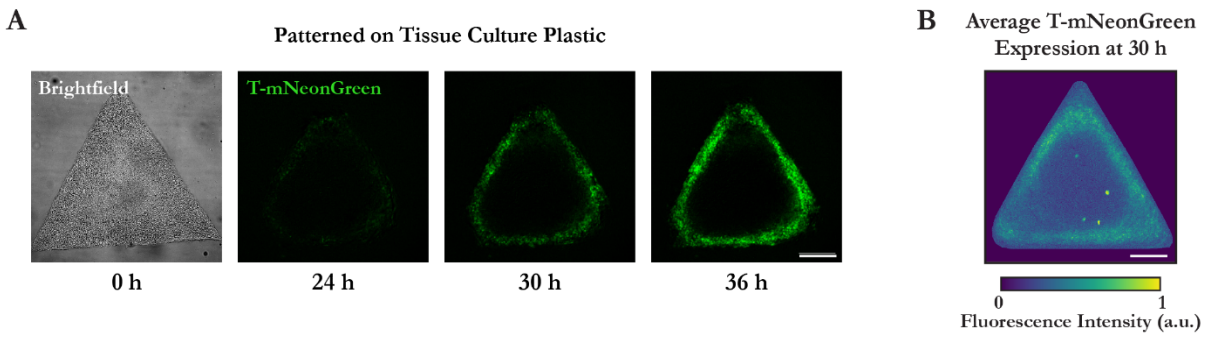

Figure 4.4: Mesoderm specification in geometrically confined triangle hESC colonies on rigid tissue culture plastic.
(A) Representative brightfield image and time-lapse T-mNeonGreen images of a geometrically confined triangle hESC colony on tissue culture plastic before and after BMP4 stimulation.
(B) Normalized average intensity map of T-mNeonGreen expression within the geometrically confined triangle hESC colonies on tissue culture plastic 30 h after BMP4 stimulation. n = 28 (7, 9, 12) colonies.
Scale bars = 250 μm.

additional evidence that the initiation of mesoderm specification at the corners of triangle colonies on compliant substrates is likely attributable to the measured pattern of cell-adhesion tension, and not merely a result of cells within these corner regions being distant and isolated from inhibitory signals endogenously secreted and concentrated at the center of colonies.

Together, these results suggest that the biophysical properties of the microenvironment, cell- and tissue-level forces, and secreted diffusible factors likely synergize, in a context-dependent manner, to direct the spatial patterning of cell fate specification.

E-Cadherin Junctions Mediate the High Cell-Adhesion Tension Required for Mesoderm Specification

To further explore the role of cell-cell tension in hESC colony self-organization and gastrulation node formation, we attenuated cell-cell adhesions. Epithelial contacts mediate the tissue-like behavior that leads to robust patterns of cell-cell tension in geometrically-defined multicellular colonies (Gomez et al., 2010; Kilian et al., 2010; J. Lee et al., 2016; C. M. Nelson et al., 2005; Q. Smith et al., 2018). Moreover, we previously showed that the adherens junction protein E-cadherin was necessary for

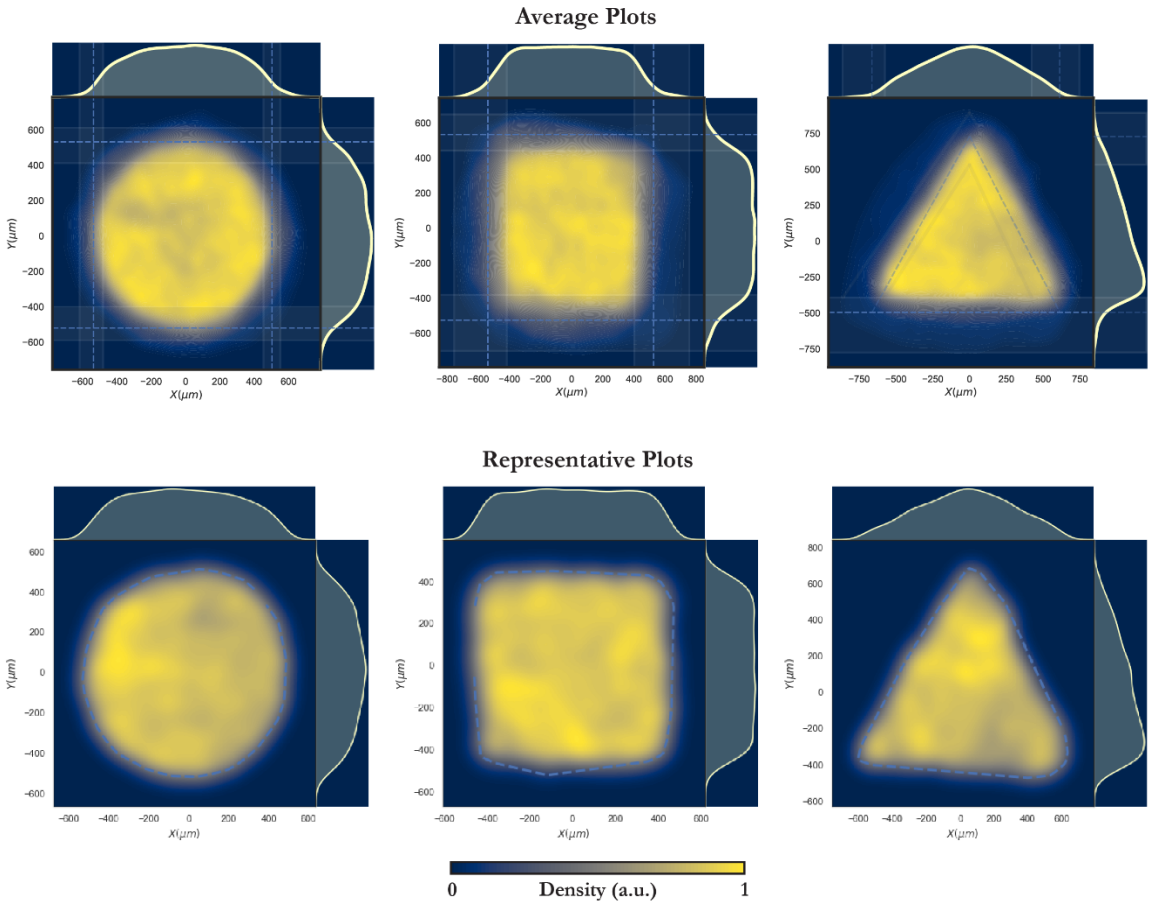

Figure 4.5: Cell density in geometrically confined colonies of hESCs on compliant hydrogels. Average (top) and representative (bottom) kernel density estimator (KDE) plots of cell density within geometrically confined hESC colonies on compliant (2,700 Pa) polyacrylamide hydrogels. For average plots, dashed blue lines represent the average X and Y positions of colony boundaries, transparent shaded regions indicate the range. For representative plots, dashed blue lines indicate the colony boundary as determined by brightfield images. n = 29 (6, 5, 18) circle colonies, n = 29 (7, 3, 19) square colonies, and n = 24 (6, 4, 14) triangle colonies. Scale bars = 250 μm.

enhanced mesoderm specification on soft hydrogels (Laralynne Przybyla et al., 2016c). Thus, we next asked whether E-cadherin was necessary to generate regions of high cell-adhesion tension and subsequent mesoderm specification.

We attenuated cell adhesions by knocking down E-cadherin using an inducible short hairpin RNA system (shE-cadherin) that achieved a 50% reduction in detectable E-cadherin mRNA expression by qPCR (Figure 4.7 A). Importantly, immunofluorescent staining revealed that shE-

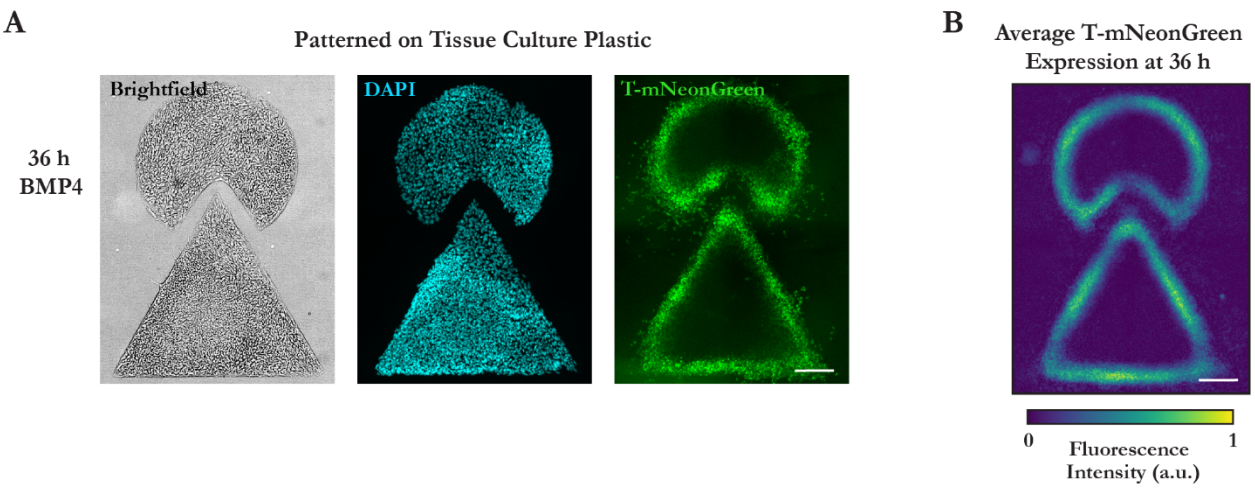

Figure 4.6: A concentration gradient of apically-secreted inhibitors is insufficient to explain observed mesoderm specification patterns.
(A) Representative brightfield and immunofluorescent images of nuclei (DAPI) and T-mNeonGreen expression for geometrically confined triangle-Pac-Man hESC colonies on tissue culture plastic 36 h after BMP4 stimulation.
(B) Normalized average intensity map of T-mNeonGreen expression within the geometrically confined triangle-Pac-Man hESC colonies on tissue culture plastic 36 h after BMP4 stimulation. n = 23 (8, 5, 10) colonies.
Scale bars = 250 μm.

cadherin knockdown significantly reduced E-cadherin expression at the protein level as well (Figure 4.7 B-C). Upon shE-cadherin knockdown we observed a significant reduction in the magnitude of cell-adhesion tension measured for patterned triangle hESC colonies prior to BMP4 stimulation, which was particularly evident at the colony corners (Figure 4.8 A-D). The lack of a complete ablation of cell-adhesion tension was likely due to the fact that E-cadherin was only partially knocked-down, rather than completely knocked-out. This partial knockdown conferred by the shE-cadherin system was beneficial for our study to determine how reduction of cell-adhesion tension affects induction of gastrulation nodes in uniform hESC colonies; whereas complete knockout of E-cadherin has been shown to cause cell sorting and tissue patterning independent of cell fate specification (Libby et al., 2018; Chapter 5). In fact, the partial knockdown of E-cadherin and measured reduction of cell-adhesion tension was sufficient to significantly reduce mesoderm specification in hESC colonies

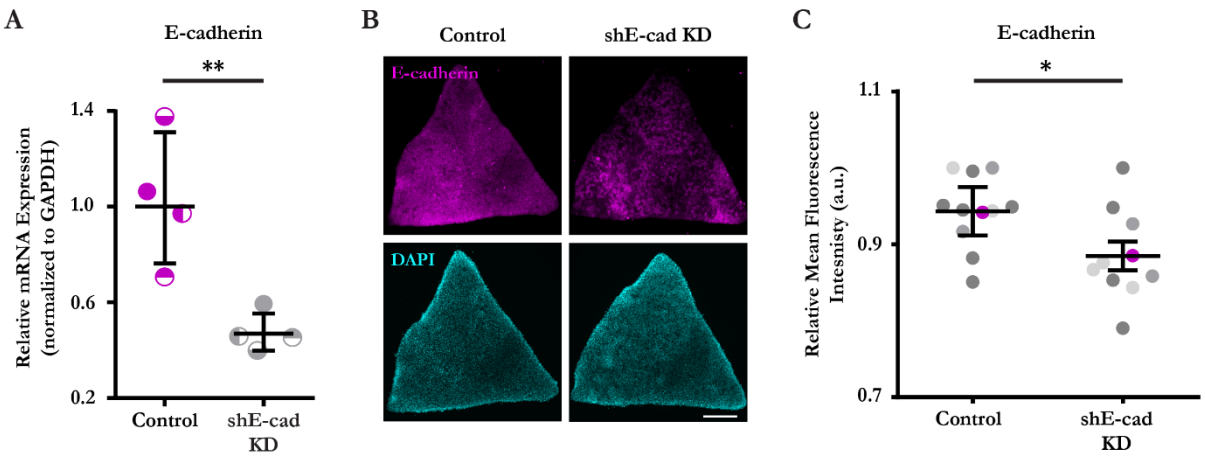

Figure 4.7: E-cadherin knockdown in geometrically confined hESC colonies on compliant hydrogels using inducible shRNA.
(A) Relative E-cadherin mRNA expression with and without shE-cadherin knockdown.
(B) Representative images of E-cadherin expression and nuclei (DAPI) in geometrically confined triangle hESC colonies on compliant (2,700 Pa) polyacrylamide hydrogels with and without shE-cadherin knockdown. Scale bar = 250 μm.
(C) Plot of relative E-cadherin mean fluorescence intensity in geometrically confined triangle hESC colonies on compliant (2,700 Pa) polyacrylamide hydrogels with and without shE-cadherin knockdown. Magenta data points correspond to the images shown in (B). n = 11 (2, 2, 7) control colonies and n = 10 (3, 2, 5) knockdown colonies.
For (A) and (C): Line and bars represent mean ± 95% CI. *$p < 0.05$ and **$p < 0.01$. For (C): Data from independent experiments represented by different shades of gray. shE-cad KD = shE-cadherin knockdown. a.u. = arbitrary units.

(Figure 4.8 E-F). This sensitivity to loss of E-cadherin and the resulting loss of cell-adhesion tension emphasizes the importance of cell-cell adhesions in mediating the localization of high tension that directs mesoderm specification in hESC colonies.

Ablating Regions of High Cell-Adhesion Tension Inhibits, Whereas Mechanical Stretching Promotes Mesoderm Specification

To definitively establish the roles of tissue organization and cell-adhesion tension in mesoderm specification, we directly ablated tension in patterned colonies of hESCs. We generated precise cuts across the corners of the triangle hESC colonies using an eyebrow knife (Sive et al., 2000), which disrupted the spatially-restricted regions of high cell-adhesion tension (Figure 4.9 A-B). Consistent

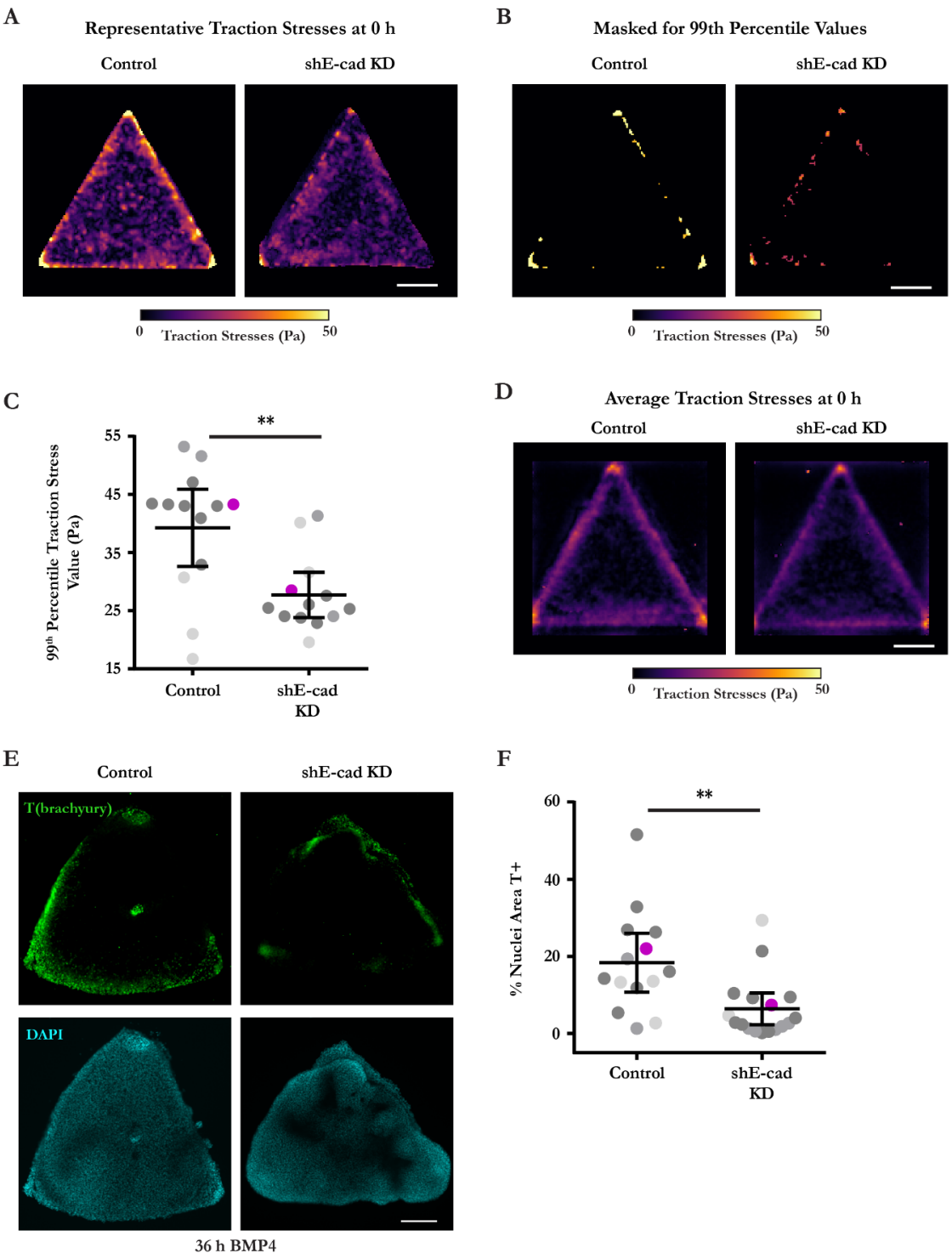

Figure 4.8: E-cadherin knockdown reduces cell-adhesion tension and subsequent mesoderm specification.

(A) Representative traction stress maps for geometrically confined triangle hESC colonies on compliant (2,700 Pa) polyacrylamide hydrogels with and without shE-cadherin knockdown.

(B) Representative maps of average traction stresses measured within geometrically confined triangle hESC colonies on compliant (2,700 Pa) polyacrylamide hydrogels with (*caption continued on next page*)

(*caption continued from previous page)* and without shE-cadherin knockdown, masked to only display traction stresses greater than the 99th percentile value for each map. Unmasked representative maps are shown in (A).
(C) Plot of the 99th percentile traction stress values from maps of geometrically confined triangle hESC colonies on compliant (2,700 Pa) polyacrylamide hydrogels with and without shE-cadherin knockdown. n = 13 (3, 2, 8) colony maps. Magenta data points correspond to maps in (A).
(D) Maps of average traction stresses measured within geometrically confined triangle hESC colonies on compliant (2,700 Pa) polyacrylamide hydrogels with and without shE-cadherin knockdown. n = 13 (3, 2, 8) colonies from each condition.
(E) Representative images of T(brachyury) expression and nuclei (DAPI) in geometrically confined triangle hESC colonies on compliant (2,700 Pa) polyacrylamide hydrogels with and without shE-cadherin knockdown at 36 h BMP4 stimulation.
(F) Plot of the % of nuclear area marked T-positive in geometrically confined triangle hESC colonies on compliant (2,700 Pa) polyacrylamide hydrogels with and without shE-cadherin knockdown at 36 h BMP4 stimulation. Magenta data points correspond to the images shown in (E). n = 14 (3, 3, 8) control colonies and n = 17 (2, 6, 9) knockdown colonies.
All scale bars = 250 μm. For (C) and (F): Line and bars represent mean ± 95% CI and data from independent experiments are represented by different shades of gray. **p < 0.01. shE-cad KD = shE-cadherin knockdown. Pa = pascals.

with our assertion that localized regions of high cell-adhesion tension direct the gastrulation nodes that promote mesoderm specification, we noted a significant delay in BMP4-induced T-reporter expression in the cut corners of these colonies (Figure 4.9 C-D).

Due to the fact that physically ablating hESC colonies may have produced confounding effects that delayed mesoderm specification, we sought further evidence of a causal link between localized cell-adhesion tension and the development of gastrulation nodes. We thus designed Pac-Man patterned surfaces that generate low cell-adhesion tension at the concave edge of the hESC colony, corresponding to the "mouth" of the Pac-Man (Figure 4.10 A). Although BMP4-stimulation of these patterned Pac-Man hESC colonies induced T-reporter expression at the convex edges of the Pac-Man, T-reporter expression was clearly excluded from the low-tension concave edge (Figure 4.10 A-C). The results provide support for our assertion that high cell-adhesion tension directs the spatial localization of gastrulation nodes that specify mesoderm in hESC colonies on compliant substrates.

We next tested whether cell-adhesion tension is sufficient to induce mesoderm specification. Colonies of hESCs were cultured on flexible PDMS microdevices that subjected the low-tension,

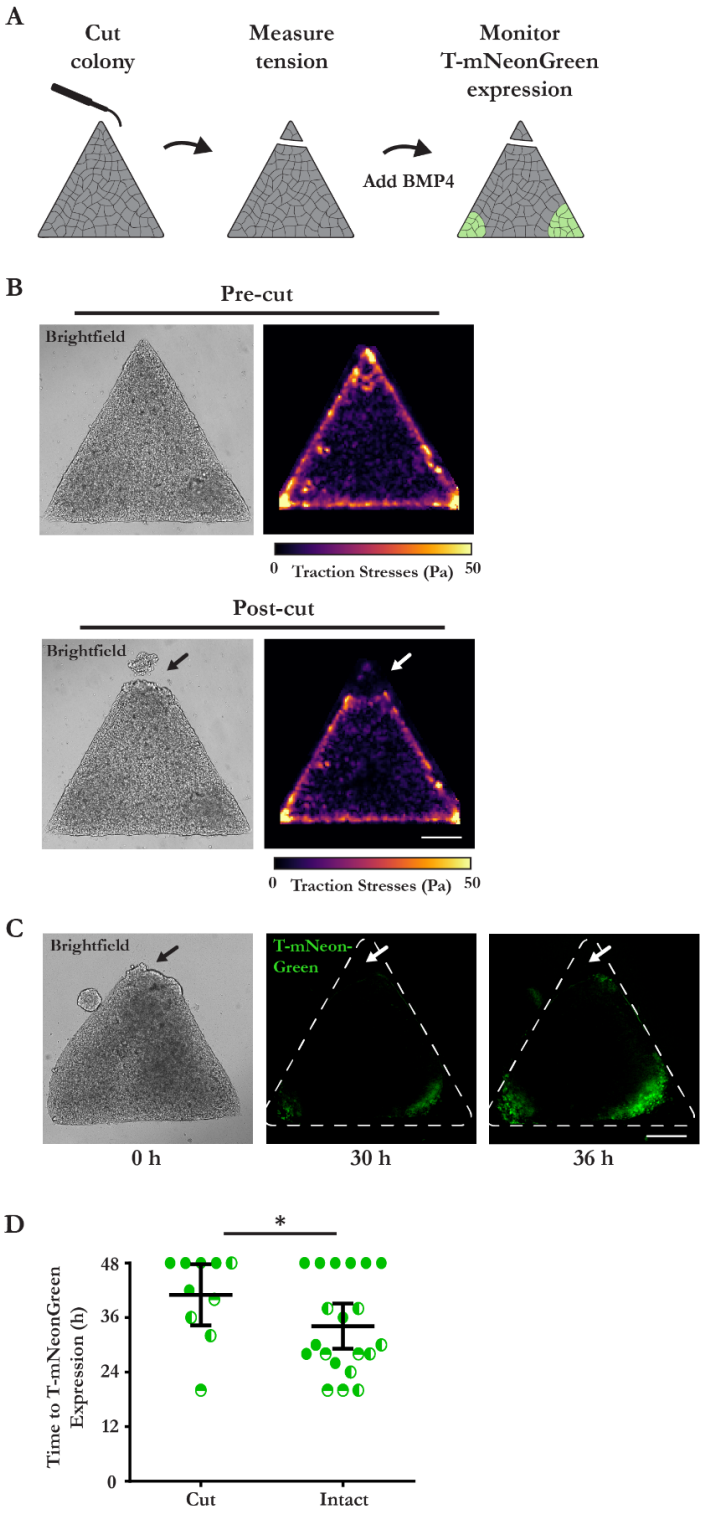

Figure 4.9: Ablating regions of high cell-adhesion tension inhibits mesoderm specification.
(A) Cartoon of eyebrow knife experiment.
(B) Representative brightfield images and traction stress maps of geometrically confined triangle hESC colonies on compliant (2,700 Pa) polyacrylamide hydrogels before (*caption continued on next page*)

(*caption continued from previous page*) and after eyebrow knife ablation.
(C) Representative brightfield and time-lapse images of T-mNeonGreen expression following BMP4 stimulation of geometrically confined triangle hESC colonies on compliant (2,700 Pa) polyacrylamide hydrogels with one corner ablated using the eyebrow knife prior to BMP4 stimulation. Arrow indicates site of eyebrow knife ablation.
(D) Plot of time to T-mNeonGreen expression in the corners of geometrically confined triangle hESC colonies on compliant (2,700 Pa) polyacrylamide hydrogels with and without eyebrow knife ablation. Line and bars represent mean ± 95% CI for n = 10 (2, 5, 3) colonies.
Scale bars = 250 μm. Pa = pascals. *p < 0.05.

central region of circular colonies to mechanical stress via prolonged stretching (Figure 4.11 A; Xue et al., 2018). Consistent with our prediction, mechanical stretching induced BMP-dependent mesoderm specification within the otherwise low-tension central colony region (Figure 4.11 B-C). The

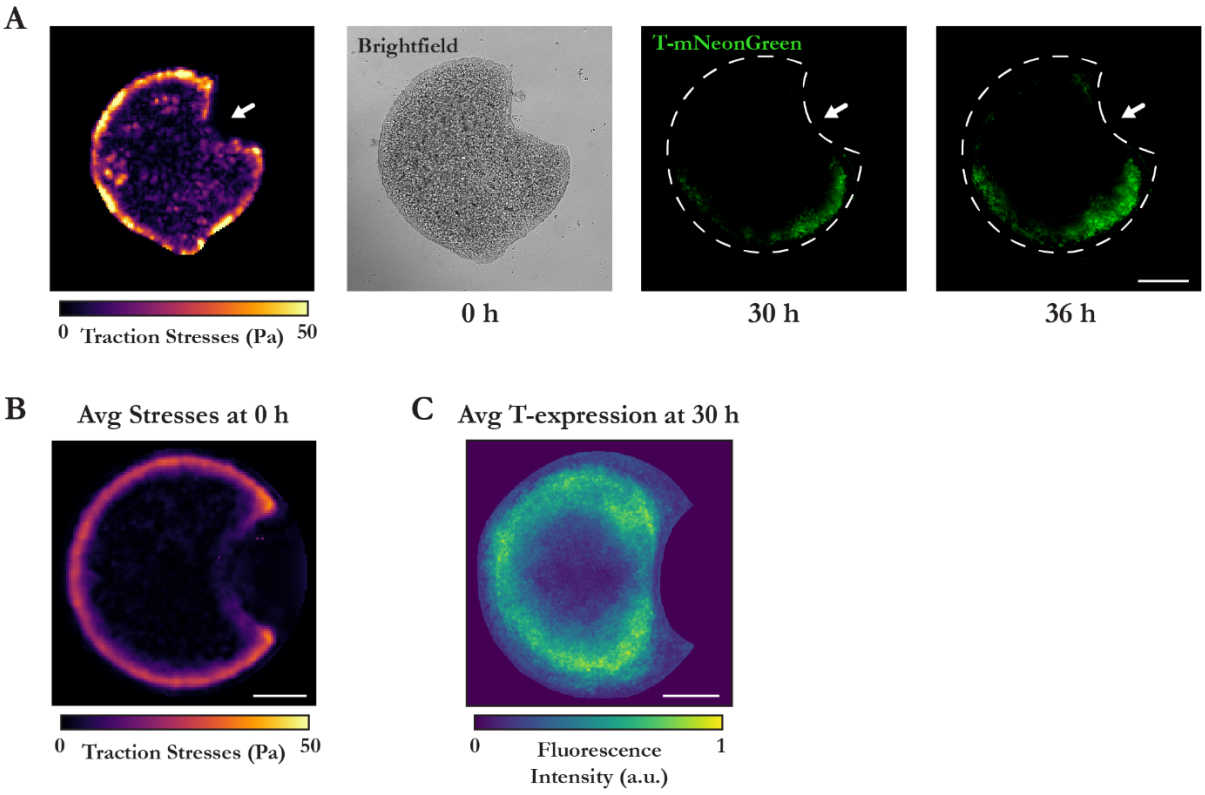

Figure 4.10: Geometric patterning of low cell-adhesion tension at the hESC colony edge spatially restricts mesoderm specification.
(A) Representative traction stress map prior to BMP4 stimulation and corresponding time-lapse images of T-mNeonGreen expression following BMP4 stimulation for (*caption continued on next page*)

(*caption continued from previous page*) geometrically confined Pac-Man hESC colonies on compliant (2,700 Pa) polyacrylamide hydrogels. Arrow indicates concave edge ("mouth") of Pac-Man.
(B) Map of average traction stresses measured for geometrically confined Pac-Man hESC colonies on compliant (2,700 Pa) polyacrylamide hydrogels prior to BMP4 stimulation. n = 20 (3, 10, 4, 3) colonies.
(C) Normalized average intensity map of T-mNeonGreen expression within geometrically confined Pac-Man hESC colonies on compliant (2,700 Pa) polyacrylamide hydrogels at 30 h BMP4 stimulation. n = 20 (3, 10, 4, 3) colonies.
All scale bars = 250 μm. Pa = pascals. Avg = average. a.u. = arbitrary units.

data indicate that tension, per se, can collaborate with BMP signaling to drive mesoderm specification in hESCs, even in colony regions exposed to high concentrations of endogenously secreted inhibitory signals (Etoc et al., 2016; Tewary et al., 2017).

High Tension Promotes β-catenin Release from Cell Junctions to Specify Mesoderm

Mesoderm specification in hESC colonies depends on Wnt/β-catenin signaling and is enhanced by growth on a compliant matrix (Laralynne Przybyla et al., 2016c). Accordingly, we examined whether localized cell-adhesion tension specifies mesoderm by promoting the release of β-catenin from E-cadherin adhesion complexes, specifically in regions of high tension. We observed the preferential loss of β-catenin from E-cadherin junctions within the localized regions of high cell-adhesion tension 24 hours following BMP4 stimulation (Figure 4.12 A-B). Activated phospho-Src-family kinases (pSFKs) phosphorylate junctional β-catenin to facilitate its release from adherens junction complexes (Bienz, 2005; Gayrard et al., 2018; Gottardi & Gumbiner, 2004; Howard et al., 2011; Lilien & Balsamo, 2005; Laralynne Przybyla et al., 2016c). We detected high levels of pSFKs within 6 hours of BMP4 stimulation, specifically within regions of high cell-adhesion tension (Figure 4.13 A-B). Blocking pSFK activity, using the Src inhibitor PP1, prevented β-catenin release at the E-cadherin junctions within the regions of high tension (Figure 4.14 A-B). Furthermore, preventing β-catenin release via Src inhibition resulted in a significant loss of mesoderm specification, as indicated by decreased T(brachyury), goosecoid, and Snai2 expression, and elevated Sox2 levels (Figure 4.14 C).

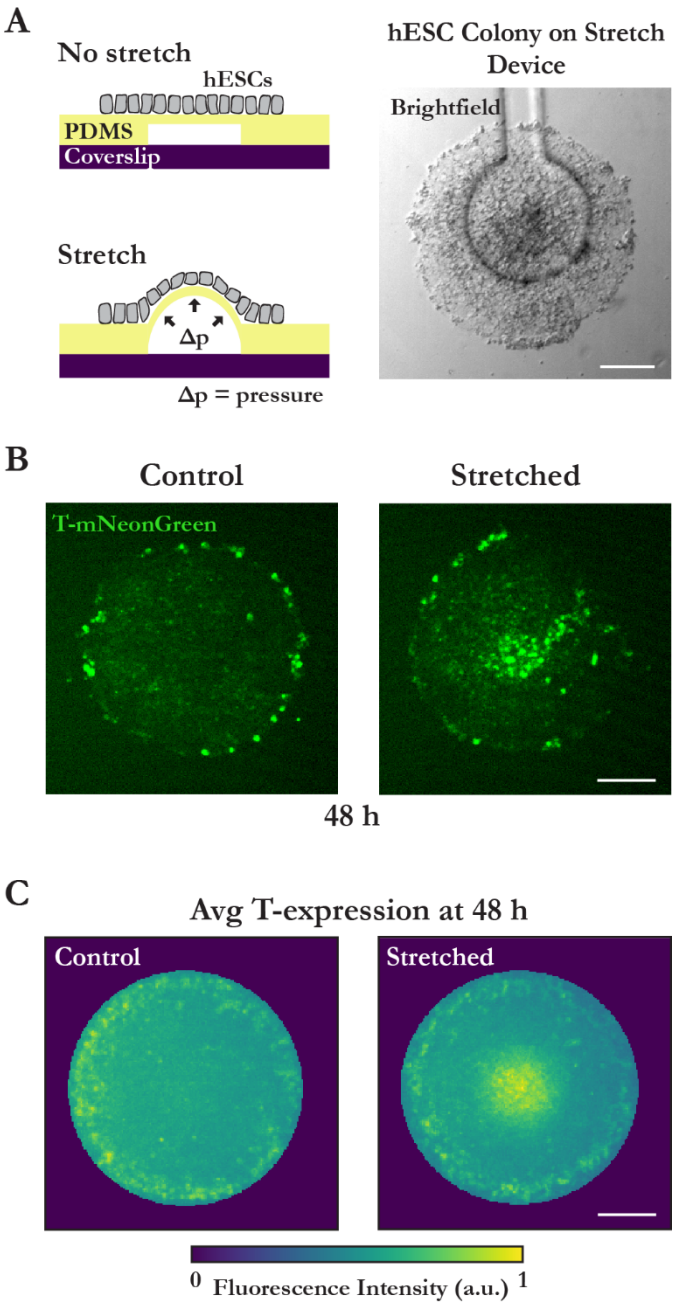

Figure 4.11: Mechanical stress applied via stretching is sufficient to induce BMP4-mediated mesoderm specification.
(A) Cartoon of mechanical stretching experiment and representative brightfield image of an hESC colony cultured on the stretching device.
(B) Representative images of T-mNeonGreen expression for hESC colonies with and without mechanical stretching during 48 h BMP4 stimulation.
(C) Normalized average intensity maps of T-mNeonGreen expression for hESC colonies with and without mechanical stretching during 48 h BMP4 stimulation. n = 27 (12, 8, 7) stretched colonies and n = 39 (21, 10, 8) control colonies.
All scale bars = 100 μm. Avg = average. a.u. = arbitrary units.

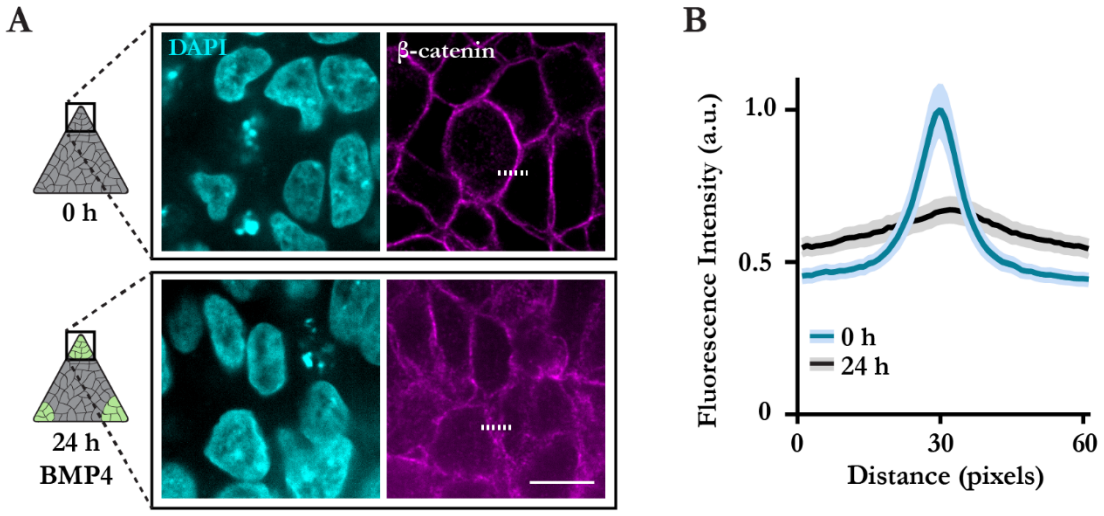

Figure 4.12: β-catenin is released from adherens junctions upon BMP4 stimulation.
(A) Representative images of β-catenin expression and nuclei (DAPI) in the corners of geometrically confined triangle hESC colonies on compliant (2,700 Pa) polyacrylamide hydrogels before and 24 h after BMP4 stimulation. Scale bar = 10 μm. Rectangles on colony cartoons indicate imaged regions.
(B) Plot of mean (solid line) ± 95% CI (shaded regions) fluorescence intensity of β-catenin at cell junctions in the corners of geometrically confined triangle hESC colonies on compliant (2,700 Pa) polyacrylamide hydrogels before and 24 h after BMP4 stimulation. Dashed lines in (A) indicate plotted fluorescence intensity profiles. N = 130 profiles per condition from n = 26 (9, 8, 9) imaged colony corner ROIs. a.u. = arbitrary units.

Molecular dynamic simulations showed tension across E-cadherin junctions exposes the tyrosine 654 (Y654) of cadherin-bound β-catenin (Röper et al., 2018). Therefore, we asked whether high cell-adhesion tension fosters a conformational change in β-catenin that permits its phosphorylation on Y654 to spatially pattern mesoderm specification at the nodes of high tension. We detected enhanced binding of an antibody specific to the β-catenin Y654 in the cells at the corners of the triangle hESC colonies, as well as at the convex edges of Pac-Man colonies, suggesting the higher cell-adhesion tension in these regions exposed the Y654 phosphorylation site (Figure 4.15 A-B). The data demonstrate that the structure of junctional β-catenin is physically modified by cell-adhesion tension, that the release of junctional β-catenin is regulated by pSFKs, and that the subsequent availability of β-catenin for nuclear translocation and transcriptional activity initiates

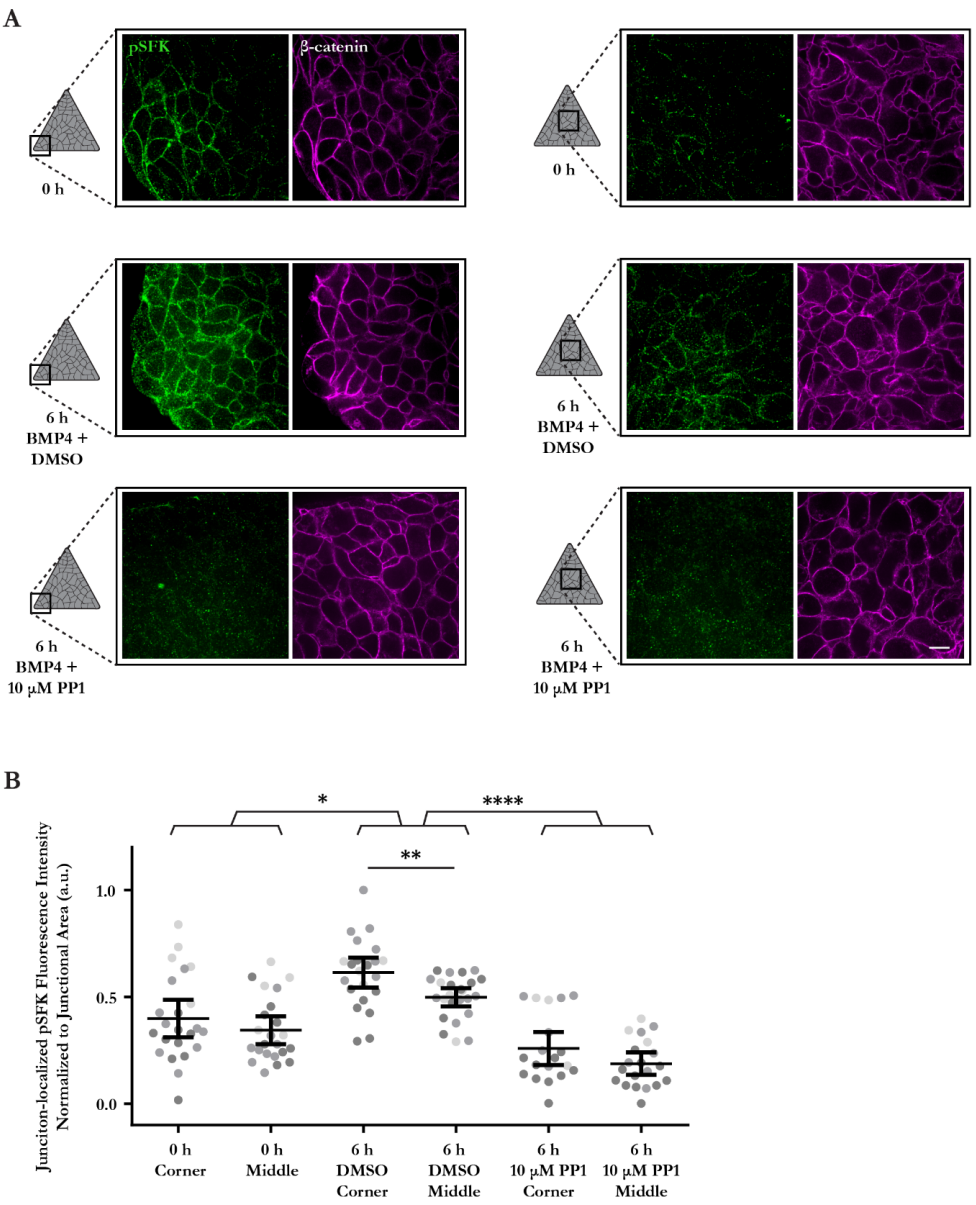

Figure 4.13: Phosphorylated Src-family kinases are upregulated and localized to adherens junctions upon BMP4 stimulation.

(A) Representative immunofluorescent images of phosphorylated Src-family kinases and β-catenin in the corner and middle of typical geometrically confined triangle hESC colonies on compliant (2,700 Pa) polyacrylamide hydrogels prior to and after 6 h stimulation with BMP4 plus either vehicle (DMSO) or Src inhibitor (PP1; 10 μM). Rectangles on colony cartoons indicate imaged regions. Scale bar = 10 μm.

(B) Quantification of junction-localized phosphorylated Src-family kinases fluorescence intensity, normalized to junctional area measured using β-catenin fluorescence in the corner and middle of geometrically confined triangle hESC colonies on compliant (2,700 Pa) polyacrylamide hydrogels prior to and after 6 h stimulation with BMP4 plus either vehicle (DMSO) or Src inhibitor (PP1; 10 μM). *$p < 0.05$, **$p < 0.01$, and ****$p < 0.0001$. pSFK = phosphorylated Src-family kinases. a.u. = arbitrary units.

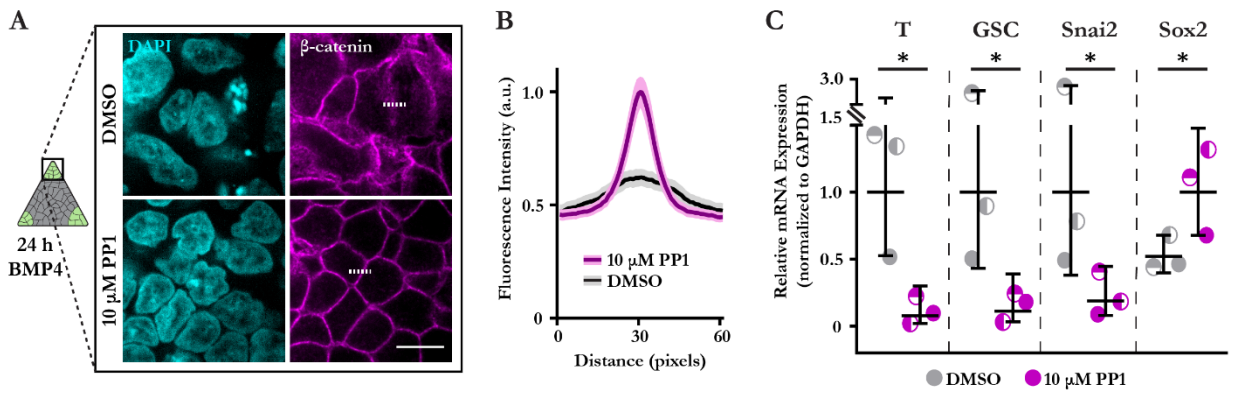

Figure 4.14: Src-mediated β-catenin release from adherens junctions is critical for mesoderm specification.
(A) Representative images of β-catenin expression in the corners of geometrically confined triangle hESC colonies on compliant (2,700 Pa) polyacrylamide hydrogels after 24 h stimulation with BMP4 plus either vehicle (DMSO) or Src inhibitor (PP1; 10 μM). Rectangle on colony cartoon indicates imaged region. Scale bar = 10 μm.
(B) Plot of mean (solid line) ± 95% CI (shaded regions) fluorescence intensity of β-catenin at cell junctions in the corners of geometrically confined triangle hESC colonies on compliant (2,700 Pa) polyacrylamide hydrogels after 24 h stimulation with BMP4 plus either vehicle (DMSO) or Src inhibitor (PP1; 10 μM). Dashed lines in (A) indicate plotted fluorescence intensity profiles. N = 130 profiles per condition from n = 26 (9, 8, 9) imaged colony corner ROIs.
(C) Relative mesoderm gene expression levels after 36 h stimulation with BMP4 plus either vehicle (DMSO) or Src inhibitor (PP1; 10 μM). Line and bars represent mean ± 95% CI. *$p < 0.05$.
GSC = goosecoid. a.u. = arbitrary units.

mesoderm specification in regions of high tension (Figure 4.16).

Wnt Signaling Reinforces Mesoderm Specification in Regions of High Tension

To determine whether canonical Wnt/β-catenin signaling is involved in promoting mesoderm specification following its initiation in regions of high cell-adhesion tension, we used FACS to isolate T-positive cells from geometrically-confined hESC colonies following BMP4 stimulation (36 h; subsequent to junctional β-catenin release), and evaluated Wnt ligand expression (Figure 4.17 A). Gene expression analysis revealed that the canonical Wnt ligands Wnt3a and Wnt8a, which are critical for mesoderm specification (Chhabra et al., 2019; Kemp et al., 2005; Lindsley et al., 2006; Martyn et al., 2019; Laralynne Przybyla et al., 2016c), were expressed at higher levels in the T-positive cells isolated

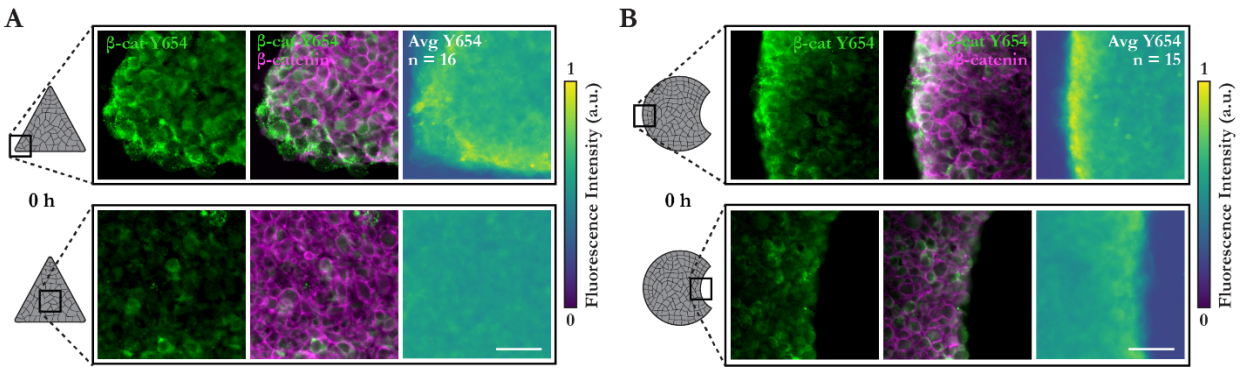

Figure 4.15: High cell-adhesion tension at adherens junctions exposes β-catenin Y654 for Src-mediated phosphorylation.
(A) Representative images of β-catenin Y654 (green; left), composite β-catenin Y654 and normal β-catenin (merge; middle), and normalized average intensity map of β-catenin Y654 expression (right) within geometrically confined triangle hESC colonies on compliant (2,700 Pa) polyacrylamide hydrogels prior to BMP4 stimulation. n = 16 (3, 7, 6) colonies.
(B) Representative images of β-catenin Y654 (green; left), composite β-catenin Y654 and normal β-catenin (merge; middle), and normalized average intensity map of β-catenin Y654 expression (right) within geometrically confined Pac-Man hESC colonies on compliant (2,700 Pa) polyacrylamide hydrogels prior to BMP4 stimulation. n = 15 (5, 5, 5) colonies.
Scale bars = 50 μm. Rectangles on colony cartoons indicate imaged regions. β-cat Y654 = tyrosine 654 of β-catenin. a.u. = arbitrary units. Avg = average.

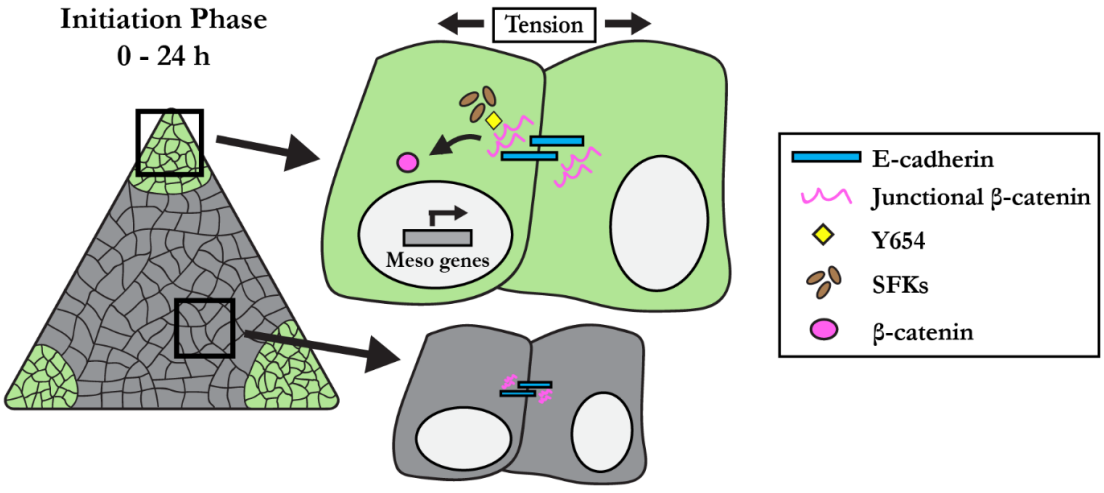

Figure 4.16: Mechanism of the initiation phase of mesoderm specification in regions of high cell-adhesion tension.
Cartoon summarizing the mechanism by which regionally-localized high cell-adhesion tension exposes β-catenin Y654 to facilitate its phosphorylation and subsequent release, mediated by pSFKs, upon BMP4 stimulation.
Y654 = tyrosine 654 of β-catenin. SFKs = Src-family kinases.

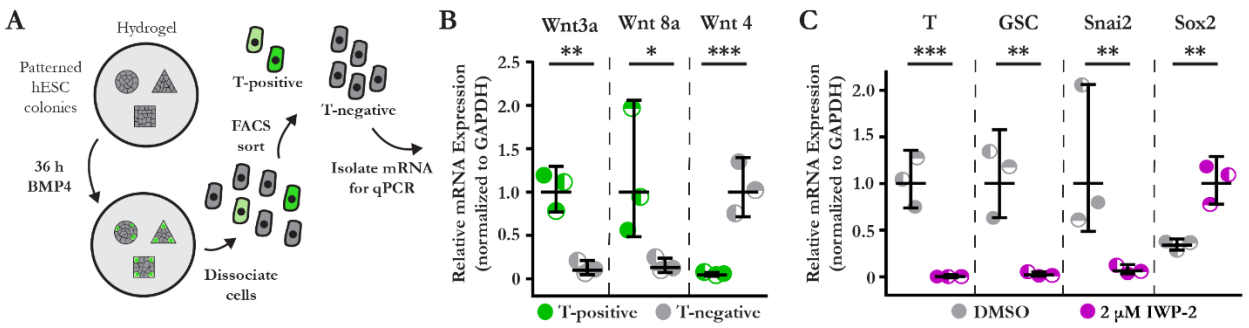

Figure 4.17: Canonical Wnt signaling is required to facilitate the observed levels of mesoderm specification in regions of high cell-adhesion tension.
(A) Cartoon of isolation protocol to compare Wnt ligand expression between T-positive and T-negative cells in geometrically confined hESC colonies on compliant (2,700 Pa) polyacrylamide hydrogels.
(B) Relative Wnt ligand expression levels in T-positive and T-negative hESCs isolated from geometrically confined colonies on compliant (2,700 Pa) polyacrylamide hydrogels after 36 h BMP4 stimulation.
(C) Relative mesoderm gene expression levels in geometrically confined hESC colonies on compliant (2,700 Pa) polyacrylamide hydrogels after 36 h stimulation with BMP4 plus either vehicle (DMSO) or Wnt inhibitor (IWP-2; 2 μM).
Line and bars represent mean ± 95% CI. *$p < 0.05$, **$p < 0.01$, and ***$p < 0.001$.

from the regions of high cell-adhesion tension (Figure 4.17 B). By contrast, levels of the non-canonical ligand Wnt4 were higher in the isolated T-negative cells (Figure 4.17 B). Moreover, blocking Wnt ligand processing and secretion with the inhibitor IWP-2 (2 μM) resulted in a significant loss of mesoderm specification, as indicated by decreased T(brachyury), goosecoid, and Snai2 expression, and elevated Sox2 levels (Figure 4.17 C).

In situ hybridization via hybridization chain reaction (ISH-HCR; Choi et al., 2018) verified that Wnt3a transcription was upregulated in response to BMP4 within the same high-tension colony regions (Figure 4.18 A-D). Moreover, because blocking SFK activity with PP1 prevented upregulation of the mesoderm-inducing Wnts, Src-mediated release and transcriptional activity of β-catenin appears to be necessary for tension-regulated Wnt ligand expression (Figure 4.19 A-C). Collectively, the findings elucidate a two-part mechanism whereby high cell-adhesion tension initiates a spatially-

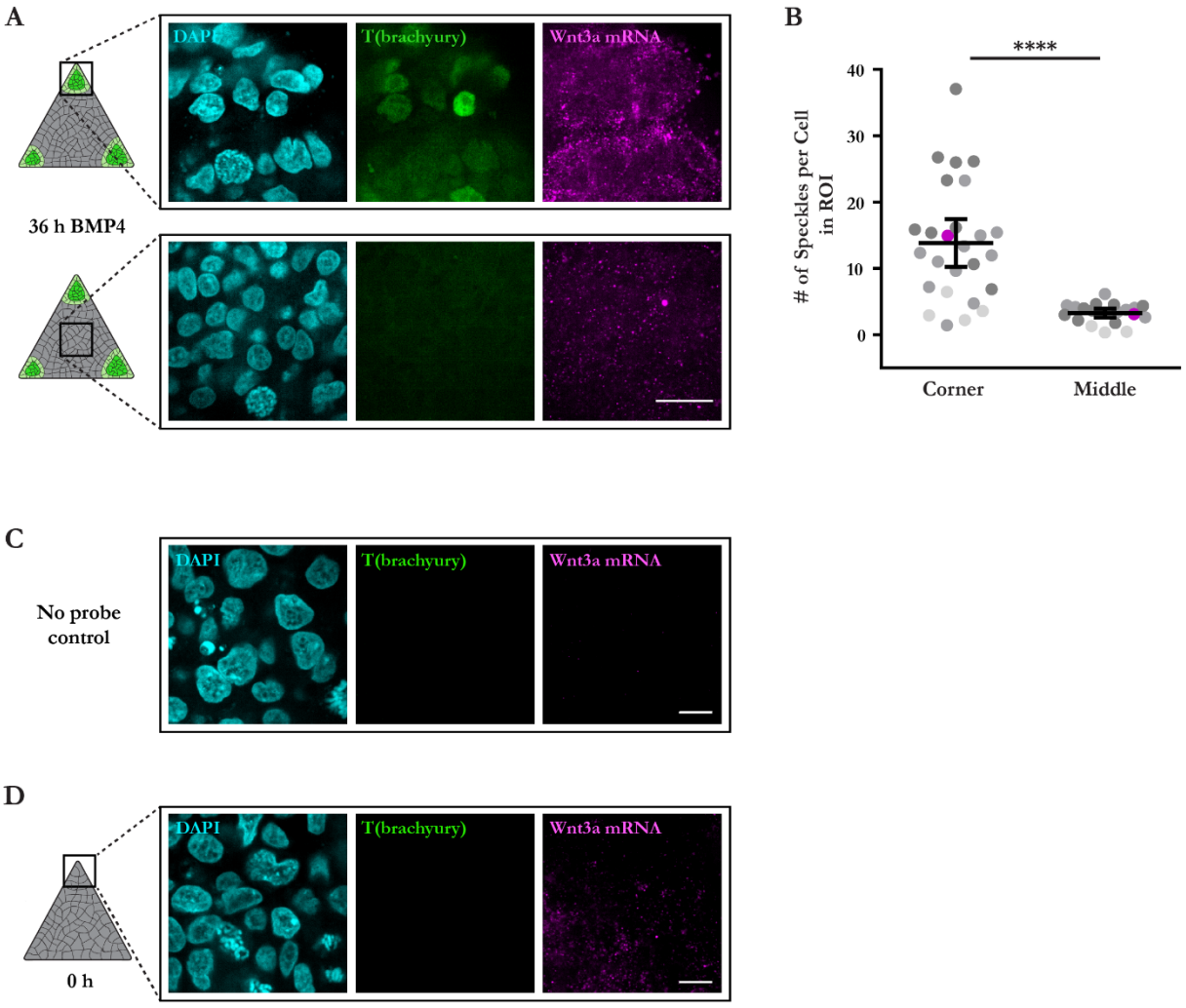

Figure 4.18: ISH-HCR enables visualization of Wnt3a expression in geometrically confined hESC colonies on compliant hydrogels.

(A) Representative images of T(brachyury) protein expression, *in-situ*-detected Wnt3a mRNA, and nuclei (DAPI) in the corner and middle of geometrically confined triangle hESC colonies on compliant (2,700 Pa) polyacrylamide hydrogels after 36 h BMP4 stimulation.

(B) Plot of *in-situ*-detected Wnt3a speckles in the corner and middle of geometrically confined triangle hESC colonies on compliant (2,700 Pa) polyacrylamide hydrogels after 36 h BMP4 stimulation. Magenta data points correspond to images shown in (A). Data from independent experiments represented by different shades of gray. Line and bars represent mean ± 95% CI for n = 26 (4, 12, 10) imaged corner ROIs and n = 20 (3, 8, 9) imaged middle ROIs. ****$p < 0.0001$.

(C) Representative images of T(brachyury) protein expression, *in-situ*-detected Wnt3a mRNA, and nuclei (DAPI) in geometrically confined triangle hESC colonies on compliant (2,700 Pa) polyacrylamide hydrogels with no split initiator probes targeting Wnt3a prior to amplification with fluorescent probes.

(D) Same as in (C), but including split initiator probes in geometrically confined triangle hESC colonies on compliant (2,700 Pa) polyacrylamide hydrogels prior to BMP4 stimulation.

Rectangles on colony cartons indicate imaged regions. For (A): scale bar = 20 μm. For (C-D): scale bars = 10 μm.

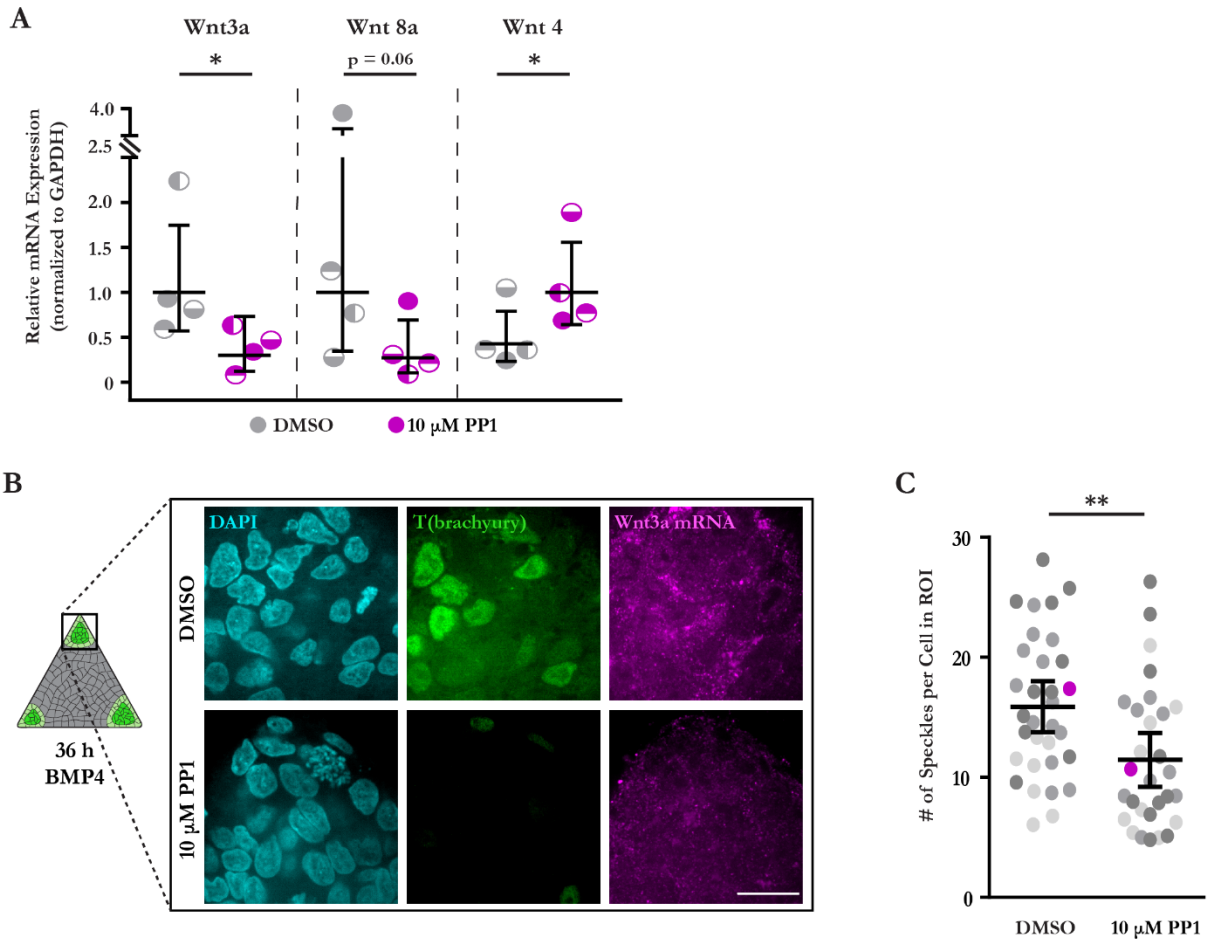

Figure 4.19: Canonical Wnt signaling in regions of high cell-adhesion tension is downstream of Src-mediated β-catenin release from adherens junctions.

(A) Relative Wnt ligand expression levels in geometrically confined hESC colonies on compliant (2,700 Pa) polyacrylamide hydrogels after 36 h stimulation with BMP4 plus either vehicle (DMSO) or Src inhibitor (PP1; 10 μM).

(B) Representative images of T(brachyury) protein expression, *in-situ*-detected Wnt3a mRNA, and nuclei (DAPI) in the corners of geometrically confined triangle hESC colonies on compliant (2,700 Pa) polyacrylamide hydrogels after 36 h stimulation with BMP4 plus either vehicle (DMSO; top) or Src inhibitor (PP1; 10 μM; bottom). Rectangle on colony carton indicates imaged region. Scale bar = 20 μm.

(C) Plot of *in-situ*-detected Wnt3a speckles in the corners of geometrically confined triangle hESC colonies on compliant (2,700 Pa) polyacrylamide hydrogels after 36 h stimulation with BMP4 plus either vehicle (DMSO) or Src inhibitor (PP1; 10 μM). Magenta data points correspond to images shown in (B). Data from independent experiments represented by different shades of gray. n = 26 (4, 12, 10) imaged ROIs from DMSO condition and n = 20 (3, 8, 9) imaged ROIs from PP1 condition. Line and bars represent mean ± 95% CI. *$p < 0.05$ and **$p < 0.01$

restricted, Src-mediated release of β-catenin from adherens junctions, which then feeds forward to drive canonical Wnt signaling that promotes further mesoderm specification to reinforce the gastrulation phenotype (Figure 4.20).

DISCUSSION

It has long been recognized that mechanical forces are necessary to direct tissue organization and drive cell rearrangements within developing embryos (Hamada, 2015; Ko & Martin, 2020; Paré & Zallen, 2020; Voiculescu et al., 2014; Williams & Solnica-Krezel, 2017), and we provide compelling evidence that these same forces may regulate cell fate specification by spatially promoting Wnt/β-catenin signaling via junctional release of β-catenin that feeds forward to drive Wnt ligand expression. Notably, Wnt/β-catenin signaling is conserved among model organisms and plays multiple roles throughout the course of embryogenesis and in adult stem cells (Clevers, 2006; Eliazer et al., 2019; Petersen & Reddien, 2009; van Amerongen & Nusse, 2009), implying that the tension-regulated activation of the

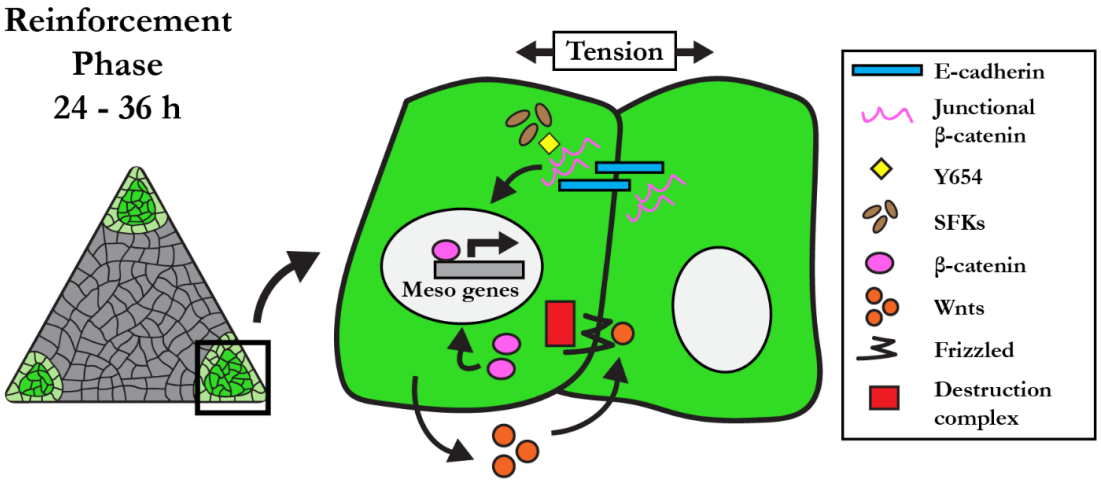

Figure 4.20: Mechanism of the reinforcement phase of mesoderm specification facilitated by canonical Wnt signaling in regions of high cell-adhesion tension.
Cartoon summarizing the mechanism by which regions of high cell-adhesion tension direct mesoderm specification. The Src-mediated release of junctional β -catenin feeds forward and upregulates Wnt ligand expression to promote mesoderm specification.
Y654 = tyrosine 654 of β-catenin. SFKs = Src-family kinases.

pathway that we illustrate here is likely also conserved and re-used throughout development. In fact, Farge and colleagues demonstrated that the same Src-mediated phosphorylation at Y654 and subsequent release of junctional β-catenin occurs during mesoderm invagination in both zebrafish and *Drosophila* embryos (Brunet et al., 2013; Röper et al., 2018). A recent study of the tissue-level forces underlying gastrulation in avian embryos revealed that higher contractile forces are generated at the posterior of the embryo, in the margin between the epiblast and extraembryonic tissue (Saadaoui et al., 2020). We propose that the contractile forces identified by Saadaoui et al., in combination with presumed forces transduced across cell junctions as epiblast cells are pulled towards the midline, act to mechanically stretch and expose β-catenin Y654 to initiate the signaling cascade that leads to synchronized ingression and mesoderm specification at the primitive streak. Our findings illustrate a critical interplay between the mechanics that drive tissue development and the molecular signaling that regulates cell fate specification.

Prior studies illustrated that variations in BMP receptor accessibility and secreted morphogen concentrations lead to patterning of mesoderm specification within a concentric ring inwards from the hESC colony edge (Chhabra et al., 2019; Etoc et al., 2016; Manfrin et al., 2019; Martyn et al., 2019; Tewary et al., 2017, 2019; Warmflash et al., 2014). Our studies expand upon these findings to suggest that colonies of hESCs cultured on compliant substrates are particularly useful for studying the physical and molecular regulators of early embryogenesis, because they self-organize discrete gastrulation nodes that expand radially, distinctly resembling the formation and elongation of the primitive streak in the developing embryo (Mikawa et al., 2004; Voiculescu et al., 2014). Previous work in 2D *in vitro* systems suggested that mesoderm specification occurs at regions of low local cell density (Blin et al., 2018); however, studies in the chicken embryo suggest that primitive streak formation occurs in regions of higher cell density (H. C. Lee et al., 2020; Spratt & Haas, 1960). Our analysis of cell density reveals that there is no clear correlation between local density and the observed patterns

of mesoderm specification. Additional studies are needed to understand precisely how cell density might regulate cell fate specification, perhaps by altering signaling, as suggested for contact-mediated patterning in 3D embryoid bodies (Sagy et al., 2019).

To address the role of endogenously secreted factors in our system, we positioned triangle colonies with one corner inside the mouth of Pac-Man colonies, and showed that mesoderm specification arises in the triangle corner positioned in the mouth at the same levels observed in the distal corners. This finding, together with our observation that T(brachyury) expression arises uniformly around the periphery of colonies on rigid substrates, suggests that the observed initiation of mesoderm specification in the corners of triangle colonies on compliant substrates is indeed a result of the measured pattern of cell-adhesion tension, and not merely due to these cells being located farther away from presumed high concentrations of endogenously secreted inhibitors at the interior of colonies. While this should not be taken as evidence to diminish the role of endogenously secreted factors, it constrains the models of inhibitor diffusion that are likely to pattern fate specification. A gradient arising from apical secretion should not have been significantly affected by the gap between triangle and Pac-Man colonies; thus, the result argues that inhibitor diffusion via the basal intercellular space, which is spatially constrained by the apical junctional complex (AJC), is much more likely to be involved in fate patterning. Future studies should be aimed at understanding how mechanical cues and signaling gradients are integrated to determine cell fate.

Remarkably, ESCs aggregated in 3D undergo key aspects of early embryogenesis, including germ layer specification, axial organization, elongation, expression of Hox genes, and somitogenesis (Beccari et al., 2018; Harrison et al., 2017; Sozen et al., 2018; van den Brink et al., 2020; Van Den Brink et al., 2014). In our pseudo-2D system, we are limited to observing the initial events of gastrulation, namely, coordinated morphogenesis akin to "Polonaise" movements and ingression of mesoderm progenitors. Studies that implement tools such as molecular force sensors are needed to investigate

the role of cell-adhesion tension in the later events of axial mesoderm/definitive endoderm segregation and somitiogenesis, which apparently occur exclusively in 3D models. Nevertheless, the observed similarities between the dynamics of gastrulation node formation in pseudo-2D hESC colonies on compliant substrates and embryonic primitive streak morphogenesis are striking. Thus, this system could prove to be a powerful model with which to dissect the interplay between tissue-level forces, cell-adhesion tension, and the signaling and transcriptional programs that regulate early human embryogenesis.

CHAPTER 5

Cell Adhesions and Contractility Influence Tissue Patterning of Pluripotent Stem Cells

This chapter is adapted from work published in the peer-reviewed article titled "Spatiotemporal mosaic self-patterning of pluripotent stem cells using CRISPR interference" by Ashley R.G. Libby, David A. Joy, Po-Lin So, Mohammad A. Mandegar, **Jonathon M. Muncie**, Frederico N. Mendoza-Camacho, Valerie M. Weaver, Bruce R. Conklin, and Todd C. McDevitt in Elife (2018).

INTRODUCTION

Morphogenesis involves interactions of asymmetric cell populations that form complex multicellular patterns and structures comprised of distinct cell types. Morphogenic asymmetries arise from reorganization of cells due, in part, to local changes in mechanical tissue stiffness and cell adhesions that facilitate the physical organization of developing embryos (Krieg et al., 2008; Maître et al., 2012). Mechanical rearrangement is necessary for many aspects of morphogenesis, including cell polarity, collective movement, multicellular organization, and organ size regulation (Arboleda-Estudillo et al., 2010; Maître, 2017). Differential adhesion (Foty & Steinberg, 2004, 2005) and cortical tension (Krieg et al., 2008; Van Essen, 1997) are critical determinants of mechanically driven cell sorting, in which both processes are known to contribute to tissue organization (Lecuit & Lenne, 2007). In cortical-tension-dominated sorting, variable actin cytoskeleton cortex tension stimulates sorting of individual cells, whereas differential adhesion sorting promotes segregation of cell populations due to intercellular homophilic adhesions.

Rho-associated coiled-coil containing protein kinase (ROCK1) and E-cadherin (CDH1) are interesting orthogonal gene targets to interrogate human pluripotent stem cell (hPSC) population organization by altering the intrinsic mechanics of distinct cell populations. ROCK1 regulates actin-myosin dynamics (Figure 5.1 A), which contribute to a cell's cortical tension (Salbreux et al., 2012). In addition, ROCK inhibition is often used in hPSC culture to promote survival during passaging and has been implicated in pluripotency maintenance (McBeath et al., 2004; Ohgushi et al., 2015). Similarly, CDH1, a classic type I cadherin adhesion molecule (Figure 5.1 A), is widely associated with pluripotency and early morphogenesis (Heasman et al., 1994; Laralynne Przybyla et al., 2016c; Ringwald et al., 1987), and its down-regulation coincides with the induction of patterning events via differential adhesion.

In this study, we explored whether genetic manipulation of these proteins that regulate the mechanics of hPSCs results in controllable cell-driven self-organization into consistent multicellular (i.e. tissue) patterns. We employed an inducible CRISPR interference (CRISPRi) system in human induced pluripotent stem cells (hiPSCs) to silence key proteins that regulate cell adhesion (CDH1) and cortical tension (ROCK1). We genetically controlled symmetry-breaking events within hiPSC colonies by creating mixed populations of hiPSCs with and without the CRISPRi system. Mosaic knockdown was then induced within the mixed hiPSC populations to interrogate how the creation of physical asymmetries in an otherwise homogeneous population leads to multicellular organization and tissue pattern formation. We show that mosaic knockdown of ROCK1 or CDH1 results in "bottom-up" tissue patterning within hiPSC colonies due to cellular self-organization, while retaining an epithelial pluripotent phenotype.

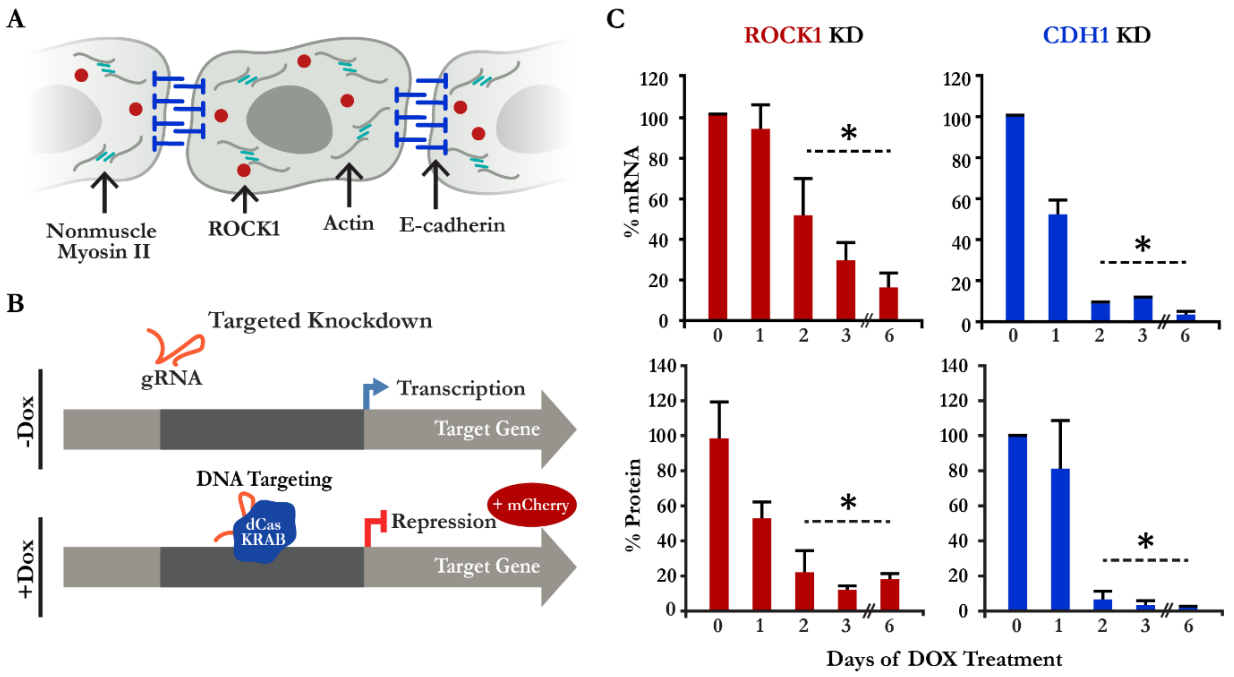

Figure 5.1: CRISPRi of ROCK1 and CDH1.
(A) Schematic of ROCK1 and E-cadherin within a cell. E-cadherin is a trans-membrane adhesion molecule that locates to the borders of cells and ROCK1 is a cytoplasmic kinase that acts upon non-muscle myosin II.
(B) Schematic of the CRISPRi system. Doxycycline addition to the hiPSC culture media leads to the expression of mCherry and dCas9-KRAB to induce knockdown of target gene.
(C) Relative mRNA (qPCR; top) and protein (Western Blot; bottom) levels of ROCK1 (red; left) and CDH1 (blue; right) over a time-course of knockdown. Nearly complete knockdown of both mRNA and protein was achieved by day three of DOX treatment when compared to untreated hiPSCs. Bars represent mean ± SD from three independent experiments. *$p < 0.05$.
DOX = doxycycline. KD = knockdown.

RESULTS

CRISPRi KD in Human iPSCs Modulates Epithelial Morphology

To establish inducible CRISPRi knockdown systems for ROCK1 and CDH1, we used a doxycycline (DOX)-inducible CRISPRi hiPSC line (Figure 5.1 B; CRISPRi-Gen1C; Mandegar et al., 2016). Guide RNA (gRNA) sequences designed to target the transcription start site of ROCK1 or CDH1 were introduced into CRISPR-Gen1C hiPSCs and knockdown was induced by the addition of DOX (2 μM) into cell culture media. After 3 days of DOX induction, ROCK1 mRNA levels were reduced to

<30% of levels in hiPSCs without DOX treatment, and CDH1 mRNA levels were reduced to <10% of levels in hiPSCs without DOX treatment (Figure 5.1 C). Protein knockdown followed a similar trend, wherein DOX induced populations compared to untreated controls resulted in <20% ROCK1 protein and <10% of CDH1 protein by day three of DOX treatment. Moreover, reduced protein levels were maintained through day six of DOX induction (Figure 5.1 C).

Both the ROCK1 knockdown (KD) cells and the CDH1 KD cells retained epithelial hiPSC morphologies and did not exhibit single cell migration away from the colonies (Figure 5.2 A). However, CDH1 KD hiPSCs displayed irregular colony shapes that maintained smooth peripheral edges, but contained regions lacking cells within colonies (Figure 5.2 A). Conversely, ROCK1 KD hiPSCs displayed round colony shapes (similar to wildtype hiPSCs) but individual cells along the border of ROCK1 KD colonies extended protrusions radially out and away from the colony edge (Figure 5.2 A).

To further confirm the physical effects of knocking down CDH1 or ROCK1 selectively in hiPSCs, we performed immunofluorescent (IF) staining of CDH1 expression. After 5 days of DOX treatment, CDH1 KD hiPSCs exhibited a complete loss of CDH1 expression, as expected, whereas the ROCK1 KD hiPSCs and the control hiPSCs (with off-target CRISPRi guide) maintained robust expression of CDH1 along cell junctions (Figure 5.2 B). Direct measurements of hiPSC elasticity were taken using atomic force microscopy after 6 days of DOX-induced knockdown and revealed that ROCK1 KD cells displayed a two-fold higher cortical stiffness than the control and CDH1 KD populations, whereas the elasticity of the latter groups did not differ significantly from one another (Figure 5.2 C). Therefore, CRISPRi silencing of targeted genes associated with cellular mechanical properties resulted in distinct physical differences between the otherwise similar cell populations.

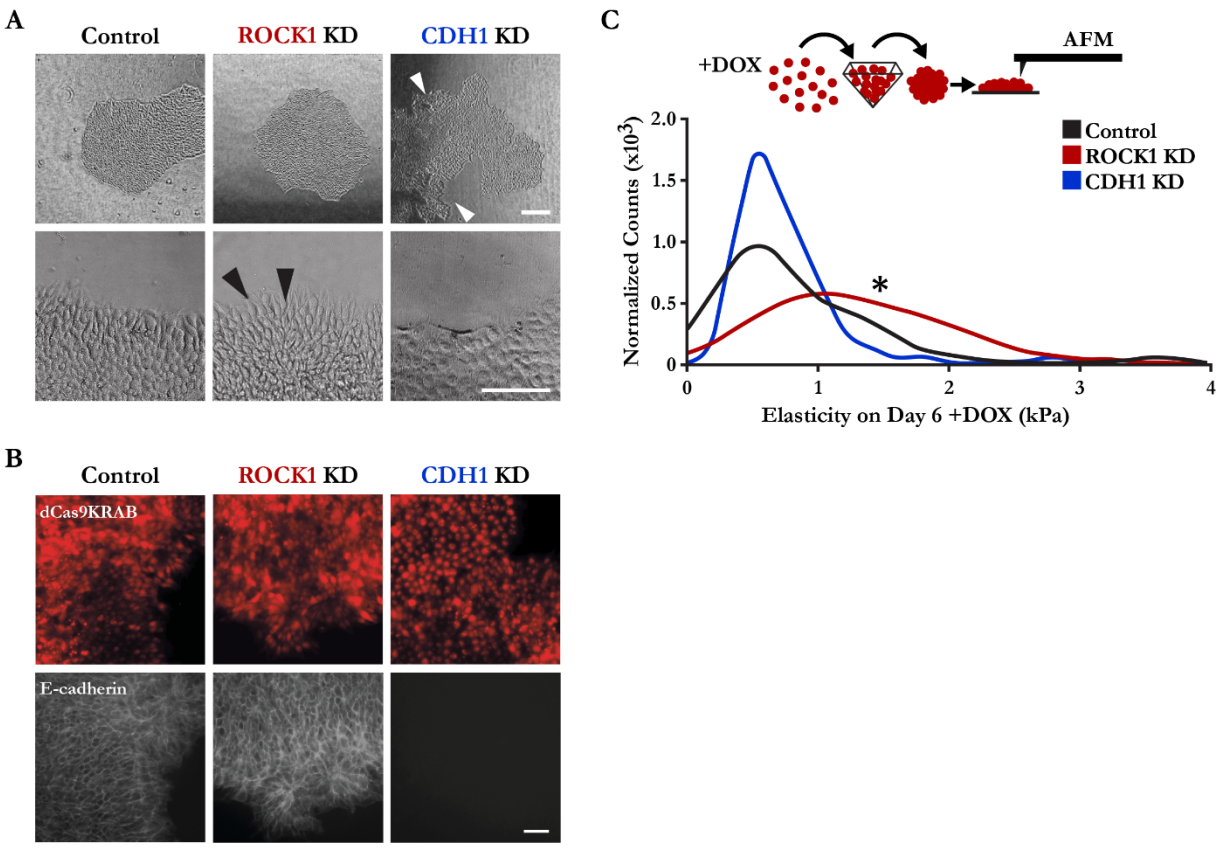

Figure 5.2: ROCK1 and CDH1 knockdown alter morphology and physical properties of hiPSCs.
(A) Representative brightfield images of hiPSC colonies with CRISPRi control (left), ROCK1 knockdown (middle; black arrows indicate cell extensions), and CDH1 knockdown (right; white arrows indicate altered colony shape). Scale bars = 200 μm.
(B) Representative immunofluorescent images of dCas9-KRAB-expressing CRISPRi hiPSCs (red; top) and immunostained E-cadherin (gray; bottom) in hiPSC colonies with off-target control guide RNA (left), ROCK1 knockdown (middle), and CDH1 knockdown (right). Scale bar = 100 μm.
(C) Atomic force microscopy measurements of the elasticity (Young's elastic modulus) of control, ROCK1 knockdown, and CDH1 knockdown CRISPRi hiPSCs. Control n = 36, ROCK1 knockdown n = 65, CDH1 knockdown = 72. Each n represents a single elasticity measurement made on a colony of hiPSCs, with measurements pooled from three independent experiments. Area under curves = 1. *$p < 0.05$.
KD = knockdown. AFM = atomic force microscopy. kPa = kilopascals. DOX = doxycycline.

Mosaic CRISPRi Silencing Results in Multicellular Organization

To examine whether mosaic knockdown of a single molecule impacted hiPSC organization, ROCK1- or CDH1-CRISPRi populations were pre-treated with DOX for 5 days and then mixed with isogenic wildtype hiPSCs that constitutively expressed GFP (WT-GFP) at a 1:3 ratio. Forced aggregation of

ROCK1 KD: WT-GFP hiPSCs or CDH1 KD: WT-GFP hiPSCs and subsequent re-plating were used to create individual colonies of randomly mixed ROCK1 KD hiPSCs or CDH1 KD hiPSCs with the WT-GFP cells (Figure 5.3 A). After 5 days in mixed culture, ROCK1 KD cells sorted radially from the WT-GFP cells, clustering primarily at the edges of the colonies (Figure 5.3 B). However, separation of the ROCK1 KD cells did not result in distinct smooth borders between the WT-GFP and ROCK1 KD hiPSC subpopulations. In contrast, CDH1 KD cells robustly separated from the GFP-WT subpopulation, forming clusters throughout the colonies with sharp boundaries between subpopulations, irrespective of their spatial location within the colony (Figure 5.3 B).

Based on the sorting behaviors of ROCK1 KD: WT-GFP and CDH1 KD: WT-GFP colonies when the knockdown of ROCK1 and CDH1 was induced prior to mixing, we next examined whether induction of mosaic knockdown after mixing resulted in similar sorting patterns. This scenario more accurately models the onset of initial symmetry-breaking events among seemingly homogeneous pluripotent cells during early embryonic development. Non-induced CRISPRi populations were mixed with WT-GFP hiPSCs (1:3 ratio), re-plated, and then treated with DOX to induce knockdown (Figure 5.4 A). ROCK1 KD post-mixing within mosaic colonies did not result in noticeable radial segregation of ROCK1 KD hiPSCs from WT-GFP hiPSCs (Figure 5.4 B), as observed for pre-mixed colonies. Instead, the post-mixing ROCK1 KD mosaic colonies exhibited increased vertical stacking of ROCK1 KD cells and WT-GFP cells in the z-plane of the mixed colonies (Figure 5.4 B); whereas the pre-induced mixed colonies had remained segregated primarily in a 2D planar manner (Figure 5.3 B). In contrast, the mosaic knockdown of CDH1 post-mixing maintained robust segregation of the CDH1 KD cells from the WT-GFP hiPSCs (Figure 5.4 B), although the borders between cell subpopulations lacking CDH1 and neighboring WT-GFP cells were somewhat less distinct than the pre-induced CDH1 KD: WT-GFP mixed colonies (Figure 5.3 B). Overall, the inducible CRISPRi mixed colonies

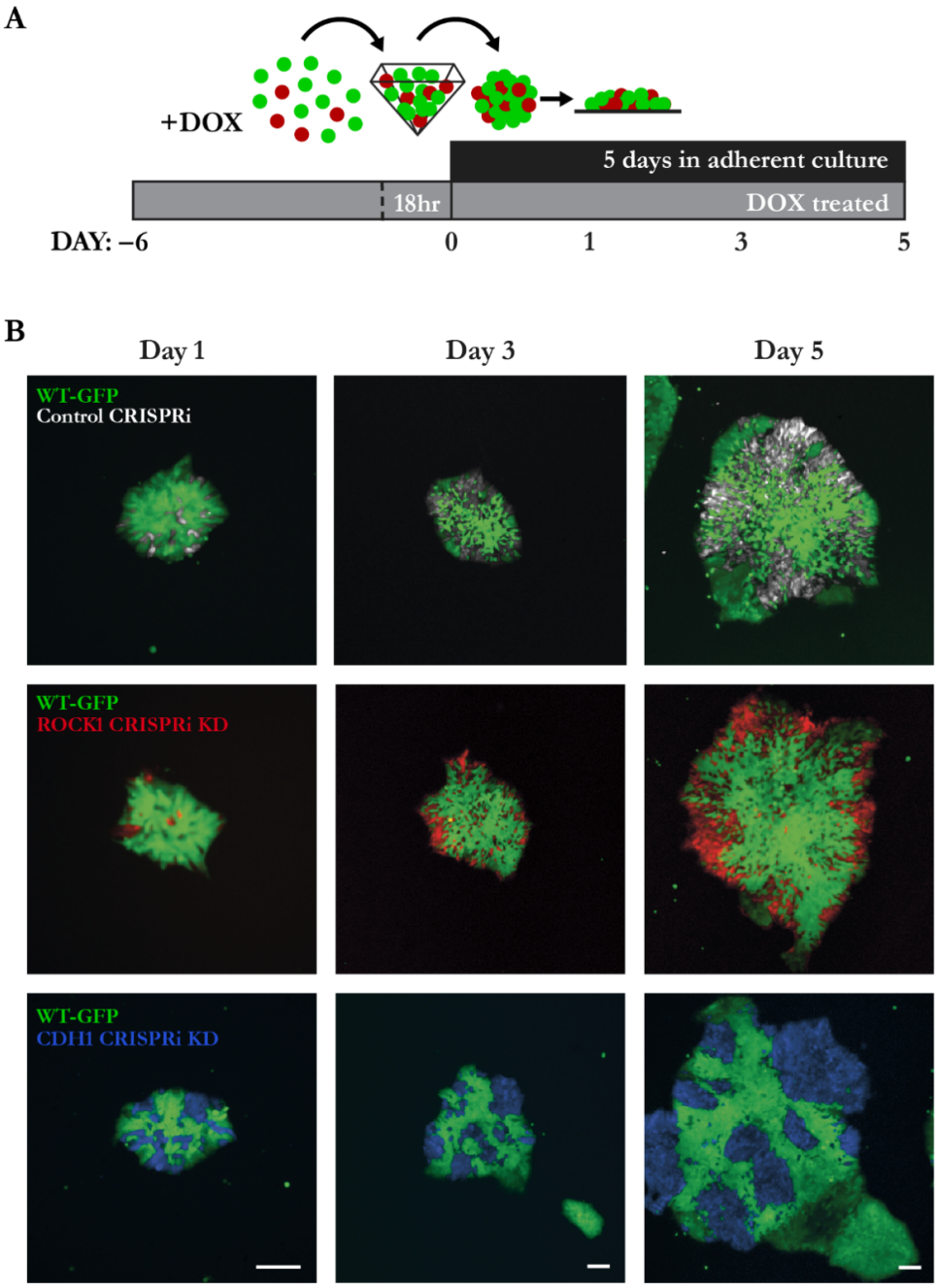

Figure 5.3: Mixed colonies of CRISPRi and WT hiPSCs exhibit distinct tissue patterns.
(A) Schematic of the experimental procedure for examining pattern formation in colonies of mixed CRISPRi and wildtype hiPSCs with CRISPRi knockdown induced prior to mixing.
(B) Representative immunofluorescent images of dCas9-KRAB and mCherry expressing CRISPRi hiPSCs (top row: CRISPRi control = white; middle row: ROCK1 knockdown = red; bottom row: CDH1 knockdown = blue) and GFP in wildtype hiPSCs (green; all images) with CRISPRi knockdown induced prior to mixing. Scale bars = 100 μm.
DOX = doxycycline. WT = wildtype. KD = knockdown.

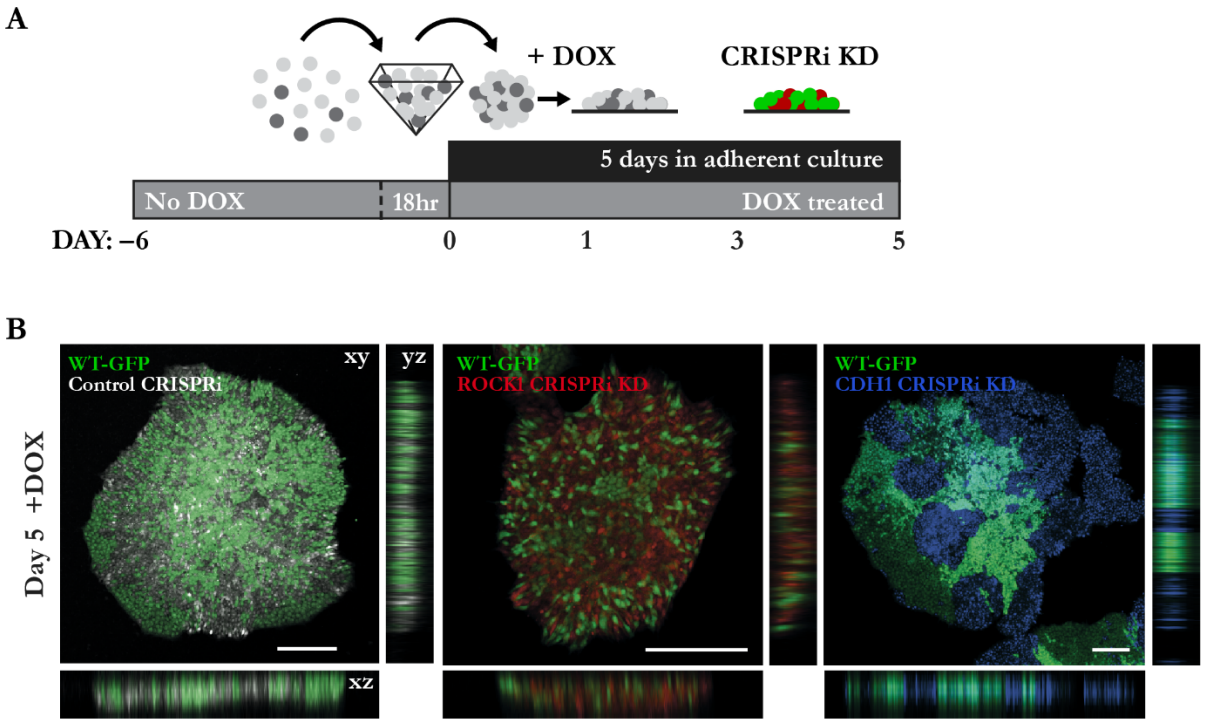

Figure 5.4: Tissue patterns emerge in mixed colonies of hiPSCs with CRISPRi induced post-mixing.
(A) Schematic of the experimental procedure for examining pattern formation in colonies of mixed CRISPRi and wildtype hiPSCs with CRISPRi knockdown induced after mixing.
(B) Representative immunofluorescent images of dCas9-KRAB and mCherry expressing CRISPRi hiPSCs (left: CRISPRi control = white; middle: ROCK1 knockdown = red; right: CDH1 knockdown = blue) and GFP in wildtype hiPSCs (green; all images) with CRISPRi knockdown induced after mixing. Projections of the xz plane are shown below each image and projections of the yz plane are shown to the right of each image. Scale bars = 200 μm.
DOX = doxycycline. WT = wildtype. KD = knockdown.

displayed the ability to generate a variety of different patterns of intrinsic symmetry-breaking events that resulted in distinct cell sorting and multicellular pattern formation.

Mosaic hiPSC Colonies Retain a Pluripotent Phenotype

Colony morphology and expression of epithelial markers, such as epithelial cell adhesion molecule (EpCAM), were examined to determine if the cells that lost CDH1 expression segregated from their WT-GFP neighbors due to delamination, or due to loss of the epithelial phenotype characteristic of hiPSCs. ROCK1 KD: WT-GFP and CDH1 KD: WT-GFP colonies maintained an epithelial

morphology throughout 6 days of CRISPRi silencing (Figure 5.5) with no observed migration by CRISPRi-KD cells away from the colonies. Both ROCK1 KD and CDH1 KD hiPSCs within mixed colonies expressed EpCAM at cell-cell junctions after 6 days of CRISPRi induction, despite changes in cortical tension or intercellular adhesion due to the loss of ROCK1 or CDH1, respectively (Figure 5.5). Since downregulation of CDH1 is commonly associated with loss of pluripotency in PSCs, we next examined the expression and localization of the common pluripotency transcription factor, Oct-3/4. Despite the physical segregation of cells induced by knockdown in mixed populations, no heterogeneity was observed in pluripotency marker expression (Figure 5.5). In other words, both WT

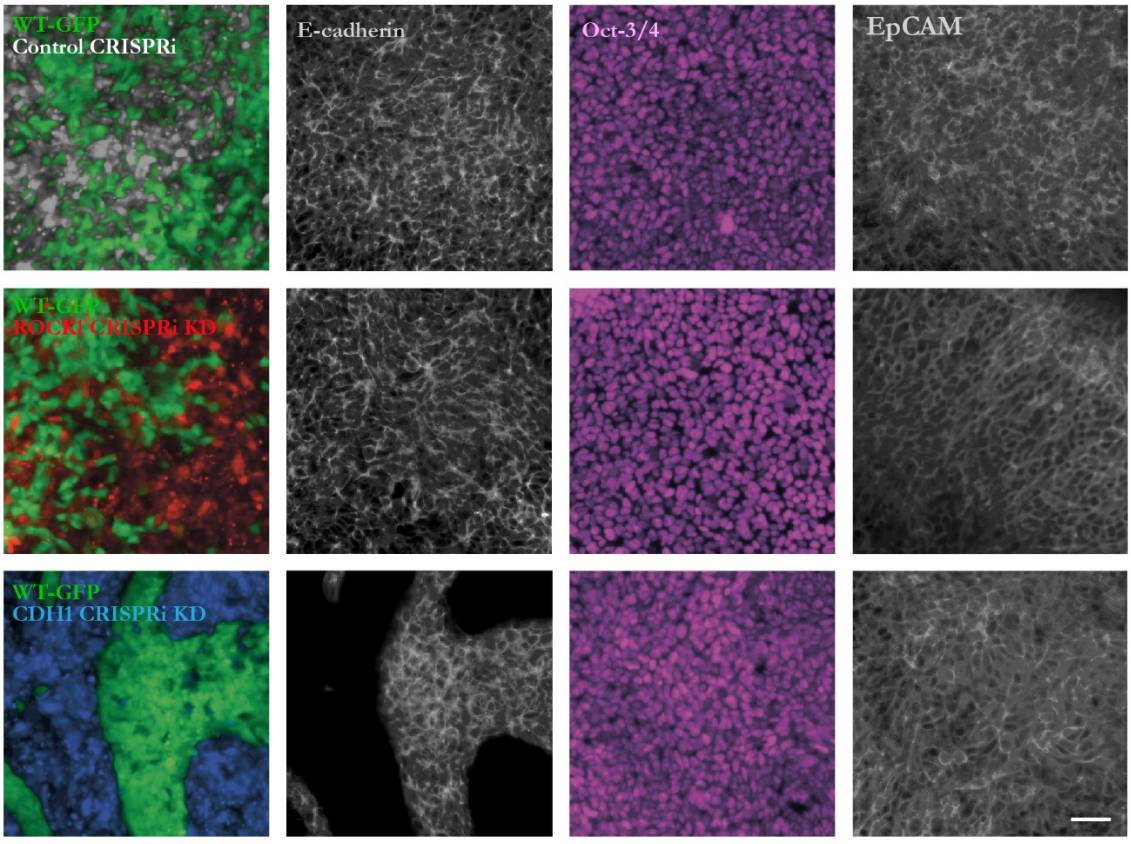

Figure 5.5: Mixed colonies of CRISPRi and WT hiPSCs remain pluripotent.
Representative immunofluorescent images of mixed wildtype (green; far left) and dCas9-KRAB plus mCherry expressing CRISPRi hiPSCs (white, red, and blue; far left), immunostained E-cadherin (gray; middle-left), immunostained Oct-3/4 (magenta; middle-right), and immunostained EpCAM (gray; far right) in hiPSC colonies with off-target control guide RNA (top), ROCK1 knockdown (middle), and CDH1 knockdown (bottom). Scale bar = 100 μm. WT = wildtype. KD = knockdown.

and KD cells within mixed colonies maintained equivalent levels of Oct-3/4 expression. These results indicate that the loss of ROCK1 or CDH1 is not sufficient to induce an immediate exit from the pluripotent state.

DISCUSSION

In this study we examined the effect of inducing specific genetic knockdown of proteins that regulate cellular mechanics in subpopulations of hiPSC colonies that can otherwise be characterized as a homogeneous population of pluripotent cells. Previous works published in this field used small-molecule chemical inhibitors, antibodies, and homogeneous genetic knockouts to interrogate the molecular mechanisms involved in morphogenesis (Lecuit & Lenne, 2007; McBeath et al., 2004; Salbreux et al., 2012). However, these methods are incapable of selectively discriminating between different cells, or they fail to address how the co-emergence of heterotypic interactions affects multicellular tissue organization. Here, we report that silencing of target genes by CRISPRi within selective subpopulations of hiPSC colonies provides multiple avenues to genetically control the emergence of asymmetric cell phenotypes and the development of multicellular tissue patterns. Specifically, we demonstrated that mosaic knockdown of target genes ROCK1 or CDH1 result in distinct tissue patterns whereby cell-driven segregation dictates colony organization without loss of pluripotency (Figure 5.6).

ROCK1 regulates actin-myosin contractility (McBeath et al., 2004), facilitates expansion of PSCs (Ohgushi et al., 2015; Park et al., 2015), and its acute inhibition by small molecules leads to a mechanically "relaxed" cell phenotype with decreased stiffness (Kinney et al., 2014; J. S. H. Lee et al., 2006). However, we found that prolonged silencing of ROCK1 in hiPSCs (6 days) resulted in cells that were two-fold stiffer, as measured by AFM, than either the CDH1 KD cells or the control

CRISPRi cells (Figure 5.2 C). These contradictory results (decreased cortical stiffness with homogeneous ROCK inhibition vs. increased cortical stiffness with ROCK1 KD in mixed colonies) may be explained by some mechanistic difference between the inhibition of previously transcribed

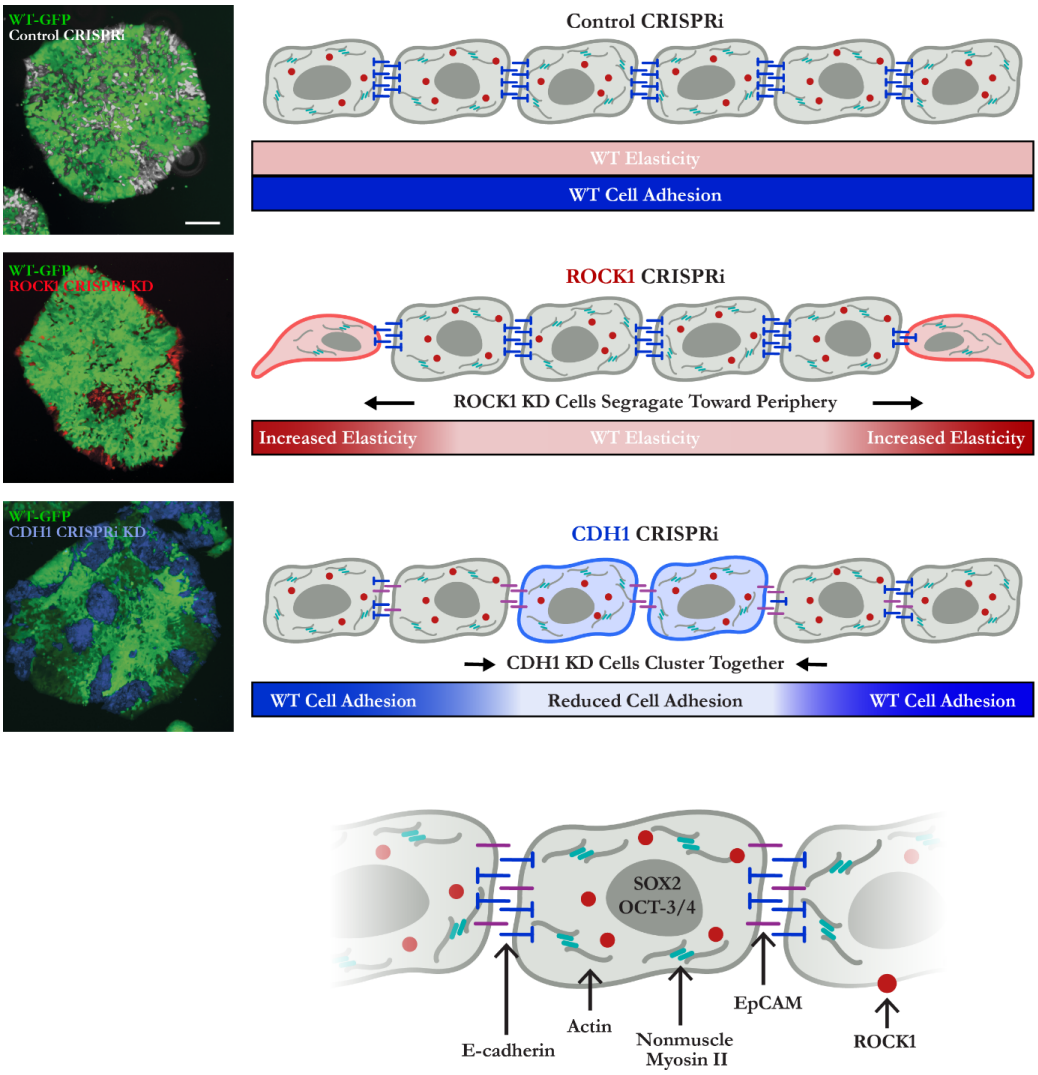

Figure 5.6: Working model for the emergence of tissue patterns driven by CRISPRi knockdown of molecules that regulate the physical properties of hiPSCs.
Schematic of the working model for how controlled changes in cellular stiffness or cellular adhesion result in specific hiPSC colony pattern formation. Mixed colonies with mosaic ROCK1 knockdown display continuous radial separation of knockdown cells from wildtype, presumably due to increased contractility and stiffness of ROCK1 knockdown cells. Mixed colonies with mosaic CDH1 knockdown exhibit discrete islands or clusters of knockdown cells surrounded by wildtype cells, driven by the reduced cell-cell adhesions of CDH1 knockdown cells. Scale bar = 200 μm. WT = wildtype. KD = knockdown.

proteins and knockdown of protein expression at the level of transcription. Small molecule inhibitors prevent the function of previously transcribed proteins, such that some fraction of functioning protein may escape the inhibitor's effect. In contrast, CRISPRi must only target the ROCK1 gene loci at two alleles to completely abolish genetic transcription and subsequent protein translation, thus highlighting the functional significance of such a genetic perturbation. Another possible explanation for these differences is that the heterotypic cell-cell interactions between distinct subpopulations in our mixed hiPSC colonies may induce a unique stiffening phenotype in ROCK1 KD cells through an undefined mechanism that is independent of the pathway through which small molecule ROCK inhibitors homogeneously reduce cortical tension. Moreover, small molecule inhibitors may have undefined off-target effects that alter cell phenotype.

Additionally, ROCK inhibition is often performed transiently (24 hr), whereas long-term CRISPRi knocdown of ROCK1 (6 days) may induce compensatory effects that are responsible for the phenotype that contrasts with small molecule inhibition. Long-term ROCK1 KD compensation is a likely partial explanation for why ROCK1 KD prior to mixing resulted in radially partitioned populations, whereas post-mixing knockdown resulted in less clearly segregated populations. The increased vertical stacking of the ROCK1 KD population with post-mixing knockdown induction could also reflect a difference between short-term and long-term ROCK1 KD and potential compensation effects. For example, the generation of multilayer colonies, specifically the 3D accumulation of ROCK1 KD cells that experience impaired cytoskeletal contraction, may occur passively and result from cell-cell tension transmitted between the surrounding WT cells.

The emergence of autonomous cell sorting and tissue patterning is often coincident with the onset of differentiation or fate commitment. Up- and down-regulation of CDH1 in particular regulates morphogenesis in a diverse range of species (Burdsal et al., 1993; D. Li et al., 2010). Historically, CDH1 expression is often associated with pluripotency in mouse embryonic stem cells (L. Li et al.,

2012; Soncin & Ward, 2011). However, although CDH1 is commonly expressed by pluripotent cells, and although CDH1 can replace Oct-3/4 during fibroblast reprogramming to pluripotency (Redmer et al., 2011), nevertheless, CDH1 is not essential for pluripotency (Larue et al., 1996; Soncin et al., 2009; Ying et al., 2008). Our results reinforce this by demonstrating that CDH1 KD in hiPSCs does not adversely affect the expression of pluripotency markers, nor does it necessarily lead to a loss of epithelial phenotype. The maintenance of pluripotency upon CRISPRi KD of CDH1 illustrates that downregulation of CDH1 alone is not sufficient to induce differentiation, and that other factors, such as sufficient cell density and local intercellular signaling, preserve pluripotent colony integrity and buffer against changes in cell phenotype.

The observed mosaic patterns of ROCK1 KD hiPSCs demonstrate that the spatial location of subpopulations within a colony can be driven by targeted gene knockdown without altering differentiation potential. Conversely, the mosaic CDH1 KD demonstrates dual control of spatial positioning and lineage potential, given that CDH1 expression is intimately tied to cell differentiation. Therefore, the system described here enables interrogation of multicellular organization and morphogenic processes in parallel, via manipulation of local multicellular domains through subpopulation organization and priming to specific lineage fates.

The ability to manipulate distinct cell populations within hiPSC colonies allows for robust modeling of human morphogenic events and, thus, an expanded understanding of human development that can be exploited to develop physiologically realistic *in vitro* human embryo models. We propose that effects due to cellular location within pluripotent colonies may, in fact, parallel effects due to cell location within early developing blastocysts. For example, a cell's location within the early embryo relays signals that dictate initial symmetry-breaking events, such as the decision to become trophectoderm versus inner cell mass. Cells located within the center of an embryo maintain different adhesion contacts (Stephenson et al., 2010) and are subjected to higher tension generated by

neighboring cells (Samarage et al., 2015), which then feed back into lineage fate decisions. Specifically, Hippo pathway signaling is regulated by a cell's position within the early blastocyst, wherein the outer cell layer has the ability to polarize and sequester the signaling molecule angiomotin away from adherens junctions, preventing the phosphorylation and activation that occurs in the more internal blastocyst cells that maintain cell-cell contacts on all sides (Hirate et al., 2013). Likewise, *in vitro* micropatterned PSC colonies have been reported to display spatially dependent germ layer specification upon induction of differentiation (Etoc et al., 2016; Tewary et al., 2017; Warmflash et al., 2014). Our studies have built on these observations to show that spatially localized cell fate specification is regulated by cell-cell tension via a mechanism that acts not through the Hippo pathway, but through induced Wnt/β-catenin signaling (Chapters 2-4; Muncie et al., 2019, 2020). Together, these results demonstrate that multiple signaling pathways critical for proper embryonic development can be modulated by cell position, cytoskeletal contractility, and cell-cell tension to regulate cell differentiation and tissue patterning.

Ultimately, this study identifies a novel strategy to direct the emergence of heterotypic cell populations to control multicellular organization in pluripotent stem cells, and subsequently facilitates the creation of robust models of morphogenesis necessary for the mechanistic study of human developmental tissue patterning.

CHAPTER 6

The Niche Regulates Muscle Stem Cells via Rho Activity and Cytoskeletal Contractility

This chapter is adapted from work published in the peer-reviewed article titled "Wnt4 from the niche controls the mechno-properties and quiescent state of muscle stem cells" by Susan Eliazer, **Jonathon M. Muncie**, Josef Christensen, Xuefeng Sun, Rebecca S. D'Urso, Valerie M. Weaver, and Andrew S. Brack in Cell Stem Cell (2019).

INTRODUCTION

Muscle stem cells or satellite cells (SCs) are essential for the regenerative capacity of skeletal muscle. SCs reside in a quiescent and immotile state wedged between the basal lamina and the sarcolemma of the muscle fiber (the niche; Bischoff, 1990). In response to injury, SCs exit this dormant state and transition toward activation, which includes metabolic activation, cell-cycle entry, and migration. Once dividing, the majority of SCs differentiate, while a subset self-renew to restore the quiescent SC pool.

The quiescent state is critical to maintain stem cell capacity across different niches (Cheung & Rando, 2013; Orford & Scadden, 2008). In contexts that yield increased SC turnover, such as in muscular dystrophy, aging, or in transgenic mice harboring cell-cycle mutations, SC function is impaired (Brack & Muñoz-Cánoves, 2016; Brack & Rando, 2007; Chakkalakal et al., 2014). For many years, SC quiescence has been considered to be a reversible but homogeneous state, denoted by the absence of proliferation and regulated by cell intrinsic factors (Bjornson et al., 2012; Boonsanay et al., 2016; Cheung et al., 2012; Philippos et al., 2012). An intermediate quiescent state referred to as G_{Alert}

was recently characterized (Rodgers et al., 2014). This transition state is metabolically active, is dependent on mTORC1, and can be induced by systemic hepatocyte growth factor activator (Rodgers et al., 2014, 2017). SCs in the G_{Alert} state enter the cell cycle more rapidly, mount a more efficient regeneration process, and retain stem cell capacity. The mechanisms that promote or repress the transition from quiescence to activation are not well understood.

The niche is a conserved regulator of stem cell quiescence and maintenance. A fundamental but unanswered question in stem cell biology is the identity of specific cell types and paracrine-acting factors that control quiescence and the transition toward activation. The Wnt signaling pathway has been demonstrated to act as a conserved regulator of stem cell function via canonical (β-catenin) and non-canonical (planar cell polarity [PCP] and calcium) signaling (Clevers et al., 2014). Wnt signaling plays a critical role in coordinating SC state transitions from asymmetric division, proliferation, commitment, and differentiation (Brack et al., 2008, 2009; A. E. Jones et al., 2015; Lacour et al., 2017; Le Grand et al., 2009; Parisi et al., 2015; Rudolf et al., 2016). However, there is a dearth of information addressing the requirement of specific Wnt ligands, in part due to the possible redundancy between the 19 family members. Recent studies have disrupted Wnt activity using Porcupine (*Porcn*) or *Wntless* loss of function alleles in different tissues to disrupt the processing of the Wnt ligand family (Nabhan et al., 2018; Tammela et al., 2017; Zepp et al., 2017). While these studies provide proof of principle for the importance of Wnt ligands, they did not elucidate the identity of the most relevant Wnt family members. Moreover, whether Wnt ligands, from an anatomically defined niche cell, control SC quiescence remains unknown. Identifying the specific niche and the signaling molecules that regulate quiescence is critical to understanding regenerative biology and the development of therapeutics to harness muscle stem cell function.

Using an inducible genetic approach to specifically target the muscle SC niche, we provide the first evidence of a specific paracrine-acting niche factor, Wnt4, that reinforces SC quiescence through

activation of Rho-GTPase and repression of YAP. In summary, Wnt4 levels in the niche regulate SC contractility and dictate the depth of SC quiescence during homeostasis, their activation response, and regenerative potential.

RESULTS

Wnt4 From the Adult Muscle Fiber Niche Maintains Stem Cell Quiescence

To identify Wnts that regulate SC quiescence in the adult muscle, we first analyzed Wnt ligand expression by microarray analysis and qPCR, on freshly isolated single muscle fibers. Although a number of different Wnts were expressed, Wnt4 was significantly enriched in uninjured muscle fibers (data not shown). We next assessed Wnt4 transcript levels in whole muscle during the early stages of muscle repair (Polesskaya et al., 2003). We found that Wnt4 transcript levels are between 45%–50% lower at 18 and 24 h after $BaCl_2$ injury, compared to muscles of non-injured mice (Figure 6.1 A). To test the requirement of niche-derived Wnt4 for SC quiescence *in vivo*, we conditionally deleted Wnt4 in adult muscle fibers (Kobayashi et al., 2011), using tamoxifen (TMX)-inducible Cre-recombinase under the control of Human Skeletal Actin (Tg: $HSA^{CreMER/+}$; $Wnt4^{fl/fl}$, herein referred to as Myofiber [MF]-$Wnt4^{fl/fl}$; McCarthy et al., 2012). Adult mice (3-4 months old) were given TMX for 5 days, followed by a 6- or 14-day chase (Figure 6.1 B). Bromodeoxyuridine (BrdU) was given in the drinking water during the chase to label cycling SCs. We observed an increase in the number of SCs (Figure 6.1 C-D), the fraction that incorporated BrdU (Figure 6.1 E), and the fraction that expressed MyoD in a Wnt4-depleted niche, compared to controls (Figure 6.1 F-G). Together, these results demonstrate that Wnt4 activity from muscle fibers is required for SC quiescence through paracrine action.

Wnt4 From the Niche Regulates Muscle Regeneration

In response to an injury stimulus, SCs enter the cell cycle. We asked whether depletion of Wnt4 from the niche influenced SC activation and cell cycle entry following injury (Figure 6.2 A). Upon mitogen

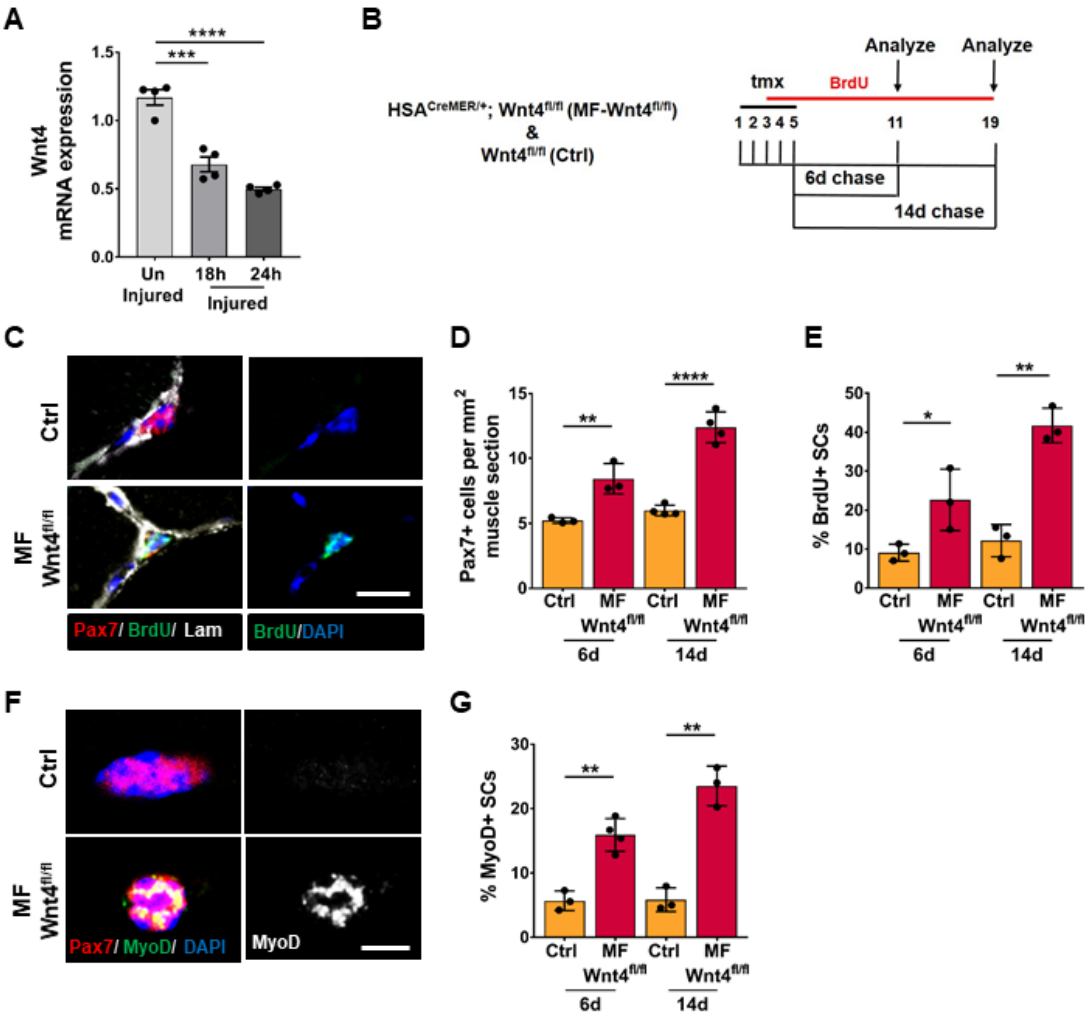

Figure 6.1: Wnt4 from the adult muscle fiber niche maintains stem cell quiescence.
(A) Relative Wnt4 mRNA levels (normalized to GAPDH) in wildtype uninjured mice as well as 18 and 24 h following injury.
(B) Schematic representation of experimental design for conditional Wnt4 deletion.
(C) Representative immunofluorescent images of Pax7 (red), BrdU (green), laminin (white), and nuclei (DAPI; blue) in tibialis anterior (TA) muscle sections isolated from mice with control (top) and Wnt4-depeted (bottom) niches. Scale bar = 10 μm.
(D) Quantification of Pax7+ cells in TA muscle sections from mice with control and Wnt4-depeted niches 6 days and 14 days following Wnt4-depletion.
(E) Quantification of BrdU+ SCs in TA muscle sections from mice with control and Wnt4-depeted niches 6 days and 14 days following Wnt4-depletion.
(F) Representative immunofluorescent images of Pax7 (red), MyoD (green, left; white, right), and nuclei (DAPI; blue) in tibialis anterior (TA) muscle sections isolated from mice with control (top) and Wnt4-depeted (bottom) niches. Scale bar = 5 μm.
(G) Quantification of MyoD+ SCs in TA muscle sections from mice with control and Wnt4-depeted niches 6 days and 14 days following Wnt4-depletion.
Bars and lines represent mean ± SEM from three independent experiments. *$p < 0.05$, **$p < 0.01$, ***$p < 0.001$, and ****$p < 0.0001$. tmx = tamoxifen. Lam = laminin.

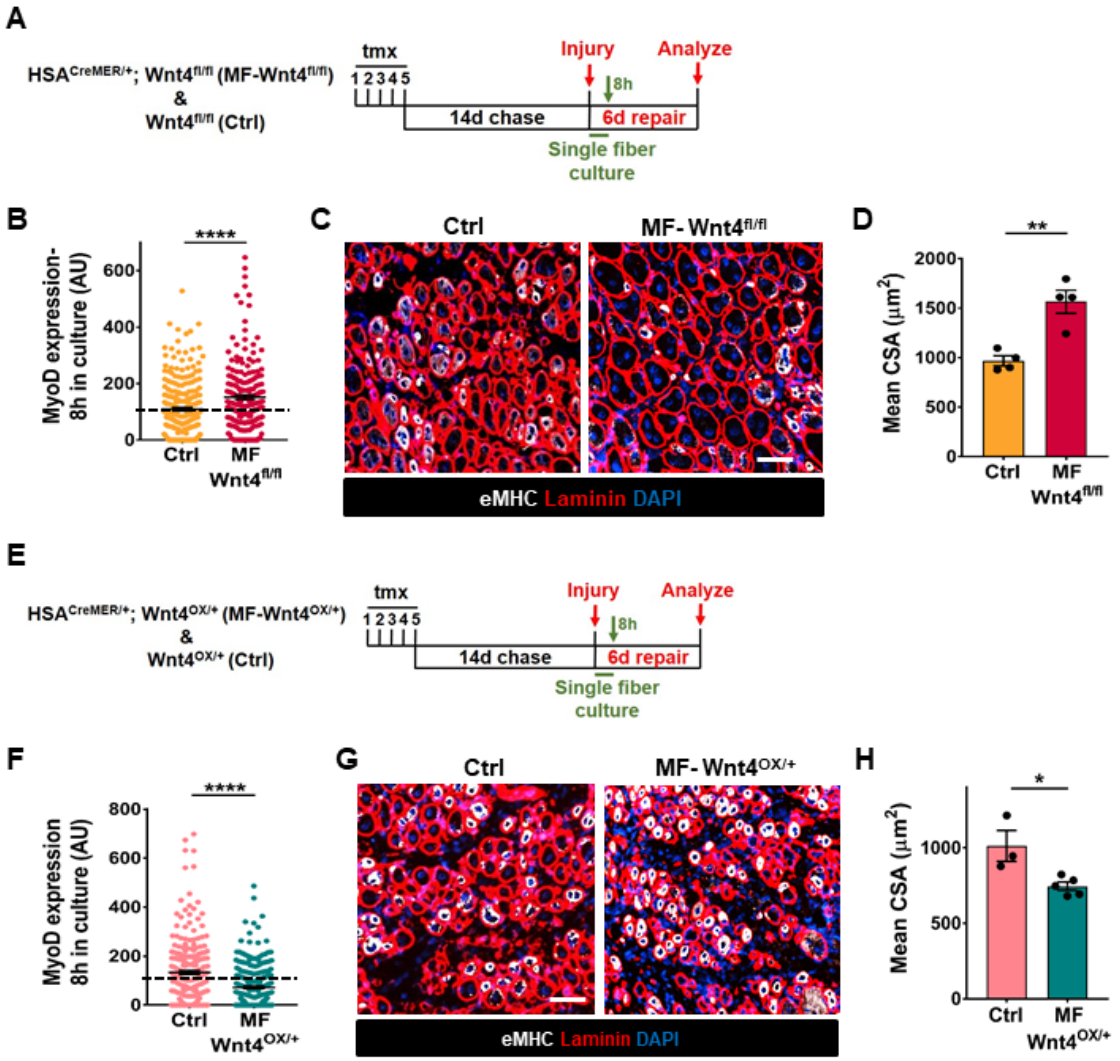

Figure 6.2: Wnt4 from the niche regulates muscle regeneration.
(A) Schematic representation of experimental design for conditional Wnt4 deletion followed by injury and analysis of muscle repair response.
(B) Quantification of MyoD expression in single muscle fibers cultured for 8 h following injury in mice with control and Wnt4-depleted niches.
(C) Representative immunofluorescent images of embryonic myosin heavy chain (eMHC; white), laminin (red), and nuclei (DAPI; blue) in TA sections 6 days following injury in mice with control (left) and Wnt4-depleted (right) niches.
(D) Quantification of cross-sectional area (CSA) of centrally nucleated fibers in TA sections 6 days following injury in mice with control and Wnt4-depleted niches, as represented in (C).
(E) Schematic representation of experimental design for conditional Wnt4 overexpression followed by injury and analysis of muscle repair response.
(F) Quantification of MyoD expression in single muscle fibers cultured for 8 h following injury in mice with control and Wnt4-overexpressing niches.
(G) Representative immunofluorescent images of embryonic myosin heavy chain (eMHC; white), laminin (red), and nuclei (DAPI; blue) in TA sections 6 days following (*caption continued on next page*)

(*caption continued from previous page*) injury in mice with control (left) and Wnt4-overexpressing (right) niches.
(H) Quantification of cross-sectional area (CSA) of centrally nucleated fibers in TA sections 6 days following injury in mice with control and Wnt4-overexpressing niches, as represented in (G).
Bars and lines represent mean ± SEM from three independent experiments. *$p < 0.05$, **$p < 0.01$, and ****$p < 0.0001$. Dashed lines on (B) and (F) represent fluorescence intensity detectable by eye. Scale bars = 50 μm. tmx = tamoxifen. AU = arbitrary units.

stimulation *in vitro*, we observed increased activation (MyoD+) of SCs on single muscle fibers from a Wnt4-depleted niche, compared to controls (Figure 6.2 B). We next tested the effect of niche-derived Wnt4 on the ability of SCs to regenerate muscle. In the TMX-inducible $HSA^{CreMER/+}$;$Wnt4^{fl/fl}$ genetic model, adult fibers are depleted of Wnt4, but the SCs are wildtype. In response to injury, wildtype SCs formed wildtype muscle (data not shown). Therefore, any regenerative phenotype observed after Wnt4 deletion is directly due to the altered niche signal prior to injury. We found that the size of regenerating muscle fibers (6 days after injury) was significantly increased and the number of eMHC+ (embryonic myosin heavy chain) fibers decreased after Wnt4 depletion in the niche, compared to control mice (Figure 6.2 C-D).

To determine whether increasing Wnt4 in the niche reinforces quiescence, we used an inducible transgenic gain-of-function approach to overexpress Wnt4 (H. H. Lee & Behringer, 2007) in adult muscle fibers (Figure 6.2 E; Tg: $HSA^{CreMER/+}$; $Wnt4^{OX/+}$, herein referred to as Myofiber [MF]-$Wnt4^{OX/+}$). Upon mitogen stimulation *in vitro*, we observed decreased activation (MyoD+) of SCs in a Wnt4-overexpressing niche, compared to controls (Figure 6.2 F), indicating an increase in the number of cells that remain in a quiescent state (MyoD-) in a Wnt4-overexpressing niche. In response to injury, muscle fiber size was smaller and the number of eMHC+ fibers greater in Myofiber-$Wnt4^{OX/+}$, compared to controls (Figure 6.2 G-H). These data suggest that Wnt4 from the niche is sufficient to reinforce SC quiescence and delay muscle regeneration. Therefore, the levels of a single Wnt ligand (Wnt4) from a single type of niche cell (the muscle fiber) regulates the depth of SC quiescence and muscle regenerative potential.

Niche-Derived Wnt4 Stimulates Muscle Stem Cell Rho Activity

Wnt ligands signal in a paracrine manner through canonical or non-canonical pathways (Komiya & Habas, 2008). We observed no difference in expression of β-catenin or Axin2, markers of canonical Wnt signaling, in SCs from a Wnt4-depleted niche, compared to controls (data not shown), indicating that canonical Wnt signaling is not responsible for maintaining quiescence of SCs and regulating muscle regeneration. Rho GTPase is a well-characterized downstream component of the non-canonical Wnt signaling pathway, first identified during gastrulation, to promote polarized cell shape changes and migration (Habas et al., 2003; Schlessinger et al., 2009). The Rho family of GTPases play a key role in cytoskeletal remodeling (Sit & Manser, 2011) and have been implicated in hematopoietic stem cell (HSC) self-renewal (Schreck et al., 2017). We found that active Rho was reduced in sorted quiescent satellite cells (QSCs) from a Wnt4-depleted niche, compared to controls (Figure 6.3 A-B).

To investigate how Wnt4-regulated Rho signaling affects the highly interconnected cytoskeletal network in QSCs, we analyzed phosphorylated myosin light chain (pMLC), a downstream target of Rho that regulates actomyosin network assembly, contractility, and stress fiber formation (Chrzanowska-Wodnicka & Burridge, 1996; Kimura et al., 1996). pMLC was expressed at lower levels in SCs on isolated single muscle fibers from a Wnt4-depleted niche than the controls (Figure 6.3 C-D). Rho also regulates the formation of focal adhesions (Ridley & Hall, 1992). Phosphorylated focal adhesion kinase (pFAK) was also decreased in SCs from a Wnt4-depleted niche (Figure 6.3 E-F). Together, these results demonstrate that Wnt4 from the niche acts through a non-canonical pathway and stimulates Rho activity, modulates cytoskeletal signaling, and results in the phosphorylation (activation) of key regulators of contractility and adhesions in QSCs.

Wnt4-Rho Signaling Regulates Cytoskeletal Contractility of Adult Muscle Stem Cells

Cells rapidly respond to mechanical cues from the cytoskeleton by changing their cell shape, cytoskeletal contractility, and migration (Burridge & Guilluy, 2016). We observed that resident SCs on

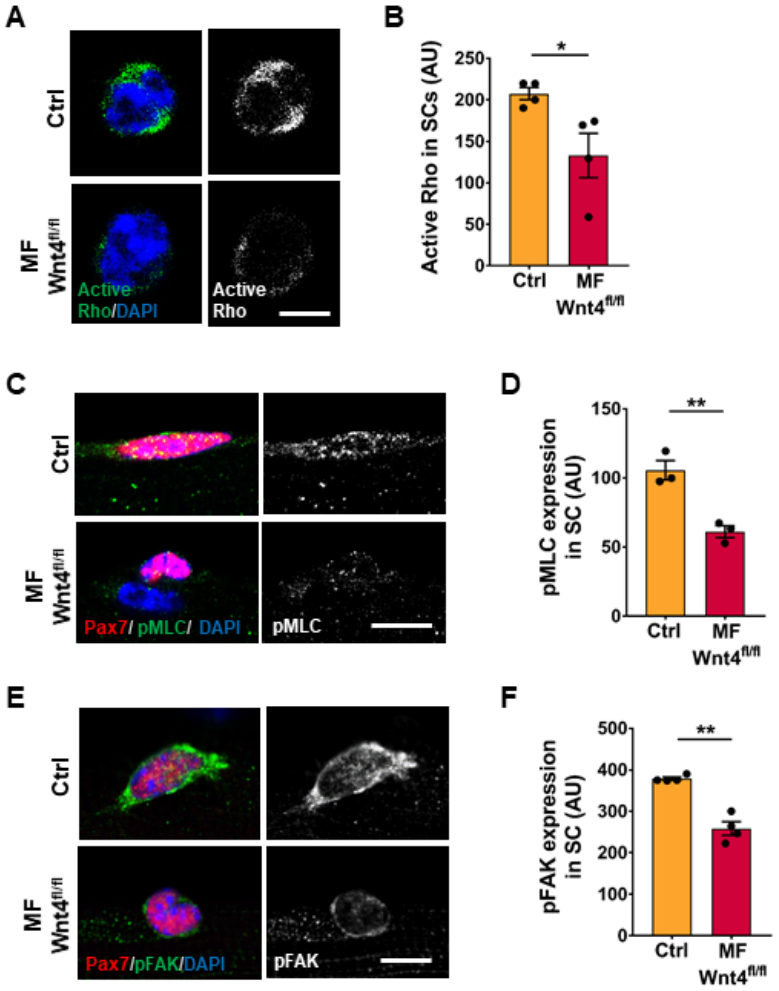

Figure 6.3: Niche-derived Wnt4 stimulates muscle stem cell Rho activity.
(A) Representative immunofluorescent images of active Rho (green, left; white, right) and nuclei (DAPI; blue) in SCs from control (top) and Wnt4-depleted (bottom) niches, 14 days following depletion.
(B) Quantification of active Rho in SCs from control and Wnt4-depleted niches from four independent experiments, as represented in (A).
(C) Representative immunofluorescent images of Pax7 (red), phosphorylated myosin light chain (pMLC; green, left; white, right), and nuclei (DAPI; blue) in SCs from control (top) and Wnt4-depleted (bottom) niches, 14 days following depletion.
(D) Quantification of pMLC in SCs from control and Wnt4-depleted niches from three independent experiments, as represented in (C).
(E) Representative immunofluorescent images of Pax7 (red), phosphorylated focal adhesion kinase (pFAK; green, left; white, right), and nuclei (DAPI; blue) in SCs from control (top) and Wnt4-depleted (bottom) niches, 14 days following depletion.
(F) Quantification of pFAK in SCs from control and Wnt4-depleted niches from four independent experiments, as represented in (E).
Bars and lines represent mean ± SEM from the indicated number of independent experiments. *$p < 0.05$ and **$p < 0.01$. All scale bars = 5 μm. AU = arbitrary units.

isolated single muscle fibers in a Wnt4-depleted niche had a more rounded shape than the controls (Figure 6.4 A). We used AFM to measure the elasticity of sorted QSCs, as a readout of their cytoskeletal contractility. We found that the elastic modulus of QSCs was 50% less for cells isolated from a Wnt4-depleted niche compared to controls (Figure 6.4 B), and similar to the elasticity of QSCs isolated from control fibers and treated with a Rho inhibitor (C3 Transferase; Figure 6.4 B). We observed that 33% of SCs in a Wnt4-depleted niche (approximately six-fold increase over controls) were located in the interstitial space, outside the basal lamina *in vivo* (Figure 6.4 C-D). Using a TMX-inducible, SC-specific approach to reduce Rho *in vivo* (Tg: $Pax7^{CreER/+}$; $RhoA^{fl/+}$, herein referred to as SC-$RhoA^{fl/+}$; Jackson et al., 2011), we found 35% of SCs were located outside the niche (approximately five-fold increase over controls) after direct genetic reduction of Rho activity (Figure 6.4 E-F). These results together demonstrate that a signaling axis, initiated by Wnt4 from the niche and transmitted through Rho signaling, regulates the contractility and niche-retention of QSCs.

Rho Activity Stimulated by Niche-Derived Wnt4 Maintains Stem Cell Quiescence

The observations of altered SC morphology and cytoskeletal signaling during SC activation and in response to Wnt4 depletion from the niche prompted us to ask whether the decrease in Rho and cytoskeletal signaling was sufficient to induce SC activation in uninjured muscle. To answer this question, we analyzed SC-$RhoA^{fl/+}$ and littermate control mice. We found lower levels of active Rho (sorted SCs; Figure 6.5 A) and pMLC (SCs on single muscle fibers; Figure 6.5 B), an expanded SC pool (Figure 6.5 C), and increased BrdU+/Pax7+ SCs (in muscle sections; Figure 6.5 D) in SC-$RhoA^{fl/+}$ mice compared to controls. Thus, Rho activity not only regulates contractility and niche-retention, but also maintains SC quiescence.

Consistent with the expansion of SCs in uninjured muscle through the reduction in Rho (in QSCs) or Wnt4 (from the niche), acute treatment of isolated wildtype single muscle fibers with a Rho inhibitor (C3 Transferase) accelerated cell-cycle entry of SCs, as measured by MyoD expression

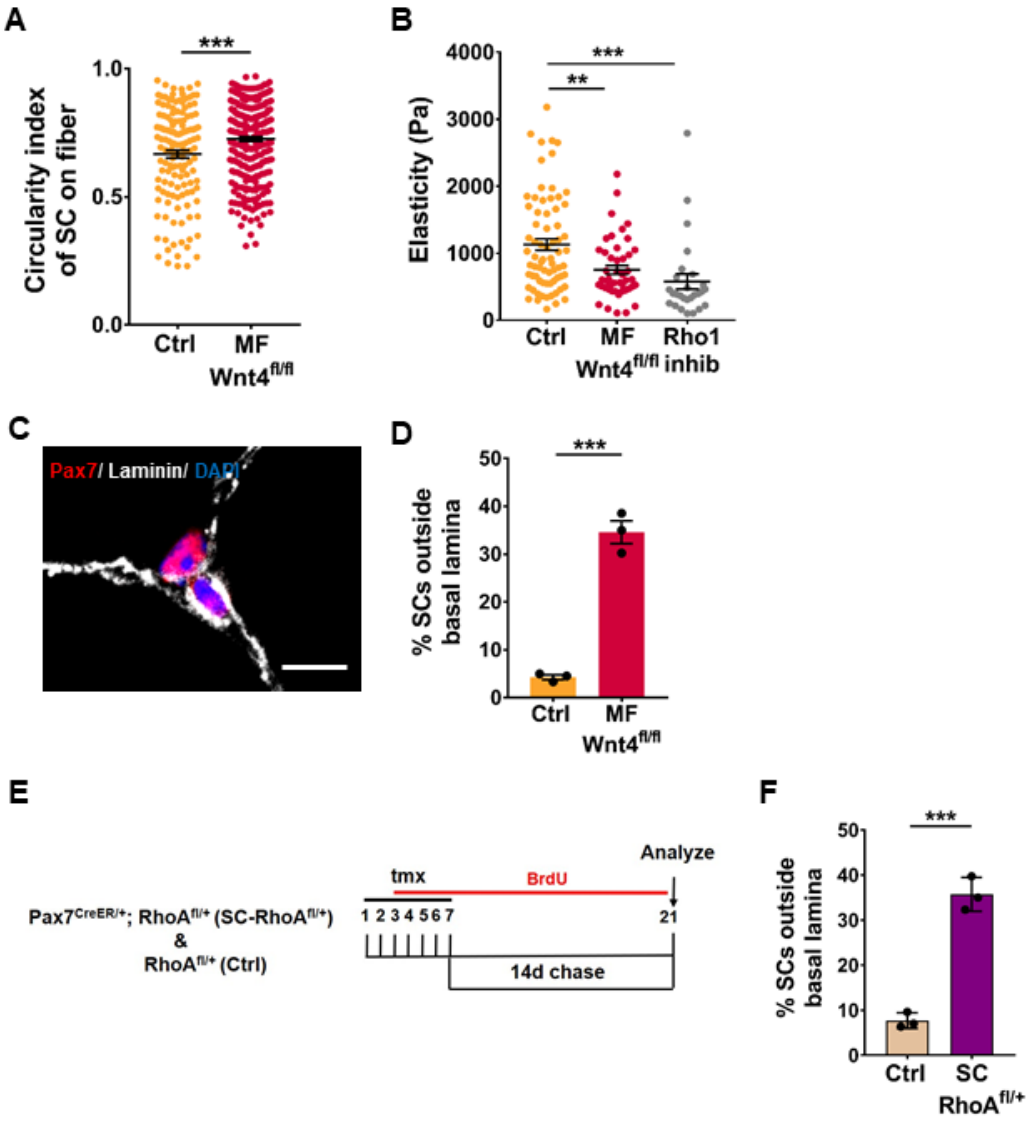

Figure 6.4: Wnt4-Rho signaling regulates cytoskeletal contractility of adult muscle stem cells.
(A) Quantification of the circularity index of SCs on muscle fibers isolated from control and Wnt4-depleted niches, 14 days following depletion.
(B) Quantification of the elasticity of QSCs, as measured by AFM, for SCs isolated from control and Wnt4-depleted niches, 14 days following depletion and 2 h following isolation, and SCs isolated from control niches and treated with Rho inhibitor for 2 h.
(C) Representative immunofluorescent image of Pax7 (red), laminin (white), and nuclei (DAPI; blue) of SCs in TA muscle sections, 14 days following depletion. Scale bar = 10 μm.
(D) Quantification of SCs located outside the basal lamina in control and Wnt4-depleted niches, 14 days following depletion.
(E) Schematic representation of the experimental design for RhoA reduction.
(F) Quantification of SCs located outside the basal lamina in control and RhoA-reduced SCs, 14 days following reduction.
Bars and lines represent mean ± SEM from three independent experiments. **p < 0.01 and ***p < 0.001. Pa = pascals. tmx = tamoxifen.

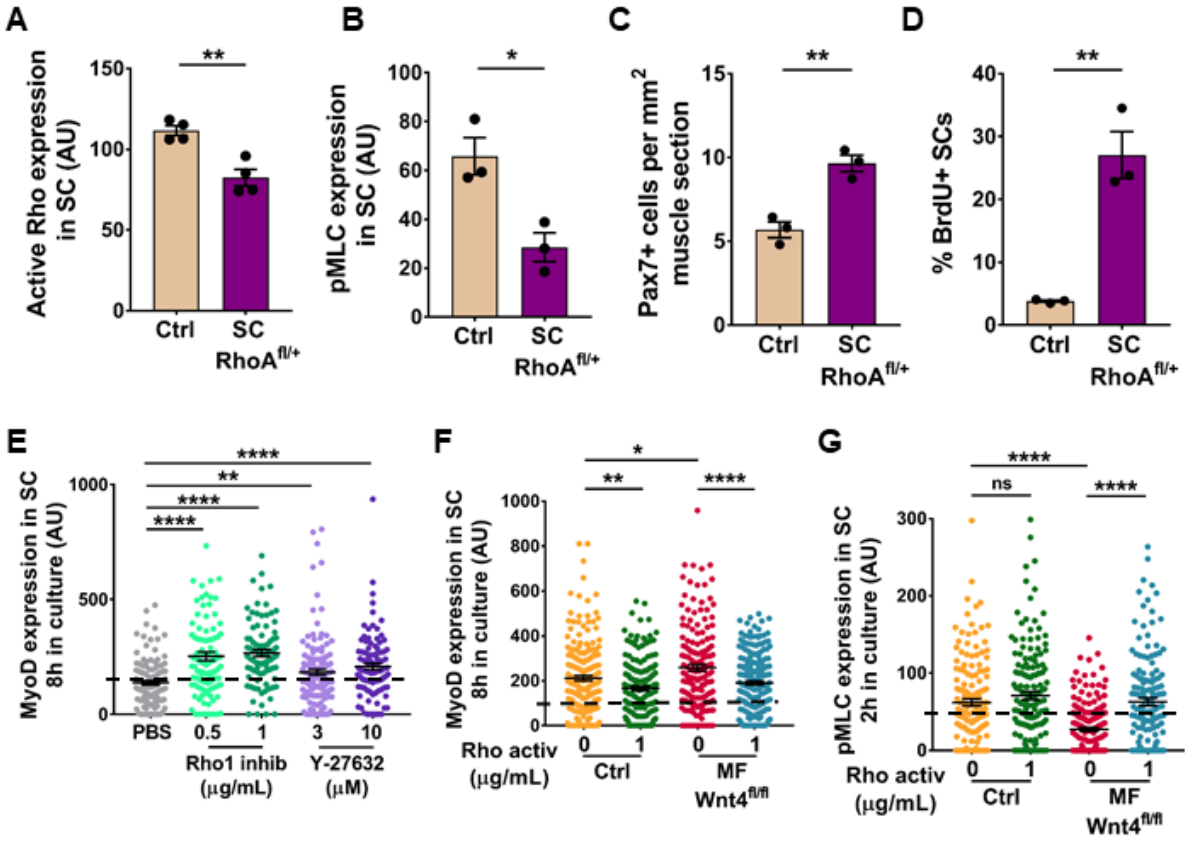

Figure 6.5: Rho activity stimulated by niche-derived Wnt4 maintains stem cell quiescence.
(A) Quantification of active Rho expression in sorted SCs from control and SC-RhoAfl/+ mice from four independent experiments.
(B) Quantification of pMLC expression in SCs on single muscle fibers from control and SC-RhoAfl/+ mice from three independent experiments.
(C) Quantification of Pax7+ cells in muscle sections from control and SC-RhoAfl/+ mice from three independent experiments.
(D) Quantification of BrdU+ SCs in muscle sections from control and SC-RhoAfl/+ mice from three independent experiments.
(E) Quantification of MyoD expression in SCs following 8 h in culture with control (PBS), Rho1 inhibitor (C3 Transferase; 0.5 and 1.0 μg/ml), or ROCK inhibitor (Y-27632; 3 and 10 μM) from two independent experiments.
(F) Quantification of MyoD expression in SCs from control and Wnt4-depleted niches following 8 h in culture without and with Rho activation (Rho Activator II; 0 or 1 μg/ml) from three independent experiments.
(G) Quantification of pMLC expression in SCs from control and Wnt4-depleted niches following 2 h in culture without and with Rho activation (Rho Activator II; 0 or 1 μg/ml) from three independent experiments.
Bars and lines represent mean ± SEM from the indicated number of independent experiments. Dashed lines on (E-G) represent fluorescence intensity detectable by eye. *$p < 0.05$, **$p < 0.01$, and ****$p < 0.0001$. AU = arbitrary units.

(Figure 6.5 E). Therefore, Rho acts in a cell-autonomous manner to maintain SC quiescence under tissue homeostasis. Rho GTPase activates Rho kinase (ROCK), which either directly activates myosin light chain (MLC) or inactivates myosin phosphatase, subsequently activating MLC (Kimura et al., 1996). We found that SCs on isolated wildtype single muscle fibers activated more rapidly *in vitro* in the presence of ROCK inhibitor (Y-27632; Figure 6.5 E), suggesting that SC quiescence is regulated through a Rho-ROCK axis.

Finally, we asked whether active Rho was sufficient to repress activation of SCs in a Wnt4-depleted niche. In control single muscle fibers, transient Rho activation (Rho Activator II) maintained the quiescent state, whereas in a Wnt4-depleted niche, Rho activation reestablished quiescence (Figure 6.5 F). Moreover, activating Rho in SCs with a Wnt4-depleted niche restored pMLC levels to those observed in control SCs (Figure 6.5 G). Together these results demonstrate that Rho activity, stimulated by Wnt4 from the niche, regulates the mechano-properties of SCs and reinforces quiescence.

DISCUSSION

Despite numerous studies on the role of Wnt signaling in adult stem cell biology, there is little known about the specific Wnt ligands, their source, and how they signal to stem cells *in vivo* (Clevers et al., 2014). Our results provide direct evidence of a specific paracrine-acting Wnt ligand from a defined niche cell that is required to maintain mammalian stem cell quiescence during tissue homeostasis. We found that Wnt4 is produced in adult muscle fibers and activates Rho-GTPase within the SCs to maintain quiescence during tissue homeostasis (Figure 6.6). In the absence of niche-derived Wnt4, SCs transition toward a more activated state, which accelerates muscle tissue repair in adult mice.

The Wnt signaling pathway is divided into two branches: canonical and non-canonical arms, based on the involvement of β-catenin or lack thereof (Komiya & Habas, 2008). While the specific

Wnt ligands required for canonical signaling during SC lineage progression remain unknown, it is clear that SC proliferation and differentiation depend on intracellular canonical Wnt signaling; whereas asymmetric division of activated SCs and myotube hypertrophy depend on non-canonical Wnt signaling (Lacour et al., 2017; Le Grand et al., 2009; Von Maltzahn et al., 2012). Thus, Wnt signaling plays critical roles during SC lineage progression. In QSCs, we find undetectable levels of nuclear β-catenin and low levels of Axin2. Therefore, we propose that canonical Wnt signaling is inactive in QSCs. Rather, non-canonical Wnt signaling is active and functionally required for SC quiescence.

Wnt ligands can act antagonistically (Mikels & Nusse, 2006; Topol et al., 2003; Westfall et al., 2003), leading to either intracellular canonical or non-canonical Wnt signaling. In the present study,

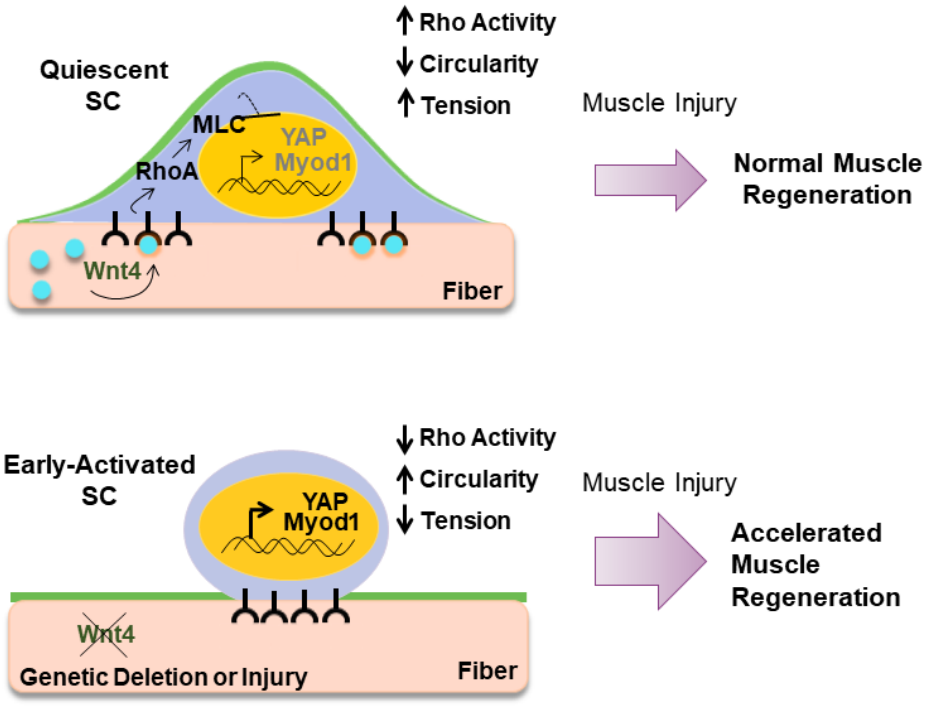

Figure 6.6: Working model for how Rho activity and cytoskeletal contractility stimulated by niche-derived Wnt4 regulate muscle stem cell quiescence and activation.
Wnt4 from the muscle fiber regulates muscle stem cell quiescence via RhoA and cytoskeletal signaling. With normal Wnt4 from the niche QSC Rho activity and cytoskeletal tension are high and muscle regeneration occurs at a normal rate. SCs from a Wnt4 depleted niche exhibit decreased Rho activity and cytoskeletal tension, increased circularity, and the response to injury is exaggerated, leading to accelerated muscle regeneration.

deletion of Wnt4 and Porcn from adult fibers did not induce canonical signaling, arguing against antagonism between canonical and non-canonical Wnt signaling in QSCs. With the generation of inducible genetic approaches, it is now possible to define the cell sources and specific Wnt ligands required for SC function during tissue homeostasis and regeneration.

The Wnt-PCP pathway has been widely studied in *Drosophila*, *Xenopus*, and Zebrafish. Specific Wnt family members including Wnt5, Wnt11, and Wnt4 signal via Frizzled receptors to Dishevelled (Dvl), an adaptor protein that becomes polarized at the apical membrane to regulate morphology, polarization, and migration of cell structures in the developing epithelium (Jussila & Ciruna, 2017; Sokol, 2015; Yang & Mlodzik, 2015). The defining feature of this pathway is its regulation of the actin cytoskeleton via Rho-GTPase (Schlessinger et al., 2009). Given that we observed similar regulation of SCs via Rho-GTPas and downstream components of cytoskeletal contractility, we define a requirement for Wnt-PCP signaling in adult mammalian muscle stem cell quiescence.

Analysis of whole muscle revealed that Wnt4 transcript levels decreased during early stages of regeneration after $BaCl_2$ injury. It has been reported that Wnt4 levels undergo a transient increase, before ultimately decreasing in response to cardiotoxin injury (Polesskaya et al., 2003). It is possible that the type of injury, in this case $BaCl_2$ versus cardiotoxin, elicits different dynamics of the cellular response (Gayraud-Morel et al., 2009). Studying paracrine regulation between different cell types within regenerating muscle tissue could uncover new modes of intercellular communication.

The important role of mechano-properties on cell fate across different contexts from development to stem and progenitor cell differentiation *in vitro* is becoming increasingly appreciated (Behrndt et al., 2012; Engler et al., 2006; Gilbert et al., 2010). The fate of activated SCs to self-renew or differentiate can be skewed based on the stiffness of the extracellular matrix (ECM). We find that disruption of Wnt4-Rho signaling decreases the apparent stiffness and displacement of SCs from the

niche. Therefore, a specific niche factor acting in a paracrine manner alters the mechanical properties and quiescent state of an adult mammalian stem cell.

Consistent with the notion that quiescence is essential for adult stem cell preservation, deregulation of quiescence in muscle stem cells during tissue homeostasis leads to their depletion through apoptosis, precocious differentiation, or incorporation into the center of the muscle fiber, reminiscent of a regenerative event (Bjornson et al., 2012; Cheung et al., 2012; Goel et al., 2017; Philippos et al., 2012). In contrast, the results in the present study and those of Goel et al. (2017) suggest that the SC pool can establish a new homeostatic set point. While there are many possibilities that explain the discrepancy, including the cell type and specific genes that are disrupted, based on the present results, SC depletion, differentiation, and fusion are not obligate when quiescence is broken during tissue homeostasis.

Preservation of the SC pool after injury is critical for long-term tissue homeostasis. In response to injury, we observed an expanded SC pool in the Wnt4-depleted niche mutant, compared to control muscle. Interestingly, pool size was also restored to the elevated pre-injured levels observed in Wnt4-depleted niches. Initially, we predicted that the SC pool would return back to control wildtype levels, due to the reformation of muscle fibers and the SC pool by genetically wildtype (non-recombined) SCs. Instead, our data raise a couple of intriguing possibilities: (1) Wnt4 in regenerating myofibers does not set the size of the SC pool post-injury, (2) the size of the SC pool in regenerated muscle is instructed prior to injury, i.e., in the QSCs, to ensure a return to the homeostatic set point. If true, this would involve a counting mechanism at the level of the stem cell or available niche sites, or (3) Wnt4 from the niche regulates the number of asymmetrically and symmetrically dividing daughters. This is less likely due to the decline in Wnt4 levels upon injury. These possibilities each warrant further investigation.

To fulfill their roles during tissue repair, stem cells must exit quiescence, proliferate, and mobilize to the site of injury. During the transition between quiescence and activation, SCs pass through a distinct molecular and functional state termed G_{Alert}, denoted by its increase in cell size and mTORC1 activation (Rodgers et al., 2014). Acute induction of the G_{Alert} state promotes muscle repair (Rodgers et al., 2014, 2017). In the present study, we used single cell analysis to dissect novel molecular states as SCs break quiescence. Our data reveal that the QSC pool undergoes dynamic transitions, with changes in morphology, mechano-properties, and cytoskeleton signaling, all preceding cell-cycle entry. Using time-lapse imaging, we recently demonstrated that SC motility occurs early in the activation response (Kimmel et al., 2018). Based on the time points we analyzed *in vitro* in the present study, changes in cytoskeletal signaling either precede or are coincident with mTORC1 activation, followed by induction of YAP and MyoD. We speculate that a decrease in Wnt4-Rho signaling initiates a migration program to reach an injury site, coupled with increased biomass licensing QSCs for activation.

In line with the concept that the cytoskeletal machinery functions as an early regulator of SC activation, miR-708 upregulates Tensin3, a positive regulator of pFAK activity, to delay cell-cycle entry (Baghdadi et al., 2018). In the present study, we find that inhibition of Rho decreased mTORC1 and pFAK *in vitro*, whereas RhoA deletion in SCs in uninjured muscle *in vivo* did not affect mTORC1 and pFAK. Therefore, it is possible that pFAK, which is regulated by mTORC1 activity *in vitro*, is part of a molecular pathway deployed when SCs break quiescence in a stimulatory (mitogenic or injured) environment. This would suggest a rapid remodeling of the signaling pathways regulated by Rho in the absence or presence of activation stimuli. This awaits further investigation.

Using inducible cell-specific genetic approaches to target a component of the muscle stem cell niche, the muscle fiber, we demonstrate that Wnt4 regulates the depth of SC quiescence under tissue homeostasis and regenerative potential in response to injury. Our findings have implications for

regenerative medicine, as a means to mobilize quiescent stem cells and facilitate tissue repair after injury or in disease.

CHAPTER 7

Characterization of the Biophysical Properties of the Hematopoietic Stem Cell Niche

INTRODUCTION

Hematopoiesis is the complex and tightly regulated process by which all the mature cellular components of blood are formed. Hematopoiesis begins with a rare population of cells called hematopoietic stem cells (HSCs), which are maintained in a quiescent state until becoming activated. Upon activation, HSCs undergo sequential differentiation steps through lineage-restricted progenitors to produce the various specialized cell types that make up the mature cellular components of blood (Orkin & Zon, 2008). HSCs reside in the heterogenous microenvironment of the bone marrow, and more specifically, they occupy specialized "niches" that regulate HSC self-renewal and homeostasis, as well as the cell fate decisions that occur throughout hematopoiesis (Morrison & Scadden, 2014). While much is known about the soluble factors and cooperative cell types that direct hematopoiesis (Schepers et al., 2015), much less is known about how the niche ECM may maintain HSC quiescence or trigger activation and hematopoiesis. More specifically, it is unclear whether the heterogeneous compartments of the bone marrow microenvironment exhibit different biophysical properties that cause these individual niches to promote specific cell fate decisions during hematopoiesis.

The bone marrow can be subdivided into three distinct compartments that represent different HSC niches: the endosteum, the perivasculature, and the central marrow (Hines et al., 2008). The endosteum is the "outer" region of bone marrow, and is defined as the region within 15 μm of the inner bone surface. The perivasculature refers to the vascular components of the bone marrow,

including arterioles and venous sinusoid capillaries, as well as all bone marrow within 5 μm of these vascular components. The non-vascular central marrow is loosely defined as everything else within the bone marrow that is neither endosteum nor perivasculature. Prior studies have examined the ECM components that makeup each niche and found that fibronectin is highly expressed in the endosteum and surrounding vasculature-associated megakaryocytes, and more diffusely spread throughout the central marrow (Malara et al., 2014; Nilsson et al., 1998). Fibrillar collagens Col I and Col III have been primarily detected within the endosteum, whereas basement membrane proteins Col IV and laminin were identified specifically localized to the vasculature (Klamer & Voermans, 2014; Nilsson et al., 1998; Reddi et al., 1977; S. W. Volk et al., 2014). Lineage tracing strategies have revealed that HSCs reside primarily within perivasculature niches, including near arterioles that are mostly found within the endosteum, as well as near the venous sinusoid capillaries that are found throughout the central marrow cavity (Kunisaki et al., 2013; Nombela-Arrieta et al., 2013; Sugiyama et al., 2006). These findings suggest that laminin- and fibronectin-rich ECM niches may support optimal HSC growth and function. Indeed, *in vitro* studies demonstrate that fibronectin-modified surfaces support HSC survival (Kurth et al., 2009; Muth et al., 2013; Prewitz et al., 2013). However, the use of unfractionated cells from the bone marrow in these studies, likely containing very few true HSCs, makes it difficult to make definitive conclusions. Moreover, these studies failed to evaluate and recapitulate the complete ECM makeup of the native bone marrow niche. As such, there is a need for better characterization of the *in vivo* bone marrow microenvironment.

Various ECM components not only impart biochemical properties and induce cellular signaling (e.g. via integrins) within the microenvironment, but they also provide the basis for the mechanical structure and biophysical properties of the niche. Importantly, the elasticity (E = Young's modulus; stiffnesss) of the ECM can regulate stem cell growth and viability (Gilbert et al., 2010) and also direct cell fate decisions (Engler et al., 2006; Laralynne Przybyla et al., 2016c). Consistent with

this paradigm, HSCs respond to ECM stiffness and alter their phenotype in response to different substrate material properties (J. S. Choi & Harley, 2017; Holst et al., 2010; Lee-Thedieck et al., 2012; Shin et al., 2011, 2014). However, these studies also utilized either unfractionated bone marrow cells or immortalized HSC lines, and as such, it is unclear whether the findings accurately represent the behavior of native HSCs within the bone marrow microenvironment. Previous efforts to quantify the biophysical properties of the bone marrow yielded a wide range of elasticity values and failed to differentiate between the various heterogeneous components of the bone marrow niche (Bryant et al., 1989; Jansen et al., 2015; Z. Zhong & Akkus, 2011). Thus, we utilized AFM to specifically measure the elasticity of the various heterogenous bone marrow compartments with high spatial resolution. Our findings reveal that distinct bone marrow compartments exhibit different biophysical properties, suggesting that the elasticity of the niche should be considered as a potential factor regulating HSC quiescence and activation during hematopoiesis.

RESULTS

Atomic Force Microscopy Measurements of the Heterogeneous Bone Marrow Microenvironment

In order to characterize the biophysical properties of the HSC niche, we developed a protocol for preparing sections of mouse femur bone marrow that would be suitable for indentation with AFM along with simultaneous brightfield and fluorescent imaging to effectively determine the spatial localization of elasticity measurements. Most importantly, we sought to fluorescently label the vasculature within the bone marrow in order to identify and segregate measurements of the perivasculature, non-vascular central marrow, and endosteum. To accomplish this, we injected adult mice with DyLight488-Lectin and then rapidly excised and snap-froze the femurs in OCT. The femurs were then cryosectioned into 10 μm slices. Immediately prior to measurement, each section was

thawed and mounted on the stage of an inverted Nikon TE2000-U microscope equipped with an MFP3D-BIO atomic force microscope. The DyLight488-Lectin non-specifically bound the vasculature endothelium, and due to the rapid excision and snap-freezing of samples, in most cases effectively labeled the perivasculature without diffusing throughout the bone marrow cavity (Figure 7.1 A). Once samples were thawed, the AFM was used to indent regions of interest using silicon nitride cantilevers with spring constants ranging from 0.04 to 0.07 N/m, modified with spherical borosilicate glass tips with 5 μm diameters. A maximum force of 2 nN was used to indent samples, and following

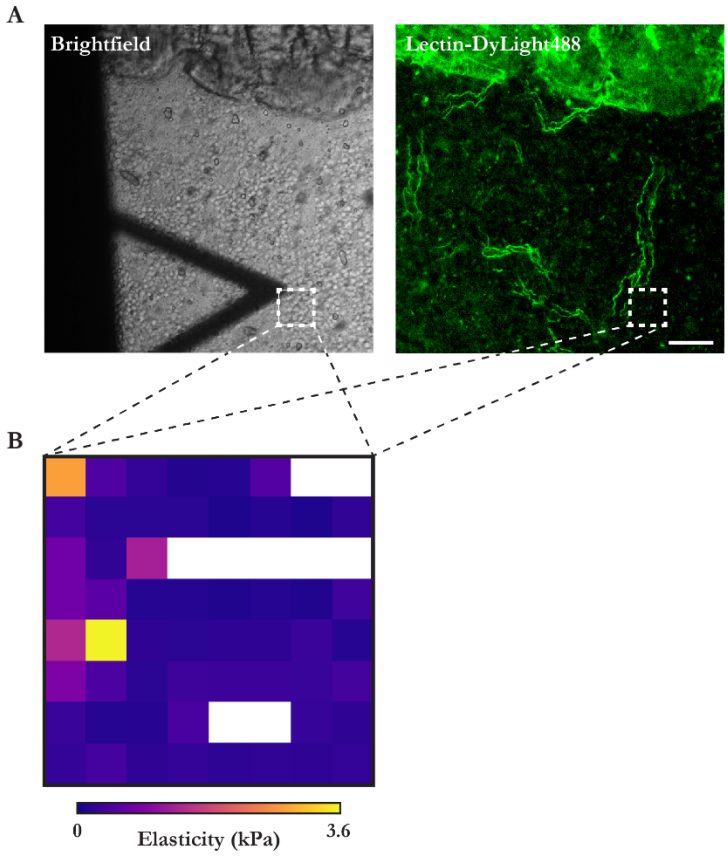

Figure 7.1: Elasticity measurements of mouse femur bone marrow.
(A) Representative brightfield and fluorescent images of a mouse femur section with Lectin-DyLight488 labeled blood vessels prepared for atomic force microscopy (AFM) measurements. Dashed rectangles indicate the region measured by AFM and plotted as a heat map in (B). Scale bar = 50 μm.
(B) Heat map representing AFM elasticity measurements of mouse femur bone marrow measured in the region indicated in (A). White boxes indicate AFM measurements that yielded irregular force curves incompatible with calculation of elasticity via the Hertz model. kPa = kilopascals.

the acquisition of force curves, the Hertz model was applied to calculate the elasticity of the tissue at each indented location. The resulting data could then be plotted as a heat map of elasticity values corresponding to each indentation within the region of interest (Figure 7.1 B). Variations in the topography or disruptions to tissue architecture within the region of interest occasionally led to force curves that were incompatible with elasticity calculations using the Hertz model; therefore, these indentations were disregarded in subsequent analyses.

We utilized a combination of brightfield and fluorescence imaging to target the measured regions of interest to the various heterogenous niches within the bone marrow, allowing us to gather data for the endosteum, perivasculature, and non-vascularized central marrow. Measurements within 15 μm of the clearly identifiable inner bone surface were defined as endosteum, measurements taken within 5 μm (the XY spatial resolution of indentation measurements) of clearly identifiable vasculature, determined by DyLight488-Lectin signal, were defined as the perivasculature, and all other measurements were attributed to the central marrow (Figure 7.2 A). Using these criteria, we obtained elasticity values ranging from 46 Pa to 3.6 kPa with a mean value of 252 Pa for the central marrow region, and values ranging from 49 Pa to 2.8 kPa with a mean value of 394 Pa for the perivasculature (Figure 7.2 B). As expected, we obtained much stiffer elasticity measurements for the endosteum, with values ranging from 407 Pa to 104 kPa with a mean of 12.8 kPa (Figure 7.2 B). Interestingly, measurements within the endosteum seemed to separate into two distinct groups: one of softer measurements, similar to those obtained in the central marrow and perivasculature, and another of much stiffer measurements of the order of 10^4 Pa (Figure 7.2 B). By examining the heat maps of elasticity measurements for regions of interest in the endosteum, we found that elasticity values increased by orders of magnitude as the bone edge was approached (Figure 7.2 C-D), demonstrating a clear relationship between the spatial location within the bone marrow and the stiffness of the tissue. Together, our data indicate that distinct bone marrow niches with known differences in ECM

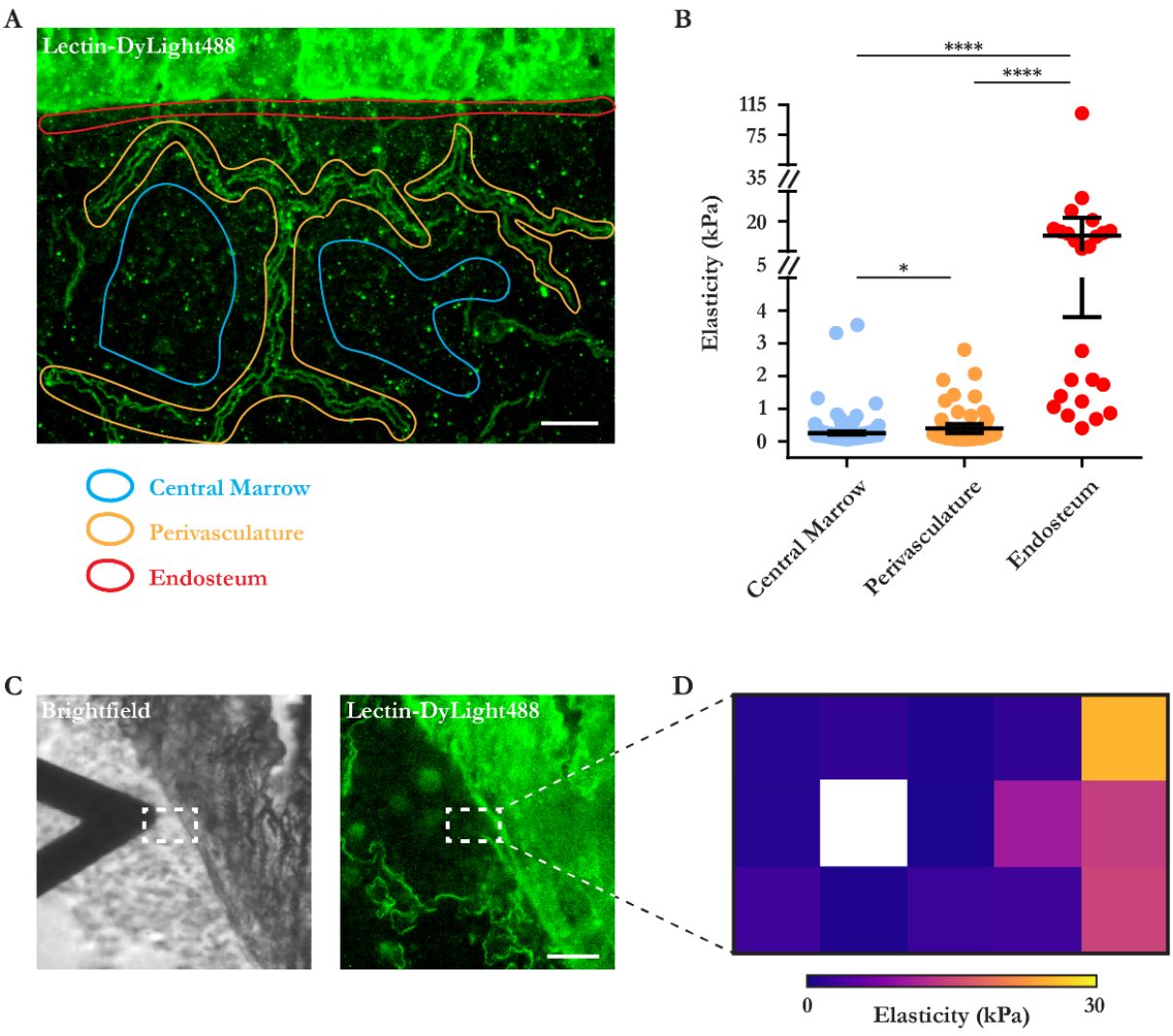

Figure 7.2: Characterization of the elasticity of distinct bone marrow niches.
(A) Representative fluorescent image of a mouse femur section with Lectin-DyLight488 labeled blood vessels. Colored outlines indicate the distinct bone marrow niches: endosteum, perivasculature, and central marrow. Scale bar = 50 μm.
(B) Atomic force microscopy (AFM) measurements of mouse femur bone marrow, grouped by the distinct bone marrow niches within which the measurements were taken. Data was collected on three separate days with N = 3 femur sections measured (1 section each day) and n = 280 total elasticity measurements. Central marrow mean = 253 Pa (n = 195), perivasculature mean = 394 Pa (n = 61), and endosteum mean = 12.8 kPa (n = 24). Line and bars represent mean ± 95% CI. *$p < 0.05$ and ****$p < 0.0001$. kPa = kilopascals.
(C) Representative brightfield and fluorescent images of a mouse femur section with Lectin-DyLight488 labeled blood vessels prepared for AFM measurements of the endosteum. Dashed rectangles indicate the region measured by AFM and plotted as a heat map in (D). Scale bar = 25 μm.
(D) Heat map representing AFM elasticity measurements of the endosteum measured in the region indicated in (C). White box indicates an AFM measurement that yielded an irregular force curve incompatible with calculation of elasticity via the Hertz model. kPa = kilopascals.

composition also exhibit unique ranges of elasticity, presenting the intriguing possibility that these variations in tissue stiffness may co-regulate HSC self-renewal and activation.

Comparison of Snap-Frozen and Thawed versus Freshly Isolated Mouse Femur Bone Marrow Sections

Our presented protocol for measuring the elasticity of the bone marrow microenvironment has the important advantage of enabling spatially-directed measurements of the various heterogeneous niches. However, the process of snap-freezing and thawing bone marrow sections leads to the possibility that tissue organization and architecture could be disrupted during the freeze-thaw cycle, which could affect the measured biophysical properties. Thus, we sought to compare AFM elasticity measurements taken from both freshly isolated and freeze-thawed sections of mouse femur bone marrow. Fresh samples were prepared by excising mouse femurs and manually generating transverse sections, or thin discs, which were then mounted for AFM measurements (Figures 7.3 A). Without DyLight488-Lectin labeling, it was impossible to distinguish between the perivasculature and the non-vascular central marrow. However, we did perform measurements both near and distal from the bone edge, with the intent of capturing measurements within the endosteum as well as the central marrow regions. By comparing these measurements of fresh bone marrow tissue to the pooled data previously collected for freeze-thawed sections, we found there was no statistically significant difference between the mean elasticity value for each group (Figure 7.3 B). Elasticity measurements of fresh tissue ranged from 47 Pa to 30.2 kPa with a mean of 1.8 kPa, while measurements for freeze-thawed tissue ranged from 46 Pa to 104 kPa with a mean of 1.4 kPa. These findings validated that our protocol for measuring and comparing the stiffness of heterogeneous regions within the bone marrow niche produced values that faithfully reflected the elasticity of the native tissue, despite the freeze-thaw cycle. Thus, our protocol should prove useful in future studies to more completely characterize the variations in elasticity of the

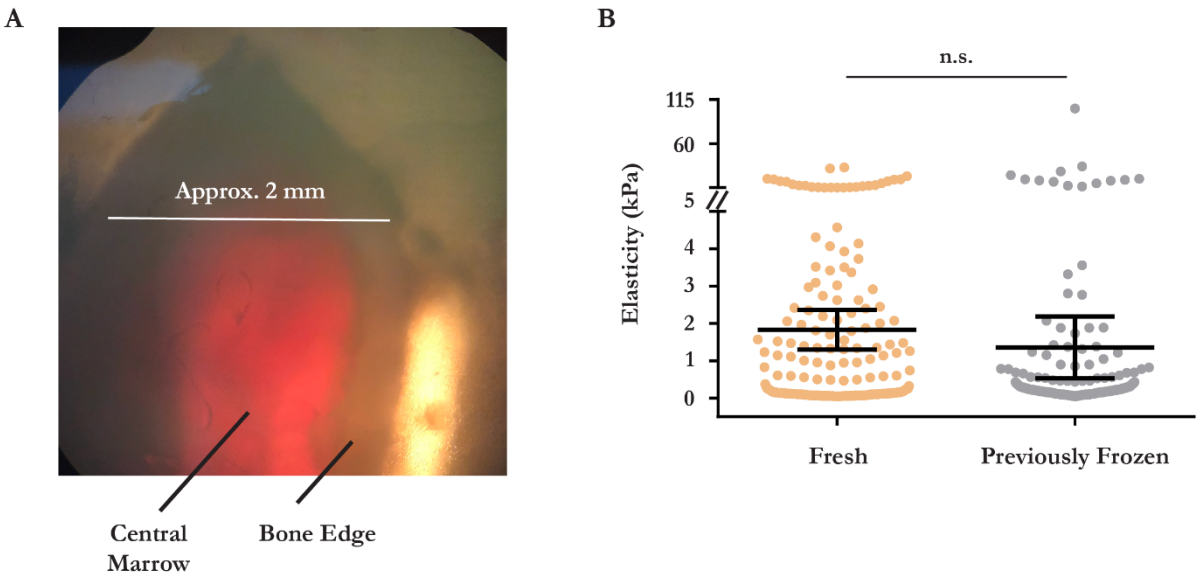

Figure 7.3: Comparison of elasticity measurements from fresh and previously frozen mouse femur bone marrow.
(A) Representative brightfield image of a freshly isolated mouse femur section prepared for atomic force microscopy (AFM) elasticity measurements.
(B) AFM measurements of fresh and previously frozen mouse femur bone marrow sections. Data from fresh sections was collected on a single day with N = 3 femur sections measured and n = 230 total elasticity measurements. Data from previously frozen sections was collected on three separate days with N = 3 femur sections measured (1 section each day) and n = 280 total elasticity measurements (the same data set plotted in Figure 7.2 B, but with data from all three niches pooled). Fresh mean = 1.8 kPa and previously frozen mean = 1.4 kPa. Line and bars represent mean ± 95% CI. n.s. = not significant. kPa = kilopascals.

bone marrow that reflect tissue heterogeneity and lead to a better understanding of how the mechanical properties of the niche co-regulate HSCs.

DISCUSSION

The work presented in this chapter demonstrates the development of a novel and effective protocol for measuring the elasticity of specific regions within the bone marrow microenvironment. Our preliminary findings indicate that the elasticity of the bone marrow varies widely, spanning multiple orders of magnitude, with recorded values ranging from 47 Pa to 104 kPa. By designing our methodology to enable brightfield and fluorescence imaging of samples while performing AFM

indentations, we were able to identify and probe the stiffness of three heterogeneous sub-regions of the bone marrow within which HSCs are known to reside: the endosteum, the perivasculature, and the non-vascular central marrow. By comparing our results to measurements of freshly isolated bone marrow sections, we were able to validate that the snap-freezing used in our sample preparation preserves the native tissue elasticity and is a useful and efficient methodology for examining the biophysical properties of various niches within the bone marrow.

Using our protocol, we found that the endosteum was much stiffer (mean = 12.8 kPa) than both the perivasculature (mean = 394 Pa) and non-vascular central marrow (mean = 252 Pa). Moreover, it was clear that the endosteum was stiffer as it approached the junction with the inner bone surface. This may be due to additional connective tissue within this region responsible for maintaining the structural integrity of the bone marrow, consistent with the previous findings of increased fibronectin and fibrillar collagens within the endosteum (Klamer & Voermans, 2014; Malara et al., 2014; Nilsson et al., 1998; S. W. Volk et al., 2014). It should be noted that some of these highest elasticity measurements within the endosteum may alternatively have been due to fine projections of mineralized bone into the endosteum that weren't visible by our imaging. Although our measurements of the endosteum were somewhat softer than what was previously reported (Engler et al., 2006; Shin et al., 2014), these earlier measurements were made on *ex vivo* generated osteo-lineage cell microenvironments and after lengthy culture periods, and thus they may not truly reflect the biophysical properties of the endosteum *in vivo*.

Interestingly, while the perivasculature and non-vascular central marrow exhibited a statistically significant difference in mean elasticity (394 Pa and 252 Pa, respectively), it is unclear whether the magnitude of this difference is biologically significant. We expected the perivasculature to exhibit a more dramatic increase in stiffness relative to the non-vascular central marrow, at least a two-fold increase or even an order of magnitude, due to the smooth muscle that surrounds arterioles

and the increased basement membrane ECM proteins found at both arterioles and sinusoids (Klamer & Voermans, 2014; Nilsson et al., 1998; Reddi et al., 1977). One limitation to our method that may have prevented us from detecting a notable increase in perivasculature stiffness was the non-specific labeling of blood vessels with DyLight488-Lectin. Due to its non-specific and weak association with the vasculature, we observed that in nearly half of our prepared samples, the labeling would dilute and wash away upon thawing of the sample and mounting for AFM, forcing us to discard of these samples. Even in samples that appeared to be robustly labeled, it is possible that the DyLight488-Lectin had diffused through the vasculature somewhat, causing us to inaccurately attribute central marrow measurements to the perivasculature. This limitation could be easily and effectively avoided in future studies by using genetic mouse models that feature constitutive fluorescent labeling of the vasculature. This would also eliminate the need to perform injections of mice prior to sacrifice and sample preparation, further simplifying the workflow.

Additional studies are needed to more completely characterize the bone marrow microenvironment. As suggested throughout this discussion, significant improvements in the statistical and biological significance of the presented findings could be achieved by analysis of a larger number of samples, improved labeling of the vasculature, and measurements of sequential sections to examine how the biophysical properties change with depth into the central marrow. Our hypothesis remains that heterogenous regions of the bone marrow, which represent different HSC niches, will exhibit unique biophysical properties. Future studies should also be aimed at moving beyond characterization of bone marrow stiffness and examine how the mechanical properties of the niche co-regulate HSC growth and function. The results of multiple studies presented in this dissertation and elsewhere have illustrated that the mechanical properties of native tissues are sensed by cells through various mechanosensitive signaling pathways and alter pluripotent, multipotent, and adult stem cell behavior. Thus, we anticipate there is yet much to discover regarding how the biophysical

properties of the niche regulate HSC survival, self-renewal, and cell fate decisions that are critical for hematopoiesis.

CHAPTER 8

Conclusions and Future Impact

Mechanical forces have long been recognized as being critical for sculpting the early embryo and facilitating tissue and organ functions in the adult organism. In this dissertation, we sought to determine if and how these mechanical forces might also regulate cell fate in models of early development and in adult stem cells. Using a variety of model systems and techniques we demonstrated that mechanical forces can directly modulate conserved cell signaling pathways that are critical regulators of cell fate decisions. We also found that the biophysical properties of the adult stem cell niche influence the signaling pathways that regulate stem cell quiescence and activation. This body of work provides substantial evidence that the cell- and tissue-level forces inherent to both morphogenesis and homeostasis are critical determinants of cell differentiation and tissue development.

MECHANICS IN HUMAN PLURIPOTENT STEM CELLS

Our initial studies, presented in Chapter 2, focused on generating and characterizing an hESC model system for studying human gastrulation. We accomplished this by culturing hESCs on compliant hydrogels that recapitulated the biophysical properties of the early embryo, and demonstrated that such conditions facilitated morphogenesis and cell fate specification reminiscent of gastrulation upon stimulation with BMP4. Specifically, we observed that in colonies of hESCs on compliant substrates, collective cell movements drove the formation and elongation of distinct nodes near the periphery of colonies. Cells that reached and contributed to these nodes expressed markers of EMT, ingressed to form additional cell layers, and expressed key markers indicative of mesoderm specification.

Interestingly, these gastrulation nodes arose in regions of colonies that demonstrated high mechanical tension prior to the induction of differentiation, suggesting that tension may regulate the spatiotemporal patterning of gastrulation and mesoderm specification. This observation motivated us to further refine our system to better understand the relationship between mechanical tension and the gastrulation phenotype, as described in Chapters 3-4.

Due to the consistent appearance of high tension and subsequent gastrulation-like phenotype at the periphery of hESC colonies, we reasoned that colony geometry (and more generally, tissue geometry) dictates the distribution of tension throughout hESC colonies. To test this hypothesis, we developed a method to precisely pattern the geometry of hESCs on compliant hydrogels. After confirming that hESCs were not spontaneously induced to differentiate by our method of geometric patterning, we proceeded to examine the patterns of mechanical tension and mesoderm specification resulting from various geometries. As predicted, we found that geometries with apexes or corners, such as triangles, led to nodes of maximal tension within those apexes (Figure 8.1 A). By contrast, concave curvatures, such as the "mouth" of a Pac-Man geometry, led to reduced mechanical tension. By stimulating hESC colonies patterned in these geometries with BMP4, we confirmed our hypothesis that mechanical tension promotes mesoderm specification. We found that mesoderm specification was induced precisely in the regions of high tension, and was excluded from the regions of lowest tension (Figures 8.1 A & 8.2 B). Mechanical stretching of hESC colonies induced mesoderm specification in the otherwise low-tension central region of colonies, illustrating the causal link between tension and mesoderm specification.

We went on to identify a molecular mechanism responsible for linking mechanical tension to mesoderm specification. We found that high tension, transmitted across adherens junctions, exposed Y654 of junctional β-catenin. Upon BMP4 stimulation, pSFKs mediated the release of junctional β-catenin in cells experiencing high tension via phosphorylation of the exposed Y654. The increase in

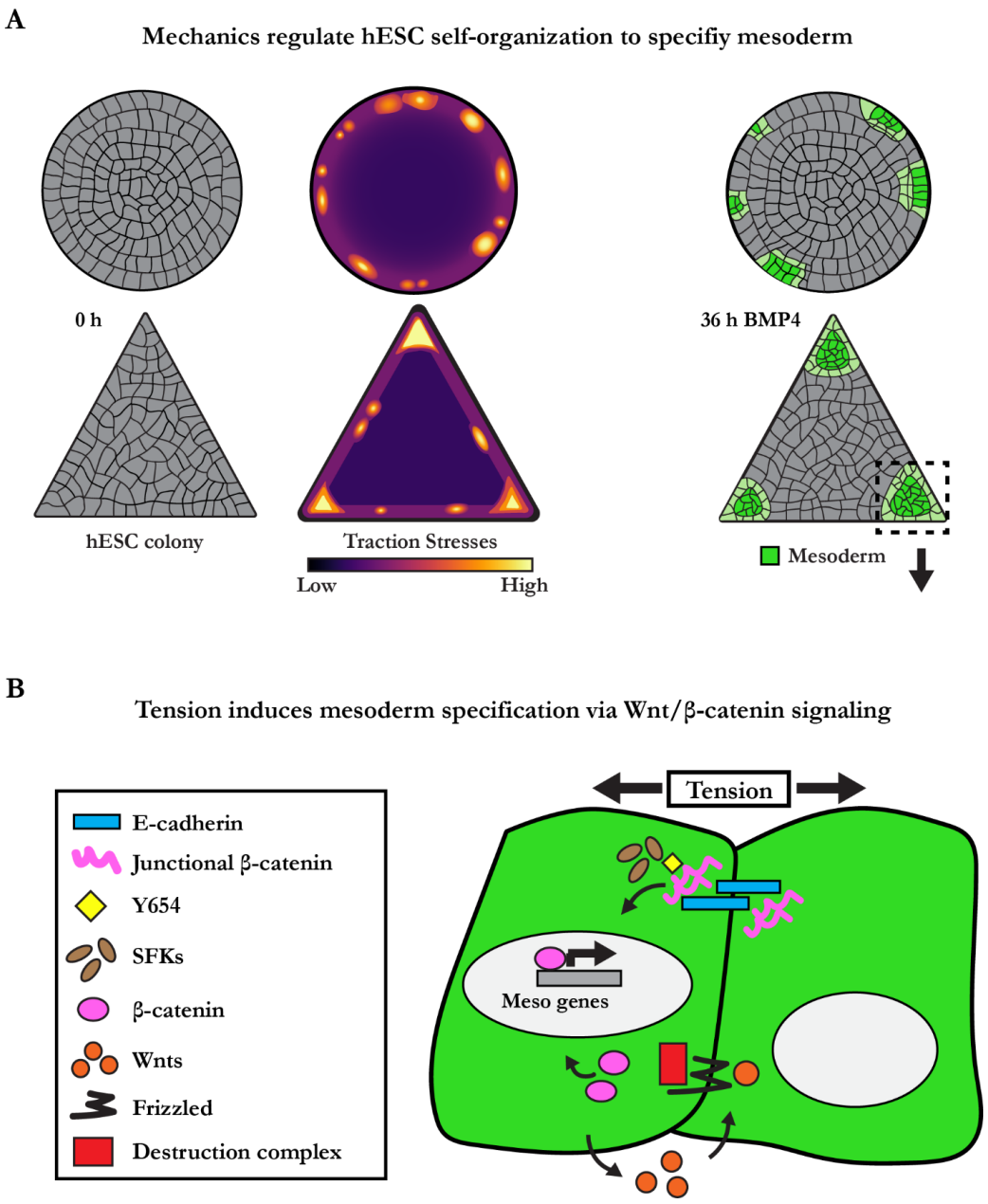

Figure 8.1: Mechanics regulate hESC self-organization and foster tension-mediated mesoderm specification via Wnt/β-catenin signaling.
(A) Cartoon summarizing the findings that hESC colony geometry regulates the spatial patterns of high cell-adhesion tension that direct gastrulation node development and mesoderm specification upon BMP4 stimulation.
(B) Cartoon summarizing the mechanism by which mesoderm specification is induced in regions of high cell-adhesion tension upon BMP4 stimulation due to tension-mediated exposure of β-catenin Y654, and the subsequent phosphorylation and release of junctional β-catenin via pSFKs. Following presumed nuclear translocation of the released junctional β-catenin, mesoderm specification is reinforced by enhanced expression of canonical Wnt ligands within the spatially localized nodes of high cell-adhesion tension.

cytoplasmic β-catenin presumably led to increased nuclear translocation and induction of mesoderm specifying genes. This initial pulse of β-catenin was reinforced by canonical Wnt signaling, which we demonstrated was specifically upregulated in regions of high mechanical tension. Thus, we concluded that tension directly modulates the Wnt/β-catenin pathway to stimulate mesoderm specification (Figure 8.1 B).

Interestingly, in the work presented in Chapter 5, we showed that regulators of cytoskeletal tension and cell adhesions are also capable of modulating tissue pattering in hiPSCs, independent of cell fate specification. Specifically, we showed that CRISPRi KD of CDH1 and ROCK1 led to distinct patterns of cells in mixed colonies of KD and WT cells (Figure 8.2 A). This suggests that tension, contractility, and tissue organization not only modulate cell fate decisions, but can pre-pattern tissue organization prior to differentiation.

Together, these studies illustrate that substrate compliance and mechanical forces are key regulators of pluripotent stem cell behavior, with the capacity to regulate both cell fate and tissue development (Figure 8.2 C). Notably, we demonstrated that mechanics can directly modulate Wnt/β-catenin signaling, a pathway that is highly conserved through evolution and important at multiple stages of development, suggesting that mechanics likely regulate cell fate at various additional stages of development subsequent to gastrulation. These studies also lay the groundwork for a number of future studies that will be necessary to fully understand the role of mechanics in development. Our hESC model system of gastrulation is ideal for high resolution imaging studies and compatible with various sequencing techniques. Utilizing these methodologies would enable precise tracking of cell movements combined with an unbiased analysis of gene expression in this model of early human development, allowing for a detailed examination of the transcriptional programs that drive both the morphogenesis and cell fate decisions associated with gastrulation. Additionally, future studies should examine whether mechanics directly influence BMP signaling. This question is of particular interest

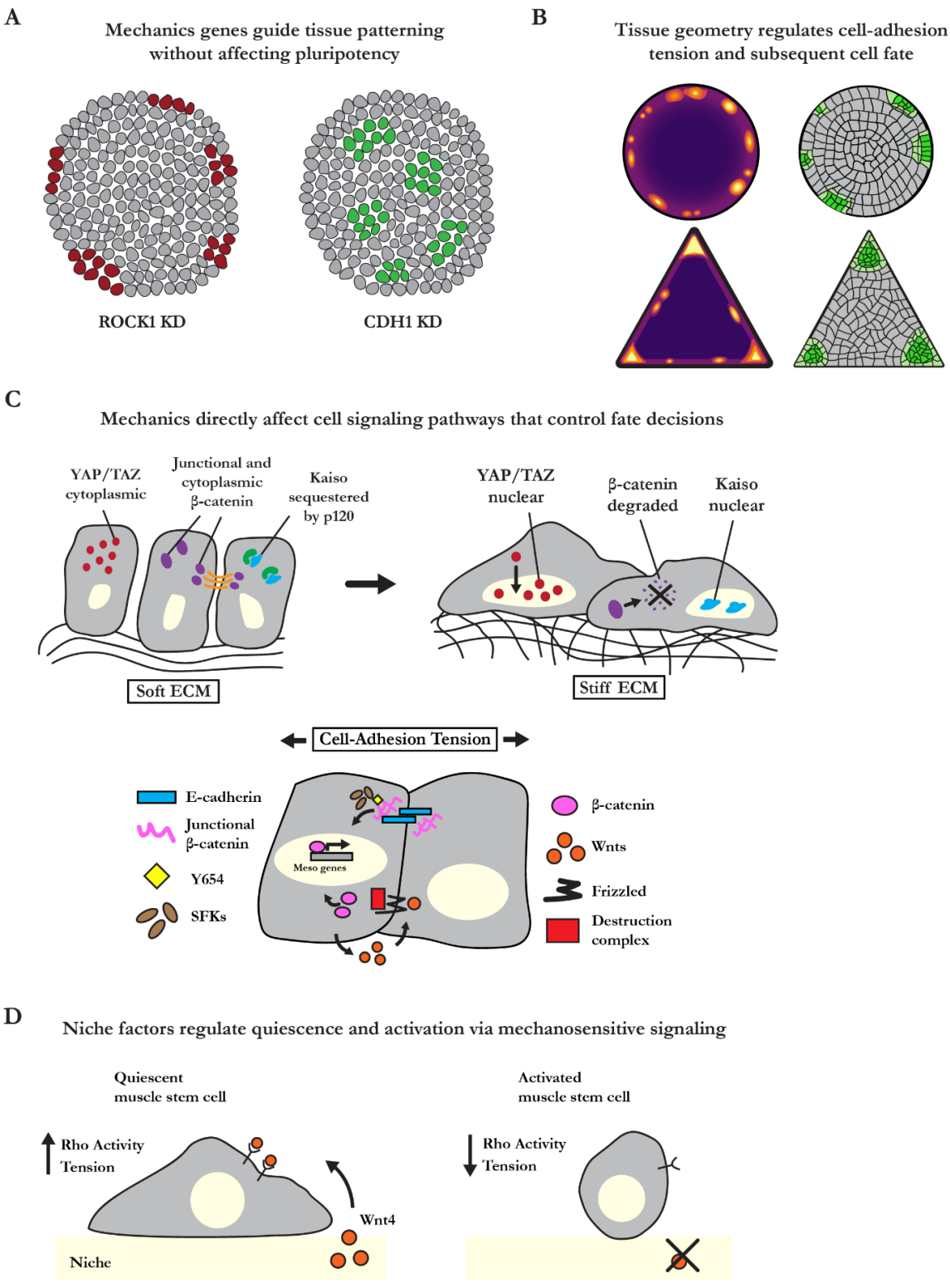

Figure 8.2: Mechanics regulate stem cell differentiation and tissue development.
(A) Carton illustrating the finding that CRISPR-silencing of ROCK1 and CDH1, genes that regulate cell contractility and adherens junctions, led to distinct and consistent (*caption continued on next page*)

(*caption continued from previous page*) patterns of cell-sorting within colonies of iPSCs, without affecting pluripotency. These results suggest that mechanics can regulate tissue organization, independent of cell fate specification.
(B) Cartoon illustrating the finding that altering the tissue geometry of hESC colonies alters the pattern of cell-adhesion tension, which subsequently regulates mesoderm specification. These results suggest that mechanics, and cell-adhesion tension in particular, can regulate the spatial patterning of cell fate specification.
(C) Schematic illustrating the various mechanisms by which mechanics directly modify cell signaling pathways to regulate cell fate specification. Top: ECM stiffness regulates both YAP/TAZ and β-catenin signaling. Bottom: Cell-adhesion tension exposes β-catenin Y654, mediating junctional release of β-catenin that feeds forward to drive Wnt signaling.
(D) Cartoon illustrating the finding that secreted factors from the muscle stem cell niche regulate quiescence and activation by modulating Rho activity and contractility. This result demonstrates that mechanics also regulate the behavior of adult stem cells.

given that BMP4 is the key morphogen responsible for inducing differentiation in our system and BMPs are known to play critical signaling roles at multiple stages of embryonic development. Finally, more complex methodologies are required to characterize the mechanical forces generated as the embryo generates three-dimensional tissues, and to dissect how these forces act in 3D to regulate cell fate. This could be accomplished using deformable or magnetic beads, or by employing FRET sensors, either in our hESC model or in the embryos of model organisms.

In conclusion, our work with human pluripotent stem cell models of early development definitively illustrates that mechanical forces are a key regulator of cell differentiation and tissue development. The findings we present in this dissertation provide both a descriptive and mechanistic understanding of how mechanics regulate early development, and gastrulation in particular. This work should inspire future studies that build upon our discoveries to precisely determine how mechanics are integrated with molecular signaling to drive the transcriptional changes necessary for proper morphogenesis, differentiation, and ultimately, development of a functional organism.

MECHANICS IN ADULT STEM CELLS

In addition to examining the role of mechanics in early development, we also performed studies to understand how the mechanical properties of the adult stem cell niche regulate quiescence/activation and differentiation of adult stem cells. We focused first on the muscle stem cell (SC) niche, utilizing the mouse system to understand the interplay between mechanics and niche-secreted factors in regulating SC behavior. We found that Wnt4, secreted from the SC niche, stimulates Rho signaling and contractility in SCs, which together maintain quiescence (Figure 8.2 D). In the absence of Wnt4, SCs exhibit reduced Rho activity and increased activation in response to injury. Atomic force microscopy confirmed that SCs measured "softer," indicative of reduced contractility, in response to a Wnt4-depleted niche. Furthermore, overexpression of Wnt4 in the niche resulted in a decrease in the number of activated SCs following injury. These findings demonstrate that a niche-derived signal (Wnt4) regulates SC contractility to modulate the depth of quiescence and regenerative capacity of SCs.

We proceeded to examine the role of mechanics in the hematopoietic stem cell niche, the bone marrow. For these studies, we sought to develop a novel method for probing the elasticity of the bone marrow microenvironment. In particular, we aimed to create a workflow that would allow us to differentiate and probe subregions of the hematopoietic niche, specifically the central marrow, perivasculature, and endosteum. We accomplished this by injecting mice with DyLight488-Lectin to label the endothelial cells of the vasculature. By immediately sacrificing mice following injection, dissecting and snap-freezing the femurs, and sectioning through the bone marrow, we were able to perform simultaneous fluorescent imaging and atomic force microscopy on the DyLight488-Lectin-labeled sections. This allowed us to precisely register our elasticity measurements with images of the bone marrow that had clearly identifiable subregions, in order to determine the specific biophysical properties of the central marrow, perivasculature, and endosteum. While we demonstrated the general

feasibility and effectiveness of the workflow, and were able to validate our measurements with fresh bone marrow sections, we had limited success with the DyLight488-Lectin labeling. Due to reliance on its non-specific binding to the vascular endothelium, many of our samples exhibited washed out fluorescent signal once mounted on the atomic force microscope. We are confident that using our workflow with mice that are bred with an endogenous fluorescent reporter to more robustly label the vasculature would enable precise characterization and comparison of the biophysical properties of the central marrow, perivasculature, and endosteum.

These studies illustrate that the mechanical properties of the adult stem cell niche play important roles in regulating stem cell behavior. While a complete characterization of the elasticity of the hematopoietic stem cell niche is still lacking, our results from the muscle stem cell niche indicate that secreted factors and mechanical forces are integrated to regulate stem cell quiescence and activation. Additional studies in this area should be focused on discovering additional means by which mechanics may regulate stem cell behavior. For instance, do mechanical forces only play a role in regulating quiescence/activation? Or, can these same forces also regulate growth, proliferation, and differentiation of these progenitor cells upon activation to modulate the response to injury and the maintenance of homeostasis? This may be especially important in the context of various diseases, such as fibrosis or cardiac hypertrophy, when the mechanical properties of the stem cell niche are clearly altered and the response of adult stem cells fails to restore healthy tissue functioning. In this way, a better understanding of how mechanics influence stem cell behavior may not only inform our fundamental understanding of stem cell biology, but may lead to innovations that vastly improve human health.

CHAPTER 9

Methods

Here I provide a list of key resources and detailed descriptions of the methods used to conduct the experiments presented in this dissertation. Methods are reported in the STAR Methods (Structured, Transparent, Accessible Reporting) format introduced and used by Cell Press journals.

Table 9.1: Key resources for methods utilized throughout dissertation

Reagent or Resource	Source	Identifier
Antibodies		
Goat polyclonal anti-T(brachyury)	R&D Systems	Cat# AF2085; RRID: AB_2200235
Rabbit monoclonal anti-E-cadherin (24E10)	Cell Signaling Technology	Cat# 3195; RRID: AB_2291471
Rabbit monoclonal anti-Slug (C19G7)	Cell Signaling Technology	Cat# 9585; RRID: AB_2239535
Mouse monoclonal anti-Fibronectin (2F12)	Abcam	Cat# ab25583; RRID: AB_470662
Rabbit polyclonal anti-β-catenin-Y654	Sigma	Cat# SAB4300586; RRID: AB_10623284
Rabbit monoclonal anti-β-catenin (D10A8)	Cell Signaling Technology	Cat# 8480; RRID: AB_11127855
Mouse monoclonal anti-β-catenin (M1181)	ECM Biosciences	Cat# CM1181
Rabbit monoclonal anti-phospho-Src Family (Tyr416) (D49G4)	Cell Signaling Technology	Cat# 6943; RRID: AB_10013641
Rabbit polyclonal anti-Oct-3/4 (H-134)	Santa Cruz Biotechnology	Cat# sc-9081; RRID: AB_2167703
Mouse monoclonal anti-ROCK1	Abcam	Cat# ab58305; RRID: AB_945285
Mouse monoclonal anti-E-cadherin (HECD-1)	Abcam	Cat# ab1416; RRID: AB_300946
Goat polyclonal anti-GAPDH	Thermo Fisher Scientific	Cat# PA1-9046; RRID: AB_1074703
Goat polyclonal anti-Oct-3/4 (C-20)	Santa Cruz Biotechnology	Cat# sc-8629; RRID: AB_2167705
Mouse monoclonal anti-EpCAM (mAb 8)	Millipore	Cat# MAB4444; RRID: AB_11213082
Mouse monoclonal anti-Pax7-c	Developmental Studies Hybridoma Bank	Cat# PAX7; RRID: AB_2299243
Rabbit polyclonal anti-MyoD (M-318)	Santa Cruz Biotechnology	Cat# sc-760; RRID: AB_2148870
Rabbit polyclonal ani-Laminin	Abcam	Cat# ab11575; RRID: AB_298179

Reagent or Resource	Source	Identifier
Antibodies		
Rat monoclonal anti-BrdU (Clone BU1/75 ICR1)	Abcam	Cat# ab6326; RRID: AB_305426
Rabbit polyclonal anti-Phospho Myl9 (Thr18, Ser19)	Thermo Fisher Scientific	Cat# PA5-17727; RRID: AB_10980950
Recombinant rabbit monoclonal anti-Phospho FAK (Tyr397) (31H5L17)	Thermo Fisher Scientific	Cat# 700255; RRID: AB_2532307
Rabbit polyclonal anti-Syndecan 4	Abcam	Cat# ab24511; RRID: AB_448112
Mouse monoclonal anti-Embryonic Myosin	Developmental Studies Hybridoma Bank	Cat# F1.652; RRID: AB_528358
DAPI	Invitrogen	Cat# D3571; RRID: AB_2307445
Hoescht stain	Life Technologies	Cat# H3570
Alexa Fluor 488 goat anti-mouse IgG	Abcam	Cat# ab150113; RRID: AB_2576208
Alexa Fluor 568 goat anti-mouse IgG	Abcam	Cat# ab175473
Alexa Fluor 488 goat anti-rabbit IgG	Abcam	Cat# ab150077; RRID: AB_2630356
Alexa Fluor 568 goat anti-rabbit IgG	Abcam	Cat# ab175471; RRID: AB_2576207
Alexa Fluor 488 donkey anti-goat IgG	Abcam	Cat# ab150129; RRID: AB_2687506
Anti-glutathione S-transferase, Alexa Fluor 488 conjugate	Invitrogen	Cat# A11131; RRID: AB_2534137
CD31 Antibody, PE-Cy7 Conjugated (MEC 13.3)	BD Biosciences	Cat# 553373; RRID: AB_394819
CD45 Antibody, PE-Cy7 Conjugated (Clone 30-F11)	BD Biosciences	Cat# 552848; RRID: AB_394489
Sca1 (Ly-6A/E) Antibody, APC-Cy7 Conjugated (Clone D7)	BD Biosciences	Cat# 560654; RRID: AB_1727552
VCAM-1 Antibody, PE Conjugated (M/K-2)	Thermo Fisher Scientific	Cat# RMCD10604; RRID: AB_2556576
α7 integrin, APC Conjugated	AbLab	Cat# 67-0010-05

Reagent or Resource	Source	Identifier
Antibodies		
DyLight488 Labeled Lycopersicon Esculentum Lectin	Vector Laboratories	Cat# DL-1174 RRID: AB_2336404
Bacterial and Virus Strains		
pX330-U6-Chimeric_BB-CBh-hSpCas9	Laboratory of Feng Zhang	Addgene plasmid# 42230; RRID: Addgene_42230
pBluescript II KS+	Stratagene	N/A
pLKO.1 neo	Laboratory of Sheila Stewart	Addgene plasmid# 13425; RRID: Addgene_13425
pMD2.G envelope vector	Laboratory of Didier Trono	Addgene plasmid# 12259; RRID: Addgene_12259
psPAX2 packaging vector	Laboratory of Didier Trono	Addgene plasmid# 12260; RRID: Addgene_12260
Chemicals, Peptides, and Recombinant Proteins		
2-Hydroxy-4'-(2-hydroxyethoxy)-2-methylpropiophenone (Irgacure D-2959)	Sigma	Cat# 410896; CAS: 106797-53-9
2% bis-acrylamide solution	BioRad	Cat# 1610142
40% acrylamide solution	BioRad	Cat# 1610140
5-Bromo-2'-deoxyuridine	Sigma	Cat# B5002
5-Ethynyl-2'-deoxyuridine	Carbosynth	Cat# NE08701
Barium chloride	Sigma	Cat# 202738
cOmplete, Mini Protease Inhibitor Cocktail	Roche	Cat# 11836153001
Cultrex Basement Membrane Extract, Type 2, Pathclear (rBM; Matrigel equivalent)	R&D Systems	Cat# 3532-005-02
Cultrex Human Vitronectin, Pathclear	Trevigen	Cat# 3421-001-01
Denhardt's solution, 50x	Sigma	Cat# D2532
Dextran sulfate, avg M_w >500,000	Sigma	Cat# D8906; CAS: 9011-18-1
Diethyl pyrocarbonate (DEPC)	Sigma	Cat# D5758; CAS: 1609-47-8
Di(trimethylolpropane) tetraacrylate	Sigma	Cat# 408360; CAS: 94108-97-1
Doxycycline	Sigma	Cat# D9891
Essential 8 (E8) medium	Gibco	Cat# A1517001
Formamide	Sigma	Cat# 11814320001; CAS: 75-12-7
G-418	Sigma	Cat# 4727878001; CAS: 108321-42-2

Reagent or Resource	Source	Identifier
Chemicals, Peptides, and Recombinant Proteins		
Glutaraldehyde, 70% aqueous	Electron Microscopy Sciences	Cat# 16350
Heparin sodium salt from porcine intestinal mucosa	Sigma	Cat# H3393; CAS: 9041-08-1
Isopropyl-β-D-thiogalactoside (IPTG)	Sigma	Cat# 10724815001; CAS: 367-93-1
IWP-2 (Wnt processing and secretion inhibitor)	MedChem Express	Cat# HY-13912; CAS: 686770-61-6
Knockout DMEM	Gibco	Cat# 10829018
Knockout Serum Replacement	Gibco	Cat# 10828028
M-MLV Reverse Transcriptase	BioChain	Cat# Z5040002
mTeSR1 medium	STEMCELL Technologies	Cat# 85850
Norland Optical Adhesive 74 (NOA-74)	Norland Products, Inc.	Cat# NOA74
N-succinimidyl acrylamidohexanoic acid (N6)	Lakins et al., 2012	N/A
Polydimethylsiloxane (PDMS), SYLGARD™ 184 Silicone Elastomer Kit	Dow	Cat# 4019862
Polyethylenimine, branched (PEI)	Sigma	Cat# 408719; CAS: 25987-06-8
Potassium persulfate	Sigma	Cat# 216224; CAS: 7727-21-1
PP1 (Src inhibitor)	Sigma	Cat# 567809; CAS: 172889-26-8
Rapamycin	LC Laboratories	Cat# R-5000
Recombinant human FGF-basic (bFGF, 154 a.a.)	PeproTech	Cat# 100-18B
Recombinant human BMP-4	PeproTech	Cat# 120-05ET
Rho activator II	Cytoskeleton, Inc.	Cat# CN03-A
Rho inhibitor I	Cytoskeleton, Inc.	Cat# CT04-A
Rhotekin-RBD protein	Cytoskeleton, Inc.	Cat# RT01-A
Ribonucleoside vanadyl complexes	Sigma	Cat# R3380
Streptavidin, Alexa Fluor 555 conjugate	Thermo Fisher Scientific	Cat# S21381
SU-8 3050 negative photoresist	Kayaku Advanced Materials, Inc.	Cat# SU-8 3000
Tamoxifen	Sigma	Cat# T5648
TEMED (N,N,N',N'-tetramethylethylenediamine)	BioRad	Cat# 161-0800
Tth DNA Polymerase	Sigma	Cat# 11480022001
Vent DNA Polymerase	New England BioLabs, Inc.	Cat# M0254S
Y-27632 dihydrochloride (ROCK inhibitor)	Tocris	Cat# 1254
Click-iT EdU Cell Proliferation Kit for Imaging, Alexa Fluor 594 dye	Invitrogen	Cat# C10339

Reagent or Resource	Source	Identifier
Critical Commercial Assays		
Fast SYBR Green Master Mix	Thermo Fisher Scientific	Cat# 4385612
iScript cDNA Synthesis Kit	BioRad	Cat# 1708891
PerfeCTa SYBR Green FastMix	Quantabio	Cat# 95072-05K
Pierce BCA Protein Assay Kit	Thermo Fisher Scientific	Cat# 23250
Platinum SYBR Green qPCR SuperMix-UDG w/ROX	Thermo Fisher Scientific	Cat# 11744500
RNeasy Mini Kit	QIAGEN	Cat# 74106
Superscript First Strand Synthesis System for RT-PCR	Invitrogen	Cat# 11904018
Surveyor Assay	Transgenomics	Cat# 706020
TRIzol	Invitrogen	Cat# 15596-018
Experimental Models: Cell Lines		
Human: H9 ES cell line	Laboratory of Susan Fisher	N/A
Human: H2B-mCherry H9 cell line	Muncie et al., 2020	N/A
Human: shE-cadherin H9 cell line	Muncie et al., 2020	N/A
Human: T-mNeonGreen H9 cell line	Muncie et al., 2020	N/A
Human: Human embryonic kidney (HEK) 293T cell line	Laboratory of Warren Pear	N/A
Mouse: Mouse embryonic fibroblasts (MEFs), derived from CF-1 mice	Laboratory of Susan Fisher	N/A
Human: CRISPRi no guide hiPSC	Mandegar et al., 2016	N/A
Human: CRISPRi control guide hiPSC	Mandegar et al., 2016	N/A
Human: CRISPRi ROCK1 hiPSC	Mandegar et al., 2016	N/A
Human: CRISPRi CDH1 hiPSC	Libby, A.R.G. et al. 2018	N/A
Human: WT-GFP hiPSC	Libby, A.R.G. et al. 2018	N/A
Experimental Models: Organsims/Strains		
Mouse C57BL/6J	Jackson Laboratories	Cat# 000664; RRID: IMSR_JAX:000664
Mouse C57BL/6-CD45.2	Laboratory of Emmanuelle Passegue	N/A
Mouse Human Skeletal Actin^{CreMER}	McCarthy et al., 2012	N/A
Mouse Pax7^{CreER}	Nishijo et al., 2009	N/A
Mouse Wnt4$^{flox/flox}$	Kobayashi et al., 2011	N/A
Mouse Wnt4$^{OX/+}$	(H. H. Lee & Behringer, 2007)	N/A
Mouse RhoA$^{flox/+}$	Jackson et al., 2011	N/A

Reagent or Resource	Source	Identifier
Oligonucleotides		
Guide RNA for Cas9 targeting to T(brachyury) gene: 5' -GCCTTGCTGCTTCACATGGA - 3'	Muncie et al., 2020	N/A
Guide RNA for CDH1 CRISPRi: 5' – GCAGTTCCGACGCCACTGAG – 3'	Libby, A.R.G., et al. 2018	N/A
Guide RNA for ROCK1 CRISPRi: 5' – CGGGGCGCGGACGCTCGGAA – 3'	Mandegar et al., 2016	N/A
Off-target guide RNA (KCNH2) for CRISPRi control: 5' – TTCTGGGCGCGCGAGTCCCA – 3'	Mandegar et al., 2016	N/A
Short hairpin for shE-cadherin knockdown: 5' - GAACGAGGCTAACGTCGTAAT - 3'	Laralynne Przybyla et al., 2016c	N/A
qPCR primers: See Table 9.2	Integrated DNA Technologies	N/A
Random Hexamers	Applied Biosystems	Cat# N8080127
Split initiator hybridization probes: See Table 9.3	Integrated DNA Technologies	N/A
Software and Algorithms		
CellProfiler	McQuin et al., 2018	https://cellprofiler.org
Elveflow Smart Interface Software	Elveflow	https://www.elveflow.com/microfluidic-products
FIJI	Schindelin et al., 2012	https://imagej.net/Fiji
FTTC plugin for FIJI	Tseng et al., 2012	https://sites.google.com/site/qingzongtseng/tfm
ilastik	Berg et al., 2019	https://www.ilastik.org
Imaris	Oxford Instruments	https://imaris.oxinst.com
Jython	Jython	https://www.jython.org
MATLAB	MathWorks	https://www.mathworks.com/products/matlab.html
Perceptually uniform colormap functions for MATLAB	Biguri, A. 2020. MATLAB Central File Exchange	https://www.mathworks.com/matlabcentral/fileexchange/51986-perceptually-uniform-colormaps

Reagent or Resource	Source	Identifier
Software and Algorithms		
PIV plugin for FIJI	Tseng et al., 2012	https://sites.google.com/site/qingzongtseng/piv
Prism 6	GraphPad	https://www.graphpad.com/scientific-software/prism/
Python	Python	https://www.python.org/
Traction Force Microscopy analysis and visualization scripts	Muncie et al., 2020	https://github.com/jmmuncie/TF_hESC
Other		
FluoSpheres™ carboxylate-modified microspheres, 1.0 μm, red fluorescent (580/605), 2% solids	Invitrogen	Cat# F8821
Mask aligner (for photolithography)	Karl Suss America, Inc.	Cat# MJB3
Photomask	Muncie et al., 2019	CAD design upon request.
Silicon wafer	Electron Microscopy Sciences	Cat# 71893-06

RESOURCE AVAILABILITY

Lead Contact

Further information and requests for resources and reagents should be directed to and will be fulfilled by Valerie M. Weaver (valerie.weaver@ucsf.edu).

Materials Availability

Modified plasmids and CAD drawings for 3D-printed parts can be made available upon request.

Data and Code Availability

The code generated during these studies for analysis and visualization of traction force microscopy data is publicly available on GitHub: https://github.com/jmmuncie/TF_hESC.

EXPERIMENTAL MODELS AND SUBJECT DETAILS

Cell Lines

Human embryonic stem cells (parental line H9, female) were obtained as a gift from the Laboratory of Susan Fisher at UCSF and maintained in a humidified incubator at 37 °C with 5% CO2. T-mNeonGreen, H2B-mCherry, and shE-cadherin lines were all generated from H9s, as detailed in the subsequent sections of the Method Details.

T-mNeonGreen reporter cells were maintained on γ-irradiated primary mouse embryonic fibroblasts (PMEFs) in KSR media consisting of knockout-DMEM (Gibco) with 20% knockout serum replacement (Gibco), 2 mM L-glutamine (Gibco), 1 mM non-essential amino acids (Gibco), 1× antibiotic-antimycotic (Gibco), 100 μM β-mercaptoethanol, supplemented with 10 ng/ml bFGF (PeproTech), and passaged with collagenase type IV (Gibco) at 1 mg/ml in knockout-DMEM (Gibco). PMEFs, derived from CF-1 mice, were obtained as a gift from the Laboratory of Susan Fisher at UCSF and were cultured in a humidified hypoxic incubator at 37 °C with 5% O2 and 5% CO2 on tissue culture plastic coated with 0.1% gelatin (Sigma) and in media consisting of DMEM, high glucose, with L-glutamine and sodium pyruvate (GenClone) supplemented with 10% fetal bovine serum (HyClone), 4 mM L-glutamine (Gibco), 1× antibiotic-antimycotic (Gibco), 10 ng/ml insulin (Roche), 20 ng/ml transferrin (Sigma), and 30 nM sodium selenite (VWR). PMEFs were γ-irradiated with a total dose of 40 Gy to induce mitotic arrest and frozen aliquots were stored in liquid nitrogen prior to being thawed and plated onto tissue culture plastic coated with 0.1% gelatin (Sigma) for passaging of T-mNeonGreen reporter cells.

H9, H2B-mCherry, and shE-cadherin lines were maintained in feeder-free conditions on tissue culture plastic coated with reconstituted basement membrane extract (rBM; Matrigel equivalent; R&D Systems) in media consisting of 50% PMEF-conditioned KSR media and 50% complete Essential 8 media (E8; Gibco), supplemented with 10 ng/ml bFGF (PeproTech). PMEF-conditioned KSR media

was generated by plating γ-irradiated PMEFs on tissue culture plastic coated with 0.1% gelatin (Sigma), feeding with KSR media supplemented with 4 ng/ml bFGF (PeproTech), and collecting and replacing the media every 24 h for 10-14 days. Cells in feeder-free conditions were passaged with 0.5 mM EDTA (Fisher) in PBS and plated into media supplemented with 10 μM Y-27632 (ROCK inhibitor; Tocris) to promote survival. After 24 h, media was replaced with media lacking Y-27632.

The human embryonic kidney (HEK) 293T cell line, obtained as a gift from the Laboratory of Warren Pear at UPenn, was used for transfection and production of lentivirus, and was maintained in a humidified incubator at 37 °C with 5% CO2. HEK 293T cells were cultured in DMEM, high glucose, with L-glutamine and sodium pyruvate (GenClone) supplemented with 10% fetal bovine serum (HyClone), 4 mM L-glutamine (Gibco), and 1× antibiotic-antimycotic (Gibco), and upon reaching 75% confluency, were passaged with 0.05% trypsin-EDTA (Gibco).

Human iPSC lines were derived from the WTC 11 line (Coriell) where the species of origin was confirmed by a LINE assay. After genetic manipulation, all cell lines were karyotyped by Cell Line Genetics and were deemed karyotypically normal before proceeding with experiments. Human iPSC lines were cultured in feeder-free media conditions on growth factor-reduced Matrigel (Corning Life Sciences) and fed daily with mTeSR™-1 medium (STEMCELL Technologies). Accutase (STEMCELL Technologies) was used to dissociate hiPSCs to single cells during passaging. Cells were passaged at a seeding density of 12,000 cells per cm^2 and 10 μM Y-27632 (ROCK inhibitor; Tocris) was added to the media upon passaging to promote survival.

All cell lines were routinely tested and confirmed to be negative for mycoplasma contamination. All experiments involving hESCs and hiPSCs were approved by the University of California San Francisco Human Gamete, Embryo and Stem Cell Research Committee (UCSF GESCR).

Animals

Mice were housed and maintained in accordance with the guidelines of the Laboratory Animal Research Center (LARC) of University of California, San Francisco. Previously published HSA^{CreMER} (McCarthy et al., 2012), $Wnt4^{flox/flox}$ (Kobayashi et al., 2011), $Wnt4^{OX/+}$ (H. H. Lee & Behringer, 2007), $Pax7^{CreER}$ (Nishijo et al., 2009), and $RhoA^{flox/+}$ (Jackson et al., 2011) were used in the work presented in Chapter 6. C57BL/6 mice were obtained from Jackson Laboratory. All mice used for experiments in Chapter 6 were adults, between 12-16 weeks of age. Wildtype C57BL/6-CD45.2 mice used in Chapter 7 were obtained from the Passegue Lab and were adults, between 8-12 weeks of age. The control and experimental mice used were littermates in all experiments. Approximately equal numbers of male and female mice were used in all experiments. Animals were genotyped by PCR using tail DNA. Primer sequences are available upon request.

METHOD DETAILS

Generation of T-mNeonGreen Reporter

H9 hESCs expressing a C-terminal fusion of the T-box transcription factor T (TBXT) gene [T(brachyury)] with the mNeonGreen fluorophore were prepared by CRISPR-Cas9 facilitated homology-directed repair (HDR). Guide RNAs (gRNAs) directing CRISPR-Cas9 double stranded cleavage near the end of the coding sequence of the human TBXT gene were cloned into a modified derivative of pX330-U6-Chimeric_BB-CBh-hSpCas9 (Addgene; modification: Lakins et al., in preparation) and screened for activity using the Surveyor Assay (Transgenomics) following transient transfection in HEK 293T cells. The gRNA with target sequence 5' - GCCTTGCTGCTTCACATGGA - 3' demonstrated the best activity and was cloned into a second modified version of pX330 for use in H9 cells, which we call SpCas9 U6 gRNA (Lakins et al., in preparation). Briefly, this derivative features gRNA under control of the U6 promoter as in pX330, a T2A polyprotein of SpCas9 and the human RAD51 gene under transcriptional control of the tetracycline-regulated TetO heptamerized minimal CMV promoter, an expression cassette for the advanced reverse tetracycline transcriptional transactivator rtTAs-M22 (Urlinger et al., 2000), and the origin of replication from Epstein-Barr virus (OriP). For the targeting construct, approximately 1,000 base pairs upstream and downstream of the CRISPR-Cas9 cleavage site/TBXT gene stop codon was prepared by Long Range PCR using a Vent-Tth Polymerase mix (Sigma; New England BioLabs; Cheng et al., 1994) and cloned into pBluescript II KS+ (Stratagene) modified by the addition of OriP. This targeting construct was further modified by silent mutation of the gRNA targeting sequence, removal of the natural TBXT gene stop codon, and insertion of a 22 amino acid glycine/serine/alanine rich flexible linker N-terminal to mNeonGreen in frame with the TBXT gene coding sequence. Following mNeonGreen, the construct included a Floxed expression cassette containing an mCherry

fluorophore for assessing transfection efficiency and the puromycin resistance gene for selection of stably transfected cells.

H9 cells were co-transfected via electroporation with the described targeting construct, the SpCas9 U6 gRNA, and an in vitro transcribed capped, polyadenylated mRNA for the Epstein-Barr virus nuclear antigen 1 (EBNA-1) lacking the GA rich domain (Howden et al., 2006; targeting construct and SpCas9 U6 gRNA: Lakins et al., in preparation). Transfected H9s were re-plated on rBM-coated dishes in the presence of 10 μM Y-27632 (Tocris) to promote survival and 1 μg/ml of Doxycycline to induce the targeted CRISPR-Cas9 double-stranded break and subsequent homology-directed repair. Doxycycline was removed after 24 h and cells were allowed to recover an additional 24 h before selection with 0.25 μg/ml of puromycin. Following selection, individual surviving colonies were mechanically passaged into separate wells, expanded, and then screened for gene targeting via Long Range PCR of genomic DNA using one primer anchored in mNeonGreen and a second in the TBXT gene upstream of the end of the 5' homology arm. Positive clones were expanded and subsequently transiently transfected with a plasmid expressing an EGFP-Cre fusion to remove the puromycin selection cassette. Transfected cells were FACS-sorted for EGFP expression 24 h later, re-plated in rBM-coated dishes in the presence of 10 μM Y-27632, and following outgrowth of individual colonies, mechanically passaged into separate wells and screened by PCR for loss of the expression cassette. These cells were then characterized for expression of nuclear mNeonGreen expression following BMP4 differentiation, and verified by the concordance of mNeonGreen expression and detection of T(brachyury) by immunostaining.

Generation of H2B-mCherry

To generate the hESC line with fluorescent H2B-mCherry-labelled nuclei, an N-terminal fusion of human histone H2B to mCherry, under control of the human phosphoglycerate kinase promoter, was cloned into a transfer vector for transfection into HEK 293T cells, along with packaging and envelope

vectors for self-inactivating transgenic lentivirus production, and subsequent transduction into H9s. Twenty-four hours prior to transfection, HEK 293T's were plated at a density of 0.8 x 106 cells into a 35 mm tissue culture plastic dish. The next day, HEK 293T's were washed once with PBS very gently to remove serum, and media was replaced with Opti-MEM (Gibco). To begin transfection, 1 μg of total DNA consisting of 0.33 μg psPAX2 packaging vector (Addgene), 0.16 μg pMD2.G envelope vector (Addgene), and 0.55 μg H2B-mCherry transfer vector was mixed with Opti-MEM media to a total volume of 100 μL and incubated for 5 min at room temperature. Simultaneously, 3 μg of polyethylenimine (PEI; Sigma) was mixed with 100 μL Opti-MEM media and incubated for 5 min at room temperature. Following incubation, these two solutions were combined and incubated an additional 15 min at room temperature before being added to HEK 293T's. Six hours following transfection, media was replaced for normal HEK 293T growth media. Forty-eight hours post-transfection, viral supernatant was collected, cell debris was removed with 2x 5 min centrifugation at 500 x g, carefully collecting supernatant and discarding pellets each time, and polybrene (Sigma) was added to the final supernatant at 4 μg/ml. H9s plated on rBM-coated tissue culture plastic were immediately transduced by mixing viral supernatant 1:4 with E8 media (Gibco) supplemented with 10 ng/ml bFGF (PeproTech) and culturing cells in this media for 24 h, after which the media was replaced with fresh media and cultured for an additional 48 h. A pure population of cells expressing H2B-mCherry-labelled nuclei was obtained in two steps: first by enrichment via several rounds of mechanically picking morphologically undifferentiated colonies containing mCherry-positive cells and passaging as colony fragments onto γ-irradiated PMEFs, and then subsequently by FACS to purify. Single cells isolated by FACS were plated onto rBM-coated tissue culture plastic in E8 media (Gibco) supplemented with 10 ng/ml bFGF (PeproTech) and 10 μM Y27632 (Tocris) to promote survival. Fresh media was added every 24 h and Y27632 was reduced to 5 μM, 2.5 μM, and 0 μM on successive days, after which self-supporting undifferentiated colonies were obtained.

Generation of shE-cadherin

We utilized the same inducible shE-cadherin hESC line from our previous work (Laralynne Przybyla et al., 2016c). To generate the hESC line with inducible short hairpin RNA (shRNA) knockdown of E-cadherin, candidate shRNA hairpins were cloned into a transfer vector for transfection into HEK 293T cells along with packaging and envelope vectors for transgenic lentivirus production and subsequent transduction into H9s. The transfer vector consisted of a modified pLKO.1 neo plasmid (Addgene) with expression of the shRNA sequences under control of 3x copies of the lac operator, and contained a copy of the mNeonGreen fluorophore to assess transfection efficiency. The successful E-cadherin shRNA had the following sequence: 5' - GAACGAGGCTAACGTCGTAAT - 3'. Transgenic lentivirus was produced in HEK 293T's as described in the preceding section for generation of the H2B-mCherry line. H9s plated on rBM-coated tissue culture plastic were immediately transduced by mixing viral supernatant 1:4 with E8 media (Gibco) supplemented with 10 ng/ml bFGF (PeproTech) and culturing cells in this media for 24 h, after which the media was replaced with fresh media and cultured for an additional 24 h, prior to selection with 200 μg/ml G-418 (Sigma). shE-cadherin cells were maintained with 200 μg/ml G-418 prior to seeding for experiments to prevent loss of inducible E-cadherin knockdown. E-cadherin knockdown was induced with 200 μM isopropyl-β-D-thiogalactoside (IPTG; Sigma).

Generation of CRISPRi hiPSCs

The generation of the ROCK1 CRISPRi line was previously created and described by Mandegar et al., 2016. For the generation of the CDH1 CRISPRi lines, five CRISPRi gRNAs were designed to bind within 150 bp of the TSS of CDH1 and cloned into the gRNA-CKB vector using BsmBI ligation following the previously described protocol (Mandegar et al., 2016). gRNA expression vectors were nucleofected into the CRISPRi-Gen1C human hiPSC line from the Conklin Lab using the Human Stem Cell Nucleofector Kit 1 solution with the Amaxa nucleofector 2b device (Lonza). Nucleofected

cells were seeded into three wells of a 6-well plate (~7400 cell/cm^2) in mTeSR™-1 media with Y-27632 (10 μM; Tocris) for 2 days, and treated with blasticidin (10 μg/ml; ThermoFisher Scientific) for a selection period of 7 days. Surviving colonies were pooled and passaged in mTeSR™-1 with blasticidin and Y-27632 for a single day then transitioned to mTeSR™-1 media only. Once stable polyclonal populations of CDH1 CRISPRi hiPSCs for each of the five guides were established, the cells were incubated with doxycycline (2 μM) for 96 hr. KD efficiency was evaluated by mRNA collection and subsequent qPCR, comparing levels of transcript with a time-matched control of the same line without CRISPRi induction. The CRISPRi CDH1 cell line with the guide consisting of the sequence 5' – GCAGTTCCGACGCCACTGAG – 3' produced the best KD and was selected for use in all experiments presented here.

Generation of WT-GFP hiPSCs

To generate the WT-GFP hiPSC line, 2 million WTC clone11 hiPSCs were nucleofected as previously described with the knock-in plasmid containing a CAG promoter-driven EGFP and AAVS1 TALEN pair vectors. After cell recovery, puromycin (0.5 μg/ml) was added to the media for a selection period of 7 days. Individual stable EGFP-expressing colonies were picked using an EVOS FL microscope (Life Technologies) and transferred to individual wells of a 24-well plate in mTeSR media with Y-27632 (10 μM) and subsequently expanded into larger vessels.

Formation of Mixed hiPSC Colonies

Cell aggregates of ~100 cells were created using 400 × 400 μm PDMS microwell inserts in 24-well plates (~975 microwell per well) similar to previously published protocols (Hookway et al., 2016; Ungrin et al., 2008). Dissociated hiPSC cultures were resuspended in mTeSR™-1 supplemented with Y-27632 (10 μM), mixed at proper ratios and concentration (100 cells/well), added to microwells, and centrifuged (200 rcf). After 18 h of formation, 100 cell aggregates were transferred in mTeSR™-1 to Matrigel-coated 96-well plates (~15 aggregates/cm^2) and allowed to spread into 2D colonies.

Atomic Force Microscopy

All AFM indentations were performed using an MFP3D-BIO inverted optical atomic force microscope (Asylum Research) mounted on a Nikon TE2000-U inverted fluorescent microscope. Silicon nitride cantilevers were used with spring constants ranging from 0.04 to 0.07 N/m and borosilicate glass spherical tips 5 μm in diameter (Novascan Tech). Each cantilever was calibrated using the thermal oscillation method prior to each experiment. Samples were indented at rates ranging from 0.75 to 1.25 μm/s loading rate, with a maximum force of 4.5 nN. The Hertz model was applied to the force curves obtained from each indentation to calculate the elastic modulus (Young's modulus, stiffness). All samples were assumed to be incompressible; therefore, a Poisson's ratio of 0.5 was used in the calculation of the elastic modulus.

For AFM measurements of chicken embryos (Chapter 2), embryos were dissected from fertilized chicken eggs (Petaluma Farms) and cultured on top of filter paper to maintain tension across the blastoderm and vitelline membranes (Chapman et al., 2001) until Hamburger and Hamilton (HH) stage 3+ to 4, when the primitive streak is fully formed and mesodermal cells are actively ingressing (Hamburger & Hamilton, 1992; Voiculescu et al., 2014). Gastrulation-stage embryos were then mounted onto glass slides and placed on the stage of the AFM for indentation. The FMAP function of the IGOR PRO build supplied by Asylum Research was used to automatically perform indentations in a 4 x 4 raster pattern every five microns for a total of 16 data points per area of interest measured.

For AFM measurements of CRISPRi hiPSCs (Chapter 5), hiPSC colonies were cultured on glass slides and placed on the stage of the AFM for indentation. The FMAP function of the IGOR PRO build supplied by Asylum Research was used to automatically perform indentations in a 6 x 6 raster pattern every five microns for a total of 36 data points per area of interest measured. Two 30 μm by 30 μm areas of interest were probed for each sample.

For AFM measurements of SCs (Chapter 6), SCs were isolated from mice, sorted by FACS (as described in a subsequent section of method details), and seeded onto chamber slides. SCs were allowed to recover for 2 h in a humidified incubator at 37 °C with 5% CO_2 with or without treatment with Rho inhibitor (1 μg/ml; C3 Transferase; Cytoskeleton, Inc). Chamber slides were then placed on the stage of the AFM for indentation. The FMAP function of the IGOR PRO build supplied by Asylum Research was used to automatically perform indentations in a 2 x 2 raster pattern every five microns per single isolated SC. Due to the small size of isolated SCs in culture (typically < 10 μm diameter), only a single force curve from the 2 x 2 raster corresponded to indentation of the isolated cell, with the remaining indentations corresponding to the glass slide and easily identifiable by elasticity values > 10 kPa. For each FMAP, the single force curve corresponding to the isolated SC was selected and used for analysis. At least ten cells per condition were measured per experimental replicate.

For AFM measurements of bone marrow (Chapter 7), wildtype C57BL/6-CD45.2 mice were injected with 100 μL of 1:2 DyLight488 Labeled Lycopersicon Esculentum Lectin (Vector Laboratories):PBS 15 min prior to euthanizing. Femurs were harvested, snap-frozen in OCT (Tissue-Tek) and stored at -80°C until sectioning. Frozen samples were cryosectioned (10 μm) using a Cryostat equipped with a tungsten blade onto CryoJane adhesive tape windows (Leica Microsystems). Tape windows were then mounted section-side-up onto a standard microscopy slide and kept on dry ice until use. Samples were not exposed to UV light, as sections were not transferred off the tape windows. Samples were rapidly thawed and imaged for brightfield and immunofluorescence before being immersed in PBS with protease inhibitors (Roche, cOmplete Mini Protease Inhibitor Cocktail) for the duration of the AFM measurements. Freshly isolated, non-frozen femurs were sectioned along the transverse plane using a low speed bone saw (Buehler) and a diamond wafering bone blade (Buehler). Sectioned femur discs were kept in ice-cold PBS with protease inhibitors, and AFM measurements were performed within 1 h of femur isolation.

Fabrication of Non-patterned Hydrogels

Polyacrylamide hydrogels were fabricated as described previously (Lakins et al., 2012; L. Przybyla et al., 2016b). First, #1 18 mm glass coverslips (Electron Microscopy Sciences) were modified with glutaraldehyde to promote attachment of polyacrylamide during polymerization. Coverslips were submerged in 0.2 M HCl (Fisher) overnight with gentle shaking, washed with ultrapure water, submerged in 0.1 M NaOH (Fisher) for 1 h with gentle shaking, washed with ultrapure water, submerged in a 1:200 dilution of 3-aminopropyltrimethoxysilane (Acros Organics) in ultrapure water for 1 h with gentle shaking, washed with ultrapure water, and finally submerged in a 1:140 dilution of 70% glutaraldehyde (Electron Microscopy Sciences) in PBS for 1 h with gentle shaking, washed with ultrapure water, and dried. Polyacrylamide solutions yielding the desired elastic moduli (E) were prepared and pipetted onto glutaraldehyde-modified coverslips with custom-made plastic spacers of approximately 100-200 μm thickness. For hydrogels of E = 400 Pa, the polyacrylamide solution consisted of 3% acrylamide (Bio-Rad), 0.05% Bis-acrylamide (Bio-Rad), 1x PBS, 1% TEMED (Bio-Rad) and 1% potassium persulfate (Sigma). For hydrogels of E = 2,700 Pa, the polyacrylamide solution consisted of 7.5% acrylamide (Bio-Rad), 0.035% Bis-acrylamide (Bio-Rad), 1x PBS, 1% TEMED (Bio-Rad) and 1% potassium persulfate (Sigma). A Rain-X-coated (Rain-X) coverslip was placed atop each glutaraldehyde-modified coverslip with polyacrylamide solution to form a polyacrylamide "sandwich", and these were incubated for 1 h at room temperature to allow polymerization. The Rain-X coverslips and plastic spacers were then removed and the glutaraldehyde-modified coverslips with attached polyacrylamide gels were placed into custom 3D-printed holders (CAD drawings available upon request) with rubber gaskets to form sealed wells with the polyacrylamide hydrogels at the bottom of each well.

Next, the surfaces of the polyacrylamide gels were functionalized with N-succinimidyl acrylamidohexanoic acid (N6), which was synthesized in the lab as previously described (Lakins et al.,

2012), to enable ECM ligands to bind to the surface and promote cell attachment. A solution consisting of 50 mM HEPES (Fisher), pH 6.0, 0.01% Bis-acrylamide (Bio-Rad), 25% ethanol, 0.01% N6 (custom-synthesized), 0.002% Di(trimethylolpropane) tetraacrylate (Sigma), and 0.025% Irgacure D-2959 (Sigma) was prepared, pipetted into each well containing a polyacrylamide gel, and exposed for 10 min with a medium-wavelength UV source (Spectroline EN-180, 306 nm peak). The gels were then washed 2x 10 min with ice-cold 25 mM HEPES (Fisher), pH 6.0 and 2x 10 min with ice-cold 0.9% NaCl (Fisher). rBM was diluted to a concentration of 250 μg/ml in ice-cold 100 mM HEPES (Fisher), 100 mM NaCl (Fisher), pH 8.0, added to each well containing a gel, and incubated at 4° C overnight with gentle rocking. The gels were then washed 5x 10 min with PBS and stored at 4° C in sterile conditions with PBS prior to beginning experiments.

Fabrication of Patterned Hydrogels

Patterned polyacrylamide hydrogels were fabricated as described previously (Muncie et al., 2019). Glutaraldehyde-modified coverslips were generated as described in the previous section for non-patterned hydrogels. Additional #1 18 mm coverslips (Electron Microscopy Services) were cleaned by overnight submersion in 1 M HCl (Fisher) with gentle rocking. Custom silicon wafers containing desired geometric patterns were generated using negative photoresist according to manufacturer's instructions (SU-8; Kayaku Advanced Materials, Inc.). Polydimethylsiloxane (PDMS; Dow) stamps with desired patterns were then fabricated on these custom silicon wafers. Stencils were generated by placing these PDMS stamps onto flat slabs of PDMS, wicking a UV-curable adhesive NOA-74 (Norland Products, Inc.) between the stamps and the flat slabs, and curing the adhesive via 10 min exposure with a medium-wavelength UV source (Spectroline EN-180, 306 nm peak). Next, stencils were firmly pressed onto the acid-washed coverslips and incubated overnight at 4° C with 250 μg/ml rBM in ice-cold 100 mM HEPES (Fisher), 100 mM NaCl (Fisher), pH 8.0. Stencils were then removed

from the patterned coverslips and the coverslips were washed by two sequential submersions in PBS and a single submersion into ultrapure water before being dried under nitrogen gas (Airgas).

Polyacrylamide gels were then fabricated as described in the preceding section, with polyacrylamide solution being pipetted onto a glutaraldehyde-modified coverslip with plastic spacer and a patterned coverslip being placed on top, with the rBM-patterned side in contact with the polyacrylamide. These polyacrylamide "sandwiches" were incubated for 1 h at room temperature to allow polymerization, then submerged in PBS and incubated at room temperature with gentle rocking for an additional 2 h. The patterned top coverslips were removed using a scalpel while the "sandwich" remained submerged in PBS, and then the glutaraldehyde-modified coverslips with attached polyacrylamide gels were assembled into custom 3D-printed holders (CAD drawings available upon request) with rubber gaskets to form sealed wells with the polyacrylamide hydrogels at the bottom of each well. The gels were then washed 5x 10 min with PBS and stored at 4° C in sterile conditions with PBS prior to beginning experiments.

Micropatterning of Tissue Culture Plastic

Custom silicon wafers containing desired geometric patterns were generated using negative photoresist according to manufacturer's instructions (SU-8; Kayaku Advanced Materials, Inc.). Polydimethylsiloxane (PDMS; Dow) stamps with desired patterns were then fabricated on these custom silicon wafers. The stamps were then incubated overnight at 4° C with 250 μg/ml rBM in ice-cold 100 mM HEPES (Fisher), 100 mM NaCl (Fisher), pH 8.0. The next day, stamps were dried under nitrogen gas (Airgas), inverted and pressed onto the surface of tissue culture plastic 12-well plates, and incubated for 30 min at 37° C. Stamps were then removed and the wells were incubated at room temperature for 90 min with 1% BSA (Fisher), PBS. The BSA/PBS solution was removed and plates were stored at 37° C with knockout-DMEM (Gibco) prior to cell seeding.

Traction Force Microscopy

Polyacrylamide hydrogels were fabricated as described in the preceding sections and in previous work (Lakins et al., 2012; L. Przybyla et al., 2016b), with 1 μm diameter fluorescent microspheres (Invitrogen) added to the polyacrylamide solution at a final concentration of 0.03% solids. Upon adding the polyacrylamide solution between two coverslips, the coverslip "sandwiches" were centrifuged in swing-buckets at 200 x g for 10 min with the Rain-X coverslip at the bottom, and incubated in this configuration at room temperature for an additional 1 h to allow for polymerization. The centrifugation step forced all the microspheres into a single XY-plane at what ultimately became the surface of the hydrogel upon removal of the Rain-X coverslip.

hESC colonies were plated onto hydrogels as described in the following section. At timepoints for which traction force measurements were desired, images of the fluorescent microspheres ("stressed images") were captured using a Nikon Eclipse TE200 U (Nikon) inverted microscope with a 10x objective, equipped with a motorized positioning stage (Prior Scientific HLD 117) and an ORCA Flash 4.0LT CMOS camera (Hamamatsu). hESCs were then lysed using 2% sodium dodecyl sulfate (Sigma) and images were captured of the fluorescent microspheres from the same regions of interest ("unstressed images"). For each region of interest, "stressed" and "unstressed" images were aligned using Fiji software plugin Linear Alignment with SIFT (Schindelin et al., 2012). Bead movements resulting from cell traction forces were determined using a Fiji software plugin for computing particle image velocimetry (PIV) measurements (Tseng et al., 2012), and these PIV measurements were converted to traction stresses using the Fiji software plugin FTTC (Tseng et al., 2012). MATLAB (MathWorks) was used to visualize the maps of traction stress magnitudes. For the traction stress maps shown, binary masks representing hESC colony areas were generated from brightfield images and used to remove traction stress noise from regions outside the colony area. A 10-pixel-wide border of zero values was added to all traction stress maps of patterned triangle colonies to provide clearer

visualization of the corners. The perceptually uniform colormap "inferno" was applied to all traction stress plots (Biguri, 2020).

Maps of average traction stress magnitudes for geometrically-confined colonies were generated by using brightfield images of the colonies to align replicate traction stress maps for each geometry. The replicate traction stress maps were then cropped to a uniform size, and magnitude values at each voxel were averaged across all the maps. The number of colonies used to generate average traction stress maps can be found in the figure captions. MATLAB (MathWorks) was used to determine the 99th percentile traction stress value (in Pascals) for each individual traction stress map of geometrically-confined triangle hESC colonies with (shE-cad KD) and without (control) shE-cadherin knockdown.

The code generated to analyze and display traction force data is publicly available on GitHub (https://github.com/jmmuncie/TF_hESC).

Plating hESCs onto Hydrogels

Twenty-four hours prior to plating hESCs, knockout-DMEM (Gibco) was added to the hydrogels and incubated at 37° C in a humidified cell culture incubator with 5% CO2. Prior to plating on hydrogels, T-mNeonGreen reporter cells cultured on γ-irradiated PMEFs were passaged into secondary cultures in feeder-free conditions on tissue culture plastic coated with rBM and fed with PMEF-conditioned KSR media supplemented with 10 ng/ml bFGF (PeproTech). hESC lines that were maintained in feeder-free conditions (H9, H2B-mCherry, and shE-cadherin) were passaged to hydrogels directly. hESCs were released from rBM-coated plastic via 10 min incubation at 37° C with 0.05% trypsin-EDTA (Gibco) supplemented with 10 μM Y-27632 (Tocris), and counted using a hemocytometer.

Unconfined colonies of hESCs were generated on non-patterned hydrogels by placing custom 3D-printing plating guides (3 mm diameter; CAD drawings available upon request) onto the surface

of the hydrogels and pipetting 20,000 cells through each opening of the plating guides. Guides were removed after incubation for 1 h to ensure cell attachment.

Patterned hESC colonies were generated by seeding 200,000 cells onto each of the patterned gels and very gently replacing the media after 3 h to remove non-attached cells. T-mNeonGreen reporter cells were plated in PMEF-conditioned KSR media, while the other cell lines were plated in 50% PMEF-conditioned KSR, 50% E8 media (Gibco). For shE-cadherin experiments, IPTG (200 μM; Sigma) was added to the media one passage (72 h) prior to seeding on hydrogels to induce shE-cadherin knockdown. All cell lines were plated in media supplemented with 10 ng/ml bFGF (PeproTech) and 10 μM Y-27632 (Tocris). The Y-27632 was diluted out of the media over the course of 72 h to prevent dissociation of hESCs from the hydrogels: 24 h after plating, media was replaced with media containing 5 μM Y-27632; 48 h after plating, media was replaced with media lacking Y-27632; 72 h after plating, experiments began.

BMP4 Differentiation

Differentiation was induced by removing maintenance media from hESC colonies on hydrogels and replacing it with Stemline II Hematopoietic Stem Cell Expansion Medium (Sigma) supplemented with 10 ng/ml bFGF (PeproTech) and 50 ng/ml BMP4 (PeproTech). hESC colonies were differentiated for the amount of time described for each experiment. For shE-cadherin experiments, IPTG (200 μM; Sigma) was added to the differentiation media in the knockdown condition to maintain shE-cadherin knockdown. For Src inhibition experiments, the Src-family kinase inhibitor (PP1; 10 μM; Sigma) or equal volume of vehicle (DMSO) was added to the standard differentiation media. For Wnt inhibition experiments, the Wnt processing and secretion inhibitor (IWP-2; 2 μM; MedChem Express) or equal volume of vehicle (DMSO) was added to the standard differentiation media.

Time-lapse Imaging

hESC colonies seeded on polyacrylamide gels in custom 3D printed holders were loaded into a custom-built stage mount as previously described (L. Przybyla et al., 2016b; CAD drawings for gel holders and stage mount available upon request), and differentiation was induced as described in the preceding section. The stage mount was sealed, enabling a low-pressure flow of mixed gas containing 5% CO2, 95% air (Airgas) to maintain the pH of standard differentiation media, and the mount was placed onto a motorized positioning stage (Prior Scientific HLD 117) attached to a Nikon Eclipse TE200 U (Nikon) inverted epifluorescent microscope. The microscope stage, condenser, and objectives were encased in a Plexiglas box and a forced air temperature feedback control (In Vivo Scientific) was used to maintain the temperature of the entire setup at 37° C. Images were captured using a 10x objective at specified timepoints.

For Chapter 2, "gastrulation-like" nodes were manually identified and counted in colonies of H2B-mCherry cells by utilizing both brightfield and fluorescent images. "Gastrulation-like" nodes were initially identifiable as regions of increased cell density in both brightfield and fluorescent channels. Subsequently, as cells ingressed and formed additional layers that caused fluorescent light scattering, nodes appeared as regions that seemingly lacked mCherry signal, but clearly contained densely-packed cells as revealed by the brightfield channel.

For Chapter 2, "gastrulation-like" nodes were manually counted in colonies of T-mNeonGreen reporter cells by identifying regions with detectable nuclear T-mNeonGreen expression above background levels. Nearly twice as many "gastrulation-like" nodes were identified by 48 h of differentiation using the T-reporter because by not relying on visible morphological changes, smaller nodes were identified with much higher sensitivity based on T-mNeonGreen expression alone.

For Chapter 2, the size of "gastrulation-like" nodes were measured manually in both H2B-mCherry and T-mNeonGreen hESC colonies using the NIS-Elements (Nikon) software. Lines were

drawn and measured across each node along the radial axis of the colony (i.e. along the line connecting the center of the colony to the edge of the colony nearest each node), the axis along which nodes were observed to elongate. Thus, the measurement of node size over time was designed to be akin to measuring the anterior elongation of the primitive streak in the embryo.

For Chapter 2, the "distance from edge" measurements for "gastrulation-like" nodes identified in T-mNeonGreen hESC colonies after 36 h of BMP4 stimulation were likewise measured along the radial axis of the colony.

For Chapter 4, maps of normalized average intensity of T-mNeonGreen expression for triangle, Pac-Man, and triangle-in-Pac-Man patterned colonies were generated by using brightfield images to align the colonies from each replicate and crop the images to a uniform size. For time-lapse experiments, background signal was first removed by subtracting the image of mNeonGreen background expression at 20 h of BMP4 stimulation (prior to detectable T-mNeonGreen expression above background) from the image of T-mNeonGreen expression at the timepoint of interest. For the triangle-in-Pac-Man colonies on tissue culture plastic, the raw T-mNeonGreen images from colonies fixed at 36 h of BMP4 treatment were used. The intensity values at each pixel in the resulting images were then divided by the number of replicates for each experiment, and summed across all the replicates to generate average expression plots. These average intensity maps were then normalized to the maximum intensity value within each map and visualized using MATLAB (MathWorks; display script available at https://github.com/jmmuncie/TF_hESC). The perceptually uniform colormap "viridis" was applied to the normalized average intensity maps (Biguri, 2020).

Immunofluorescence Staining and Imaging

hESC colonies on polyacrylamide gels (Chapters 2-4) were fixed slowly in cold conditions to prevent detachment of cells from the hydrogels. Prior to fixation, hESC colonies on gels were placed on ice and gently rocked for 10 min. Media was removed, ice-cold 4% paraformaldehyde (Sigma) was

carefully added, and the samples were fixed at 4° C overnight. Prior to fixation, samples for β-catenin-Y654 staining were briefly washed with a hot "TNS" solution of 0.03% Triton-X 100 (Sigma), 0.4% NaCl (Fisher) at 90° C, and shook vigorously for 30 s to remove cytosolic β-catenin but leave junction β-catenin intact, as described previously (Röper et al., 2018). A larger volume of ice-cold TNS was then immediately added to rapidly cool each sample, after which all the TNS was removed and replaced with ice-cold 4% paraformaldehyde and samples were fixed at 4° C overnight.

After fixation, hESC samples (Chapters 2-4) were washed 3x 10 min with PBS and then simultaneously blocked and permeabilized with a 1 h incubation at room temperature in "IF Buffer" containing 0.1% bovine serum albumin (Fisher), 0.2% Triton-X 100 (Sigma), 0.05% Tween-20 (Sigma), 130 mM NaCl (Fisher), 13 mM Na2HPO4 (Fisher), 3.5 mM NaH2PO4 (Fisher), and 0.05% sodium azide (Sigma), supplemented with 10% goat serum (Sigma). Samples were then incubated overnight with primary antibodies diluted in IF Buffer plus 10% goat serum at 4° C with gentle rocking. The next day, samples were washed 3x 10 min with IF Buffer at room temperature and then incubated for 2 h with secondary antibodies diluted in IF Buffer plus 10% goat serum at room temperature with gentle shaking. Samples were then washed 3x 10 min with IF Buffer, 1x 5 min with 0.5 μg/ml DAPI (Invitrogen) in PBS, and 2x 10 min with PBS. Samples were then removed from the custom gel holders, inverted onto #1 22 x 55 mm glass coverslips (VWF) and imaged.

Human iPSC colonies (Chapter 5) were fixed for 30 min in 4% paraformaldehyde (VWR) and washed 3x with PBS. Fixed colonies were permeabilized with 0.3% Trition X-100 (Sigma Aldrich) throughout blocking and antibody incubation steps. Samples were incubated in primary antibodies overnight at 4°C, subsequently washed with PBS and incubated in secondary antibodies for 1 h at room temperature.

Fixed myofibers (Chapter 6) were permeabilized with 0.2% Triton X-100/PBS and blocked with 10% goat serum/0.2% Triton X-100/PBS. Stained fibers were mounted in Fluoromount-G

mounting medium (SouthernBiotech). For most of the staining, images were taken using a 20x Plan Fluor objective. Anti-Phospho-MLC2 and active Rho stained images were obtained with a 40x Plan Fluor objective.

Epifluorescent images were captured using a Nikon Eclipse TE200 U (Nikon) inverted microscope with a 10x, 20x, 40x, or 60x objective and an ORCA Flash 4.0LT CMOS camera (Hamamatsu). Confocal images were captured using a Nikon Eclipse Ti inverted microscope (Nikon) equipped with a 60x objective, a CSU-X1 spinning disk confocal scanner (Yokogawa), and a Zyla sCMOS camera (Andor).

Primary antibodies used were: anti-T(brachyury) (RRID: AB_2200235, R&D Systems, 1:40), anti-E-cadherin (RRID: AB_2291471, CST, 1:200), anti-Slug (RRID: AB_2239535, CST, 1:400), anti-Fibronectin (RRID: AB_470662, Abcam, 1 μg/ml), anti-β-catenin-Y654 (RRID: AB_10623284, Sigma, 1:50), anti-β-catenin (RRID: AB_11127855, CST, rabbit, 1:200), anti-β-catenin (ECM Biosciences, mouse, 1:250), anti-phospho-Src Family (RRID: AB_10013641, CST, 1:100), anti-Oct-3/4 (RRID: AB_2167703, Santa Cruz Biotechnology, 1:100), anti-Oct-3/4 (RRID: AB_2167705, SantaCruz Biotechnology, 1:400), anti-EpCAM (RRID: AB_11213082, Millipore, 1:200), anti-BrdU (RRID: AB_305426, Abcam), anti-Pax7 (RRID: AB_2299243, DSHB), anti-MyoD (RRID: AB_2148870, Santa Cruz Biotechnology), anti-Laminin (RRID: AB_298179, Abcam), anti-Syndecan4 (RRID: AB_448112, Abcam), anti-phospho-Myl9 (RRID: AB_10980950, Thermo Fisher Scientific), anti-phospho-FAK (RRID: AB_2532307, Thermo Fisher Scientific), and anti-embryonic myosin heavy chain (RRID: AB_528358, DSHB). Secondary antibodies used were: Alexa Fluor 488 goat anti-mouse IgG (RRID: AB_2576208, Abcam, 1:1000), Alexa Fluor 568 goat anti-mouse IgG (Abcam, 1:1000), Alexa Fluor 488 goat anti-rabbit IgG (RRID: AB_2630356, Abcam, 1:1000), Alexa Fluor 568 goat anti-rabbit IgG (RRID: AB_2576207, Abcam, 1:1000), Alexa Fluor 488 donkey anti-goat IgG (RRID: AB_2687506, Abcam, 1:1000). Note: when anti-T(brachyury) and Alexa Fluor 488 donkey

anti-goat IgG antibodies were used, donkey serum was used in place of goat serum during all blocking and staining steps described above.

Images were analyzed in Fiji (Schindelin et al., 2012), unless otherwise noted.

For Chapter 2, quantification of correlation between the T-mNeonGreen reporter expression and the T-antibody was performed by first pre-processing images by histogram matching all images from each channel to a randomly selected image from the same channel. After pre-processing, nuclei were identified and counted from images of DAPI staining using a trained classifier in the Pixel Classification pipeline of ilastik (Berg et al., 2019). Training was performed with 8 images. Next, the probability maps of the nuclei were processed with an ImageJ Jython script that used a Minimum filter (sigma = 5), Median filter (sigma = 10), and a Gaussian Blur filter (sigma = 5). Filtered images were then auto-thresholded using the Moments method, and the Watershed function was applied. Using the ROI manager, the resulting ROIs from the nuclei thresholds were used to calculate the mean intensity values in the T-reporter and the T-antibody histogram-matched images. The mean intensity values for all nuclei-ROIs for all images for either T-reporter or T-antibody, across three independent experiments, were plotted against each other using Python, with a regression line indicating the level of correlation of the values between both channels.

For Chapter 4, quantification of cell density was performed by first pre-processing images by histogram matching DAPI stained images in ImageJ using a randomly selected image. After pre-processing, nuclei were identified from DAPI staining using a trained classifier in the Cell Density Counting pipeline on ilastik. Training was performed with two independent data sets, separate from an additional three independent experiments used for analysis. A Jython script was used for post-processing the probability images output from ilastik. Probability images were processed first using a Gaussian Filter (sigma = 2), auto-thresholded using the Moments method, and then a Watershed algorithm was applied to separate overlapping nuclei. Brightfield images were used to construct an

outline of each colony, by first subtracting background using the Rolling Ball method with a radius of 50 pixels, then applying the Gamma function with a value 1.70, a Gaussian Filter (sigma = 5), and finally creating a mask with the auto-thresholding method Otsu. Nuclei ROIs within the Brightfield outline were then counted using the Analyze Particles function and the area and centroid of each nuclei particle were recorded per image, along with the centroid of the Brightfield outline. To normalize the location of colonies, the X and Y centroid of each nuclei particle per colony were subtracted by the corresponding X and Y centroid value of the colony, such that the centroid of each colony would be at the origin (0, 0). With the normalized centroid values of all colonies, a Python script was used to coalesce all data per shape (circle, square, and triangle) and a Kernel Density Estimate (KDE) plot was calculated per shape using the Matplotlib and Seaborn packages. To represent the margins of each colony, the minimum and maximum X and Y centroid values from all colonies per shape were isolated during data collection and used to create a shaded range of colony edges, with a dashed line indicating the average value. Representative images were created using the same KDE plot, and for these plots, the colony outline was created using a ConvexHull function from the SciPy package around all the centroid values.

For Chapter 4, plot of relative mean fluorescence intensity for E-cadherin expression was generated by cropping all images to equivalent sizes and measuring the raw integrated density (RawIntDen, sum of pixel values). The RawIntDen values were normalized by dividing the RawIntDen value for each replicate within an experiment by the maximum RawIntDen value measured within that experiment. These normalized values were then plotted. Plot of % nuclei area T-positive was generated by first subtracting background from T and DAPI stained images using the Rolling Ball method with a radius of 50 pixels, then thresholding and converting images to binary, and finally taking the ratio of the threshold area of the T staining relative to the threshold area of DAPI staining.

For Chapter 4, quantification of β-catenin release from cell junctions was performed by measuring the fluorescence intensity profiles along lines of 60 pixels centered at cell junctions, for five cell junctions in each image analyzed. Measurements from all profiles from each condition were then normalized to the maximum value between compared conditions and plotted as mean ± 95% CI for each condition.

For Chapter 4, maps of normalized average intensity of β-catenin Y654 expression for triangle and Pac-Man patterned colonies were generated by using brightfield images to align the colonies from each replicate and crop the images to a uniform size. Images were then converted to ".txt" format and manipulated using MATLAB (MathWorks). Each replicate pair of images (triangle corner vs. middle and Pac-Man concave vs. convex) were normalized to the maximum intensity value of the pair. The intensity values at each pixel in the resulting images were then divided by the number of replicates for each experiment, and summed across all the replicates to generate average expression plots. These average intensity maps were then normalized to the maximum intensity value within each pair of maps (triangle corner average vs. middle average and Pac-Man concave average vs. convex average) and visualized (display script at https://github.com/jmmuncie/TF_hESC) using the perceptually uniform colormap "viridis" (Biguri, 2020).

For Chapter 4, quantification of junctional pSFK expression was performed by using β-catenin to create masks of cell junctions within imaged regions and using these to mask junctional pSFK expression from total pSFK expression. Masks were created by subtracting background from images of β-catenin using the Rolling Ball method with a radius of 50 pixels, thresholding the background-subtracted images with the Otsu method, and dividing the resultant binary images by 255 such that pixel values were either zero or one. The Image Calculator function (FIJI) was used to multiply the β-catenin mask by the pSFK image for each region to mask junctional pSFK. The resultant junctional

expression was measured (RawIntDen), normalized to the area of the β-catenin mask (junctional area), and these values were plotted.

For Chapter 6, plots of fluorescence intensity were generated by manually drawing regions of Interest (ROIs) on $Pax7^+$ SCs. Fiji was used to automatically measure the mean pixel intensity of the ROIs in each channel. The ROI was then copied onto another region lacking a $Pax7^+$ cell to calculate the background intensity. The background intensity was subtracted and the mean intensity (minus background) was plotted for each measured cell.

Quantitative PCR (qPCR)

For hESC experiments (Chapters 2-4), total RNA was isolated from either full colonies of hESCs or FACS-sorted populations of T-mNeonGreen reporters as indicated in the main text and figure captions using TRIzol (Invitrogen) according to the manufacturer's protocol. cDNA was synthesized from RNA using M-MLV Reverse Transcriptase (BioChain) and Random Hexamers (Applied Biosystems) as primers. qPCR was performed in triplicates from 10 ng of RNA per reaction using PerfeCTa SYBR Green FastMix (Quantabio) on a Mastercycler RealPlex2 detection system (Eppendorf). All reactions for qPCR were performed using the following conditions: 95 °C for 30 s followed by 40 cycles of a three-step reaction of denaturation at 95 °C for 10 s, annealing at 65 °C for 10 s, and further annealing at 68 °C for 20 s to reduce the likelihood of non-specific products, with reads taken at the end of each 68 °C step. At the end of each reaction, melting curves were generated to validate the quality of amplified products using the following conditions: 95 °C for 15 s, 60 °C for 15 s, ramp to 95 °C in 10 min. Relative gene expression was determined by normalizing to the housekeeping gene GAPDH.

For hiPSC experiments (Chapter 5), total RNA isolation was performed using an RNeasy Mini Kit (QIAGEN) according to manufacturer's instructions and quantified with a Nanodrop 2000c Spectrometer (ThermoFisher Scientific). cDNA was synthesized by using an iScript cDNA Synthesis

kit (BIORAD) and the reaction was run on a SimpliAmp thermal cycler (Life Technologies). To quantify relative expression of individual genes, qPCR reactions were performed in triplicate on a StepOnePlus Real-Time PCR system (Applied Biosciences) and detected using Fast SYBR Green Master Mix (ThermoFisher Scientific). Relative gene expression was determined by normalizing to the housekeeping gene 18S. Gene expression was displayed as fold change of each sample (ROCK1 CRISPRi or CDH1 CRISPRi) versus the off-target guide control (KCNH2 CRISPRi).

For muscle SC experiments (Chapter 6), total RNA was isolated from single muscle fibers (from EDL muscle) or SCs using Trizol (Invitrogen) according to the manufacturer's protocol. The RNA was DNase treated using Turbo DNA Free Kit (Life Technologies). cDNA was synthesized from RNA using the Superscript First Strand Synthesis System (Invitrogen). qPCR was performed in triplicates from 5 ng of RNA per reaction using Platinum SYBR Green qPCR Super Mix-UDG w/ROX (Invitrogen) on a ViiA7 qPCR detection system (Life Technologies). All reactions for qPCR were performed using the following conditions: 50 °C for 2 min, 95 °C for 2 min, 40 cycles of a two-step reaction of denaturation at 95 °C for 15 min and annealing at 60 °C for 30 s. Relative gene expression was determined by normalizing to the housekeeping gene GAPDH.

In all experiments, the mean C_T values from triplicates were used to calculate the ΔC_T values relative to GAPDH or 18S expression. The means of the ΔC_T values from independent experiments were used to calculate mean fold change of expression using the $2\text{-}\Delta\Delta C_T$ method. For each gene evaluated, the 95% CI (Chapters 2-4), SD (Chapter 5), or SEM (Chapter 6) of the ΔC_T values was calculated and used to generate positive and negative error values in the $2\text{-}\Delta\Delta C_T$ fold change space. Plots of qPCR data display line and bars representing the mean fold change ± 95% CI, SD, or SEM, and individual points representing the fold change value for each experimental replicate relative to the mean. All primers used for qPCR in this study are listed in Table 9.2.

Table 9.2: Primer sequences used for qPCR

Gene	Forward Primer Sequence 5' to 3'	Reverse Primer Sequence 5' to 3'
18S	CTTCCACAGGAGGCCTACAC	CTTCGGCCCACACCCTTAAT
CDH1 (E-cadherin; Chapter 4)	CGGCCTGAAGTGACTCGTA	GCCGCTTTCAGATTTTCATC
CDH1 (E-cadherin; Chapter 5)	CGGGAATGCAGTTGAGGATC	AGGATGGTGTAAGCGATGGC
FN1	ACAGCTCATCCGTGGTTGTA	TCTTGGTGGGCTGACATTCT
GAPDH (Chapters 2 and 4)	CAGCCTCAAGATCATCAGCA	TGTGGTCATGAGTCCTTCCA
GAPDH (Chapter 6)	GGCAAAGTGGAGATTGTTGC	AATTTGCCGTGAGTGGAGTC
GSC	TCTCAACCAGCTGCACTGTC	CGTTCTCCGACTCCTCTGAT
MMP2	GAAGGATGGCAAGTACGGCT	GGAATGGAAACTTGCAGGGC
MMP14	CCCAACATCTGTGACGGGAA	TTGGTTATTCCTCACCCGCC
MSGN1	TGTTGGACCCACCAGAACAC	TTGCAAAGGATGAGCCTCCC
NANOG	AGATGCCTCACACGGAGACT	AAGTGGGTTGTTTGCCTTTG
OCT-3/4	AGTGAGAGGCAACCTGGAGA	ACACTCGGACCACATCCTTC
OSR1	TCCCTGGTTCCCTCATGTCA	CGGATCTTCTTGCGTTGCTG
ROCK1	GTTCCCCTTCCGAGCGTC	TGTCCGCCTTCCTGTTCAAA
RSPO3	ACTTGCGACTGATTTCTTGGC	TCCTTGGCAGCCTTGACTAA
SNAI2	TTGTGTTTGCAAGATCTGCGG	TGCAAATGCTCTGTTGCAGT
SOX2	AGGATAAGTACACGCTGCCC	TAACTGTCCATGCGCTGGTT
T (TBXT)	CAGCAAAGTCAAGCTCACCA	TGGACCCCCAACTCTCACTA
TBX6	GAACCGGGAGCTATGGAAGG	AGAAACAAGTAGCGGGCCTC
WNT3A	GCCCCACTCGGATACTTCTT	GAGGAATACTGTGGCCCAAC
WNT4 (Chapter 4)	CCCTCATGAACCTCCACAAC	ACCTCACAGGAGCCTGACAC
WNT4 (Chapter 6)	AGACGTGCGAGAAACTCAAAG	GGAACTGGTATTGGCACTCCT
WNT8A	TGTGATGGGTCAAACAATGG	TCCTTCCCCTTCTCCAAACT

Eyebrow Knife Experiment

Eyebrow knives were fabricated by first heating 5.75" borosilicate glass Pasteur pipets (Fisher) over a Bunsen burner and pulling to generate a narrower tip. Paraffin wax (Sigma) was used to attach a plucked human eyebrow hair to the narrow tip of the pipet. (Note: Variations in the thickness and density of eyebrow hair will affect the ability to effectively manipulate hESC colonies, therefore, different eyebrow hairs from multiple individuals should be tested when adopting this method). "Stressed" microsphere images were captured for triangle patterned colonies of T-mNeonGreen reporter cells, as described in the "Traction Force Microscopy" section, prior to being cut with the eyebrow knife. Next, a Nikon SMZ800 (Nikon) dissecting microscope was used to make precise cuts with an eyebrow knife through the corners of triangle patterned colonies and additional "stressed" microsphere images were captured following the eyebrow knife cuts. The colonies were differentiated with BMP4 and time-lapse imaging was conducted to monitor T-mNeonGreen expression, as described in the "Time-lapse Imaging" section. After 48 h of differentiation, cells were lysed with 2% SDS (Sigma) and "unstressed" microsphere images were captured. Finally, the microsphere images were used to generate plots of traction stress magnitude for the colonies before and after cutting with the eyebrow knife and compared to the spatiotemporal expression of T-mNeonGreen captured during the time-lapse imaging.

The plot of time to T-mNeonGreen expression was generated by analyzing the time-lapse imaging data at each corner of the triangle patterned colonies successfully cut with the eyebrow knife. Each corner was categorized as "cut" or "intact" and the timepoint at which nuclear expression of T-mNeonGreen was detectable above background for cells within each corner was recorded and plotted.

Mechanical Stretching via Microfluidic Device

The microfluidic cell stretching device comprised a PDMS structural layer, a PDMS inlet block and a glass coverslip. The PDMS structural layer, which contained a microfluidic network for applying

pressure to simultaneously activate 64 pressurization compartments to induce PDMS membrane deformation, was fabricated using soft lithography. Briefly, the PDMS pre-polymer was spin-coated onto a silicon mold generated using photolithography and deep reactive ion etching (DRIE). The PDMS layer was thermally cured at 110 °C for at least 24 h before being peeled off the silicon mold. An inlet for fluid connections was then punched into the PDMS structural layer using a 1 mm biopsy punch (Fisher). Both the coverslip and the PDMS structural layer were briefly cleaned with 100% ethanol (Fisher) and blown dry under nitrogen gas before being treated with air plasma (Plasma Prep II; SPI Supplies) and bonded together. In parallel, another PDMS block was prepared, and an inlet for fluid connection was punched into the PDMS block with a 0.5 mm biopsy punch. After treating both with air plasma, the PDMS block and the PDMS structural layer were bonded together with their fluid inlets aligned manually. The microfluidic cell stretching device was baked at 110 °C for at least another 24 h to ensure robust bonding between layers. Deionized water was injected into the microfluidic cell stretching device before applying pressure through a microfluidic pressure pump (AF1, Elveflow). Elveflow Smart Interface software (https://www.elveflow.com/) was used for programming the pressure pump for continuous cell stretching with a square-wave pattern (pulse width of 2 h, period of 4 h and 50% duty cycle), which was applied coincident with the start and maintained throughout the 48 h BMP4 differentiation.

Microcontact printing was performed to print circular adhesive patterns with a diameter of 400 μm onto the deformable PDMS membrane on top of the pressurization compartments (with a diameter of 200 μm) in the custom-designed microfluidic cell stretching device. To this end, a custom desktop aligner designed for fabrication of multilayer microfluidic devices was used (X. Li et al., 2015). Briefly, a vitronectin-coated (20 μg/ml; Trevigen) PDMS stamp and the microfluidic cell stretching device were mounted onto the top and bottom layer holders of the aligner, respectively. Under a digital microscope, the X/Y/θ stage holding the bottom layer holder was carefully adjusted to align the

PDMS stamp and the microfluidic cell stretching device. The PDMS stamp was then gently pressed to achieve conformal contact with the microfluidic cell stretching device to transfer vitronectin from the stamp to the PDMS membrane on top of the pressurization compartments.

The plots of average T-mNeonGreen expression in control and stretched colonies after 48 h were generated by dividing the intensity values at each pixel in the T-mNeonGreen images by the number of replicates for each condition, and then summing all the replicate images. These average intensity maps were then normalized to the maximum intensity value within each map and visualized using MATLAB (MathWorks; display script available at https://github.com/jmmuncie/TF_hESC). The perceptually uniform colormap "viridis" was applied to the normalized average intensity maps (Biguri, 2020).

In Situ Hybridization via Hybridization Chain Reaction (ISH-HCR)

Third-generation ISH-HCR was performed as described previously (H. M. T. Choi et al., 2018). Samples were fixed slowly in cold conditions to prevent detachment of hESCs from the hydrogels. Prior to fixation, hESC colonies on gels were placed on ice and gently rocked for 10 min. Media was removed, ice-cold 4% paraformaldehyde (Sigma) was carefully added, and the samples were fixed at 4° C overnight. The next day, samples were washed 3x 10 min with diethyl pyrocarbonate (DEPC; Sigma) treated PBS with 0.1% Tween-20 (Sigma) to permeabilize, and then washed 1x 5 min with 5x SSC buffer with 0.1% Tween-20. Samples were incubated for 1 h at 37° C in a humidified chamber in hybridization buffer consisting of 30% de-ionized formamide (Sigma), 5x SSC, 9 mM citric acid, pH 6.0 (Sigma), 0.1% Tween-20, 50 μg/ml heparin (Sigma), 1x Denhardt's solution (Sigma), 10% dextran sulfate, avg Mw >500,000 (Sigma), and DEPC-treated ultrapure water. Samples were then hybridized overnight via incubation at 37° C in a humidified chamber with hybridization buffer plus 20 nM split initiator hybridization probes designed to target Wnt3a (Table 9.3) and 10 mM ribonucleoside vanadyl complexes (Sigma). The next day, samples were washed 5x 10 min at 37° C

with no agitation using a buffer consisting of 30% formamide, 5x SSC, and 9 M citric acid, pH 6.0. Samples were further washed 3x 10 min at room temperature with gentle shaking using a buffer of 5x SSC, 0.1% Tween-20, and 50 μg/ml heparin. Samples were incubated for 30 min at room temperature in amplification buffer consisting of 5x SSC, 0.1% Tween-20, and 10% dextran sulfate, avg Mw >500,000. Samples were then incubated overnight at room temperature in amplification buffer plus 60 nM HCR3 amplification probes conjugated with Alexa Fluor 647 (H. M. T. Choi et al., 2018). The next day, samples were washed 5x 10 min at room temperature with gentle shaking in 5x SSC with 0.1% Tween-20. The third wash also contained 0.5 μg/ml DAPI (Invitrogen). Finally, samples were inverted onto #1 22 x 55 mm glass coverslips (VWF) and imaged using a Nikon Eclipse Ti inverted microscope (Nikon) equipped with a 60x objective, a CSU-X1 spinning disk confocal scanner (Yokogawa), and a Zyla sCMOS camera (Andor). Split initiator hybridization probe sequences targeting Wnt3a mRNA transcripts are listed in Table 9.3.

Quantification of ISH-HCR speckles was performed by first subtracting background from Wnt3a-ISH images using the Rolling Ball method with a radius of 20 pixels and thresholding the resulting images. The Analyze Particles function (FIJI) was then used to count speckles within each image, with min-max size parameters set to 5-Infinity pixels and min-max circularity parameters set to 0.3-1.0. In order to determine an approximation of speckles per cell within each analyzed image, nuclei were identified and counted from images of DAPI staining using the Primary Object Identifier in CellProfiler (McQuin et al., 2018). Speckle counts for each imaged region were then divided by the number of nuclei identified and these values were plotted.

Table 9.3: Split initiator hybridization probe sequences used for Wnt3a ISH-HCR

Probe	Sequence, 5' to 3'
WNT3A_1a	AAAGTCTAATCCGTCCCT TT AGTAAGAAGTATCCGAGTGGGGCCA
WNT3A_1b	CCCAGAGCCTGCTTCAGGCTGCAGA TT GCCTCTATATCTCCACTC
WNT3A_2a	AAAGTCTAATCCGTCCCT TT CAGCGACCACCAGATCGGGTAGCTG
WNT3A_2b	CAGGGAGGAATACTGTGGCCCAACA TT GCCTCTATATCTCCACTC
WNT3A_3a	AAAGTCTAATCCGTCCCT TT TAGTTCCTGCAGAAGCGGAGCTGCT
WNT3A_3b	TCGGCCACGCTGGGCATGATCTCCA TT GCCTCTATATCTCCACTC
WNT3A_4a	AAAGTCTAATCCGTCCCT TT CCGAAGATGGCCAGGCTGTCGTGGA
WNT3A_4b	TCCCTGGTAGCTTTGTCCAGCACGG TT GCCTCTATATCTCCACTC
WNT3A_5a	AAAGTCTAATCCGTCCCT TT CTGAGGCAATGGCGTGGACAAAGGC
WNT3A_5b	AGCGTGTCACTGCAAAGGCCACACC TT GCCTCTATATCTCCACTC
WNT3A_6a	AAAGTCTAATCCGTCCCT TT ACTTCCAGCCCTTGCCTGGTGAGCC
WNT3A_6b	ACTCGATGTCCTCGCTACAGCCACC TT GCCTCTATATCTCCACTC
WNT3A_7a	AAAGTCTAATCCGTCCCT TT GGTTGCGACCACCAGCATGTCTTCA
WNT3A_7b	AGGAAGTCACCGATGGCGCGGAAGT TT GCCTCTATATCTCCACTC
WNT3A_8a	AAAGTCTAATCCGTCCCT TT ACCTTGAAGTAGGTGTAGCGCGGCC
WNT3A_8b	TAGTAGACCAGGTCGCGCTCCGTGG TT GCCTCTATATCTCCACTC
WNT3A_9a	AAAGTCTAATCCGTCCCT TT AGTGGAACACGCAGCGGCACTTCTC
WNT3A_9b	ACTCCTGGCAGCTGACGTAGCAGCA TT GCCTCTATATCTCCACTC
WNT3A_10a	AAAGTCTAATCCGTCCCT TT CAGGGAAAAGCCCACCCTCAGGCAG
WNT3A_10b	CCGTTTAGGTGGGAGTCCTGCTCCA TT GCCTCTATATCTCCACTC
WNT3A_11a	AAAGTCTAATCCGTCCCT TT AGCCCTGCCTTCAGGTAGGAGTTCT
WNT3A_11b	AGAGAGGAGACACTAGCTCCAGGGA TT GCCTCTATATCTCCACTC
WNT3A_12a	AAAGTCTAATCCGTCCCT TT TGGAGCTCCGCCTCATTCAGGAGCA
WNT3A_12b	AAGCCAACGCAGAGCCCCTCCCCAT TT GCCTCTATATCTCCACTC
WNT3A_13a	AAAGTCTAATCCGTCCCT TT GCCCAATCTGTAGCCCCGCCTCTGT
WNT3A_13b	AGCCCTGTCCCACCCAAGAGAAGCC TT GCCTCTATATCTCCACTC
WNT3A_14a	AAAGTCTAATCCGTCCCT TT ACCCAGAGCCACGCCCTTACTGGGA
WNT3A_14b	GGTAGAAGCCTACCTAGTGCCCCGC TT GCCTCTATATCTCCACTC
WNT3A_15a	AAAGTCTAATCCGTCCCT TT ATAAAACCCCACTCCTAAGGAGGC
WNT3A_15b	CCCATCCAGGAAGAAGCCTCATCCA TT GCCTCTATATCTCCACTC
WNT3A_16a	AAAGTCTAATCCGTCCCT TT AAGGAGCCTATGCAGGCCACGCCCA
WNT3A_16b	TGGTCCCAGAGAAGCCCCACCCACA TT GCCTCTATATCTCCACTC
WNT3A_17a	AAAGTCTAATCCGTCCCT TT GAAGAGTCCCACCCGCGGAGAGAAG
WNT3A_17b	GCCTTAATCAGGAGGGCGGTTCCCA TT GCCTCTATATCTCCACTC
WNT3A_18a	AAAGTCTAATCCGTCCCT TT TCTGGAGCCGGGATTCCTGCAGAAG
WNT3A_18b	AGGTGGCTGGTGGGCTGAATTTCCT TT GCCTCTATATCTCCACTC
WNT3A_19a	AAAGTCTAATCCGTCCCT TT ATGGAACCTTACAGGGGGTTGGGGA
WNT3A_19b	AACCTTCCCAGCTCGACGCAGGGGT TT GCCTCTATATCTCCACTC
WNT3A_20a	AAAGTCTAATCCGTCCCT TT TGGGTGGTCAAACCCCAGGCTGAGG
WNT3A_20b	TTTCCCCAGGTAGGGCCCCTGGTCA TT GCCTCTATATCTCCACTC

Western Blotting

Human iPSCs were washed with cold PBS, incubated for 10 min on ice in RIPA Buffer (Sigma-Aldrich), and supernatant collected. Three replicates were used for each condition. The supernatant protein content was determined using a Pierce BCA Protein Assay kit (Thermo Fisher Scientific) colorimetric reaction and quantified on a SpectraMax i3 Multi-Mode Platform (Molecular Devices). Subsequently, 20 μg of protein from each sample was resolved by SDS-PAGE, and transferred to a nitrocellulose membrane (Invitrogen). The membranes were incubated overnight at 4°C with primary antibodies: anti-ROCK1 (RRID: AB_945285, AbCAM, 1:200), anti-CDH1 (RRID: AB_300946, AbCAM, 1:200), and anti-GAPDH (RRID: AB_1074703, Invitrogen, 1:10,000), followed by incubation (30 min at room temperature) with infrared secondary antibodies: IRDye 800CW and IRDye 680CW (LI-COR 1:13,000), and imaged on the Odyssey Fc Imaging System (LI-COR Biosciences). Protein levels were quantified using Image Studio Lite (LI-COR Biosciences).

Animal Procedures

Tamoxifen (Sigma) was dissolved in corn oil at a concentration of 20 mg/ml. Both control and experimental mice were administered tamoxifen at a concentration of 150 mg/kg per day for five continuous days (for HSA^{CreMER} mice) or 7 continuous days (for $Pax7^{CreER}$ mice) by intraperitoneal injection. To assess *in vivo* cell proliferation, control and experimental mice were administered 0.5 mg/ml Bromodeoxyuridine (BrdU; Sigma) in drinking water supplemented with 5% sucrose continuously throughout the course of the experiment starting from the 3rd day of tamoxifen. Rapamycin (LC Laboratories) was dissolved in 10% Polyethylene glycol 400 (Hampton Research) and 10% Tween-80 (Sigma) and administered intraperitoneally at a dose of 4 mg/kg daily starting from the 3rd day of tamoxifen till the end of the experiment (2 weeks of chase) for a total of 17 days.

Tibialis Anterior Muscle Injury

Control and experimental mice were anesthetized by isofluorane inhalation and 50 ml of 1.2% $BaCl_2$ was injected into and along the length of the tibialis anterior (TA) muscle. After 6 days or 35 days of regeneration, mice were euthanized and the injured TA muscle was fixed immediately in 4% PFA and frozen in 20% sucrose/OCT medium. 8 mm cross-sections of the muscle were made and stained for anti-laminin. 10x images were collected at three regions in the mid-belly of each muscle. Only mice that had more than 80% injury in their TA were analyzed. All the regenerating fibers in the entire TA section were analyzed for fiber size. The average cross-sectional area of the fibers was determined using ImageJ software. To assess *in vivo* proliferation during 5.5 to 6 days of muscle regeneration, 10 mg BrdU was given to the mice by intraperitoneal injection 12 h before the mice were sacrificed on day 6.

Isolation of SCs and Fluorescence Assisted Cell Sorting (FACS)

Satellite cells were isolated from hindlimb and forelimb muscles. The mice were euthanized, the hindlimb and forelimb skeletal muscles were removed, chopped finely, and digested using 0.2% Collagenase type 2 (Worthington) in DMEM media for 90 min in shaking water bath at 37 °C. The digested muscle was washed twice with Rinsing media (Ham's F10, 10% horse serum). A second digestion was performed with 0.2% Collagenase type 2 and 0.4% Dispase (GIBCO) in Rinsing media for 30 min in shaking water bath at 37 °C. The digested tissue was passed through a 20-gauge needle three times, then passed through a 40 mm filter and a 20 mm filter. The mononuclear muscle cells were stained for PE-Cy7 anti-mouse CD31 (clone 390; BD Biosciences; RRID: AB_394819), PE-Cy7 anti-mouse CD45 (clone 30-F11; BD Biosciences; RRID: AB_394489), APC-Cy7 anti-mouse Sca1 (clone D7; BD Biosciences; RRID: AB_1727552), PE anti-mouse CD106/VCAM-1 (Invitrogen; RRID: AB_2556576), and APC anti-α7 integrin (clone R2F2; AbLab; Cat# 67-0010-05). FACS was

performed using FACS Aria II (BD Biosciences) with gating for $CD31^-/CD45^-/Sca1^-/\alpha7$ $integrin^+/VCAM1^+$ to isolate SCs.

Isolation of Single Muscle Fibers

Single muscle fibers were isolated from the Extensor Digitorum Longus (EDL) muscle of the adult mouse. The EDL muscle was removed from the hindlimb of the mouse and digested with 0.2% Collagenase type I (GIBCO) for 90 min in shaking water bath at 37 °C. Single muscle fibers were obtained by gently triturating the digested muscle using a glass pipet in plating media (DMEM, 10% horse serum). The single fibers were manually collected under a dissection microscope, fixed immediately in 4% PFA for 10 min or cultured in plating media.

***In vitro* Treatment of Single Muscle Fibers**

The isolated single fibers from the EDL were cultured in plating media (DMEM, 10% horse serum) for 8 h. The fibers were then fixed and stained for anti-Pax7 (Developmental Studies Hybridoma Bank; RRID: AB_2299243) and anti-MyoD (Santa Cruz Biotechnology; RRID: AB_2148870). For *in vitro* cell cycle entry assays, single muscle fibers from control and MF-$Wnt4^{fl/fl}$ mice were harvested and cultured in plating media containing EdU (10 μM; Carbosynth) for 30 h. Single fibers from C57BL/6 mice were cultured in plating media with either PBS or Rho1 inhibitor (0.5 and 1 mg/ml; Cytoskeleton Inc.) for different time points: 2 h for pFAK expression, 8 h for MyoD expression and for cell cycle entry, in media containing EdU for 30 hours. Single fibers from C57BL/6 mice were cultured in plating media with either PBS or ROCK inhibitor Y-27632 (3 and 10mM; Tocris) for 8 h and stained for MyoD protein expression. For *in vitro* rescue experiments, control and MF-$Wnt4^{fl/fl}$ single muscle fibers were cultured in plating media with PBS or Rho activator (0.5 and 1 mg/ml; Cytoskeleton Inc.) for different time points: 2 h for pMLC expression, 8 h for MyoD expression and for cell cycle entry, in media containing EdU for 36 hours. The fibers were then fixed and stained for the different antibodies. EdU staining was done using the Click-iT Plus EdU Alexa Fluor 594 Imaging

Kit (Invitrogen) followed by staining with anti-Pax7 antibody (Developmental Studies Hybridoma Bank; RRID: AB_2299243).

In situ Binding Assay for Rho-GTPase Activity

FACS isolated SCs were fixed with 4% PFA for 25 min. The SCs were then washed with PBS and permeabilized in 0.05% Triton X-100/PBS for 10 min. Cells were blocked in 5% FBS/PBS and incubated for 1 h at room temperature with GST tagged Rhotekin-Rho binding domain (RBD) (Cytoskeleton Inc.) which binds specifically to active Rho. This was followed by PBS washes and incubation with fluorophore conjugated anti-GST antibody (Invitrogen; RRID: AB_2534137) and DAPI (Life Technologies) for 1 h at room temperature. The cells were washed with PBS and mounted for imaging.

Circularity Index Measurement of SCs

Single muscle fibers were stained with anti-Syndecan4 (Abcam; RRID: AB_448112) and anti-Pax7 (Developmental Studies Hybridoma Bank; RRID: AB_2299243) antibodies. Images were taken using a 20x Plan Fluor objective with a Nikon Eclipse Ti microscope. Using the NIS Elements software and thresholding feature, a mask was drawn around each $Pax7^+$ cell. The masks were drawn such that they overlapped with the Syndecan4 staining to include the membrane of the cell. The area and circularity index of the cells (masked regions) were automatically calculated using the NIS Elements software. The circularity index is a feature of how circular the cell is. It ranges from 0 to 1, with 1 being a perfect circle.

QUANTIFICATION AND STATISTICAL ANALYSIS

Tests of significance for comparisons between two experimental groups were performed using the two-tailed unpaired Student's t-test in Prism 6 software (GraphPad), except for the data presented in Figures 4.14 C and 4.19 A, for which one-tailed unpaired Student's t-tests were used because previous results suggested the expected direction of change in gene expression levels. Tests of significance for comparisons between more than two experimental groups were performed using a one-way Analysis of Variance (ANOVA) test in Prism 6 software (GraphPad). Parametric tests were used to provide greater statistical power and to avoid assumptions of symmetric distributions and/or equal variance between groups required by nonparametric tests. Differences were determined to be statistically significant at $p < 0.05$, and statistical significance was denoted by asterisks in the figure panels, with * = $p < 0.05$, ** = $p < 0.01$, *** = $p < 0.001$, **** = $p < 0.0001$. Differences that were determined to not be statistically significant were either denoted "n.s." or the p-value was noted above the data. For immunofluorescent image data, the figure panels illustrate representative results from at least $n = 3$ independent experiments where a minimum of three replicate hESC colonies were imaged for each condition in each experiment. For qPCR data n = the number of independent experiments, with hESCs pooled from at least three different hydrogels for each condition in each experiment. All other definitions of n can be found in the figure captions. Where plotted, bars and lines represent mean ± 95% confidence interval (CI) of the data. Statistical parameters plotted in each figure are also described in the figure captions.

REFERENCES

Abdel-Latif, A., Zuba-Surma, E. K., Case, J., Tiwari, S., Hunt, G., Ranjan, S., Vincent, R. J., Srour, E. F., Bolli, R., & Dawn, B. (2008). TGF-??1 enhances cardiomyogenic differentiation of skeletal muscle-derived adult primitive cells. *Basic Research in Cardiology*, *103*(6), 514–524. https://doi.org/10.1007/s00395-008-0729-9

Adams, J. C., & Watt, F. M. (1993). Regulation of development and differentiation by the extracellular matrix. *Development (Cambridge, England)*, *117*(4), 1183–1198.

Akhurst, R. J., Lehnert, S. a, Faissner, a, & Duffie, E. (1990). TGF beta in murine morphogenetic processes: the early embryo and cardiogenesis. *Development (Cambridge, England)*, *108*(4), 645–656. http://www.ncbi.nlm.nih.gov/pubmed/1696875

Alfandari, D., Cousin, H., Gaultier, A., Hoffstrom, B. G., & DeSimone, D. W. (2003). Integrin α5β1 supports the migration of Xenopus cranial neural crest on fibronectin. *Developmental Biology*, *260*(2), 449–464. https://doi.org/10.1016/S0012-1606(03)00277-X

An, C., Cheng, Y., Yuan, Q., & Li, J. (2010). IGF-1 and BMP-2 induces differentiation of adipose-derived mesenchymal stem cells into chondrocytes-like cells. *Annals of Biomedical Engineering*, *38*(4), 1647–1654. https://doi.org/10.1007/s10439-009-9892-x

Arboleda-Estudillo, Y., Krieg, M., Stühmer, J., Licata, N. A., Muller, D. J., & Heisenberg, C. P. (2010). Movement Directionality in Collective Migration of Germ Layer Progenitors. *Current Biology*. https://doi.org/10.1016/j.cub.2009.11.036

Arteaga-Solis, E., Gayraud, B., Lee, S. Y., Shum, L., Sakai, L., & Ramirez, F. (2001). Regulation of limb patterning by extracellular microfibrils. *Journal of Cell Biology*, *154*(2), 275–281. https://doi.org/10.1083/jcb.200105046

Aumailley, M., Bruckner-Tuderman, L., Carter, W. G., Deutzmann, R., Edgar, D., Ekblom, P., Engel, J., Engvall, E., Hohenester, E., Jones, J. C. R., Kleinman, H. K., Marinkovich, M. P., Martin, G. R., Mayer, U., Meneguzzi, G., Miner, J. H., Miyazaki, K., Patarroyo, M., Paulsson, M., … Yurchenco, P. D. (2005). A simplified laminin nomenclature. In *Matrix Biology* (Vol. 24, Issue 5, pp. 326–332). https://doi.org/10.1016/j.matbio.2005.05.006

Avigdor, A., Goichberg, P., Shivtiel, S., Dar, A., Peled, A., Samira, S., Kollet, O., Hershkoviz, R., Alon, R., Hardan, I., Ben-Hur, H., Naor, D., Nagler, A., & Lapidot, T. (2004). CD44 and hyaluronic acid cooperate with SDF-1 in the trafficking of human CD34+ stem/progenitor cells to bone marrow. *Blood*, *103*(8), 2981–2989. https://doi.org/10.1182/blood-2003-10-3611

Baghdadi, M. B., Firmino, J., Soni, K., Evano, B., Di Girolamo, D., Mourikis, P., Castel, D., & Tajbakhsh, S. (2018). Notch-Induced miR-708 Antagonizes Satellite Cell Migration and Maintains Quiescence. *Cell Stem Cell*. https://doi.org/10.1016/j.stem.2018.09.017

Baker, N. E., Mlodzik, M., & Rubin, G. M. (1990). Spacing differentiation in the developing Drosophila eye: a fibrinogen-related lateral inhibitor encoded by scabrous. *Science (New York, N.Y.)*, *250*(4986), 1370–1377. https://doi.org/10.1126/science.2175046

Baneyx, G, Baugh, L., & Vogel, V. (2001). Coexisting conformations of fibronectin in cell culture imaged using fluorescence resonance energy transfer. *Proceedings of the National Academy of Sciences of the United States of America*, *98*(25), 14464–14468. https://doi.org/10.1073/pnas.251422998

Baneyx, Gretchen, Baugh, L., & Vogel, V. (2002). Fibronectin extension and unfolding within cell matrix fibrils controlled by cytoskeletal tension. *Proceedings of the National Academy of Sciences of the United States of America*, *99*(8), 5139–5143. https://doi.org/10.1073/pnas.072650799

Beccari, L., Moris, N., Girgin, M., Turner, D. A., Baillie-Johnson, P., Cossy, A. C., Lutolf, M. P.,

Duboule, D., & Arias, A. M. (2018). Multi-axial self-organization properties of mouse embryonic stem cells into gastruloids. In *Nature*. https://doi.org/10.1038/s41586-018-0578-0

Behrens, J., Von Kries, J. P., Kühl, M., Bruhn, L., Wedlich, D., Grosschedl, R., & Birchmeier, W. (1996). Functional interaction of β-catenin with the transcription factor LEF- 1. *Nature*. https://doi.org/10.1038/382638a0

Behrndt, M., Salbreux, G., Campinho, P., Hauschild, R., Oswald, F., Roensch, J., Grill, S. W., & Heisenberg, C. P. (2012). Forces driving epithelial spreading in zebrafish gastrulation. *Science*. https://doi.org/10.1126/science.1224143

Benito-Jardón, M., Klapproth, S., Gimeno-Lluch, I., Petzold, T., Bharadwaj, M., Müller, D. J., Zuchtriegel, G., Reichel, C. A., & Costell, M. (2017). The fibronectin synergy site re-enforces cell adhesion and mediates a crosstalk between integrin classes. *ELife*, *6*. https://doi.org/10.7554/eLife.22264.001

Berg, S., Kutra, D., Kroeger, T., Straehle, C. N., Kausler, B. X., Haubold, C., Schiegg, M., Ales, J., Beier, T., Rudy, M., Eren, K., Cervantes, J. I., Xu, B., Beuttenmueller, F., Wolny, A., Zhang, C., Koethe, U., Hamprecht, F. A., & Kreshuk, A. (2019). ilastik: interactive machine learning for (bio)image analysis. *Nature Methods*. https://doi.org/10.1038/s41592-019-0582-9

Bertocchini, F., Skromne, I., Wolpert, L., & Stern, C. D. (2004). Determination of embryonic polarity in a regulative system: Evidence for endogenous inhibitors acting sequentially during primitive streak formation in the chick embryo. *Development*. https://doi.org/10.1242/dev.01178

Bertocchini, F., & Stern, C. D. (2002). The hypoblast of the chick embryo positions the primitive streak by antagonizing nodal signaling. *Developmental Cell*. https://doi.org/10.1016/S1534-5807(02)00318-0

Bienz, M. (2005). β-catenin: A pivot between cell adhesion and Wnt signalling. In *Current Biology*. https://doi.org/10.1016/j.cub.2004.12.058

Biguri, A., 2020. Perceptually uniform colormaps. (https://www.mathworks.com/matlabcentral/fileexchange/51986-perceptually-uniform-1369colormaps) MATLAB Central File Exchange. Retrieved April 24, 2020.

Bischoff, R. (1990). Interaction between satellite cells and skeletal muscle fibers. *Development*.

Bissell, M. J., Hall, H. G., & Parry, G. (1982). How does the extracellular matrix direct gene expression? *Journal of Theoretical Biology*, *99*(1), 31–68. https://doi.org/10.1016/0022-5193(82)90388-5

Biteau, B., & Jasper, H. (2014). Slit/Robo Signaling Regulates Cell Fate Decisions in the Intestinal Stem Cell Lineage of Drosophila. *Cell Reports*, *7*(6), 1867–1875. https://doi.org/10.1016/j.celrep.2014.05.024

Bjornson, C. R. R., Cheung, T. H., Liu, L., Tripathi, P. V., Steeper, K. M., & Rando, T. A. (2012). Notch signaling is necessary to maintain quiescence in adult muscle stem cells. *Stem Cells*. https://doi.org/10.1002/stem.773

Blin, G., Wisniewski, D., Picart, C., Thery, M., Puceat, M., & Lowell, S. (2018). Geometrical confinement controls the asymmetric patterning of brachyury in cultures of pluripotent cells. *Development (Cambridge)*. https://doi.org/10.1242/dev.166025

Bonnans, C., Chou, J., & Werb, Z. (2014). Remodelling the extracellular matrix in development and disease. *Nature Reviews Molecular Cell Biology*, *15*(12), 786–801. https://doi.org/10.1038/nrm3904

Boonsanay, V., Zhang, T., Georgieva, A., Kostin, S., Qi, H., Yuan, X., Zhou, Y., & Braun, T. (2016). Regulation of Skeletal Muscle Stem Cell Quiescence by Suv4-20h1-Dependent Facultative Heterochromatin Formation. *Cell Stem Cell*. https://doi.org/10.1016/j.stem.2015.11.002

Boucaut, J. C., Darribere, T., Poole, T. J., Aoyama, H., Yamada, K. M., & Thiery, J. P. (1984). Biologically active synthetic peptides as probes of embryonic development: A competitive peptide inhibitor of fibronectin function inhibits gastrulation in amphibian embryos and neural cell migration in avian embryos. *Journal of Cell Biology*, *99*(5), 1822–1830. https://doi.org/10.1083/jcb.99.5.1822

Boucaut, J. C., Darribere, T., Shi De Li, Boulekbache, H., Yamada, K. M., & Thiery, J. P. (1985). Evidence for the role of fibronectin in amphibian gastrulation. *Journal of Embryology and Experimental Morphology*, *89*(SUPPL.).

Boudreau, N., Sympson, C. J., Werb, Z., & Bissell, M. J. (1995). Suppression of ICE and apoptosis in mammary epithelial cells by extracellular matrix. *Science*, *267*(5199), 891–893. https://doi.org/10.1126/science.7531366

Bourguignon, L. Y. W., Ramez, M., Gilad, E., Singleton, P. a, Man, M.-Q., Crumrine, D. a, Elias, P. M., & Feingold, K. R. (2006). Hyaluronan-CD44 interaction stimulates keratinocyte differentiation, lamellar body formation/secretion, and permeability barrier homeostasis. *The Journal of Investigative Dermatology*, *126*(6), 1356–1365. https://doi.org/10.1038/sj.jid.5700260

Bourikas, D., Pekarik, V., Baeriswyl, T., Grunditz, Å., Sadhu, R., Nardó, M., & Stoeckli, E. T. (2005). Sonic hedgehod guides commissural axons along the longitudinal axis of the spinal cord. *Nature Neuroscience*. https://doi.org/10.1038/nn1396

Brack, A. S., Conboy, I. M., Conboy, M. J., Shen, J., & Rando, T. A. (2008). A Temporal Switch from Notch to Wnt Signaling in Muscle Stem Cells Is Necessary for Normal Adult Myogenesis. *Cell Stem Cell*. https://doi.org/10.1016/j.stem.2007.10.006

Brack, A. S., & Muñoz-Cánoves, P. (2016). The ins and outs of muscle stem cell aging. In *Skeletal*

Muscle. https://doi.org/10.1186/s13395-016-0072-z

Brack, A. S., Murphy-Seiler, F., Hanifi, J., Deka, J., Eyckerman, S., Keller, C., Aguet, M., & Rando, T. A. (2009). BCL9 is an essential component of canonical Wnt signaling that mediates the differentiation of myogenic progenitors during muscle regeneration. *Developmental Biology*. https://doi.org/10.1016/j.ydbio.2009.08.014

Brack, A. S., & Rando, T. A. (2007). Intrinsic changes and extrinsic influences of myogenic stem cell function during aging. *Stem Cell Reviews*. https://doi.org/10.1007/s12015-007-9000-2

Briscoe, J., & Ericson, J. (2001). Specification of neuronal fates in the ventral neural tube. In *Current Opinion in Neurobiology*. https://doi.org/10.1016/S0959-4388(00)00172-0

Brower, D. L., & Jaffe, S. M. (1989). Requirement for integrins during Drosophila wing development. *Nature*, *342*(6247), 285–287. https://doi.org/10.1038/342285a0

Brunet, T., Bouclet, A., Ahmadi, P., Mitrossilis, D., Driquez, B., Brunet, A. C., Henry, L., Serman, F., Béalle, G., Ménager, C., Dumas-Bouchiat, F., Givord, D., Yanicostas, C., Le-Roy, D., Dempsey, N. M., Plessis, A., & Farge, E. (2013). Evolutionary conservation of early mesoderm specification by mechanotransduction in Bilateria. *Nature Communications*. https://doi.org/10.1038/ncomms3821

Bryant, J. D., David, T., Gaskell, P. H., King, S., & Lond, G. (1989). Rheology of bovine bone marrow. In *Proceedings of the Institution of Mechanical Engineers, Part H: Journal of Engineering in Medicine*. https://doi.org/10.1243/PIME_PROC_1989_203_013_01

Burdsal, C. A., Damsky, C. H., & Pedersen, R. A. (1993). The role of E-cadherin and integrins in mesoderm differentiation and migration at the mammalian primitive streak. *Development*.

Burridge, K., & Guilluy, C. (2016). Focal adhesions, stress fibers and mechanical tension. In

Experimental Cell Research. https://doi.org/10.1016/j.yexcr.2015.10.029

Cardoso, W. V. (2006). Regulation of early lung morphogenesis: questions, facts and controversies. *Development*, *133*(9), 1611–1624. https://doi.org/10.1242/dev.02310

Chakkalakal, J. V., Christensen, J., Xiang, W., Tierney, M. T., Boscolo, F. S., Sacco, A., & Brack, A. S. (2014). Early forming label-retaining muscle stem cells require p27kip1 for maintenance of the primitive state. *Development (Cambridge)*. https://doi.org/10.1242/dev.100842

Chang, W., Lin, Z., Kulessa, H., Hebert, J., Hogan, B. L. M., & Wu, D. K. (2008). Bmp4 is essential for the formation of the vestibular apparatus that detects angular head movements. *PLoS Genetics*, *4*(4). https://doi.org/10.1371/journal.pgen.1000050

Chapman, S. C., Collignon, J., Schoenwolf, G. C., & Lumsden, A. (2001). Improved method for chick whole-embryo culture using a filter paper carrier. *Developmental Dynamics*. https://doi.org/10.1002/1097-0177(20010301)220:3<284::AID-DVDY1102>3.0.CO;2-5

Chapman, S. C., Schubert, F. R., Schoenwolf, G. C., & Lumsden, A. (2002). Analysis of spatial and temporal gene expression patterns in blastula and gastrula stage chick embryos. *Developmental Biology*. https://doi.org/10.1006/dbio.2002.0641

Chen, G., Deng, C., & Li, Y. P. (2012). TGF-β and BMP signaling in osteoblast differentiation and bone formation. In *International Journal of Biological Sciences* (Vol. 8, Issue 2, pp. 272–288). https://doi.org/10.7150/ijbs.2929

Cheng, S., Fockler, C., Barnes, W. M., & Higuchi, R. (1994). Effective amplification of long targets from cloned inserts and human genomic DNA. *Proceedings of the National Academy of Sciences of the United States of America*. https://doi.org/10.1073/pnas.91.12.5695

Cheung, T. H., Quach, N. L., Charville, G. W., Liu, L., Park, L., Edalati, A., Yoo, B., Hoang, P., &

Rando, T. A. (2012). Maintenance of muscle stem-cell quiescence by microRNA-489. *Nature*. https://doi.org/10.1038/nature10834

Cheung, T. H., & Rando, T. A. (2013). Molecular regulation of stem cell quiescence. *Nature Reviews Molecular Cell Biology*, *14*(6), 329–340. https://doi.org/10.1038/nrm3591

Chhabra, S., Liu, L., Goh, R., Kong, X., & Warmflash, A. (2019). Dissecting the dynamics of signaling events in the BMP, WNT, and NODAL cascade during self-organized fate patterning in human gastruloids. *PLoS Biology*. https://doi.org/10.1371/journal.pbio.3000498

Choi, H. M. T., Schwarzkopf, M., Fornace, M. E., Acharya, A., Artavanis, G., Stegmaier, J., Cunha, A., & Pierce, N. A. (2018). Third-generation in situ hybridization chain reaction: Multiplexed, quantitative, sensitive, versatile, robust. *Development (Cambridge)*. https://doi.org/10.1242/dev.165753

Choi, J. S., & Harley, B. A. C. (2017). Marrow-inspired matrix cues rapidly affect early fate decisions of hematopoietic stem and progenitor cells. *Science Advances*. https://doi.org/10.1126/sciadv.1600455

Chrzanowska-Wodnicka, M., & Burridge, K. (1996). Rho-stimulated contractility drives the formation of stress fibers and focal adhesions. *Journal of Cell Biology*. https://doi.org/10.1083/jcb.133.6.1403

Chu, V. T., Weber, T., Wefers, B., Wurst, W., Sander, S., Rajewsky, K., & Kühn, R. (2015). Increasing the efficiency of homology-directed repair for CRISPR-Cas9-induced precise gene editing in mammalian cells. *Nature Biotechnology*. https://doi.org/10.1038/nbt.3198

Clevers, H. (2006). Wnt/β-Catenin Signaling in Development and Disease. In *Cell* (Vol. 127, Issue 3, pp. 469–480). https://doi.org/10.1016/j.cell.2006.10.018

Clevers, H., Loh, K. M., & Nusse, R. (2014). An integral program for tissue renewal and regeneration:

Wnt signaling and stem cell control. In *Science*. https://doi.org/10.1126/science.1248012

Clevers, H., & Nusse, R. (2012). Wnt/β-catenin signaling and disease. In *Cell*. https://doi.org/10.1016/j.cell.2012.05.012

Cohen, M. M. (2003). The Hedgehog Signaling Network. In *American Journal of Medical Genetics*. https://doi.org/10.1002/ajmg.a.20495

Coles, E. G., Gammill, L. S., Miner, J. H., & Bronner-Fraser, M. (2006). Abnormalities in neural crest cell migration in laminin alpha5 mutant mice. *Dev Biol*, *289*(1), 218–228. https://doi.org/S0012-1606(05)00759-1 [pii]\r10.1016/j.ydbio.2005.10.031

Dabovic, B., Chen, Y., Colarossi, C., Obata, H., Zambuto, L., Perle, M. A., & Rifkin, D. B. (2002). Bone abnormalities in latent TGF-β binding protein (Ltbp)-3-null mice indicate a role for Ltbp-3 in modulating TGF-β bioavailability. *Journal of Cell Biology*, *156*(2), 227–232. https://doi.org/10.1083/jcb.200111080

Davidson, L. A., & Keller, R. E. (1999). Neural tube closure in Xenopus laevis involves medial migration, directed protrusive activity, cell intercalation and convergent extension. *Development*.

Davidson, Lance A., Dzamba, B. D., Keller, R., & Desimone, D. W. (2008). Live imaging of cell protrusive activity, and extracellular matrix assembly and remodeling during morphogenesis in the frog, Xenopus laevis. *Developmental Dynamics*. https://doi.org/10.1002/dvdy.21600

Debelle, L., & Tamburro, A. M. (1999). Elastin: Molecular description and function. In *International Journal of Biochemistry and Cell Biology* (Vol. 31, Issue 2, pp. 261–272). https://doi.org/10.1016/S1357-2725(98)00098-3

Dickson, M. C., Slager, H. G., Duffie, E., Mummery, C. L., & Akhurst, R. J. (1993). RNA and protein localisations of TGF beta 2 in the early mouse embryo suggest an involvement in cardiac

development. *Development (Cambridge, England)*, *117*(2), 625–639. http://www.ncbi.nlm.nih.gov/pubmed/7687212

Dixon, J. E., Shah, D. A., Rogers, C., Hall, S., Weston, N., Parmenter, C. D. J., McNally, D., Denning, C., & Shakesheff, K. M. (2014). Combined hydrogels that switch human pluripotent stem cells from self-renewal to differentiation. *Proceedings of the National Academy of Sciences*, *111*(15), 5580–5585. https://doi.org/10.1073/pnas.1319685111

Dupont, S., Morsut, L., Aragona, M., Enzo, E., Giulitti, S., Cordenonsi, M., Zanconato, F., Le Digabel, J., Forcato, M., Bicciato, S., Elvassore, N., & Piccolo, S. (2011). Role of YAP/TAZ in mechanotransduction. *Nature*, *474*(7350), 179–183. https://doi.org/10.1038/nature10137

Eliazer, S., Muncie, J. M., Christensen, J., Sun, X., D'Urso, R. S., Weaver, V. M., & Brack, A. S. (2019). Wnt4 from the Niche Controls the Mechano-Properties and Quiescent State of Muscle Stem Cells. *Cell Stem Cell*. https://doi.org/10.1016/j.stem.2019.08.007

Engler, A. J., Sen, S., Sweeney, H. L., & Discher, D. E. (2006). Matrix Elasticity Directs Stem Cell Lineage Specification. *Cell*, *126*(4), 677–689. https://doi.org/10.1016/j.cell.2006.06.044

Erlebacher, A., & Derynck, R. (1996). Increased expression of TGF-β2 in osteoblasts results in an osteoporosis-like phenotype. *Journal of Cell Biology*, *132*(1–2), 195–210. https://doi.org/10.1083/jcb.132.1.195

Etoc, F., Metzger, J., Ruzo, A., Kirst, C., Yoney, A., Ozair, M. Z., Brivanlou, A. H., & Siggia, E. D. (2016). A Balance between Secreted Inhibitors and Edge Sensing Controls Gastruloid Self-Organization. *Developmental Cell*, *39*(3), 302–315. https://doi.org/10.1016/j.devcel.2016.09.016

Fässler, R., Rohwedel, J., Maltsev, V., Bloch, W., Lentini, S., Guan, K., Gullberg, D., Hescheler, J., Addicks, K., & Wobus, a M. (1996). Differentiation and integrity of cardiac muscle cells are

impaired in the absence of beta 1 integrin. *Journal of Cell Science*, *109 (Pt 1*, 2989–2999.

Flanagan, L. A., Ju, Y. El, Marg, B., Osterfield, M., & Janmey, P. A. (2002). Neurite branching on deformable substrates. *NeuroReport*, *13*(18), 2411–2415. https://doi.org/10.1097/00001756-200212200-00007

Foty, R. A., & Steinberg, M. S. (2004). Cadherin-mediated cell-cell adhesion and tissue segregation in relation to malignancy. In *International Journal of Developmental Biology*. https://doi.org/10.1387/ijdb.041810rf

Foty, R. A., & Steinberg, M. S. (2005). The differential adhesion hypothesis: A direct evaluation. *Developmental Biology*. https://doi.org/10.1016/j.ydbio.2004.11.012

Friedland, J. C., Lee, M. H., & Boettiger, D. (2009). Mechanically Activated Integrin Switch Controls 5 1 Function. *Science*, *323*(5914), 642–644. https://doi.org/10.1126/science.1168441

Gayrard, C., Bernaudin, C., Déjardin, T., Seiler, C., & Borghi, N. (2018). Src- and confinement-dependent FAK activation causes E-cadherin relaxation and β-catenin activity. *Journal of Cell Biology*. https://doi.org/10.1083/jcb.201706013

Gayraud-Morel, B., Chrétien, F., & Tajbakhsh, S. (2009). Skeletal muscle as a paradigm for regenerative biology and medicine. In *Regenerative Medicine*. https://doi.org/10.2217/17460751.4.2.293

Gilbert, P. M., Havenstrite, K. L., Magnusson, K. E. G., Sacco, A., Leonardi, N. A., Kraft, P., Nguyen, N. K., Thrun, S., Lutolf, M. P., & Blau, H. M. (2010). Substrate elasticity regulates skeletal muscle stem cell self-renewal in culture. *Science*, *329*(5995), 1078–1081. https://doi.org/10.1126/science.1191035

Goel, A. J., Rieder, M. K., Arnold, H. H., Radice, G. L., & Krauss, R. S. (2017). Niche Cadherins

Control the Quiescence-to-Activation Transition in Muscle Stem Cells. *Cell Reports*. https://doi.org/10.1016/j.celrep.2017.10.102

Gomez, E. W., Chen, Q. K., Gjorevski, N., & Nelson, C. M. (2010). Tissue geometry patterns epithelial-mesenchymal transition via intercellular mechanotransduction. *Journal of Cellular Biochemistry*. https://doi.org/10.1002/jcb.22545

Gordon, M. K., & Hahn, R. A. (2010). Collagens. In *Cell and Tissue Research* (Vol. 339, Issue 1, pp. 247–257). https://doi.org/10.1007/s00441-009-0844-4

Gottardi, C. J., & Gumbiner, B. M. (2004). Distinct molecular forms of β-catenin are targeted to adhesive or transcriptional complexes. *Journal of Cell Biology*. https://doi.org/10.1083/jcb.200402153

Goumans, M. J., de Boer, T. P., Smits, A. M., van Laake, L. W., van Vliet, P., Metz, C. H. G., Korfage, T. H., Kats, K. P., Hochstenbach, R., Pasterkamp, G., Verhaar, M. C., van der Heyden, M. A. G., de Kleijn, D., Mummery, C. L., van Veen, T. A. B., Sluijter, J. P. G., & Doevendans, P. A. (2008). TGF-β1 induces efficient differentiation of human cardiomyocyte progenitor cells into functional cardiomyocytes in vitro. *Stem Cell Research*, *1*(2), 138–149. https://doi.org/10.1016/j.scr.2008.02.003

Gräper, L. (1929). Die Primitiventwicklung des Hühnchens nach stereokinematographischen Untersuchungen, kontrolliert durch vitale Farbmarkierung und verglichen mit der Entwicklung anderer Wirbeltiere. *Wilhelm Roux' Archiv Für Entwicklungsmechanik Der Organismen*. https://doi.org/10.1007/BF02145235

Guo, X., Johnson, J. J., & Kramer, J. M. (1991). Embryonic lethality caused by mutations in basement membrane collagen of C. elegans. *Nature*, *349*(6311), 707–709.

https://doi.org/10.1038/349707a0

Habas, R., Dawid, I. B., & He, X. (2003). Coactivation of Rac and Rho by Wnt/Frizzled signaling is required for vertebrate gastrulation. *Genes and Development*. https://doi.org/10.1101/gad.1022203

Hamada, H. (2015). Role of physical forces in embryonic development. In *Seminars in Cell and Developmental Biology*. https://doi.org/10.1016/j.semcdb.2015.10.011

Hamburger, V., & Hamilton, H. L. (1992). A series of normal stages in the development of the chick embryo. *Developmental Dynamics*. https://doi.org/10.1002/aja.1001950404

Hamidouche, Z., Fromigué, O., Ringe, J., Häupl, T., Vaudin, P., Pagès, J.-C., Srouji, S., Livne, E., & Marie, P. J. (2009). Priming integrin alpha5 promotes human mesenchymal stromal cell osteoblast differentiation and osteogenesis. *Proceedings of the National Academy of Sciences of the United States of America*, *106*, 18587–18591. https://doi.org/10.1016/j.bone.2009.03.058

Han, V. K., D'Ercole, a J., & Lund, P. K. (1987). Cellular localization of somatomedin (insulin-like growth factor) messenger RNA in the human fetus. *Science*, *236*(4798), 193–197.

Hao, J., Zhang, Y., Wang, Y., Ye, R., Qiu, J., Zhao, Z., & Li, J. (2014). Role of extracellular matrix and YAP/TAZ in cell fate determination. In *Cellular Signalling* (Vol. 26, Issue 2, pp. 186–191). https://doi.org/10.1016/j.cellsig.2013.11.006

Harada, M., Murakami, H., Okawa, A., Okimoto, N., Hiraoka, S., Nakahara, T., Akasaka, R., Shiraishi, Y.-I., Futatsugi, N., Mizutani-Koseki, Y., Kuroiwa, A., Shirouzu, M., Yokoyama, S., Taiji, M., Iseki, S., Ornitz, D. M., & Koseki, H. (2009). FGF9 monomer-dimer equilibrium regulates extracellular matrix affinity and tissue diffusion. *Nature Genetics*, *41*(3), 289–298. https://doi.org/10.1038/ng.316

Harrison, S. E., Sozen, B., Christodoulou, N., Kyprianou, C., & Zernicka-Goetz, M. (2017). Assembly

of embryonic and extraembryonic stem cells to mimic embryogenesis in vitro. *Science*, *356*(6334), eaal1810. https://doi.org/10.1126/science.aal1810

Heasman, J., Crawford, A., Goldstone, K., Garner-Hamrick, P., Gumbiner, B., McCrea, P., Kintner, C., Noro, C. Y., & Wylie, C. (1994). Overexpression of cadherins and underexpression of β-catenin inhibit dorsal mesoderm induction in early Xenopus embryos. *Cell*. https://doi.org/10.1016/0092-8674(94)90069-8

Heisenberg, C. P., & Bellaïche, Y. (2013). XForces in tissue morphogenesis and patterning. In *Cell*. https://doi.org/10.1016/j.cell.2013.05.008

Hill, C. S. (2009). Nucleocytoplasmic shuttling of Smad proteins. In *Cell Research*. https://doi.org/10.1038/cr.2008.325

Hill, D. J., Clemmons, D. R., Wilson, S., Han, V. K. M., Strain, A. J., & Milner, R. D. G. (1989). Immunological distribution of one form of insulin-like growth factor (IGF)-binding protein and IGF peptides in human fetal tissues. *Journal of Molecular Endocrinology*, *2*(1), 31–38.

Hines, M., Nielsen, L., & Cooper-White, J. (2008). The hematopoietic stem cell niche: What are we trying to replicate? In *Journal of Chemical Technology and Biotechnology*. https://doi.org/10.1002/jctb.1856

Hinz, B. (2015). The extracellular matrix and transforming growth factor-β1: Tale of a strained relationship. In *Matrix Biology* (Vol. 47, pp. 54–65). https://doi.org/10.1016/j.matbio.2015.05.006

Hirate, Y., Hirahara, S., Inoue, K. I., Suzuki, A., Alarcon, V. B., Akimoto, K., Hirai, T., Hara, T., Adachi, M., Chida, K., Ohno, S., Marikawa, Y., Nakao, K., Shimono, A., & Sasaki, H. (2013). Polarity-dependent distribution of angiomotin localizes hippo signaling in preimplantation

embryos. *Current Biology*. https://doi.org/10.1016/j.cub.2013.05.014

Holst, J., Watson, S., Lord, M. S., Eamegdool, S. S., Bax, D. V., Nivison-Smith, L. B., Kondyurin, A., Ma, L., Oberhauser, A. F., Weiss, A. S., & Rasko, J. E. J. (2010). Substrate elasticity provides mechanical signals for the expansion of hemopoietic stem and progenitor cells. *Nature Biotechnology*. https://doi.org/10.1038/nbt.1687

Hong, W., & Guan, K. L. (2012). The YAP and TAZ transcription co-activators: Key downstream effectors of the mammalian Hippo pathway. In *Seminars in Cell and Developmental Biology* (Vol. 23, Issue 7, pp. 785–793). https://doi.org/10.1016/j.semcdb.2012.05.004

Hookway, T. A., Butts, J. C., Lee, E., Tang, H., & McDevitt, T. C. (2016). Aggregate formation and suspension culture of human pluripotent stem cells and differentiated progeny. *Methods*. https://doi.org/10.1016/j.ymeth.2015.11.027

Hortsch, M., & Goodman, C. S. (1991). *Cell and Substrate*.

Howard, S., Deroo, T., Fujita, Y., & Itasaki, N. (2011). A positive role of cadherin in wnt/β-catenin signalling during epithelial-mesenchymal transition. *PLoS ONE*. https://doi.org/10.1371/journal.pone.0023899

Howden, S. E., Wardan, H., Voullaire, L., McLenachan, S., Williamson, R., Ioannou, P., & Vadolas, J. (2006). Chromatin-binding regions of EBNA1 protein facilitate the enhanced transfection of Epstein-Barr virus-based vectors. *Human Gene Therapy*. https://doi.org/10.1089/hum.2006.17.833

Hsieh, J., Aimone, J. B., Kaspar, B. K., Kuwabara, T., Nakashima, K., & Gage, F. H. (2004). IGF-I instructs multipotent adult neural progenitor cells to become oligodendrocytes. *Journal of Cell Biology*, *164*(1), 111–122. https://doi.org/10.1083/jcb.200308101

Huang, J., Wu, S., Barrera, J., Matthews, K., & Pan, D. (2005). The Hippo signaling pathway coordinately regulates cell proliferation and apoptosis by inactivating Yorkie, the Drosophila homolog of YAP. *Cell*, *122*(3), 421–434. https://doi.org/10.1016/j.cell.2005.06.007

Hynes, R. O. (2002). Integrins: Bidirectional, allosteric signaling machines. In *Cell* (Vol. 110, Issue 6, pp. 673–687). https://doi.org/10.1016/S0092-8674(02)00971-6

Inoue, Y., Suzuki, M., Watanabe, T., Yasue, N., Tateo, I., Adachi, T., & Ueno, N. (2016). Mechanical roles of apical constriction, cell elongation, and cell migration during neural tube formation in Xenopus. *Biomechanics and Modeling in Mechanobiology*. https://doi.org/10.1007/s10237-016-0794-1

Ishii, N., Wadsworth, W. G., Stern, B. D., Culotti, J. G., & Hedgecock, E. M. (1992). UNC-6, a laminin-related protein, guides cell and pioneer axon migrations in C. elegans. *Neuron*, *9*(5), 873–881. https://doi.org/10.1016/0896-6273(92)90240-E

Jackson, B., Peyrollier, K., Pedersen, E., Basse, A., Karlsson, R., Wang, Z., Lefever, T., Ochsenbein, A. M., Schmidt, G., Aktories, K., Stanley, A., Quondamatteo, F., Ladwein, M., Rottner, K., Van Hengel, J., & Brakebusch, C. (2011). RhoA is dispensable for skin development, but crucial for contraction and directed migration of keratinocytes. *Molecular Biology of the Cell*. https://doi.org/10.1091/mbc.E09-10-0859

Jacobson, A. G., & Gordon, R. (1976). Changes in the shape of the developing vertebrate nervous system analyzed experimentally, mathematically and by computer simulation. *Journal of Experimental Zoology*. https://doi.org/10.1002/jez.1401970205

Jansen, L. E., Birch, N. P., Schiffman, J. D., Crosby, A. J., & Peyton, S. R. (2015). Mechanics of intact bone marrow. *Journal of the Mechanical Behavior of Biomedical Materials*.

https://doi.org/10.1016/j.jmbbm.2015.06.023

Jessell, T. M. (2000). Neuronal specification in the spinal cord: Inductive signals and transcriptional codes. In *Nature Reviews Genetics*. https://doi.org/10.1038/35049541

Jia, J., Maccarana, M., Zhang, X., Bespalov, M., Lindahl, U., & Li, J. P. (2009). Lack of L-iduronic acid in heparan sulfate affects interaction with growth factors and cell signaling. *Journal of Biological Chemistry*, *284*(23), 15942–15950. https://doi.org/10.1074/jbc.M809577200

Jikko, A., Harris, S. E., Chen, D., Mendrick, D. L., & Damsky, C. H. (1999). Collagen Integrin Receptors Regulate Early Osteoblast Differentiation Induced by BMP-2. *Journal of Bone and Mineral Research*, *14*(7), 1075–1083. https://doi.org/10.1359/jbmr.1999.14.7.1075

Jones, A. E., Price, F. D., Le Grand, F., Soleimani, V. D., Dick, S. A., Megeney, L. A., & Rudnicki, M. A. (2015). Wnt/β-catenin controls follistatin signalling to regulate satellite cell myogenic potential. *Skeletal Muscle*. https://doi.org/10.1186/s13395-015-0038-6

Jones, J. I., Gockerman, A., Busby, W. H., Camacho-Hubner, C., & Clemmons, D. R. (1993). Extracellular matrix contains insulin-like growth factor binding protein-5: Potentiation of the effects of IGF-I. *Journal of Cell Biology*, *121*(3), 679–687. https://doi.org/10.1083/jcb.121.3.679

Jürgensen, H. J., Madsen, D. H., Ingvarsen, S., Melander, M. C., Gårdsvoll, H., Patthy, L., Engelholm, L. H., & Behrendt, N. (2011). A novel functional role of collagen glycosylation: Interaction with the endocytic collagen receptor uPARAP/ENDO180. *Journal of Biological Chemistry*, *286*(37), 32736–32748. https://doi.org/10.1074/jbc.M111.266692

Jussila, M., & Ciruna, B. (2017). Zebrafish models of non-canonical Wnt/planar cell polarity signalling: fishing for valuable insight into vertebrate polarized cell behavior. *Wiley Interdisciplinary Reviews: Developmental Biology*. https://doi.org/10.1002/wdev.267

Kadler, K. E., Hill, A., & Canty-Laird, E. G. (2008). Collagen fibrillogenesis: fibronectin, integrins, and minor collagens as organizers and nucleators. In *Current Opinion in Cell Biology* (Vol. 20, Issue 5, pp. 495–501). https://doi.org/10.1016/j.ceb.2008.06.008

Kagan, H. M., & Li, W. (2003). Lysyl oxidase: Properties, specificity, and biological roles inside and outside of the cell. *Journal of Cellular Biochemistry*, *88*(4), 660–672. https://doi.org/10.1002/jcb.10413

Karabagli, H., Karabagli, P., Ladher, R. K., & Schoenwolf, G. C. (2002). Comparison of the expression patterns of several fibroblast growth factors during chick gastrulation and neurulation. *Anatomy and Embryology*. https://doi.org/10.1007/s00429-002-0264-7

Keller, R. (2005). Cell migration during gastrulation. In *Current Opinion in Cell Biology* (Vol. 17, Issue 5 SPEC. ISS., pp. 533–541). https://doi.org/10.1016/j.ceb.2005.08.006

Kemp, C., Willems, E., Abdo, S., Lambiv, L., & Leyns, L. (2005). Expression of all Wnt genes and their secreted antagonists during mouse blastocyst and postimplantation development. *Developmental Dynamics*. https://doi.org/10.1002/dvdy.20408

Khetarpal, U., Robertson, N. G., Yoo, T. J., & Morton, C. C. (1994). Expression and localization of COL2A1 mRNA and type II collagen in human fetal cochlea. *Hearing Research*, *79*(1–2), 59–73. https://doi.org/10.1016/0378-5955(94)90127-9

Kilian, K. A., Bugarija, B., Lahn, B. T., & Mrksich, M. (2010). Geometric cues for directing the differentiation of mesenchymal stem cells. *Proceedings of the National Academy of Sciences*, *107*(11), 4872–4877. https://doi.org/10.1073/pnas.0903269107

Kimmel, J. C., Chang, A. Y., Brack, A. S., & Marshall, W. F. (2018). Inferring cell state by quantitative motility analysis reveals a dynamic state system and broken detailed balance. *PLoS Computational*

Biology. https://doi.org/10.1371/journal.pcbi.1005927

Kimura, K., Ito, M., Amano, M., Chihara, K., Fukata, Y., Nakafuku, M., Yamamori, B., Feng, J., Nakano, T., Okawa, K., Iwamatsu, A., & Kaibuchi, K. (1996). Regulation of myosin phosphatase by Rho and Rho-associated kinase (Rho- kinase). *Science*. https://doi.org/10.1126/science.273.5272.245

Kinney, M. A., Saeed, R., & McDevitt, T. C. (2014). Mesenchymal morphogenesis of embryonic stem cells dynamically modulates the biophysical microtissue niche. *Scientific Reports*. https://doi.org/10.1038/srep04290

Klamer, S., & Voermans, C. (2014). The role of novel and known extracellular matrix and adhesion molecules in the homeostatic and regenerative bone marrow microenvironment http://www.tandfonline.com/doi/pdf/10.4161/19336918.2014.968501. In *Cell Adhesion and Migration*. https://doi.org/10.4161/19336918.2014.968501

Klein, E. A., Yin, L., Kothapalli, D., Castagnino, P., Byfield, F. J., Xu, T., Levental, I., Hawthorne, E., Janmey, P. A., & Assoian, R. K. (2009). Cell-Cycle Control by Physiological Matrix Elasticity and In Vivo Tissue Stiffening. *Current Biology*, *19*(18), 1511–1518. https://doi.org/10.1016/j.cub.2009.07.069

Klinowska, T. C., Soriano, J. V, Edwards, G. M., Oliver, J. M., Valentijn, A. J., Montesano, R., & Streuli, C. H. (1999). Laminin and beta1 integrins are crucial for normal mammary gland development in the mouse. *Developmental Biology*, *215*(1), 13–32. https://doi.org/10.1006/dbio.1999.9435

Knecht, A. K., & Bronner-Fraser, M. (2002). Induction of the neural crest: a multigene process. *Nature Reviews. Genetics*, *3*(6), 453–461. https://doi.org/10.1038/nrg819

Ko, C. S., & Martin, A. C. (2020). The cellular and molecular mechanisms that establish the mechanics of Drosophila gastrulation. In *Current Topics in Developmental Biology*. https://doi.org/10.1016/bs.ctdb.2019.08.003

Kobayashi, A., Allison Stewart, C., Wang, Y., Fujioka, K., Thomas, N. C., Jamin, S. P., & Behringer, R. R. (2011). β-Catenin is essential for Müllerian duct regression during male sexual differentiation. *Development*. https://doi.org/10.1242/dev.056143

Koch, F., Scholze, M., Wittler, L., Schifferl, D., Sudheer, S., Grote, P., Timmermann, B., Macura, K., & Herrmann, B. G. (2017). Antagonistic Activities of Sox2 and Brachyury Control the Fate Choice of Neuro-Mesodermal Progenitors. *Developmental Cell*. https://doi.org/10.1016/j.devcel.2017.07.021

Komiya, Y., & Habas, R. (2008). Wnt signal transduction pathways. In *Organogenesis*. https://doi.org/10.4161/org.4.2.5851

Kramer, J. M., Johnson, J. J., Edgar, R. S., Basch, C., & Roberts, S. (1988). The sqt-1 gene of C. elegans encodes a collagen critical for organismal morphogenesis. *Cell*, *55*(4), 555–565. https://doi.org/10.1016/0092-8674(88)90214-0

Krieg, M., Arboleda-Estudillo, Y., Puech, P. H., Käfer, J., Graner, F., Müller, D. J., & Heisenberg, C. P. (2008). Tensile forces govern germ-layer organization in zebrafish. *Nature Cell Biology*. https://doi.org/10.1038/ncb1705

Kubow, K. E., Klotzsch, E., Smith, M. L., Gourdon, D., Little, W. C., & Vogel, V. (2009). Crosslinking of cell-derived 3D scaffolds up-regulates the stretching and unfolding of new extracellular matrix assembled by reseeded cells. *Integrative Biology*, *1*(11–12), 635. https://doi.org/10.1039/b914996a

Kunisaki, Y., Bruns, I., Scheiermann, C., Ahmed, J., Pinho, S., Zhang, D., Mizoguchi, T., Wei, Q.,

Lucas, D., Ito, K., Mar, J. C., Bergman, A., & Frenette, P. S. (2013). Arteriolar niches maintain haematopoietic stem cell quiescence. *Nature*. https://doi.org/10.1038/nature12612

Kurth, I., Franke, K., Pompe, T., Bornhäuser, M., & Werner, C. (2009). Hematopoietic stem and progenitor cells in adhesive microcavities. *Integrative Biology*. https://doi.org/10.1039/b903711j

Kwok, J. C. F., Dick, G., Wang, D., & Fawcett, J. W. (2011). Extracellular matrix and perineuronal nets in CNS repair. *Developmental Neurobiology*, *71*(11), 1073–1089. https://doi.org/10.1002/dneu.20974

Kyprianou, C., Christodoulou, N., Hamilton, R. S., Nahaboo, W., Boomgaard, D. S., Amadei, G., Migeotte, I., & Zernicka-Goetz, M. (2020). Basement membrane remodelling regulates mouse embryogenesis. *Nature*. https://doi.org/10.1038/s41586-020-2264-2

Labrador, J. P., Azcoitia, V., Tuckermann, J., Lin, C., Olaso, E., Mañes, S., Brückner, K., Goergen, J. L., Lemke, G., Yancopoulos, G., Angel, P., Martínez, C., & Klein, R. (2001). The collagen receptor DDR2 regulates proliferation and its elimination leads to dwarfism. *EMBO Reports*, *2*(5), 446–452. https://doi.org/10.1093/embo-reports/kve094

Lacour, F., Vezin, E., Bentzinger, C. F., Sincennes, M. C., Giordani, L., Ferry, A., Mitchell, R., Patel, K., Rudnicki, M. A., Chaboissier, M. C., Chassot, A. A., & Le Grand, F. (2017). R-spondin1 Controls Muscle Cell Fusion through Dual Regulation of Antagonistic Wnt Signaling Pathways. *Cell Reports*. https://doi.org/10.1016/j.celrep.2017.02.036

Lakins, J. N., Chin, A. R., & Weaver, V. M. (2012). Exploring the link between human embryonic stem cell organization and fate using tension-calibrated extracellular matrix functionalized polyacrylamide gels. *Methods in Molecular Biology*. https://doi.org/10.1007/978-1-61779-980-8-24

Larraín, J., Bachiller, D., Lu, B., Agius, E., Piccolo, & Robertis, D. (2000). BMP-binding modules in

chordin: a model for signalling regulation in the extracellular space. *Development (Cambridge, England)*, *127*(4), 821–830. https://doi.org/10.1016/j.drugalcdep.2008.02.002.A

Larue, L., Antos, C., Butz, S., Huber, O., Delmas, V., Dominis, M., & Kemler, R. (1996). A role for cadherins in tissue formation. *Development*.

Laurent, T. C., & Fraser, J. R. (1992). Hyaluronan. *FASEB Journal : Official Publication of the Federation of American Societies for Experimental Biology*, *6*(7), 2397–2404. https://doi.org/10.1016/S0140-6736(01)35637-4

Le Grand, F., Jones, A. E., Seale, V., Scimè, A., & Rudnicki, M. A. (2009). Wnt7a Activates the Planar Cell Polarity Pathway to Drive the Symmetric Expansion of Satellite Stem Cells. *Cell Stem Cell*. https://doi.org/10.1016/j.stem.2009.03.013

Lecuit, T., & Lenne, P. F. (2007). Cell surface mechanics and the control of cell shape, tissue patterns and morphogenesis. In *Nature Reviews Molecular Cell Biology*. https://doi.org/10.1038/nrm2222

Lee-Thedieck, C., Rauch, N., Fiammengo, R., Klein, G., & Spatz, J. P. (2012). Impact of substrate elasticity on human hematopoietic stem and progenitor cell adhesion and motility. *Journal of Cell Science*. https://doi.org/10.1242/jcs.095596

Lee, H. C., Lu, H. C., Turmaine, M., Oliveira, N. M. M., Yang, Y., De Almeida, I., & Stern, C. D. (2020). Molecular anatomy of the pre-primitive-streak chick embryo. *Open Biology*. https://doi.org/10.1098/rsob.190299

Lee, H. H., & Behringer, R. R. (2007). Conditional expression of Wnt4 during chondrogenesis leads to dwarfism in mice. *PLoS ONE*. https://doi.org/10.1371/journal.pone.0000450

Lee, J., Abdeen, A. A., Wycislo, K. L., Fan, T. M., & Kilian, K. A. (2016). Interfacial geometry dictates cancer cell tumorigenicity. *Nature Materials*. https://doi.org/10.1038/nmat4610

Lee, J. S. H., Panorchan, P., Hale, C. M., Khatau, S. B., Kole, T. P., Tseng, Y., & Wirtz, D. (2006). Ballistic intracellular nanorheology reveals ROCK-hard cytoplasmic stiffening response to fluid flow. *Journal of Cell Science*. https://doi.org/10.1242/jcs.02899

Lee, S. T., Yun, J. I., Jo, Y. S., Mochizuki, M., van der Vlies, A. J., Kontos, S., Ihm, J. E., Lim, J. M., & Hubbell, J. A. (2010). Engineering integrin signaling for promoting embryonic stem cell self-renewal in a precisely defined niche. *Biomaterials*, *31*(6), 1219–1226. https://doi.org/10.1016/j.biomaterials.2009.10.054

Leptin, M., Bogaert, T., Lehmann, R., & Wilcox, M. (1989). The function of PS integrins during Drosophila embryogenesis. *Cell*, *56*(3), 401–408. https://doi.org/10.1016/0092-8674(89)90243-2

Lewis, W. H. (1947). Mechanics of invagination. *The Anatomical Record*. https://doi.org/10.1002/ar.1090970203

Li, D., Zhou, J., Wang, L., Shin, M. E., Su, P., Lei, X., Kuang, H., Guo, W., Yang, H., Cheng, L., Tanaka, T. S., Leckband, D. E., Reynolds, A. B., Duan, E., & Wang, F. (2010). Integrated biochemical and mechanical signals regulate multifaceted human embryonic stem cell functions. *Journal of Cell Biology*. https://doi.org/10.1083/jcb.201006094

Li, H., Corrales, C. E., Wang, Z., Zhao, Y., Wang, Y., Liu, H., & Heller, S. (2005). BMP4 signaling is involved in the generation of inner ear sensory epithelia. *BMC Dev Biol*, *5*, 16. https://doi.org/10.1186/1471-213x-5-16

Li, L., Bennett, S. A. L., & Wang, L. (2012). Role of E-cadherin and other cell adhesion molecules in survival and differentiation of human pluripotent stem cells. *Cell Adhesion & Migration*. https://doi.org/10.4161/cam.19583

Li, Q., Zhang, Y., Pluchon, P., Robens, J., Herr, K., Mercade, M., Thiery, J. P., Yu, H., & Viasnoff, V. (2016). Extracellular matrix scaffolding guides lumen elongation by inducing anisotropic intercellular mechanical tension. *Nature Cell Biology*. https://doi.org/10.1038/ncb3310

Li, X., Yu, Z. T. F., Geraldo, D., Weng, S., Alve, N., Dun, W., Kini, A., Patel, K., Shu, R., Zhang, F., Li, G., Jin, Q., & Fu, J. (2015). Desktop aligner for fabrication of multilayer microfluidic devices. *Review of Scientific Instruments*. https://doi.org/10.1063/1.4927197

Li, Y., Li, L., Chen, Z. N., Gao, G., Yao, R., & Sun, W. (2017). Engineering-derived approaches for iPSC preparation, expansion, differentiation and applications. In *Biofabrication* (Vol. 9, Issue 3). https://doi.org/10.1088/1758-5090/aa7e9a

Libby, A. R. G., Joy, D. A., So, P. L., Mandegar, M. A., Muncie, J. M., Mendoza-Camacho, F. N., Weaver, V. M., Conklin, B. R., & McDevitt, T. C. (2018). Spatiotemporal mosaic self-patterning of pluripotent stem cells using CRISPR interference. *ELife*. https://doi.org/10.7554/eLife.36045

Lilien, J., & Balsamo, J. (2005). The regulation of cadherin-mediated adhesion by tyrosine phosphorylation/dephosphorylation of β-catenin. In *Current Opinion in Cell Biology*. https://doi.org/10.1016/j.ceb.2005.08.009

Lindsley, R. C., Gill, J. G., Kyba, M., Murphy, T. L., & Murphy, K. M. (2006). Canonical Wnt signaling is required for development of embryonic stem cell-derived mesoderm. *Development*. https://doi.org/10.1242/dev.02551

Lodish, H., Berk, A., & Zipursky, S. (2000). Collagen: The fibrous Proteins of the Matrix. In *Molecular Cell Biology* (p. Section 22.3).

Lu, P., Takai, K., Weaver, V. M., & Werb, Z. (2011). Extracellular matrix degradation and remodeling

in development and disease. *Cold Spring Harb Perspect Biol*, *3*(12), 1–24. https://doi.org/10.1101/cshperspect.a005058

Lyuksyutova, A. I., Lu, C. C., Milanesio, N., King, L. A., Guo, N., Wang, Y., Nathans, J., Tessier-Lavigne, M., & Zou, Y. (2003). Anterior-Posterior Guidance of Commissural Axons by Wnt-Frizzled Signaling. *Science*. https://doi.org/10.1126/science.1089610

Macias, H., Moran, A., Samara, Y., Moreno, M., Compton, J. E., Harburg, G., Strickland, P., & Hinck, L. (2011). SLIT/ROBO1 signaling suppresses mammary branching morphogenesis by limiting basal cell number. *Developmental Cell*, *20*(6), 827–840. https://doi.org/10.1016/j.devcel.2011.05.012

Maître, J. L. (2017). Mechanics of blastocyst morphogenesis. In *Biology of the Cell*. https://doi.org/10.1111/boc.201700029

Maître, J. L., Berthoumieux, H., Krens, S. F. G., Salbreux, G., Jülicher, F., Paluch, E., & Heisenberg, C. P. (2012). Adhesion functions in cell sorting by mechanically coupling the cortices of adhering cells. *Science*. https://doi.org/10.1126/science.1225399

Mäki, J. M., Räsänen, J., Tikkanen, H., Sormunen, R., Mäkikallio, K., Kivirikko, K. I., & Soininen, R. (2002). Inactivation of the lysyl oxidase gene Lox leads to aortic aneurysms, cardiovascular dysfunction, and perinatal death in mice. *Circulation*, *106*(19), 2503–2509. https://doi.org/10.1161/01.CIR.0000038109.84500.1E

Makris, E. A., Gomoll, A. H., Malizos, K. N., Hu, J. C., & Athanasiou, K. A. (2015). Repair and tissue engineering techniques for articular cartilage. In *Nature Reviews Rheumatology*. https://doi.org/10.1038/nrrheum.2014.157

Malara, A., Currao, M., Gruppi, C., Celesti, G., Viarengo, G., Buracchi, C., Laghi, L., Kaplan, D. L.,

& Balduini, A. (2014). Megakaryocytes contribute to the bone marrow-matrix environment by expressing fibronectin, type IV collagen, and laminin. *Stem Cells*. https://doi.org/10.1002/stem.1626

Mandegar, M. A., Huebsch, N., Frolov, E. B., Shin, E., Truong, A., Olvera, M. P., Chan, A. H., Miyaoka, Y., Holmes, K., Spencer, C. I., Judge, L. M., Gordon, D. E., Eskildsen, T. V., Villalta, J. E., Horlbeck, M. A., Gilbert, L. A., Krogan, N. J., Sheikh, S. P., Weissman, J. S., … Conklin, B. R. (2016). CRISPR Interference Efficiently Induces Specific and Reversible Gene Silencing in Human iPSCs. *Cell Stem Cell*. https://doi.org/10.1016/j.stem.2016.01.022

Manfrin, A., Tabata, Y., Paquet, E. R., Vuaridel, A. R., Rivest, F. R., Naef, F., & Lutolf, M. P. (2019). Engineered signaling centers for the spatially controlled patterning of human pluripotent stem cells. *Nature Methods*. https://doi.org/10.1038/s41592-019-0455-2

Martí, E., & Bovolenta, P. (2002). Sonic hedgehog in CNS development: One signal, multiple outputs. In *Trends in Neurosciences*. https://doi.org/10.1016/S0166-2236(02)02062-3

Martin, D. C., Fowlkes, J. L., Babic, B., & Khokha, R. (1999). Insulin-like growth factor II signaling in neoplastic proliferation is blocked by transgenic expression of the metalloproteinase inhibitor TIMP-1. *Journal of Cell Biology*, *146*(4), 881–892. https://doi.org/10.1083/jcb.146.4.881

Martyn, I., Brivanlou, A. H., & Siggia, E. D. (2019). A wave of WNT signaling balanced by secreted inhibitors controls primitive streak formation in micropattern colonies of human embryonic stem cells. *Development (Cambridge)*. https://doi.org/10.1242/dev.172791

Matsui, T., Raya, A., Callol-Massot, C., Kawakami, Y., Oishi, I., Rodriguez-Esteban, C., & Izpisúa Belmonte, J. C. (2007). miles-apart-Mediated regulation of cell-fibronectin interaction and myocardial migration in zebrafish. *Nature Clinical Practice. Cardiovascular Medicine*, *4 Suppl*

1(February), S77-82. https://doi.org/10.1038/ncpcardio0764

Maya-Ramos, L., & Mikawa, T. (2020). Programmed cell death along the midline axis patterns ipsilaterality in gastrulation. *Science*. https://doi.org/10.1126/science.aaw2731

McBeath, R., Pirone, D. M., Nelson, C. M., Bhadriraju, K., & Chen, C. S. (2004). Cell shape, cytoskeletal tension, and RhoA regulate stem cell lineage commitment. *Developmental Cell*, *6*(4), 483–495. https://doi.org/10.1016/S1534-5807(04)00075-9

McCarthy, J. J., Srikuea, R., Kirby, T. J., Peterson, C. A., & Esser, K. A. (2012). Inducible Cre transgenic mouse strain for skeletal muscle-specific gene targeting. *Skeletal Muscle*. https://doi.org/10.1186/2044-5040-2-8

McMillen, P., & Holley, S. A. (2015). The tissue mechanics of vertebrate body elongation and segmentation. In *Current Opinion in Genetics and Development*. https://doi.org/10.1016/j.gde.2015.02.005

McQuin, C., Goodman, A., Chernyshev, V., Kamentsky, L., Cimini, B. A., Karhohs, K. W., Doan, M., Ding, L., Rafelski, S. M., Thirstrup, D., Wiegraebe, W., Singh, S., Becker, T., Caicedo, J. C., & Carpenter, A. E. (2018). CellProfiler 3.0: Next-generation image processing for biology. *PLoS Biology*. https://doi.org/10.1371/journal.pbio.2005970

Mecham, R. P. (2012). Overview of extracellular matrix. *Current Protocols in Cell Biology*, *SUPPL.57*. https://doi.org/10.1002/0471143030.cb1001s57

Mikawa, T., Poh, A. M., Kelly, K. A., Ishii, Y., & Reese, D. E. (2004). Induction and Patterning of the Primitive Streak, an Organizing Center of Glastrulation in the Amniote. In *Developmental Dynamics*. https://doi.org/10.1002/dvdy.10458

Mikels, A. J., & Nusse, R. (2006). Purified Wnt5a protein activates or inhibits β-catenin-TCF signaling

depending on receptor context. *PLoS Biology*. https://doi.org/10.1371/journal.pbio.0040115

Miroshnikova, Y. A., Rozenberg, G. I., Cassereau, L., Pickup, M., Mouw, J. K., Ou, G., Templeman, K. L., Elloumi-Hannachi, I., Gooch, K., Sarang-Sieminski, A. L., García, A. J., & Weaver, V. M. (2017). A5B1-Integrinpromotes Tension-Dependent Mammary Epithelial Cell Invasion By Engaging the Fibronectin Synergy Site. *Molecular Biology of the Cell*, mbc.E17-02-0126. https://doi.org/10.1091/mbc.E17-02-0126

Mizuno, M., Fujisawa, R., & Kuboki, Y. (2000). Type I collagen-induced osteoblastic differentiation of bone-marrow cells mediated by collagen-α2β1 integrin interaction. *Journal of Cellular Physiology*, *184*(2), 207–213. https://doi.org/10.1002/1097-4652(200008)184:2<207::AID-JCP8>3.0.CO;2-U

Molenaar, M., Van De Wetering, M., Oosterwegel, M., Peterson-Maduro, J., Godsave, S., Korinek, V., Roose, J., Destrée, O., & Clevers, H. (1996). XTcf-3 transcription factor mediates β-catenin-induced axis formation in xenopus embryos. *Cell*. https://doi.org/10.1016/S0092-8674(00)80112-9

Morita, H., Kajiura-Kobayashi, H., Takagi, C., Yamamoto, T. S., Nonaka, S., & Ueno, N. (2012). Cell Movements of the deep layer of non-neural ectoderm underlie complete neural tube closure in Xenopus. *Development*. https://doi.org/10.1242/dev.073239

Morrison, S. J., & Scadden, D. T. (2014). The bone marrow niche for haematopoietic stem cells. In *Nature*. https://doi.org/10.1038/nature12984

Mouw, J. K., Ou, G., & Weaver, V. M. (2014). Extracellular matrix assembly: a multiscale deconstruction. *Nature Reviews Molecular Cell Biology*, *15*(12), 771–785. https://doi.org/10.1038/nrm3902

Muncie, J. M., & Weaver, V. M. (2018). The physical and biochemical properties of the extracellular matrix regulate cell fate. In *Current Topics in Developmental Biology* (Vol. 130, pp. 1-37). Academic Press. https://doi.org/10.1016/bs.ctdb.2018.02.002

Muncie, J. M., Falcón-Banchs, R., Lakins, J. N., Sohn, L. L., & Weaver, V. M. (2019). Patterning the Geometry of Human Embryonic Stem Cell Colonies on Compliant Substrates to Control Tissue-Level Mechanics. *Journal of Visualized Experiments : JoVE*. https://doi.org/10.3791/60334

Muncie, J. M., Ayad, N. M., Lakins, J. N., Xue, X., Fu, J., & Weaver, V. M. (2020). Mechanical Tension Promotes Formation of Gastrulation-like Nodes and Patterns Mesoderm Specification in Human Embryonic Stem Cells. *Developmental Cell*. https://doi.org/10.1016/j.devcel.2020.10.015

Muth, C. A., Steinl, C., Klein, G., & Lee-Thedieck, C. (2013). Regulation of Hematopoietic Stem Cell Behavior by the Nanostructured Presentation of Extracellular Matrix Components. *PLoS ONE*. https://doi.org/10.1371/journal.pone.0054778

Nabhan, A. N., Brownfield, D. G., Harbury, P. B., Krasnow, M. A., & Desai, T. J. (2018). Single-cell Wnt signaling niches maintain stemness of alveolar type 2 cells. *Science*. https://doi.org/10.1126/science.aam6603

Nagel, M., Tahinci, E., Symes, K., & Winklbauer, R. (2004). Guidance of mesoderm cell migration in the Xenopus gastrula requires PDGF signaling. *Development (Cambridge, England)*, *131*, 2727–2736. https://doi.org/10.1242/dev.01141

Naylor, M. J., Li, N., Cheung, J., Lowe, E. T., Lambert, E., Marlow, R., Wang, P., Schatzmann, F., Wintermantel, T., Schüetz, G., Clarke, A. R., Mueller, U., Hynes, N. E., & Streuli, C. H. (2005). Ablation of β1 integrin in mammary epithelium reveals a key role for integrin in glandular morphogenesis and differentiation. *Journal of Cell Biology*, *171*(4), 717–728.

https://doi.org/10.1083/jcb.200503144

Nelson, C. M., Jean, R. P., Tan, J. L., Liu, W. F., Sniadecki, N. J., Spector, A. A., & Chen, C. S. (2005). Emergent patterns of growth controlled by multicellular form and mechanics. *Proceedings of the National Academy of Sciences of the United States of America*. https://doi.org/10.1073/pnas.0502575102

Nelson, W. J., & Nusse, R. (2004). Convergence of Wnt, β-Catenin, and Cadherin pathways. In *Science*. https://doi.org/10.1126/science.1094291

Nikolopoulou, E., Galea, G. L., Rolo, A., Greene, N. D. E., & Copp, A. J. (2017). Neural tube closure: Cellular, molecular and biomechanical mechanisms. In *Development (Cambridge)*. https://doi.org/10.1242/dev.145904

Nilsson, S. K., Debatis, M. E., Dooner, M. S., Madri, J. A., Quesenberry, P. J., & Becker, P. S. (1998). Immunofluorescence characterization of key extracellular matrix proteins in murine bone marrow in situ. *Journal of Histochemistry and Cytochemistry*. https://doi.org/10.1177/002215549804600311

Nishijo, K., Hosoyama, T., Bjornson, C. R. R., Schaffer, B. S., Prajapati, S. I., Bahadur, A. N., Hansen, M. S., Blandford, M. C., McCleish, A. T., Rubin, B. P., Epstein, J. A., Rando, T. A., Capecchi, M. R., & Keller, C. (2009). Biomarker system for studying muscle, stem cells, and cancer in vivo . *The FASEB Journal*. https://doi.org/10.1096/fj.08-128116

Nishimura, T., Honda, H., & Takeichi, M. (2012). Planar cell polarity links axes of spatial dynamics in neural-tube closure. *Cell*. https://doi.org/10.1016/j.cell.2012.04.021

Nombela-Arrieta, C., Pivarnik, G., Winkel, B., Canty, K. J., Harley, B., Mahoney, J. E., Park, S. Y., Lu, J., Protopopov, A., & Silberstein, L. E. (2013). Quantitative imaging of haematopoietic stem and

progenitor cell localization and hypoxic status in the bone marrow microenvironment. *Nature Cell Biology*. https://doi.org/10.1038/ncb2730

Ohashi, T., Kiehart, D. P., & Erickson, H. P. (2002). Dual labeling of the fibronectin matrix and actin cytoskeleton with green fluorescent protein variants. *Journal of Cell Science*, *115*(Pt 6), 1221–1229.

Ohgushi, M., Minaguchi, M., & Sasai, Y. (2015). Rho-Signaling-Directed YAP/TAZ Activity Underlies the Long-Term Survival and Expansion of Human Embryonic Stem Cells. *Cell Stem Cell*. https://doi.org/10.1016/j.stem.2015.07.009

Orford, K. W., & Scadden, D. T. (2008). Deconstructing stem cell self-renewal: Genetic insights into cell-cycle regulation. In *Nature Reviews Genetics*. https://doi.org/10.1038/nrg2269

Orkin, S. H., & Zon, L. I. (2008). Hematopoiesis: An Evolving Paradigm for Stem Cell Biology. In *Cell*. https://doi.org/10.1016/j.cell.2008.01.025

Ornitz, D. M. (2000). FGFs, heparan sulfate and FGFRs: Complex interactions essential for development. *BioEssays*, *22*(2), 108–112. https://doi.org/10.1002/(SICI)1521-1878(200002)22:2<108::AID-BIES2>3.0.CO;2-M

Page-McCaw, A., Ewald, A. J., & Werb, Z. (2007). Matrix metalloproteinases and the regulation of tissue remodelling. *Nature Reviews Molecular Cell Biology*, *8*(3), 221–233. https://doi.org/10.1038/nrm2125

Palmieri, D., Valli, M., Viglio, S., Ferrari, N., Ledda, B., Volta, C., & Manduca, P. (2010). Osteoblasts extracellular matrix induces vessel like structures through glycosylated collagen I. *Experimental Cell Research*, *316*(5), 789–799. https://doi.org/10.1016/j.yexcr.2009.12.006

Pankov, R., Cukierman, E., Katz, B. Z., Matsumoto, K., Lin, D. C., Lin, S., Hahn, C., & Yamada, K. M. (2000). Integrin dynamics and matrix assembly: Tensin-dependent translocation of α5β1

integrins promotes early fibronectin fibrillogenesis. *Journal of Cell Biology*, *148*(5), 1075–1090. https://doi.org/10.1083/jcb.148.5.1075

Paré, A. C., & Zallen, J. A. (2020). Cellular, molecular, and biophysical control of epithelial cell intercalation. In *Current Topics in Developmental Biology*. https://doi.org/10.1016/bs.ctdb.2019.11.014

Parisi, A., Lacour, F., Giordani, L., Colnot, S., Maire, P., & Le Grand, F. (2015). APC is required for muscle stem cell proliferation and skeletal muscle tissue repair. *Journal of Cell Biology*. https://doi.org/10.1083/jcb.201501053

Park, S., Kim, D., Jung, Y. G., & Roh, S. (2015). Thiazovivin, a Rho kinase inhibitor, improves stemness maintenance of embryo-derived stem-like cells under chemically defined culture conditions in cattle. *Animal Reproduction Science*. https://doi.org/10.1016/j.anireprosci.2015.08.003

Paszek, M. J., & Weaver, V. M. (2004). The tension mounts: Mechanics meets morphogenesis and malignancy. In *Journal of Mammary Gland Biology and Neoplasia* (Vol. 9, Issue 4, pp. 325–342). https://doi.org/10.1007/s10911-004-1404-x

Patel, V. N., Knox, S. M., Likar, K. M., Lathrop, C. A., Hossain, R., Eftekhari, S., Whitelock, J. M., Elkin, M., Vlodavsky, I., & Hoffman, M. P. (2007). Heparanase cleavage of perlecan heparan sulfate modulates FGF10 activity during ex vivo submandibular gland branching morphogenesis. *Development*, *134*(23), 4177–4186. https://doi.org/10.1242/dev.011171

Perissinotto, D., Iacopetti, P., Bellina, I., Doliana, R., Colombatti, A., Pettway, Z., Bronner-Fraser, M., Shinomura, T., Kimata, K., Morgelin, M., Lofberg, J., & Perris, R. (2000). Avian neural crest cell migration is diversely regulated by the two major hyaluronan-binding proteoglycans PG-

M/versican and aggrecan. *Development*, *127*(13), 2823–2842. http://www.ncbi.nlm.nih.gov/entrez/query.fcgi?cmd=Retrieve&db=PubMed&dopt=Citation&list_uids=10851128

Petersen, C. P., & Reddien, P. W. (2009). Wnt Signaling and the Polarity of the Primary Body Axis. In *Cell*. https://doi.org/10.1016/j.cell.2009.11.035

Philippos, M., Sambasivan, R., Castel, D., Rocheteau, P., Bizzarro, V., & Tajbakhsh, S. (2012). A critical requirement for notch signaling in maintenance of the quiescent skeletal muscle stem cell state. *Stem Cells*. https://doi.org/10.1002/stem.775

Pietri, T., Eder, O., Breau, M. A., Topilko, P., Blanche, M., Brakebusch, C., Fassler, R., Thiery, J. P., & Dufour, S. (2004). Conditional beta1-integrin gene deletion in neural crest cells causes severe developmental alterations of the peripheral nervous system. *Development*, *131*(16), 3871–3883. https://doi.org/10.1242/dev.01264

Polesskaya, A., Seale, P., & Rudnicki, M. A. (2003). Wnt signaling induces the myogenic specification of resident CD45+ adult stem cells during muscle regeneration. *Cell*. https://doi.org/10.1016/S0092-8674(03)00437-9

Pond, A. C., Bin, X., Batts, T., Roarty, K., Hilsenbeck, S., & Rosen, J. M. (2013). Fibroblast growth factor receptor signaling is essential for normal mammary gland development and stem cell function. *Stem Cells*, *31*(1), 178–189. https://doi.org/10.1002/stem.1266

Prewitz, M. C., Seib, F. P., Von Bonin, M., Friedrichs, J., Stißel, A., Niehage, C., Müller, K., Anastassiadis, K., Waskow, C., Hoflack, B., Bornhäuser, M., & Werner, C. (2013). Tightly anchored tissue-mimetic matrices as instructive stem cell microenvironments. *Nature Methods*. https://doi.org/10.1038/nmeth.2523

Przybyla, L., Muncie, J. M., & Weaver, V. M. (2016a). Mechanical control of epithelial-to-mesenchymal transitions in development and cancer. *Annual Review of Cell and Developmental Biology*, 32, 527-554. https://doi.org/10.1146/annurev-cellbio-111315-125150

Przybyla, L., Lakins, J. N., Sunyer, R., Trepat, X., & Weaver, V. M. (2016b). Monitoring developmental force distributions in reconstituted embryonic epithelia. *Methods*. https://doi.org/10.1016/j.ymeth.2015.09.003

Przybyla, Laralynne, Lakins, J. N., & Weaver, V. M. (2016c). Tissue Mechanics Orchestrate Wnt-Dependent Human Embryonic Stem Cell Differentiation. *Cell Stem Cell*, *19*(4), 462–475. https://doi.org/10.1016/j.stem.2016.06.018

Ramasubramanian, A., Chu-Lagraff, Q. B., Buma, T., Chico, K. T., Carnes, M. E., Burnett, K. R., Bradner, S. A., & Gordon, S. S. (2013). On the role of intrinsic and extrinsic forces in early cardiac S-looping. *Developmental Dynamics*. https://doi.org/10.1002/dvdy.23968

Reddi, A. H., Gay, R., Gay, S., & Miller, E. J. (1977). Transitions in collagen types during matrix-induced cartilage, bone, and bone marrow formation. *Proceedings of the National Academy of Sciences of the United States of America*. https://doi.org/10.1073/pnas.74.12.5589

Redmer, T., Diecke, S., Grigoryan, T., Quiroga-Negreira, A., Birchmeier, W., & Besser, D. (2011). E-cadherin is crucial for embryonic stem cell pluripotency and can replace OCT4 during somatic cell reprogramming. *EMBO Reports*. https://doi.org/10.1038/embor.2011.88

Ridley, A. J., & Hall, A. (1992). The small GTP-binding protein rho regulates the assembly of focal adhesions and actin stress fibers in response to growth factors. *Cell*. https://doi.org/10.1016/0092-8674(92)90163-7

Ringwald, M., Schuh, R., Vestweber, D., Eistetter, H., Lottspeich, F., Engel, J., Dölz, R., Jähnig, F.,

Epplen, J., & Mayer, S. (1987). The structure of cell adhesion molecule uvomorulin. Insights into the molecular mechanism of Ca2+-dependent cell adhesion. *The EMBO Journal*. https://doi.org/10.1002/j.1460-2075.1987.tb02697.x

Robertson, I. B., Horiguchi, M., Zilberberg, L., Dabovic, B., Hadjiolova, K., & Rifkin, D. B. (2015). Latent TGF-β-binding proteins. In *Matrix Biology* (Vol. 47, pp. 44–53). https://doi.org/10.1016/j.matbio.2015.05.005

Rodgers, J. T., King, K. Y., Brett, J. O., Cromie, M. J., Charville, G. W., Maguire, K. K., Brunson, C., Mastey, N., Liu, L., Tsai, C. R., Goodell, M. A., & Rando, T. A. (2014). MTORC1 controls the adaptive transition of quiescent stem cells from G 0 to GAlert. *Nature*. https://doi.org/10.1038/nature13255

Rodgers, J. T., Schroeder, M. D., Ma, C., & Rando, T. A. (2017). HGFA Is an Injury-Regulated Systemic Factor that Induces the Transition of Stem Cells into GAlert. *Cell Reports*. https://doi.org/10.1016/j.celrep.2017.03.066

Röper, J. C., Mitrossilis, D., Stirnemann, G., Waharte, F., Brito, I., Fernandez-Sanchez, M. E., Baaden, M., Salamero, J., & Farge, E. (2018). The major β-catenin/E-cadherin junctional binding site is a primary molecular mechano-transductor of differentiation in vivo. *ELife*. https://doi.org/10.7554/eLife.33381

Rudolf, A., Schirwis, E., Giordani, L., Parisi, A., Lepper, C., Taketo, M. M., & Le Grand, F. (2016). β-Catenin Activation in Muscle Progenitor Cells Regulates Tissue Repair. *Cell Reports*. https://doi.org/10.1016/j.celrep.2016.04.022

Saadaoui, M., Rocancourt, D., Roussel, J., Corson, F., & Gros, J. (2020). A tensile ring drives tissue flows to shape the gastrulating amniote embryo. *Science*.

https://doi.org/10.1126/science.aaw1965

Sagy, N., Slovin, S., Allalouf, M., Pour, M., Savyon, G., Boxman, J., & Nachman, I. (2019). Prediction and control of symmetry breaking in embryoid bodies by environment and signal integration. *Development (Cambridge)*. https://doi.org/10.1242/dev.181917

Saha, K., Keung, A. J., Irwin, E. F., Li, Y., Little, L., Schaffer, D. V., & Healy, K. E. (2008). Substrate Modulus Directs Neural Stem Cell Behavior. *Biophysical Journal*, *95*(9), 4426–4438. https://doi.org/10.1529/biophysj.108.132217

Salbreux, G., Charras, G., & Paluch, E. (2012). Actin cortex mechanics and cellular morphogenesis. In *Trends in Cell Biology*. https://doi.org/10.1016/j.tcb.2012.07.001

Samarage, C. R., White, M. D., Álvarez, Y. D., Fierro-González, J. C., Henon, Y., Jesudason, E. C., Bissiere, S., Fouras, A., & Plachta, N. (2015). Cortical Tension Allocates the First Inner Cells of the Mammalian Embryo. *Developmental Cell*. https://doi.org/10.1016/j.devcel.2015.07.004

San Filippo, J., Sung, P., & Klein, H. (2008). Mechanism of Eukaryotic Homologous Recombination. *Annual Review of Biochemistry*. https://doi.org/10.1146/annurev.biochem.77.061306.125255

Schepers, K., Campbell, T. B., & Passegué, E. (2015). Normal and leukemic stem cell niches: Insights and therapeutic opportunities. In *Cell Stem Cell*. https://doi.org/10.1016/j.stem.2015.02.014

Schindelin, J., Arganda-Carreras, I., Frise, E., Kaynig, V., Longair, M., Pietzsch, T., Preibisch, S., Rueden, C., Saalfeld, S., Schmid, B., Tinevez, J. Y., White, D. J., Hartenstein, V., Eliceiri, K., Tomancak, P., & Cardona, A. (2012). Fiji: An open-source platform for biological-image analysis. In *Nature Methods*. https://doi.org/10.1038/nmeth.2019

Schlessinger, K., Hall, A., & Tolwinski, N. (2009). Wnt signaling pathways meet Rho GTPases. In *Genes and Development*. https://doi.org/10.1101/gad.1760809

Schreck, C., Istvánffy, R., Ziegenhain, C., Sippenauer, T., Ruf, F., Henkel, L., Gärtner, F., Vieth, B., Florian, M. C., Mende, N., Taubenberger, A., Prendergast, Á., Wagner, A., Pagel, C., Grziwok, S., Götze, K. S., Guck, J., Dean, D. C., Massberg, S., … Oostendorp, R. A. J. (2017). Niche WNT5A regulates the actin cytoskeleton during regeneration of hematopoietic stem cells. *Journal of Experimental Medicine*. https://doi.org/10.1084/jem.20151414

Schwarzbauer, J. E., & DeSimone, D. W. (2011). Fibronectins, their fibrillogenesis, and in vivo functions. In *Cold Spring Harbor Perspectives in Biology* (Vol. 3, Issue 7, pp. 1–19). https://doi.org/10.1101/cshperspect.a005041

Sechler, J. L., Corbett, S. A., & Schwarzbauer, J. E. (1997). Modulatory Roles for Integrin Activation and the Synergy Site of Fibronectin during Matrix Assembly. *Molecular Biology of the Cell*, *8*(12), 2563–2573. https://doi.org/10.1091/mbc.8.12.2563

Sengle, G., Charbonneau, N. L., Ono, R. N., Sasaki, T., Alvarez, J., Keene, D. R., Bächinger, H. P., & Sakai, L. Y. (2008). Targeting of bone morphogenetic protein growth factor complexes to fibrillin. *The Journal of Biological Chemistry*, *283*(20), 13874–13888. https://doi.org/10.1074/jbc.M707820200

Seong, J., Tajik, A., Sun, J., Guan, J.-L., Humphries, M. J., Craig, S. E., Shekaran, A., Garcia, A. J., Lu, S., Lin, M. Z., Wang, N., & Wang, Y. (2013). Distinct biophysical mechanisms of focal adhesion kinase mechanoactivation by different extracellular matrix proteins. *Proceedings of the National Academy of Sciences*, *110*(48), 19372–19377. https://doi.org/10.1073/pnas.1307405110

Shahbazi, M. N., Jedrusik, A., Vuoristo, S., Recher, G., Hupalowska, A., Bolton, V., Fogarty, N. M. E., Campbell, A., Devito, L. G., Ilic, D., Khalaf, Y., Niakan, K. K., Fishel, S., & Zernicka-Goetz, M. (2016). Self-organization of the human embryo in the absence of maternal tissues. *Nature Cell Biology*. https://doi.org/10.1038/ncb3347

Shahbazi, M. N., Siggia, E. D., & Zernicka-Goetz, M. (2019). Self-organization of stem cells into embryos: A window on early mammalian development. *Science*. https://doi.org/10.1126/science.aax0164

Shahbazi, M. N., & Zernicka-Goetz, M. (2018). Deconstructing and reconstructing the mouse and human early embryo. In *Nature Cell Biology*. https://doi.org/10.1038/s41556-018-0144-x

Shao, Y., Taniguchi, K., Townshend, R. F., Miki, T., Gumucio, D. L., & Fu, J. (2017). A pluripotent stem cell-based model for post-implantation human amniotic sac development. *Nature Communications*, *8*(1). https://doi.org/10.1038/s41467-017-00236-w

Shin, J. W., Buxboim, A., Spinler, K. R., Swift, J., Christian, D. A., Hunter, C. A., Léon, C., Gachet, C., Dingal, P. C. D. P., Ivanovska, I. L., Rehfeldt, F., Chasis, J. A., & Discher, D. E. (2014). Contractile forces sustain and polarize hematopoiesis from stem and progenitor cells. *Cell Stem Cell*. https://doi.org/10.1016/j.stem.2013.10.009

Shin, J. W., Swift, J., Spinler, K. R., & Discher, D. E. (2011). Myosin-II inhibition and soft 2D matrix maximize multinucleation and cellular projections typical of platelet-producing megakaryocytes. *Proceedings of the National Academy of Sciences of the United States of America*. https://doi.org/10.1073/pnas.1017474108

Simunovic, M., & Brivanlou, A. H. (2017). Embryoids, organoids and gastruloids: new approaches to understanding embryogenesis. *Development*. https://doi.org/10.1242/dev.143529

Simunovic, M., Metzger, J. J., Etoc, F., Yoney, A., Ruzo, A., Martyn, I., Croft, G., You, D. S., Brivanlou, A. H., & Siggia, E. D. (2019). A 3D model of a human epiblast reveals BMP4-driven symmetry breaking. *Nature Cell Biology*. https://doi.org/10.1038/s41556-019-0349-7

Singh, P., Carraher, C., & Schwarzbauer, J. E. (2010). Assembly of fibronectin extracellular marix.

Annu Rev Cell Dev Biol, *26*, 397–419. https://doi.org/10.1146/annurev-cellbio-100109-104020

Sit, S. T., & Manser, E. (2011). Rho GTPases and their role in organizing the actin cytoskeleton. In *Journal of Cell Science*. https://doi.org/10.1242/jcs.064964

Sive, H. L., Grainger, R. M., & Harland, R. M. (2000). Early Development of Xenopus Laevis: A Laboratory Manual. *Spring*.

Skromne, I., & Stern, C. D. (2001). Interactions between Wnt and Vg1 signalling pathways initiate primitive streak formation in the chick embryo. *Development*.

Skromne, Isaac, & Stern, C. D. (2002). A hierarchy of gene expression accompanying induction of the primitive streak by Vg1 in the chick embryo. *Mechanisms of Development*. https://doi.org/10.1016/S0925-4773(02)00034-5

Smith-Berdan, S., Nguyen, A., Hassanein, D., Zimmer, M., Ugarte, F., Ciriza, J., Li, D., García-Ojeda, M. E., Hinck, L., & Forsberg, E. C. (2011). Robo4 cooperates with Cxcr4 to specify hematopoietic stem cell localization to bone marrow niches. *Cell Stem Cell*, *8*(1), 72–83. https://doi.org/10.1016/j.stem.2010.11.030

Smith, M. L., Gourdon, D., Little, W. C., Kubow, K. E., Eguiluz, R. A., Luna-Morris, S., & Vogel, V. (2007). Force-induced unfolding of fibronectin in the extracellular matrix of living cells. *PLoS Biology*, *5*(10), 2243–2254. https://doi.org/10.1371/journal.pbio.0050268

Smith, Q., Rochman, N., Carmo, A. M., Vig, D., Chan, X. Y., Sun, S., & Gerecht, S. (2018). Cytoskeletal tension regulates mesodermal spatial organization and subsequent vascular fate. *Proceedings of the National Academy of Sciences of the United States of America*. https://doi.org/10.1073/pnas.1808021115

Sokol, S. Y. (2015). Spatial and temporal aspects of Wnt signaling and planar cell polarity during

vertebrate embryonic development. In *Seminars in Cell and Developmental Biology*. https://doi.org/10.1016/j.semcdb.2015.05.002

Sokol, S. Y. (2016). Mechanotransduction During Vertebrate Neurulation. In *Current Topics in Developmental Biology*. https://doi.org/10.1016/bs.ctdb.2015.11.036

Soncin, F., Mohamet, L., Eckardt, D., Ritson, S., Eastham, A. M., Bobola, N., Russell, A., Davies, S., Kemler, R., Merry, C. L. R., & Ward, C. M. (2009). Abrogation of E-cadherin-mediated cell-cell contact in mouse embryonic stem cells results in reversible LIF-independent self-renewal. *Stem Cells*. https://doi.org/10.1002/stem.134

Soncin, F., & Ward, C. M. (2011). The function of E-cadherin in stem cell pluripotency and self-renewal. In *Genes*. https://doi.org/10.3390/genes2010229

Sozen, B., Amadei, G., Cox, A., Wang, R., Na, E., Czukiewska, S., Chappell, L., Voet, T., Michel, G., Jing, N., Glover, D. M., & Zernicka-Goetz, M. (2018). Self-assembly of embryonic and two extra-embryonic stem cell types into gastrulating embryo-like structures. *Nature Cell Biology*. https://doi.org/10.1038/s41556-018-0147-7

Spratt, N. T., & Haas, H. (1960). Integrative mechanisms in development of the early chick blastoderm. I. Regulative potentiality of separated parts. *Journal of Experimental Zoology*. https://doi.org/10.1002/jez.1401450202

Stephenson, R. O., Yamanaka, Y., & Rossant, J. (2010). Disorganized epithelial polarity and excess trophectoderm cell fate in preimplantation embryos lacking E-cadherin. *Development*. https://doi.org/10.1242/dev.050195

Streuli, C. (1999). Extracellular matrix remodelling and cellular differentiation. In *Current Opinion in Cell Biology* (Vol. 11, Issue 5, pp. 634–640). https://doi.org/10.1016/S0955-0674(99)00026-5

Sugawara, K., Tsuruta, D., Ishii, M., Jones, J. C. R., & Kobayashi, H. (2008). Laminin-332 and -511 in skin. In *Experimental Dermatology* (Vol. 17, Issue 6, pp. 473–480). https://doi.org/10.1111/j.1600-0625.2008.00721.x

Sugiyama, T., Kohara, H., Noda, M., & Nagasawa, T. (2006). Maintenance of the Hematopoietic Stem Cell Pool by CXCL12-CXCR4 Chemokine Signaling in Bone Marrow Stromal Cell Niches. *Immunity*. https://doi.org/10.1016/j.immuni.2006.10.016

Suh, H. N., & Han, H. J. (2011). Collagen I regulates the self-renewal of mouse embryonic stem cells through ??2??1 integrin- and DDR1-dependent Bmi-1. *Journal of Cellular Physiology*, *226*(12), 3422–3432. https://doi.org/10.1002/jcp.22697

Taber, L. A. (2014). Morphomechanics: Transforming tubes into organs. In *Current Opinion in Genetics and Development*. https://doi.org/10.1016/j.gde.2014.03.004

Tammela, T., Sanchez-Rivera, F. J., Cetinbas, N. M., Wu, K., Joshi, N. S., Helenius, K., Park, Y., Azimi, R., Kerper, N. R., Wesselhoeft, R. A., Gu, X., Schmidt, L., Cornwall-Brady, M., Yilmaz, Ö. H., Xue, W., Katajisto, P., Bhutkar, A., & Jacks, T. (2017). A Wnt-producing niche drives proliferative potential and progression in lung adenocarcinoma. *Nature*. https://doi.org/10.1038/nature22334

ten Dijke, P., & Hill, C. S. (2004). New insights into TGF-beta-Smad signalling. *Trends in Biochemical Sciences*, *29*(5), 265–273. https://doi.org/10.1016/j.tibs.2004.03.008

Tenni, R., Valli, M., Rossi, A., & Cetta, G. (1993). Possible role of overglycosylation in the type I collagen triple helical domain in the molecular pathogenesis of osteogenesis imperfecta. *American Journal of Medical Genetics*, *45*(2), 252–256. https://doi.org/10.1002/ajmg.1320450219

Tewary, M., Dziedzicka, D., Ostblom, J., Prochazka, L., Shakiba, N., Heydari, T., Aguilar-Hidalgo, D.,

Woodford, C., Piccinini, E., Becerra-Alonso, D., Vickers, A., Louis, B., Rahman, N., Danovi, D., Geens, M., Watt, F. M., & Zandstra, P. W. (2019). High-throughput micropatterning platform reveals Nodal-dependent bisection of peri-gastrulation–associated versus preneurulation-associated fate patterning. *PLoS Biology*. https://doi.org/10.1371/journal.pbio.3000081

Tewary, M., Ostblom, J., Prochazka, L., Zulueta-Coarasa, T., Shakiba, N., Fernandez-Gonzalez, R., & Zandstra, P. W. (2017). A stepwise model of reaction-diffusion and positional information governs self-organized human peri-gastrulation-like patterning. *Development (Cambridge)*. https://doi.org/10.1242/dev.149658

Tholozan, F. M. D., Gribbon, C., Li, Z., Goldberg, M. W., Prescott, A. R., McKie, N., & Quinlan, R. A. (2007). FGF-2 release from the lens capsule by MMP-2 maintains lens epithelial cell viability. *Molecular Biology of the Cell*, *18*(11), 4222–4231. https://doi.org/10.1091/mbc.E06-05-0416

Timpl, R., & Brown, J. C. (1994). The laminins. *Matrix Biology*, *14*(4), 275–281. https://doi.org/10.1016/0945-053X(94)90192-9

Topol, L., Jiang, X., Choi, H., Garrett-Beal, L., Carolan, P. J., & Yang, Y. (2003). Wnt-5a inhibits the canonical Wnt pathway by promoting GSK-3-independent β-catenin degradation. *Journal of Cell Biology*. https://doi.org/10.1083/jcb.200303158

Trinh, L. A., & Stainier, D. Y. R. (2004). Fibronectin regulates epithelial organization during myocardial migration in zebrafish. *Developmental Cell*, *6*(3), 371–382. https://doi.org/10.1016/S1534-5807(04)00063-2

Trounson, A., & DeWitt, N. D. (2016). Pluripotent stem cells progressing to the clinic. *Nature Reviews. Molecular Cell Biology*. https://doi.org/10.1038/nrm.2016.10

Tsang, K. Y., Cheung, M. C. H., Chan, D., & Cheah, K. S. E. (2010). The developmental roles of the

extracellular matrix: beyond structure to regulation. *Cell and Tissue Research*, *339*(1), 93–110. https://doi.org/10.1007/s00441-009-0893-8

Tseng, Q., Duchemin-Pelletier, E., Deshiere, A., Balland, M., Guilloud, H., Filhol, O., & Théry, M. (2012). Spatial organization of the extracellular matrix regulates cell-cell junction positioning. *Proceedings of the National Academy of Sciences of the United States of America*. https://doi.org/10.1073/pnas.1106377109

Turlier, H., & Maître, J. L. (2015). Mechanics of tissue compaction. In *Seminars in Cell and Developmental Biology*. https://doi.org/10.1016/j.semcdb.2015.08.001

Ungrin, M. D., Joshi, C., Nica, A., Bauwens, C., & Zandstra, P. W. (2008). Reproducible, ultra high-throughput formation of multicellular organization from single cell suspension-derived human embryonic stem cell aggregates. *PLoS ONE*. https://doi.org/10.1371/journal.pone.0001565

Urlinger, S., Baron, U., Thellmann, M., Hasan, M. T., Bujard, H., & Hillen, W. (2000). Exploring the sequence space for tetracycline-dependent transcriptional activators: Novel mutations yield expanded range and sensitivity. *Proceedings of the National Academy of Sciences of the United States of America*. https://doi.org/10.1073/pnas.130192197

van Amerongen, R., & Nusse, R. (2009). Towards an integrated view of Wnt signaling in development. *Development*. https://doi.org/10.1242/dev.033910

van den Brink, S. C., Alemany, A., van Batenburg, V., Moris, N., Blotenburg, M., Vivié, J., Baillie-Johnson, P., Nichols, J., Sonnen, K. F., Martinez Arias, A., & van Oudenaarden, A. (2020). Single-cell and spatial transcriptomics reveal somitogenesis in gastruloids. *Nature*. https://doi.org/10.1038/s41586-020-2024-3

Van Den Brink, S. C., Baillie-Johnson, P., Balayo, T., Hadjantonakis, A. K., Nowotschin, S., Turner,

D. A., & Arias, A. M. (2014). Symmetry breaking, germ layer specification and axial organisation in aggregates of mouse embryonic stem cells. *Development (Cambridge)*. https://doi.org/10.1242/dev.113001

van der Kraan, P. M., Blaney Davidson, E. N., Blom, A., & van den Berg, W. B. (2009). TGF-beta signaling in chondrocyte terminal differentiation and osteoarthritis. Modulation and integration of signaling pathways through receptor-Smads. In *Osteoarthritis and Cartilage* (Vol. 17, Issue 12, pp. 1539–1545). https://doi.org/10.1016/j.joca.2009.06.008

Van Essen, D. C. (1997). A tension-based theory of morphogenesis and compact wiring in the central nervous system. In *Nature*. https://doi.org/10.1038/385313a0

Vijayraghavan, D. S., & Davidson, L. A. (2017). Mechanics of neurulation: From classical to current perspectives on the physical mechanics that shape, fold, and form the neural tube. In *Birth defects research*. https://doi.org/10.1002/bdra.23557

Voiculescu, O., Bodenstein, L., Jun, I. L., & Stern, C. D. (2014). Local cell interactions and self-amplifying individual cell ingression drive amniote gastrulation. *ELife*. https://doi.org/10.7554/eLife.01817

Volk, S. W., Shah, S. R., Cohen, A. J., Wang, Y., Brisson, B. K., Vogel, L. K., Hankenson, K. D., & Adams, S. L. (2014). Type III collagen regulates osteoblastogenesis and the quantity of trabecular bone. *Calcified Tissue International*. https://doi.org/10.1007/s00223-014-9843-x

Volk, T., Fessler, L. I., & Fessler, J. H. (1990). A role for integrin in the formation of sarcomeric cytoarchitecture. *Cell*, *63*(3), 525–536. https://doi.org/10.1016/0092-8674(90)90449-O

Voloshanenko, O., Gmach, P., Winter, J., Kranz, D., & Boutros, M. (2017). Mapping of Wnt-Frizzled interactions by multiplex CRISPR targeting of receptor gene families. *FASEB Journal*.

https://doi.org/10.1096/fj.201700144R

Von Maltzahn, J., Bentzinger, C. F., & Rudnicki, M. A. (2012). Wnt7a-Fzd7 signalling directly activates the Akt/mTOR anabolic growth pathway in skeletal muscle. *Nature Cell Biology*. https://doi.org/10.1038/ncb2404

von Mende, N., Bird, D. M., Albert, P. S., & Riddle, D. L. (1988). dpy-13: A nematode collagen gene that affects body shape. *Cell*, *55*(4), 567–576. https://doi.org/10.1016/0092-8674(88)90215-2

Wang, L., Wu, Y., Hu, T., Guo, B., & Ma, P. X. (2017). Electrospun conductive nanofibrous scaffolds for engineering cardiac tissue and 3D bioactuators. *Acta Biomaterialia*. https://doi.org/10.1016/j.actbio.2017.06.036

Wang, X., Harris, R. E., Bayston, L. J., & Ashe, H. L. (2008). Type IV collagens regulate BMP signalling in Drosophila. *Nature*, *455*(7209), 72–77. https://doi.org/nature07214 [pii]\r10.1038/nature07214

Warmflash, A., Sorre, B., Etoc, F., Siggia, E. D., & Brivanlou, A. H. (2014). A method to recapitulate early embryonic spatial patterning in human embryonic stem cells. *Nat Methods*, *11*(8), 847–854. https://doi.org/10.1038/nmeth.3016

Weiss, A., & Attisano, L. (2013). The TGFbeta superfamily signaling pathway. In *Wiley Interdisciplinary Reviews: Developmental Biology*. https://doi.org/10.1002/wdev.86

Westfall, T. A., Brimeyer, R., Twedt, J., Gladon, J., Olberding, A., Furutani-Seiki, M., & Slusarski, D. C. (2003). Wnt-5/pipetail functions in vertebrate axis formation as a negative regulator of Wnt/β-catenin activity. *Journal of Cell Biology*. https://doi.org/10.1083/jcb.200303107

Wilcox, M., DiAntonio, A., & Leptin, M. (1989). The function of PS integrins in Drosophila wing morphogenesis. *Development*.

Williams, M. L., & Solnica-Krezel, L. (2017). Regulation of gastrulation movements by emergent cell and tissue interactions. In *Current Opinion in Cell Biology*. https://doi.org/10.1016/j.ceb.2017.04.006

Winer, J. P., Janmey, P. A., McCormick, M. E., & Funaki, M. (2009). Bone Marrow-Derived Human Mesenchymal Stem Cells Become Quiescent on Soft Substrates but Remain Responsive to Chemical or Mechanical Stimuli. *Tissue Engineering Part A*, *15*(1), 147–154. https://doi.org/10.1089/ten.tea.2007.0388

Wipff, P. J., Rifkin, D. B., Meister, J. J., & Hinz, B. (2007). Myofibroblast contraction activates latent TGF-β1 from the extracellular matrix. *Journal of Cell Biology*, *179*(6), 1311–1323. https://doi.org/10.1083/jcb.200704042

Xu, R., Nelson, C. M., Muschler, J. L., Veiseh, M., Vonderhaar, B. K., & Bissell, M. J. (2009). Sustained activation of STAT5 is essential for chromatin remodeling and maintenance of mammary-specifi c function. *Journal of Cell Biology*, *184*(1), 57–66. https://doi.org/10.1083/jcb.200807021

Xue, X., Sun, Y., Resto-Irizarry, A. M., Yuan, Y., Aw Yong, K. M., Zheng, Y., Weng, S., Shao, Y., Chai, Y., Studer, L., & Fu, J. (2018). Mechanics-guided embryonic patterning of neuroectoderm tissue from human pluripotent stem cells. *Nature Materials*. https://doi.org/10.1038/s41563-018-0082-9

Yam, P. T., & Charron, F. (2013). Signaling mechanisms of non-conventional axon guidance cues: The Shh, BMP and Wnt morphogens. In *Current Opinion in Neurobiology*. https://doi.org/10.1016/j.conb.2013.09.002

Yamaguchi, Y. (2000). Lecticans: organizers of the brain extracellular matrix. *Cellular and Molecular Life Sciences*, *57*(2), 276–289. https://doi.org/10.1007/PL00000690

Yamauchi, M., & Sricholpech, M. (2012). Lysine post-translational modifications of collagen. *Essays In Biochemistry*, *52*, 113–133. https://doi.org/10.1042/bse0520113

Yang, Y., & Mlodzik, M. (2015). Wnt-Frizzled/Planar Cell Polarity Signaling: Cellular Orientation by Facing the Wind (Wnt). *Annual Review of Cell and Developmental Biology*. https://doi.org/10.1146/annurev-cellbio-100814-125315

Ying, Q. L., Wray, J., Nichols, J., Batlle-Morera, L., Doble, B., Woodgett, J., Cohen, P., & Smith, A. (2008). The ground state of embryonic stem cell self-renewal. *Nature*. https://doi.org/10.1038/nature06968

Yoon, B. S., Ovchinnikov, D. a, Yoshii, I., Mishina, Y., Behringer, R. R., & Lyons, K. M. (2005). Bmpr1a and Bmpr1b have overlapping functions and are essential for chondrogenesis in vivo. *Proceedings of the National Academy of Sciences of the United States of America*, *102*, 5062–5067. https://doi.org/10.1073/pnas.0500031102

Yost, H. J. (1992). Regulation of vertebrate left-right asymmetries by extracellular matrix. *Nature*, *357*(6374), 158–161. https://doi.org/10.1038/357158a0

Zepp, J. A., Zacharias, W. J., Frank, D. B., Cavanaugh, C. A., Zhou, S., Morley, M. P., & Morrisey, E. E. (2017). Distinct Mesenchymal Lineages and Niches Promote Epithelial Self-Renewal and Myofibrogenesis in the Lung. *Cell*. https://doi.org/10.1016/j.cell.2017.07.034

Zhang, J., Bai, S., Zhang, X., Nagase, H., & Sarras, M. P. (2003). The expression of gelatinase A (MMP-2) is required for normal development of zebrafish embryos. *Development Genes and Evolution*. https://doi.org/10.1007/s00427-003-0346-4

Zhang, Y., Su, J., Yu, J., Bu, X., Ren, T., Liu, X., & Yao, L. (2011). An essential role of discoidin domain receptor 2 (DDR2) in osteoblast differentiation and chondrocyte maturation via

modulation of Runx2 activation. *Journal of Bone and Mineral Research*, *26*(3), 604–617. https://doi.org/10.1002/jbmr.225

Zhao, B., Tumaneng, K., & Guan, K.-L. (2011). The Hippo pathway in organ size control, tissue regeneration and stem cell self-renewal. *Nature Cell Biology*, *13*(8), 877–883. https://doi.org/10.1038/ncb2303

Zheng, Y., Xue, X., Shao, Y., Wang, S., Esfahani, S. N., Li, Z., Muncie, J. M., Lakins, J. N., Weaver, V. M., Gumucio, D. L., & Fu, J. (2019). Controlled modelling of human epiblast and amnion development using stem cells. *Nature*. https://doi.org/10.1038/s41586-019-1535-2

Zhong, C., Chrzanowska-Wodnicka, M., Brown, J., Shaub, A., Belkin, A. M., & Burridge, K. (1998). Rho-mediated contractility exposes a cryptic site in fibronectin and induces fibronectin matrix assembly. *Journal of Cell Biology*, *141*(2), 539–551. https://doi.org/10.1083/jcb.141.2.539

Zhong, Z., & Akkus, O. (2011). Effects of age and shear rate on the rheological properties of human yellow bone marrow. *Biorheology*. https://doi.org/10.3233/BIR-2011-0587

Zhu, Y., Oganesian, A., Keene, D. R., & Sandell, L. J. (1999). Type IIA procollagen containing the cysteine-rich amino propeptide is deposited in the extracellular matrix of prechondrogenic tissue and binds to TGF-??1 and BMP-2. *Journal of Cell Biology*, *144*(5), 1069–1080. https://doi.org/10.1083/jcb.144.5.1069

Zusman, S., Patel-King, R. S., Ffrench-Constant, C., & Hynes, R. O. (1990). Requirements for integrins during Drosophila development. *Development (Cambridge, England)*, *108*(3), 391–402. https://doi.org/10.1038/342285a0

Publishing Agreement

It is the policy of the University to encourage open access and broad distribution of all theses, dissertations, and manuscripts. The Graduate Division will facilitate the distribution of UCSF theses, dissertations, and manuscripts to the UCSF Library for open access and distribution. UCSF will make such theses, dissertations, and manuscripts accessible to the public and will take reasonable steps to preserve these works in perpetuity.

I hereby grant the non-exclusive, perpetual right to The Regents of the University of California to reproduce, publicly display, distribute, preserve, and publish copies of my thesis, dissertation, or manuscript in any form or media, now existing or later derived, including access online for teaching, research, and public service purposes.

DocuSigned by:
Jonathon Muncie
B3BA0B5421F84C6...
Author Signature

12/2/2020
Date